Physik - Department

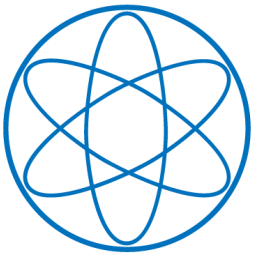

Liquid Scintillators and Liquefied Rare Gases for Particle Detectors

Background-Determination in Double Chooz and Scintillation Properties of Liquid Argon

Dissertation
von

Martin Alexander Hofmann

Technische Universität München

Technische Universität München

Lehrstuhl E15 für Experimentalphysik und Astroteilchenphysik

Liquid Scintillators and Liquefied Rare Gases for Particle Detectors

Background-Determination in Double Chooz and Scintillation Properties of Liquid Argon

Martin Alexander Hofmann

Vollständiger Abdruck der von der Fakultät für Physik der Technischen Universität München zur Erlangung des akademischen Grades eines

Doktors der Naturwissenschaften (Dr. rer. nat.)

genehmigten Dissertation.

Vorsitzender:	Univ.-Prof. Dr. A. Ibarra
Prüfer der Dissertation:	1. Univ.-Prof. Dr. L. Oberauer
	2. Priv.-Doz. Dr. A. Ulrich
	3. Priv.-Doz. Dr. H. Kroha

Die Dissertation wurde am 27.09.2012 bei der Technischen Universität München eingereicht und durch die Fakultät für Physik am 27.11.2012 angenommen.

Für meine Oma
Therese Schäufler

Abstract

Evidence for physics beyond the well-established standard model of particle physics is found in the sector of neutrino physics, in particular in neutrino oscillations, and in experimental hints requiring the presence of Dark Matter. Neutrino oscillations demand the neutrinos to be massive and at least four additional parameters, three mixing angles and one phase, are introduced. A non-vanishing value for the third mixing angle, ϑ_{13}, has only recently been found, amongst others by the reactor antineutrino disappearance experiment Double Chooz. This experiment detects $\bar{\nu}_e$'s by means of the Inverse Beta Decay (IBD), which has a clear signature that can very effectively be discriminated from most of the background.

However, some background still survives the selection cuts applied to the data, partly induced by radioactivity. In order to determine the amount of radioimpurities in the detector, germanium spectroscopy measurements and neutron activation analyses have been carried out for various parts of the Double Chooz far detector. A dedicated Monte-Carlo simulation was performed to obtain the singles event rate induced by the identified radioimpurities in the fiducial volume of Double Chooz. In the present thesis, parts from the outer detector systems, as well as components of the inner detector liquids were measured. In sum, a singles rate of less than 0.35 Hz above the antineutrino detection threshold of 0.7 MeV has been found. This is by far below the design goal of Double Chooz of ~ 20 Hz.

The analysis of bismuth-polonium (BiPo) coincidences in the first Double Chooz data allows to directly determine the number of decays from the U- and the Th-decay chain in the active detector parts. Assuming radioactive equilibrium, concentrations of $(1.71 \pm 0.08) \cdot 10^{-14} \frac{g}{g}$ for uranium and $(8.16 \pm 0.49) \cdot 10^{-14} \frac{g}{g}$ for thorium have been found, which are also well below the design goal of Double Chooz ($2 \cdot 10^{-13} \frac{g}{g}$). Both gamma spectroscopy measurements and the BiPo analysis show the high level of radiopurity reached in Double Chooz. In addition, with the BiPo analysis the α-quenching factors for the Target and the GammaCatcher liquids have been determined, respectively, to 9.94 ± 0.04 and 13.69 ± 0.02 at 7.7 MeV, and 9.05 ± 0.01 and 14.3 ± 0.1 at 8.8 MeV. The former values show a good agreement with the values obtained in a dedicated laboratory measurement. The time stability of the peak position of the ^{214}Po α-peak could be proven, too, showing a stable detector performance at low visible energies.

The direct search for Dark Matter can, amongst others, be performed with liquid rare gas detectors, which make use of the scintillation light. However, a good background discrimination is needed. Studies on the wavelength- and time-resolved scintillation properties of liquid argon have therefore been carried out with high resolution and best statistics. The results obtained for different ion beams show that particle discrimination is not feasible in any realistic experiment by means of the wavelength-resolved scintillation light only, but the time structure of the emitted light provides a good handle to distinguish between different incident particles. For heavy ions (sulfur) a ratio of the fast to the slow scintillation component of (1.6 ± 0.6) is found, while lighter particles (protons) exhibit a ratio of (0.25 ± 0.05). The outcome of the present studies shows that this ratio can also be used in wavelength-integrating measurements which have a comparable detection efficiency for wavelengths below and above ~ 170 nm. The present results demonstrate that for a number of 90 detected photons the singlet-to-triplet distributions obtained for sulfur ions and protons as exciting particles cease to overlap. In a Dark Matter experiment, if all photons produced can be detected, this corresponds to a discrimination threshold of only 2.25 keV.

Zusammenfassung

Physik jenseits des etablierten Standardmodells der Teilchenphysik kann im Sektor der Neutrinophysik, speziell bei Neutrinooszillationen, und bei den experimentellen Hinweisen auf die Existenz Dunkler Materie gefunden werden. Für das Auftreten von Neutrinooszillationen sind Neutrinos mit von Null verschiedener Masse nötig. Außerdem müssen mindestens vier weitere Parameter, drei Mischungswinkel und eine Phase, eingeführt werden. Für den dritten Mischungswinkel ϑ_{13} wurde erst kürzlich ein von Null verschiedener Wert gefunden. An dieser Messung war unter anderem das Reaktorneutrinoexperiment Double Chooz beteiligt, das als Nachweisreaktion den inversen Betazerfall nutzt, welcher eine gut zu bestimmende Signatur hat, die sehr effektiv von Untergrundereignissen unterschieden werden kann.

Einige Untergrundereignisse bleiben jedoch auch nach Anwendung der Selektionskriterien übrig, unter anderem solche, die durch Radioaktivität im Detektor verursacht werden. Deshalb wurden Germaniumspektrometrie-Messungen und Neutronenaktivierungsanalysen für verscheidene Teile des fernen Double Chooz Detektors durchgeführt, um den Gehalt an radioaktiven Verunreinigungen zu bestimmen. Mittels einer Monte-Carlo-Simulation wurde die resultierende Anzahl an Untergrundereignissen im Double Chooz Detektor bestimmt. Insgesamt verursachen die untersuchten Teile, Komponenten des äußeren Detektors sowie der Detektorflüssigkeiten, Ereignisraten von weniger als 0.35 Hz oberhalb der für die Neutrinosuche relevanten Energieschwelle von 0.7 keV, was deutlich weniger ist als die für den Detektor insgesamt angestrebten 20 Hz.

Die Zahl der Zerfälle von Radioisotopen aus den Zerfallsreihen von Uran und Thorium konnte direkt aus den Detektordaten mittels einer Analyse der BiPo-Koinzidenzen bestimmt werden. Unter der Annahme radioaktiven Gleichgewichts ergeben sich Massenkonzentrationen von $(1.71 \pm 0.08) \cdot 10^{-14}\,\frac{\mathrm{g}}{\mathrm{g}}$ für Uran und $(8.16 \pm 0.49) \cdot 10^{-14}\,\frac{\mathrm{g}}{\mathrm{g}}$ für Thorium, die beide ebenfalls weit unterhalb des angestrebten Wertes, hier $2 \cdot 10^{-13}\,\frac{\mathrm{g}}{\mathrm{g}}$, liegen. Die Ergebnisse zeigen den hohen Reinheitsgrad, der bei Double Chooz erreicht wurde. Des weiteren konnten mit der BiPo-Analyse die Quenchingfaktoren für α-Teilchen in den innersten Detektorvolumina, *Target* und *GammaCatcher*, zu 9.94 ± 0.04 bzw. 13.69 ± 0.02 bei 7.7 MeV und 9.05 ± 0.01 bzw. 14.3 ± 0.1 bei 8.8 MeV bestimmt werden. Die Werte bei 7.7 MeV bestätigen die Ergebnisse einer unabhängigen Labormessung. Auch die Stabilität des Detektors konnte verifiziert werden, indem die Position des α-Peaks von ^{214}Po als Funktion der Zeit analysiert wurde.

Verflüssigte Edelgase eignen sich für Szintillationsexperimente zur direkten Suche nach Dunkler Materie. Solche Experimente benötigen jedoch eine gute Untergrundunterdrückung, weshalb im Rahmen der vorliegenden Arbeit die Szintillationseigenschaften von verflüssigtem Argon als Funktion der Wellenlänge und der Zeit untersucht wurden. Während sich herausstellte, dass sich eine wellenlängenaufgelöste Messung alleine nicht zur Unterscheidung verschiedener Teilchen im Detektor eignet, konnte bei der Zeitstruktur des Szintillationslichts ein Parameter identifiziert werden, der eine Teilchendiskriminierung ermöglicht, das Intensitätsverhältnis von schneller zu langsamer Szintillationslichtkomponente. Für einen Schwefelstrahl liegt dieses Verhältnis bei (1.6 ± 0.6), während für einen Protonenstrahl (0.25 ± 0.05) gemessen wurde. Dieses Intensitätsverhältnis lässt sich auch in wellenlängenintegrierenden Messungen nutzen, zumindest solange die Effizienz des Detektors für Wellenlängen ober- und unterhalb von ~ 170 nm in der gleichen Größenordnung liegt. Bei 90 detektierten Photonen überlappen die Intensitätsverhältnis-Verteilungen von Schwefelionen und Protonen nicht mehr, was in einem Experiment zur Suche nach Dunkler Materie eine Trennschwelle von 2.25 keV zulässt, vorausgesetzt alle erzeugten Photonen werden letztlich auch detektiert.

Contents

Part I

Astroparticle Physics beyond the Standard Model: Open Questions in Neutrino Physics and the Search for Dark Matter

Chapter 1

Charged Leptons, Neutrinos, and Baryons in the Standard Model of Particle Physics

The standard model[1] of particle physics [Alt05, Aur97, Gai98, Hal84, Sch95] contains all experimentally proven elementary particles and describes their interactions. The only exception is the gravitational force, which is not included in the standard model[2]. The elementary particles are divided into two major groups according to their spin: the spin-$\frac{1}{2}$ fermions making up the matter, and the spin-1 gauge bosons mediating the interaction forces. Within the group of the fermions there are the light leptons and the heavier quarks, which are both again subgrouped into 3 families (see table 1.1). To each of these fermions exists one antiparticle with the same mass, but opposite electrical charge and lepton (family) number[3].

The three interaction forces contained in the standard model are the electromagnetic force with infinite range, and the short-ranged strong and weak interactions. The strong interaction is described by the theory of quantum chromodynamics [Alt05], and is mediated by 8 different gluons, which are massless and couple to colour charge. As of the fermions only quarks are coloured, leptons stay totally unaffected by this interaction. In principle, one would expect the strong force also to have infinite range, as the gauge bosons are massless, but due to the self-coupling of the gluons (they also carry colour charge) [Gai98] and the non-existence of a colour-singlet gluon [Aur97] the strong force is restricted to a range of about 1 fm [Sch95].

The other two interactions in the standard model, electromagnetic and weak forces, are, in fact, only different manifestations of the electroweak interaction as described by the Glashow-Salam-Weinberg theory (GSW) [Alt05, Wei74]. However, towards low energies a spontaneous symmetry breaking occurs, which gives mass to the gauge bosons of the weak interaction, $W^{\pm}$ and Z^0, and, thus, separates the unified force into the weak and electromagnetic interactions [Wei74]. According to the uncertainty principle, the masses of $W^{\pm}$ and Z^0 (80 GeV and

[1] Here and in the following the term "standard model" denotes always the minimal standard model without any extensions.

[2] Gravitation is described by Einstein's theory of General Relativity [Ber04, Bor03, Sex02], which is a "classical" non-quantised theory. Up to now there is no quantum field theory for the gravitational force, as well as the hypothetical graviton - the gauge boson of this force - was not detected yet in any experiment [Gai98].

[3] This is also true for neutrinos assuming the Dirac case. If neutrinos are Majorana particles, they are their own antiparticles, which differ only in helicity [Obe92, Sch97]. For a detailed discussion cf. chapter 3.

LEPTONS			
	electron e^-	muon μ^-	tau lepton τ^-
mass [MeV]	0.511	105.66	1776.82
charge [e]	-1	-1	-1
	electron neutrino ν_e	muon neutrino ν_μ	tau neutrino ν_τ
mass [MeV]	0	0	0
charge [e]	0	0	0
QUARKS			
	up quark u	charm quark c	top quark t
mass [MeV]	1.8 - 3.0	1250 - 1300	173500
charge [e]	$+\frac{2}{3}$	$+\frac{2}{3}$	$+\frac{2}{3}$
	down quark d	strange quark s	bottom quark b
mass [MeV]	4.5 - 5.5	90 - 100	4180
charge [e]	$-\frac{1}{3}$	$-\frac{1}{3}$	$-\frac{1}{3}$

Table 1.1: *The elementary fermions in the standard model of particle physics, grouped into 3 families (3 columns), and their masses and electrical charges. Natural units are used, i.e. $c = 1$, and the elementary charge e is considered to be positive. Note that in the standard model the neutrinos are massless [Aur97]. For the quarks the so-called stream quark masses are given, i.e. the masses of the "free" quarks (although there exist no free quarks). These masses are calculated from the masses of the hadrons, bound states of the quarks. For each of these particles exists one antiparticle with same mass but opposite electrical charge. All data taken from [PDG12].*

91 GeV, respectively [PDG12]) result in a very short interaction range of about 10^{-3} fm:

$$r \propto t \approx \frac{1}{2E} \overset{p \ll m}{\approx} \frac{1}{2m} \quad . \tag{1.1}$$

Therefore, the weak interaction seems to be the weakest of the three forces in the standard model at low energies (in terms of reaction cross sections) [Gai98], although its coupling constant is of the same order of magnitude as that of the electromagnetic interaction [Wei74]. However, the gauge bosons of the latter, the photons, stay massless and have no self-coupling. Therefore, electromagnetic force has infinite range, which results in larger cross sections than measured for processes of the weak interaction. The photon couples to the electrical charge, hence, all charged particles are affected by electromagnetism, but not the neutrinos. In contrast, weak interaction couples to all elementary fermions, but this coupling of the $W^\pm$ and Z^0 bosons depends on the chirality (the "handedness") of the fermion [Sch95].

As was shown by several experiments [Gar57, Sch66, Wu57], the $W^\pm$ bosons couple only to the left-handed fermion states (and right-handed antifermion states) [Alt05, Sch95], the respective other components stay completely unaffected by charged current reactions of the weak interaction. The Z^0 boson, however, couples both to the left- and right-handed fermion states, but its coupling strength to the right-handed component is proportional to the electric charge of the fermion [Alt05, Sch95], an outcome of the GSW theory. As a consequence, uncharged right-handed fermions, or uncharged left-handed antifermions, respectively, do not

participate in processes of weak interaction at all, as is the case e.g. for right-handed Dirac neutrinos.

Of all the fermions only the particles from the first family and the neutrinos are stable[4], all others decay by processes of the weak interaction where lepton number and lepton family number are conserved [Sch95]. While the leptons can be observed as free particles, the quarks form bound states of the strong interaction [Alt05, Sch95], the hadrons, either by pairing one quark and one antiquark to a meson, or three (anti)quarks to one (anti)baryon. An extract of the huge number of possible baryons and their valence quark content is given in fig. 1.1.

All mesons and all (anti)baryons, except for the (anti)proton[5], are unstable and decay by processes of the electromagnetic, strong, or weak interaction. Free neutrons also decay with a life time of 881.5 s [PDG12], however, they can exist for longer times when bound in atomic nuclei. Note that in the standard model the baryon number is also conserved, but not the family number of the quarks. The latter results from the mixing between the quark eigenstates of the weak interaction ("flavour eigenstates") and their eigenstates of the strong interaction by means of the CKM-matrix[6], a complex 3x3-matrix with 4 free parameters (3 mixing angles and one CP-violating phase) [Alt05, Gai98].

In the standard model particle masses are generated via the Higgs mechanism [Alt05, Aur97, Sch95]. This mechanism, however, predicts another free particle, the Higgs boson, with zero spin. Recently, a new particle consistent with the Higgs boson has been discovered by the LHC-experiments ATLAS and CMS in the mass region around 125-126 GeV [CER12]. In case this particle really proves to be the sought-for Higgs boson another key issue in particle physics would have been solved.

In the last decades, the standard model as presented here has proven to be very successful in describing many processes in particle physics, however, there are still some unresolved questions related to it. The standard model has 19 free parameters [Aur97, Tro11], like the particle masses, the CKM mixing parameters, or the coupling strengths, which are not determined by the theory itself, but have to be put in "by hand". This raises not only the question, why there are so many free parameters, but also if there is a more general theory which allows a calculation of the parameters' values and which, furthermore, can explain the existence of exactly three generations. In addition, as was already mentioned at the beginning of this chapter, the standard model actually does not contain gravitation, although this is one of the fundamental forces in nature. Some of these issues immediately hint to new physics beyond the standard model and an even more all-embracing theory.

As will be presented in chapter 2 of this thesis, physics beyond the standard model has already been found in the neutrino sector. From the experimentally proven existence of neutrino oscillations [PDG12] it can be derived that neutrinos need to be massive, and that there are at least four additional mixing parameters, three mixing angles and minimum one CP-violating phase [Sch97]. The numerical values of these parameters are, at present, only partly known, see section 2.3, especially the values of all phases are still undetermined. Besides this, many key points in neutrino physics are not or not fully investigated, amongst others

- The absolute mass scale of neutrino masses: oscillation experiments only allow a deter-

[4]In theories beyond the standard model also neutrino decays are imaginable [Obe92]; see short discussion in section 2.2.

[5]Some theories beyond the standard model, like grand unified theories (GUTs), predict proton decays [Per00, Sch95]. However, the experimental search for this decay could not deliver any indications for unstable protons so far [Kob05, Nis09, PDG12].

[6]CKM = Cabbibo-Kobayashi-Maskawa

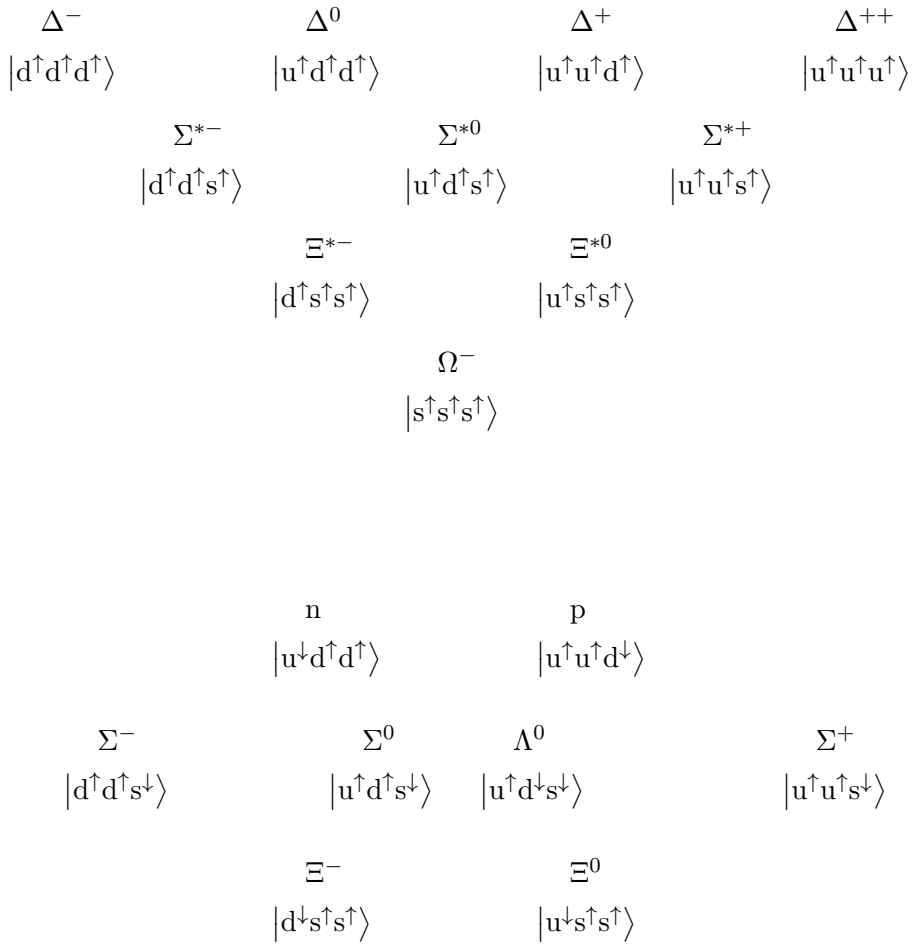

Figure 1.1: *Summary table of the ground states and singly excited states of baryons which contain only up-, down- and strange-quarks as valence quarks. The respective quark content and spin structure of the wave function are given, however, the wave functions are not yet symmetrised and the colour charge of the quarks is not indicated. The upper part of this figure shows the baryon decuplet with the spin and parity number* $J^P = \frac{3}{2}^+$*, the lower part the baryons with* $J^P = \frac{1}{2}^+$*. Note that the quark combination* $|uds\rangle$ *is found twice, once as part of an isospin triplet (*Σ^0*) and once as isospin singlet (*Λ^0*). All these baryons, except for the proton, are not stable. To each of these baryons exists an antibaryon, consisting of the corresponding antiquarks, with the same mass and half-life. Taken from [Pov04].*

mination of the mass square differences, see section 2.1, but not the absolute neutrino masses [Akh06]. So far, there exist only upper bounds from direct mass measurements and cosmology [PDG12]. But these boundaries already indicate that the neutrino masses are much smaller than those of the corresponding charged leptons, an issue also not understood yet [Tro11].

- The neutrino mass hierarchy [Akh06]. It is still unknown, whether the mass eigenvalues of the neutrinos are arranged in a normal hierarchy, i.e. $m_1 < m_2 < m_3$, where m_1 denotes the mass eigenvalue which has the biggest contribution to ν_e, or if they have an inverted hierarchy, $m_3 < m_1 < m_2$. Again, oscillation experiments can only measure the differences, not the ordering[7].

- Are neutrinos Dirac or Majorana particles? As will be discussed in chapter 3, as neutrinos are electrically neutral they can either be Dirac particles, described by a 4-component spinor with entries both for neutrino and antineutrino, in each case with spin up and spin down, or Majorana particles, where the neutrino would be its own antiparticle. The latter case allows the occurrence of the neutrinoless double β-decay [Akh00, Sch97]; see section 3.2. Kinematically, Dirac and Majorana neutrinos behave exactly the same [Akh00].

- The existence of sterile neutrinos [Akh00]. Recently, a re-analysis of data from reactor neutrino experiments gave indications for a fourth (sterile) neutrino [Men11]. This particle is neither included in the standard model, nor part of the commonly used explanations of neutrino oscillations. A perhaps heavy sterile neutrino could furthermore have a great impact on cosmology [Li11]. However, the number of active light neutrinos was precisely determined by the measurement of the Z^0-decay width at CERN [PDG12] and Big Bang Nucleosynthesis [Sar96], pinning their number down to three.

However, not only the neutrino sector clearly indicates physics beyond the standard model, but further indications come from cosmology and astrophysics, too [Tro11]. In chapter 4 the total energy content of the universe will be discussed, showing that about 70% of it are made up of Dark Energy and around 25% of Dark Matter [Lar11, Spe07]. Both cannot be explained with the standard model, neither Dark Matter, where the above listed particles do not contain a viable candidate, see sec. 4.2, nor Dark Energy, which is, at present, of completely unknown origin. Besides this, the observed matter-antimatter asymmetry [Ber04] in our universe also poses big problems to the standard model, as it clearly depicts large CP-violating processes, which probably go beyond any CP-violation contained in the standard model.

Within the scope of the present thesis experiments and experimental techniques that concern the precise measurement of the neutrino mixing angle ϑ_{13} (chapters 5 to 8) as well as the determination of the neutrino particle character, Dirac or Majorana particles, and the direct search for Dark Matter (chapters 9 to 11) shall be presented and discussed.

[7] An exception is the ordering between m_1 and m_2: from the MSW effect [Mik85, Wol78] in the sun m_2 is known to be bigger than m_1.

Chapter 2

Massive Neutrinos and Neutrino Oscillations

2.1 Quantum Mechanics of Neutrino Oscillations

The three neutrino eigenstates $(\nu_e, \nu_\mu, \nu_\tau)$ mentioned in tab. 1.1 in chapter 1 are the eigenstates of the weak interaction, the flavour eigenstates. These need not necessarily be identical to the mass eigenstates (ν_1, ν_2, ν_3); on the contrary, it was proven by several experiments on neutrino oscillations [PDG12] that they are not, but there is mixing between the two bases. This mixing can be expressed by a mixing matrix[1] and can generally be parametrised by three mixing angles ϑ_{12}, ϑ_{13}, and ϑ_{23} in addition to three phases δ, ϕ_1, and ϕ_2 [Akh00, Bil78, Bil99, Giu98, Obe92, Pon67, Sch97]:

$$|\nu_\alpha\rangle = \sum_{i=1}^{3} U_{\alpha i} |\nu_i\rangle \qquad \alpha \in \{e, \mu, \tau\}\,, \;\; i \in \{1, 2, 3\} \tag{2.1}$$

with

$$\begin{pmatrix} U_{e1} & U_{e2} & U_{e3} \\ U_{\mu 1} & U_{\mu 2} & U_{\mu 3} \\ U_{\tau 1} & U_{\tau 2} & U_{\tau 3} \end{pmatrix} = \begin{pmatrix} 1 & 0 & 0 \\ 0 & c_{23} & s_{23} \\ 0 & -s_{23} & c_{23} \end{pmatrix} \begin{pmatrix} c_{13} & 0 & s_{13} e^{-i\delta} \\ 0 & 1 & 0 \\ -s_{13} e^{i\delta} & 0 & c_{13} \end{pmatrix} \times$$
$$\times \begin{pmatrix} c_{12} & s_{12} & 0 \\ -s_{12} & c_{12} & 0 \\ 0 & 0 & 1 \end{pmatrix} \begin{pmatrix} e^{\frac{i}{2}\phi_1} & 0 & 0 \\ 0 & e^{\frac{i}{2}\phi_2} & 0 \\ 0 & 0 & 1 \end{pmatrix} \,. \tag{2.2}$$

Hereby, s_{ij} and c_{ij} denote $\sin(\vartheta_{ij})$ and $\cos(\vartheta_{ij})$, respectively.

For more than two neutrino families neutrino oscillations can, in general, violate CP-symmetry; this CP-violation is described by the phase δ [Akh00]. The two phases ϕ_1 and ϕ_2 are the so-called Majorana phases and vanish in case neutrinos are Dirac particles; furthermore, ϕ_1 and ϕ_2 cancel out for neutrino oscillations [Akh06, Bil99]. As a consequence, an experiment on neutrino oscillations can not distinguish between the pure Dirac and the pure

[1] This mixing matrix is in the literature often referred to as Pontecorvo-Maki-Nakagawa-Sakata matrix, or short PMNS matrix [Mak62].

Majorana case[2] [Akh00]. For antineutrinos the mixing is also described by eq. (2.1), but the complex conjugate matrix elements $U^*_{\alpha i}$ have to be taken [Akh00].

The neutrino flavour eigenstates are responsible for neutrino production and detection[3], the mass eigenstates for neutrino propagation (i.e. they are the solutions of the Dirac equation). By inserting the time evolution of the mass eigenstates into eq. (2.1) and projection of the result onto the flavour eigenstate $\langle\nu_\beta|$ (the detection of the neutrino is again a process of the weak interaction) the transition probability $P_{\alpha\beta}(L)$ of the flavour changing process can be calculated[4] [Sch97]:

$$P_{\alpha\beta}(L) = |A_{\alpha\beta}(L)|^2 = \sum_{i,k} U_{\alpha i} U^*_{\beta i} U^*_{\alpha k} U_{\beta k} \cdot exp\left\{-2\pi i \frac{L}{L^{osc}_{ik}}\right\} \quad . \tag{2.3}$$

L denotes hereby the distance between neutrino source and detector. In eq. (2.3) the oscillation length

$$L^{osc}_{ik} = \frac{4\pi E}{\Delta m^2_{ik}} \tag{2.4}$$

with the mass square difference $\Delta m^2_{ik} = m^2_i - m^2_k$ and the energy of the neutrino E has been defined.

Formula (2.3) illustrates the functional dependence of neutrino oscillations on its parameters: for a given neutrino energy E the wavelengths of the oscillations are given by the mass square differences Δm^2_{ik}, while the oscillation amplitudes are determined by the matrix elements $U_{\alpha i}$. These matrix elements contain the trigonometric functions of the mixing angles ϑ_{12}, ϑ_{13}, and ϑ_{23}; see eq. (2.2). Therefore, the oscillation amplitudes are determined by these mixing angles. Any effects from the phases ϕ_1 and ϕ_2, respectively, cancel out [Akh06, Bil99]. The CP-violating effect based on the phase δ can only be seen in appearance experiments, while the survival probability $P_{\alpha\alpha}$ is always CP-conserving [Akh00]. The transition probability is invariant under CPT-transformations [Akh00], which consequently leads to the equality

$$P(\nu_\alpha \to \nu_\beta) \stackrel{!}{=} P(\bar{\nu}_\beta \to \bar{\nu}_\alpha) \quad . \tag{2.5}$$

However, CP-violation could manifest itself in the comparison between neutrinos and antineutrinos, or in the time reversal:

$$P(\nu_\alpha \to \nu_\beta) \neq P(\bar{\nu}_\alpha \to \bar{\nu}_\beta) \tag{2.6}$$

$$P(\nu_\alpha \to \nu_\beta) \neq P(\nu_\beta \to \nu_\alpha) \tag{2.7}$$

Nevertheless, any CP-violating effects vanish in one of the following cases [Akh00]:

[2] However, neutrino oscillation experiments are able to distinguish the pure Dirac and Majorana cases from the more general Dirac+Majorana case, because in the latter there are also sterile neutrinos, which give rise to additional oscillation channels [Bil99]. But this shall not be discussed in detail here.

[3] If an experiment was performed where the different mass eigenstates could be determined, no oscillations would be observed [Akh11]. In that case, only a constant transition probability $P = |U_{\alpha i}|^2$ would be measured (assuming the case the neutrino is produced in the state $|\nu_\alpha\rangle$ and the mass eigenstate $|\nu_i\rangle$ is detected).

[4] Here, the "standard" plane wave approximation is made, i.e. any effects like coherence are not taken into account, and the neutrinos are taken to be relativistic. The derivation of the oscillation probability using the wave packet formalism and consequences from that can be found e.g. in [Giu98]. Natural units are used, i.e. $\hbar = c = 1$.

1. The phase δ equals 0 or $\pm\,\pi$.

2. One of the mixing angles equals 0 or $\frac{\pi}{2}$. For the case of ϑ_{13} this can immediately be seen from the parameterisation given in eq. (2.2).

3. One of the mass square differences is zero, which means that all neutrino mass eigenvalues must be different and at least two neutrino mass eigenstates must have non-vanishing masses to be able to observe CP-violating effects.

2.2 Massive Neutrino States and their Consequences

The derivation of the oscillation probability formula as given above shows two necessary preconditions for the occurrence of neutrino oscillations which contradict the minimal standard model: firstly, neutrino oscillations between different flavour eigenstates require a violation of the lepton family number conservation in flight and secondly, the oscillations cannot happen in case all mass square differences are equal to zero. The latter immediately leads to the conclusion that at least one of the three neutrino mass eigenvalues m_1, m_2, m_3 must not be zero, i.e. neutrino oscillations require massive neutrinos! The non-zero mass of the neutrinos has several important consequences:

- Compared to the expectations for a vanishing neutrino mass the energy spectrum of electrons released in a β^--decay shows deviations at the endpoint [Akh00]. In principle, these spectral deformations can be used to measure the neutrino mass directly, as is currently aimed at in experiments like KATRIN [Bor05]. However, due to the smallness of the neutrino mass these experiments need to have a good control over all systematic uncertainties and an outstanding energy resolution. In case the energy resolution is worse than the differences in the neutrino mass eigenstates, an effective neutrino mass of
$$\left\langle m_\beta^2 \right\rangle = \sum_i \left|U_{ei}\right|^2 m_i^2 \tag{2.8}$$
is measured [PDG12].

- A non-vanishing neutrino mass allows an experimental discrimination between Majorana and Dirac neutrinos [Akh00, Obe92]. Massless right-handed Dirac neutrino states and left-handed Dirac antineutrino states, respectively, do not couple to any of the four fundamental interactions (see chapter 1) and, thus, are not physical. However, for massive neutrinos these states become existing and, hence, Dirac neutrinos can be distinguished from Majorana neutrinos, for example by the neutrinoless double β-decay ($0\nu\beta\beta$); cf. also chapter 3. The latter is possible in case neutrinos were Majorana particles with a non-zero mass.

- Massive Dirac neutrinos could carry a magnetic moment [Akh97, Obe92] and by this couple to electromagnetic interaction. Furthermore, if CP-symmetry is violated they also could carry a non-vanishing electric dipole moment [Obe92].

- Decays of the heavier neutrino mass eigenstates [Obe92] into the lighter ones, e.g. the radiative decay
$$\nu_i \longrightarrow \nu_j + \gamma \quad , \tag{2.9}$$

become possible, limiting the life time. However, up to now, only lower limits on the neutrino radiative life time can be given [PDG12], e.g.

$$\frac{\tau(\nu_e)}{m(\nu_e)} > 7 \cdot 10^9 \, \frac{\mathrm{s}}{\mathrm{eV}} \quad , \tag{2.10}$$

which come, for example, from astrophysical considerations [Raf85].

- Last but not least, massive neutrinos contribute to the hot Dark Matter content of the universe [Li11]. Albeit it could be proven that neutrinos cannot account for the total energy density Ω_{DM} of the Dark Matter [Ber04], especially the cold one, their huge number of about $110\,\mathrm{cm}^{-3}$ per species [Akh00] makes them a non-negligible part of Ω_{tot}; see also discussion in chapter 4.

2.3 Already Known Oscillation Parameters

The neutrino oscillation probability (2.3) derived in section 2.1 depends on several parameters. While the energy E of the neutrino and the distance L between source and detector are fixed only by the experimental conditions (and thus may vary), there are 8 natural constants involved: the three mixing angles, the three phases (in Majorana case), and two mass square differences. In case neutrinos are Dirac particles only the phase δ is physical [Akh00, Bil80]. As the three mass square differences are connected by

$$\Delta m^2_{21} = \Delta m^2_{31} - \Delta m^2_{32} \quad , \tag{2.11}$$

only two of them are independent parameters. Table 2.1 on page 13 lists the current best fit values for the three mixing angles ϑ_{12}, ϑ_{13}, and ϑ_{23} and the two mass square differences. The values of the phases δ, ϕ_1, and ϕ_2 are not measured yet [PDG12], therefore, no values are quoted here.

The mixing angle ϑ_{13} has been found to be non-zero recently by the reactor electron antineutrino disappearance experiments Double Chooz (the resulting value is $\sin^2(2\vartheta_{13}) = 0.109 \pm 0.044$ at 68% C.L. [Abe12a], obtained from a rate plus spectral shape analysis); RENO[5] ($\sin^2(2\vartheta_{13}) = 0.113 \pm 0.013\,(\mathrm{stat.}) \pm 0.019\,(\mathrm{syst.})$ at 68% C.L. [Ahn12], rate only analysis); and Daya Bay ($\sin^2(2\vartheta_{13}) = 0.092 \pm 0.016\,(\mathrm{stat.}) \pm 0.005\,(\mathrm{syst.})$ at 68% C.L. [An12], rate only analysis). As disappearance experiments, in general, are not sensitive to CP-violation, and the reactor experiments, in particular, to first order not to ϑ_{23} due to their short baselines (see also eq. (2.15)), the only parameter that needs to be regarded for these analyses is $|\Delta m^2_{32}|$. Already in 2011, first indications for a non-vanishing value of ϑ_{13} have been reported by the accelerator experiments T2K [Abe11] and MINOS [Ada11]. However, accelerator neutrino beam experiments are not able to disentangle the ambiguity in the ϑ_{13}-δ-plane, hence, a "clean" measurement of ϑ_{13} cannot be provided.

2.4 Methods of Determining the Third Mixing Angle ϑ_{13}

The parameter overview in table 2.1 shows that besides the completely unknown phases δ, ϕ_1, ϕ_2 the neutrino mixing parameters are quite precisely determined. The values of ϑ_{12},

[5] The results of the RENO experiment are, however, under discussion; see [Las12].

Oscillation parameter	***Best fit value (90% C.L.)***	***Determining experiment(s)***
$\sin^2(2\vartheta_{12})$	$0.857^{+0.023}_{-0.025}$	*KamLAND, solar neutrinos*
$\sin^2(2\vartheta_{13})$	0.098 ± 0.013	*Double Chooz, RENO, Daya Bay*
$\sin^2(2\vartheta_{23})$	> 0.95	*Super-Kamiokande*
Δm^2_{21}	$7.50^{+0.19}_{-0.20} \cdot 10^{-5}\,\mathrm{eV}^2$	*KamLAND, solar neutrinos*
$\lvert\Delta m^2_{32}\rvert$	$2.32^{+0.12}_{-0.08} \cdot 10^{-3}\,\mathrm{eV}^2$	*MINOS*

Table 2.1: *Current best fit values at 90% confidence level of the three neutrino mixing angles and two mass square differences. For the angle ϑ_{13} the weighted average value of the reactor neutrino experiments is quoted. Besides this, also the accelerator experiments T2K [Abe11] and MINOS [Ada11] have published positive indications for a non-zero value. From the MSW effect in the sun [Mik85, Wol78] the sign of Δm^2_{21} is known to be positive, i.e. the mass eigenvalue m_2 is higher than m_1, while the sign of Δm^2_{32} is still unknown. Therefore, only the absolute value is stated. All data taken from [PDG12].*

ϑ_{23}, and the mass square differences, respectively, are already known for a longer time; the determination of ϑ_{13} happened only in 2012. The finding of a non-zero third mixing angle has important impacts on upcoming experiments, as, for example, from the parameterisation (2.2) it becomes clear that any CP-violating effects in the neutrino sector can only occur, and thus be measured, in case ϑ_{13} has a value different from zero [Akh00]. Therefore, the measured value of ϑ_{13} now allows to plan and build experiments meant to measure δ. This could be done with superbeam experiments, however, to find the optimum baseline for such experiments the value of ϑ_{13} needs to be known very precisely.

The challenge in the measurement of ϑ_{13} is the smallness of the angle causing all related oscillation effects to be very small, too. Therefore, highly precise experiments have to be performed. Two approaches turned out to be successful: superbeam experiments using neutrinos from an accelerator facility [Hub03, Men08], and reactor neutrino experiments [Obe06]. While the former can be performed either as appearance or as disappearance experiments, and thus allow a simultaneous search for CP-violation, the latter provide a pure measurement of ϑ_{13} without any ambiguities with the phase δ or other parameters. As was shown above, both methods succeeded in measuring ϑ_{13}, although with different statistical significance. In the following two sections both techniques are explained in more detail.

2.4.1 Superbeam Long Baseline Experiments

Intense neutrino or antineutrino beams from an accelerator laboratory are used for oscillation searches in superbeam experiments [Men08]. These beams provide neutrino energies up to several GeV and contain mainly ν_μ or $\bar{\nu}_\mu$, respectively, which are produced in decays of charged pions or muons. These neutrinos oscillate on their way along a secant through the earth to the detector, which is located several hundreds of kilometers away from the accelerator facility. In order to determine the size of ϑ_{13} the appearance of $\nu_e(\bar{\nu}_e)$ is looked for in these experiments. Expanding formula (2.3) as a series of the small ratio of the mass square differences

$$\alpha \equiv \frac{\Delta m^2_{21}}{|\Delta m^2_{31}|} \tag{2.12}$$

up to order α^2 and neglecting all coherence terms the transition probability $P_{\mu e}(P_{\bar{\mu}\bar{e}})$ can be written as [Fre01]

$$\begin{aligned} P_{\mu e} &\equiv P(\nu_\mu \to \nu_e) = P_0 - P_{\sin\delta} - P_{\cos\delta} + P_1 \\ P_{\bar{\mu}\bar{e}} &\equiv P(\bar{\nu}_\mu \to \bar{\nu}_e) = P_0 + P_{\sin\delta} - P_{\cos\delta} + P_1 \end{aligned} \tag{2.13}$$

with the separate terms

$$\begin{aligned} P_0 &= sin^2(\vartheta_{23}) \cdot sin^2(2\vartheta_{13}) \cdot sin^2\left(\frac{\Delta m^2_{31} \cdot L}{4E}\right) \\ P_{\sin\delta} &= \alpha \cdot sin(\delta) \cdot cos(\vartheta_{13}) \cdot sin(2\vartheta_{12}) \cdot sin(2\vartheta_{13}) \cdot \\ &\quad \cdot sin(2\vartheta_{23}) \cdot sin^3\left(\frac{\Delta m^2_{31} \cdot L}{4E}\right) \\ P_{\cos\delta} &= \alpha \cdot cos(\delta) \cdot cos(\vartheta_{13}) \cdot sin(2\vartheta_{12}) \cdot sin(2\vartheta_{13}) \cdot \\ &\quad \cdot sin(2\vartheta_{23}) \cdot cos\left(\frac{\Delta m^2_{31} \cdot L}{4E}\right) \cdot sin^2\left(\frac{\Delta m^2_{31} \cdot L}{4E}\right) \\ P_1 &= \alpha^2 \cdot cos^2(\vartheta_{23}) \cdot sin^2(2\vartheta_{12}) \cdot sin^2\left(\frac{\Delta m^2_{31} \cdot L}{4E}\right) \quad . \end{aligned} \tag{2.14}$$

In principle, for the superbeams experiments one should not take the oscillation formula for vacuum oscillations, as is (2.3), but take into account matter effects. The oscillation formula becomes much more complicated in that case [Fre01], however, the main conclusions stay the same as from eqs. (2.14): neutrino oscillations in superbeam experiments are an interference of all oscillations between the three different mass eigenstates, including effects from the CP-violating phase[6] δ [Hub03, Win10]. This is an advantage and a disadvantage at the same time: on the one hand, accelerator neutrino experiments offer the opportunity to measure all mixing angles including ϑ_{13} simultaneously with the phase δ, the mass square differences, and also the mass hierarchy, i.e. the sign of Δm^2_{13} and Δm^2_{23}. On the other hand, the big parameter space causes the results to suffer from parameter correlations and degeneracies, making it hard to extract information e.g. on one single mixing angle. Therefore, it is desired to obtain additional information on ϑ_{13} by a different experimental technique.

[6] However, matter-induced oscillation effects might mimic a CP-violation. This poses additional difficulties to the attempt to measure δ [DeR99, Fre01].

2.4.2 Reactor Neutrino Experiments

Reactor neutrino experiments [Obe06] use the intense flux of electron antineutrinos released in β^--decays of the fission products of uranium and plutonium in a nuclear power plant for oscillation searches on short baselines. These short baselines of the order of a few kilometers and the low antineutrino energies, typically below $\sim 10\,\mathrm{MeV}$, guarantee the absence of any matter effects, however, no appearance experiments can be performed.

From eq. (2.3) the survival probability $\mathrm{P}(\bar{\nu}_e \rightarrow \bar{\nu}_e)$ for electron antineutrinos on short baselines is [Hub03, Obe06]

$$P(\bar{\nu}_e \rightarrow \bar{\nu}_e) \approx 1 - sin^2(2\vartheta_{13}) \cdot sin^2\left(\frac{\Delta m^2_{32} \cdot L}{4E}\right) , \tag{2.15}$$

since all subdominant terms and oscillation effects due to $\Delta \mathrm{m}^2_{21}$, as well as coherence terms can be neglected. (2.15) clearly shows the absence of any parameter correlations and the insensitivity to the CP-violating phase δ (as is the case for all disappearance experiments), hence, reactor neutrino experiments provide a pure measurement of ϑ_{13}. The eventually limiting factor for the reachable sensitivity in all reactor neutrino experiments are mainly the systematic uncertainties [Hub03]. Statistical uncertainties can be greatly reduced by increasing, or, at least, maximising detector mass and measuring time and do not play an essential role. As was discussed above, presently the three reactor neutrino experiments[7] DayaBay [An12], RENO [Ahn12], and Double Chooz [Abe12a] have published rather precise results on the value of ϑ_{13}. The Double Chooz project will be presented in more detail in chapter 5.

The combination of both measuring techniques, accelerator-based searches and experiments with reactor electron antineutrinos, yields the most precise determination of the mixing angle ϑ_{13}. In principle, reactor neutrino experiments are more stringent for the upper limit of ϑ_{13}, accelerator based appearance experiments better constrain ϑ_{13} towards small values. However, at present, the precise measurements of ϑ_{13} with reactor neutrino experiments dominate the best fit value of $\sin^2(2\vartheta_{13})$ both for small and large values; see also fig. 8.33 in section 8.4.

[7] For a comparison between the different experiments see [Cao07, Las05].

Chapter 3

Neutrinos: Majorana or Dirac Particles?

3.1 Majorana Theory and its Consequences

In relativistic quantum dynamics the equation of motion for a free massive fermion, described by the spinor ψ, is the Dirac equation, which can be deduced by means of the Euler-Lagrange equation from the Langrangian[1] [Ait89, Aur97, Sch95]

$$-\mathcal{L} = \overline{\psi}\left(i\gamma_\alpha \partial^\alpha - m_D\right)\psi \quad , \tag{3.1}$$

where $\overline{\psi} = \psi^\dagger\gamma_0$ denotes the adjoint spinor. The first term in (3.1) gives the kinetic energy, while the second term is the mass term, in this case a Dirac mass term [Bil80, Sch97]. In the following only mass terms shall be regarded. As the Langrangian needs to be Hermitian, the Dirac mass $\mathrm{m_D}$ needs to be real:

$$-\mathcal{L}_D^\dagger = \left(m_D\overline{\psi}\psi\right)^\dagger = m_D^*\overline{\psi}\psi \stackrel{!}{=} -\mathcal{L}_D = m_D\overline{\psi}\psi \quad . \tag{3.2}$$

Disjointing the spinors into their chiral components [Obe92, Sch95] the Dirac mass term of the Langrangian can be re-written as

$$-\mathcal{L}_D = m_D\left(\overline{\psi_L} + \overline{\psi_R}\right)\left(\psi_L + \psi_R\right) = m_D\left(\overline{\psi_L}\psi_R + \overline{\psi_R}\psi_L\right) \quad . \tag{3.3}$$

As a result, it follows that for a mass term of Dirac type one needs both a lefthanded and a righthanded state of the fermion. Consequently, neutrinos cannot have a Dirac mass in the minimal standard model, as it does not contain righthanded neutrino states [Akh00, Aur97, Obe92].

In order to generalize the mass term also antifermions are taken into account. Therefore, first of all the particle-antiparticle conjugation $\hat{\mathrm{C}}$ is applied to the fermion spinor ψ to get the antifermion spinor ψ^{C} [Akh00, Sch97]:

$$\psi^C = \eta_c\gamma_0\gamma_2\overline{\psi}^T \quad . \tag{3.4}$$

[1] Unless otherwise noted the Einstein sum convention is used, i.e. it is summed over equal Greek indices. Again, natural units ($\hbar = \mathrm{c} = 1$) are used.

η_c is a phase factor with $|\eta_c| = 1$. Herewith, a more general mass term, a Majorana mass term, can be derived in addition to $\mathcal{L}_D$ [Akh00, Obe92, Sch97]:

$$-\mathcal{L}_M = \frac{1}{2}\left(m_M \overline{\psi}\psi^C + m_M^* \overline{\psi^C}\psi\right) \quad . \tag{3.5}$$

Here, m_M is the Majorana mass, in general a complex quantity. To make clear the difference between the two types of mass terms the consequences of a global phase transformation $e^{i\varphi}$ are examined [Sch97]. For the spinors ψ and ψ^C one gets

$$\left.\begin{array}{l} \psi \to e^{i\varphi}\psi \\ \overline{\psi} \to e^{-i\varphi}\overline{\psi} \\ \psi^C \to \left(e^{i\varphi}\psi\right)^C = e^{-i\varphi}\psi^C \\ \overline{\psi^C} \to e^{i\varphi}\overline{\psi^C} \end{array}\right\} \Rightarrow \left\{\begin{array}{l} \overline{\psi}\psi \to \overline{\psi}\psi \\ \overline{\psi^C}\psi^C \to \overline{\psi^C}\psi^C \\ \overline{\psi}\psi^C \nrightarrow \overline{\psi}\psi^C \\ \overline{\psi^C}\psi \nrightarrow \overline{\psi^C}\psi \end{array}\right. \tag{3.6}$$

$\overline{\psi}\psi$ and $\overline{\psi^C}\psi^C$, and thus $\mathcal{L}_D$, are invariant under this phase transformation, which leads, according to Noether's theorem, to a conserved quantum number. In case of the leptons this quantum number is the total lepton number L. Therefore, $\overline{\psi}\psi$ ($\overline{\psi^C}\psi^C$) describe transitions of the type $l \to l$ ($\bar{l} \to \bar{l}$) with $\Delta L = 0$ [Sch97]. The other two combinations, $\overline{\psi}\psi^C$ and $\overline{\psi^C}\psi$, respectively, are not invariant under transformation (3.6) and violate the lepton number L. They describe the transitions $l \to \bar{l}$ and $\bar{l} \to l$, respectively, with $\Delta L = 2$. These transitions are forbidden for charged leptons [Obe92], consequently, a Majorana mass term of type $\mathcal{L}_M$ can only occur for neutral leptons, the neutrinos[2]. The violation of the lepton number also forbids neutrino mass terms of Majorana type in the minimal standard model [Akh00].

To come to a real value for the Majorana mass the spinors ψ and ψ^C are again disjointed into their chiral projections. From that

$$\mathcal{L}_M = \mathcal{L}_M^L + \mathcal{L}_M^R \tag{3.7}$$

with

$$\begin{aligned} -\mathcal{L}_M^L &= \frac{1}{2} m_L \left(\overline{\psi_L}\psi_R^C + \overline{\psi_R^C}\psi_L\right) \\ -\mathcal{L}_M^R &= \frac{1}{2} m_R \left(\overline{\psi_L^C}\psi_R + \overline{\psi_R}\psi_L^C\right) \end{aligned} \tag{3.8}$$

can be derived [Sch97]. The second term in each parenthesis is the Hermitian conjugated to the first term, therefore, the conclusion can be drawn that both m_L and m_R are real; cf. eq. (3.2). As a last step, the two Majorana fields

$$\chi_1 \equiv \psi_L + \psi_R^C \quad , \quad \chi_2 \equiv \psi_R + \psi_L^C \tag{3.9}$$

are defined, which allows a rather simple formulation of the above given Majorana mass terms (3.8):

$$-\mathcal{L}_M^L = \frac{1}{2} m_L \overline{\chi_1}\chi_1 \quad , \quad -\mathcal{L}_M^R = \frac{1}{2} m_R \overline{\chi_2}\chi_2 \quad . \tag{3.10}$$

[2] In general, only particles that do not exhibit any additive quantum numbers like electric charge, strangeness, magnetic and electric moments, ... can be of Majorana type [Sch97].

Noticing that $\chi_{\mathrm{i}}^{\mathrm{C}} = \chi_{\mathrm{i}}$, $\mathrm{i} = 1, 2$, it immediately follows that in the Majorana case the particle is identical to its own antiparticle [Obe92, Sch97].

In the most general case, which shall not be discussed in detail here, the Langrangian is a sum of a Dirac and a Majorana mass term with three mass parameters, the Dirac mass $\mathrm{m_D}$ and two Majorana masses $\mathrm{m_{L,R}}$ [Akh00]. From this, in the special case $\mathrm{m_L} = \mathrm{m_R} = 0$, it can be seen that the Dirac field is the sum of two degenerate Majorana fields, i.e. the pure Dirac case is a special case of the more general Majorana theory [Sch97]. Another special case is $\mathrm{m_R} \gg \mathrm{m_D}$ and $\mathrm{m_L} = 0$, the so-called Seesaw model [Akh00, Bil99]. The latter gives a possible explanation for the smallness of the neutrino masses compared to the charged lepton masses, as within the Seesaw model one of the neutrino mass eigenvalues, derived from a diagonalisation of the mass matrix, has the value

$$m_\nu = \frac{m_D^2}{m_R} \quad , \tag{3.11}$$

hence, a very heavy righthanded Majorana neutrino "pushes" the mass of the light left-handed Majorana neutrino to very small values.

The above given calculations are valid for one neutrino species. In order to extend them to three neutrino families each of the spinors ψ becomes a three component vector in the flavour space. All derivations then follow similarly to the ones given above [Akh00].

3.2 Neutrinoless Double Beta Decay

As was deduced from the mass terms in section 3.1, in the Majorana case neutrinos are their own antiparticles[3]. But as was experimentally proven neutrino and antineutrino cannot be exactly identical, as e.g. the reaction

$$\bar{\nu}_e + p \longrightarrow e^+ + n \tag{3.12}$$

can take place, while

$$\nu_e + p \longrightarrow e^+ + n \tag{3.13}$$

is not observed, although it should have the same cross section as the reaction (3.12) in case neutrino and antineutrino are the same [Sch97]. This implies that either neutrinos are Dirac particles or ν and $\bar{\nu}$ need to differ from each other at least in one property. Due to the maximal parity violation of the weak interaction [Sch95] in the standard model (ch. 1) it is known that (massless) neutrinos always appear with helicity $\lambda = -\frac{1}{2}$, while antineutrinos have $\lambda = \frac{1}{2}$ [Gol58]. Therefore, the neutrino, if of Majorana type, in reaction (3.13) has the wrong helicity to initiate it. For massless neutrinos there is no possibility to distinguish between the Dirac case, where the reaction (3.13) cannot occur because of the wrong particle type, or the Majorana case, in which the ν_{e} simply has the wrong helicity.

However, as was shown in section 2.2, from neutrino oscillations it is known that neutrinos posses mass. But for a massive particle, helicity is no longer a good quantum number, because for $\mathrm{m}_\nu > 0$ always a reference frame can be found by a Lorentz transformation which moves

[3] In the following the particle emitted together with an electron in a β^--decay is called electron *antineutrino*, while the phrase electron *neutrino* denotes the particle emitted together with a positron in a β^+-decay. Analogous for muon and tau neutrinos.

faster than the neutrino causing the neutrino's momentum vector, and by this its helicity, to be flipped in this system [Sch95]. Hence, massive neutrinos allow a discrimination between Dirac and Majorana case: if the antineutrino $\bar{\nu}_+$ with helicity $\lambda = \frac{1}{2}$, which is the CPT-partner of a neutrino with $\lambda = -\frac{1}{2}$ (ν_-), is identical to the neutrino ν_+ with positive helicity, then the neutrino is a Majorana particle, allowing, in principle, for reactions like (3.13).

One of the most important consequences of the neutrino being a Majorana particle would be the possible existence of the neutrinoless double β-decay ($0\nu\beta\beta$) [Akh00, Bil80, Obe92]. The "normal" two-neutrino double β-decay[4] ($2\nu\beta\beta$) can happen for isotopes which decay by two subsequent β^--decays[5] [Del60, Sch66]. But most often, the $2\nu\beta\beta$ decay is concealed by the single β^--decays, as the latter are much faster [Sch97]. However, for isotopes which are neutron-rich but cannot decay by a single β^--decay, as the corresponding daughter isotope lies energetically higher, see fig. 3.1, the two-neutrino double β-decay is the dominant decay process.

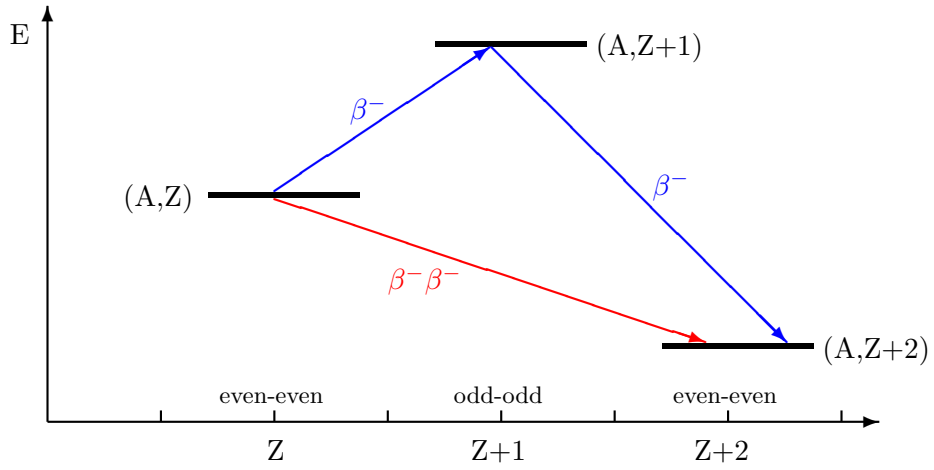

Figure 3.1: *Schematic energy level diagram for the double β-decay, plotted as a function of the atomic number Z. The decay of the even-even nucleus (A,Z) into (A,Z+2) by means of two subsequent single β-decays is not possible, as the intermediate odd-odd nucleus (A,Z+1) lies energetically higher. The red arrow depicts the possible double β-decay, while the blue arrows indicate the forbidden sequence of the two single decays.*

For several isotopes fulfilling this condition the existence of the $2\nu\beta\beta$ decay was already experimentally proven [Bar11, Del60]. In principle, the $2\nu\beta\beta$ decay can be thought to be two β^--decays at the same time, see fig. 3.2 (a). But for massive Majorana neutrinos, the antineutrino emitted at the first interaction vertex can be absorbed at the second vertex as a neutrino, as both particles are identical. According to the above considerations the emitted antineutrino has no longer only positive helicity (λ is no longer a good quantum number), but has $\lambda = -\frac{1}{2}$ with the probability [Sch97]

$$P(\lambda = -\frac{1}{2}) = \frac{1}{2}\left(1 - \frac{v}{c}\right) \approx \left(\frac{m_\nu}{2E_\nu}\right)^2 \quad . \tag{3.14}$$

[4]This decay was for the first time directly observed with the isotope ^{82}Se in 1987 [Ell87].

[5]In principle, the double β-decay can also be twice an electron capture or β^+-decay. However, the number of viable isotopes for these decays is very limited [Akh00], making any experiments rather impossible, hence, the focus here will be on the β^--decay.

This "wrong" helicity consequently allows the neutrinoless double β-decay, fig. 3.2 (b). Therefore, the experimental proof of the $0\nu\beta\beta$ decay could decide the question on the neutrino's particle type in favour of the Majorana case.

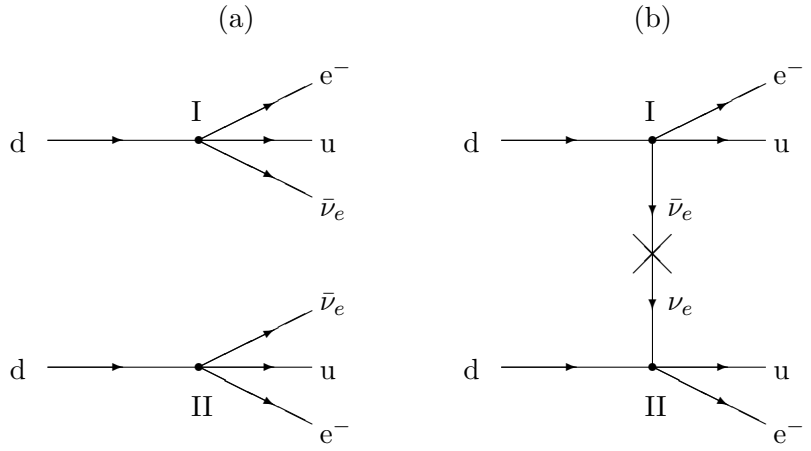

Figure 3.2: *Feynman-diagrams for the two-neutrino (a) and the neutrinoless (b) double β-decay on the quark level. The weak interaction processes at each vertex are considered to be point-like. The $2\nu\beta\beta$ decay is, in principle, just two simultaneously occurring single β^--decays. In the simplest version of the $0\nu\beta\beta$ decay the antineutrino emitted at the first vertex (I) is re-absorbed as a neutrino at the second vertex (II), which is possible because for massive neutrinos the helicity is no longer fixed, but takes the "wrong" value with a certain probability. However, there are further more sophisticated graphs with a more complex intermediate structure [Kla88], which shall not be discussed here.*

3.3 Experimental Approaches Searching for the $0\nu\beta\beta$

The two-neutrino double β-decay

$$(A, Z) \longrightarrow (A, Z{+}2) + 2e^- + 2\bar{\nu}_e \tag{3.15}$$

leads, analogously to the well-known single β^--decay, to a continuous energy distribution of the emitted electrons, as part of the decay energy is taken away by the two electron antineutrinos. On the contrary, the two electrons released in the neutrinoless double β-decay

$$(A, Z) \longrightarrow (A, Z{+}2) + 2e^- \tag{3.16}$$

have in sum a discrete energy [Kla88, Sch97], which is equal to the Q-value of the double β-decay[6]. Figure 3.3 shows these two different energy spectra.

The differences in the kinematics of the two processes allow an experimental discrimination [Kla88]. Experiments looking for the $0\nu\beta\beta$ decay normally record the full electron energy spectrum of the decay of a viable isotope and search for the peak at the endpoint energy as an indication for the occurrence of the $0\nu\beta\beta$ decay. But as the expected half-lives of

[6]The recoil energy of the daughter nucleus can be neglected, as the latter is much heavier than the electrons and, thus, takes away only little kinetic energy because of momentum conservation.

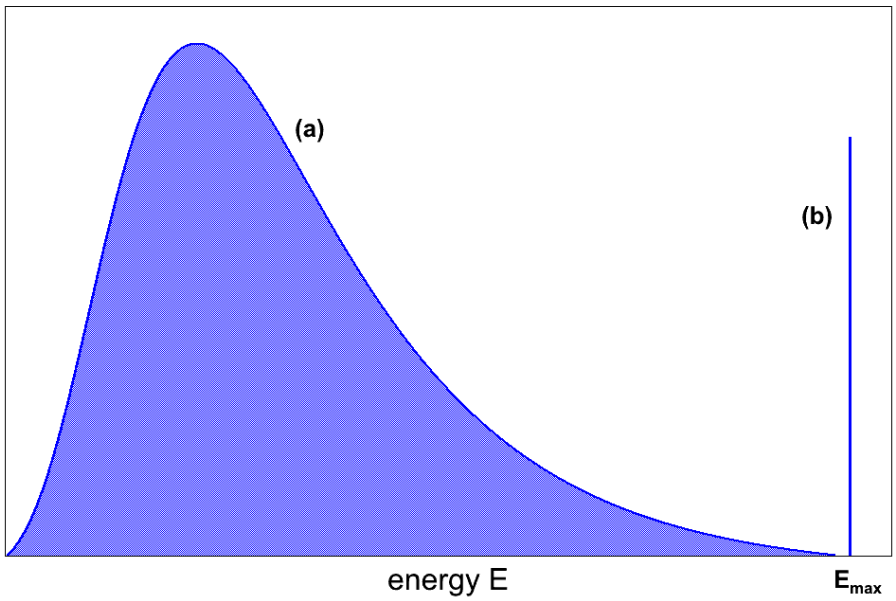

Figure 3.3: *Schematic drawing of the summed electron energy spectra of the two neutrino (a) and the neutrinoless (b) double β-decay, respectively [Sch97]. E_{max} denotes the Q-value of the decay. In the $2\nu\beta\beta$ decay part of the energy is carried away by the two neutrinos emitted, therefore, the energy spectrum of the electrons is continuous. In contrast, the electrons emitted in the $0\nu\beta\beta$ decay have in sum a well-defined energy, the Q-value of the decay, as the recoil energy of the daughter nucleus is negligible.*

the $0\nu\beta\beta$ decay channel are extremely long - current lower limits are of the order of 10^{22} to 10^{25} years [Bar11] - any double β-decay experiment must, independently of its energy measurement technique, fulfill very strict requirements on a very low background and a good energy resolution. In addition, a big detector mass and, if possible, a high enrichment of the used isotope in the source are also favoured. The excellent energy resolution needed ensures a clear discrimination between events from the neutrinoless and the two-neutrino double β-decay, respectively, and prefers isotopes unstable to double β-decay which can serve as source and detector at the same time, e.g. ^{76}Ge used in germanium semi-conductor detectors [Aal02, Aal10, Cal91, Kla01, Smo08, Vas90], or ^{136}Xe as (part of) the detector material in time projection chambers (TPCs) [Ack11, Alv11] or scintillation counters [Ber02, Ter08]. In this way, any energy losses of the electrons on their way from the source to the detector are eliminated.

The background reduction is mainly based on two approaches: firstly, the intrinsic background in the source and the detector, like natural and cosmogenically produced radioactivity, needs to be kept at a very low level, and secondly, an event-by-event background discrimination method is required. For the detection of cosmic muons, the latter can be performed using an active muon veto system, which can, among other ideas, be designed as a liquid argon scintillation veto, as is planned for GERDA [Smo08]. The event-wise particle discrimination in the source/detector is more challenging and requires a superior knowledge of the detector response to different incident particles. In the case of liquefied rare gases as detector materials

in scintillation counters, as well as in the case of liquid argon as muon veto scintillator, this implies a competent knowledge of the emission spectra, scintillation mechanisms, and pulse shapes of these liquids. The studies performed with liquefied argon concerning these points are presented in the chapters 9 to 11 of this thesis.

In 2001, part of the HEIDELBERG-MOSCOW collaboration has published a claim for the discovery of the neutrinoless double β-decay with ^{76}Ge [Kla01a, Kla04, Kla06], however, the rest of the HEIDELBERG-MOSCOW collaboration does not agree with this result [Bak05]. Also other groups are still in doubt [Aal02a, Str05, Zde02]. Therefore, it is up to forthcoming experiments to validate or rule out the claim, and, in case of a positive evidence for the $0\nu\beta\beta$, resolve the question about the neutrino's particle character in favour of the Majorana case.

Chapter 4

Dark Matter: New Particles beyond the Standard Model?

Hints on new physics beyond the standard model can not only be found in the neutrino sector, which was described in the last two chapters, but also in astrophysics on galactic and cosmological scales: the energy content of the universe seems to have some contributions of so far unknown origin, which do not behave like the well-known ordinary baryonic matter[1] as described by the standard model. In the 1930s, the Swiss physicist Fritz Zwicky published his results on the movement of galaxies within galaxy clusters [Zwi37], which indicated for the first time the presence of some non-luminous matter. In the last decades, more and more experimental evidence for non-baryonic Dark Matter has been found [Beg91, Clo06, Lar11, Spe07], pointing out that its contribution Ω_{DM} to the total energy density[2] even exceeds that of the "normal" baryonic matter Ω_{bar} by a factor of at least 5 [Ber04].

4.1 Experimental Evidence for Dark Matter

4.1.1 Rotational Curves of Galaxies

One of the first experimental evidence were the unexpected distributions of the rotation velocities of stars in the Milky Way and nearby galaxies [Alb86, Beg91]. According to Newtonian mechanics the rotation velocity $\mathrm{v_r}$ of a star or a gas cloud which is orbiting around the galactic centre at a distance r is given by

$$v_r = \sqrt{\frac{G \cdot M(r)}{r}} \quad , \tag{4.1}$$

where G denotes the Gravitational constant and M(r) the attracting mass of the galaxy inside the orbit. Consequently, the rotation velocities for orbits outside the major part of the luminous matter of a galaxy are expected to follow a $\frac{1}{\sqrt{\mathrm{r}}}$ distribution.

However, while for the inner stars the matching between the Newtonian theory and observations is rather good, one finds big deviations for the velocities of stellar objects at larger

[1] Although leptons like the electron are no baryons, the term "baryonic matter" denotes all standard model particles here.

[2] The contribution of one species i to the total energy density is defined as $\Omega_{\mathrm{i}} = \frac{\varrho_{\mathrm{i}}}{\varrho_{\mathrm{c}}}$, where ϱ_{i} denotes the present density of the species i and ϱ_{c} the present value of the critical density of the universe.

radii, fig. 4.1. Instead of decreasing like $\frac{1}{\sqrt{r}}$, the rotation velocities are rather constant [Beg91]. Assuming the correctness of the Newtonian laws on galactic scales, i.e. for small accelerations, this can only be explained by the presence of some additional invisible matter content, the halo, which is even bigger in size than the galaxy itself.

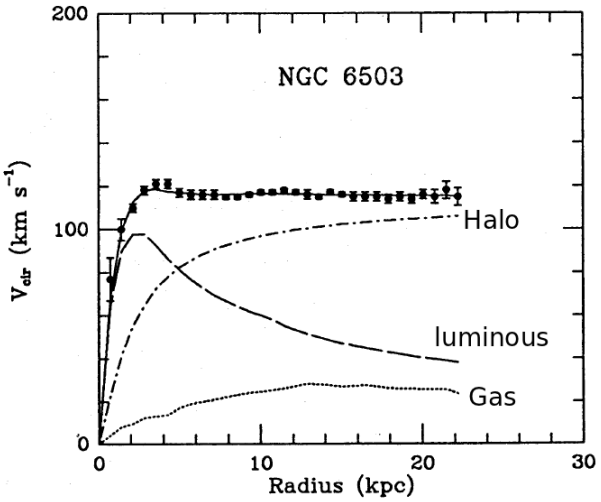

Figure 4.1: *Rotation curve of the dwarf spiral galaxy NGC 6503. This galaxy lies about 5.5 MPc away from the Milky Way and spans roughly 10.7 kPc [NAS12]. The measured rotation velocities (black data points) are fitted with a three-parameter dark-halo fit (full line). The contributions of the various components (luminous matter, gas, halo) to the observed rotation curve are shown, too [Beg91]. Copyright by John Wiley & Sons Ltd., 1991.*

4.1.2 Bullet Cluster

A more recent evidence for Dark Matter was found at the collision of two clusters of galaxies [Clo06], the so-called Bullet Cluster (fig. 4.2). The simultaneous observation of this object in the optical and in the X-ray band allowed the determination of the centre of mass of the X-ray emitting intergalactic plasma, while the analysis of gravitational microlensing effects delivered the absolute centres of mass. Surprisingly, the maxima of X-ray emission do not coincide with the mass centres, but have a significant spatial deviation [Clo06], although it is known that the intergalactic plasma contributes approximately 5 to 10 times more to the total mass of the clusters than e.g. the stellar component [All02, Vik06]. Hence, the main parts of the luminous matter and the mass of these clusters are not in the same place. This can be understood if the galaxies, and thus the clusters, mainly consist of only very weakly or even non-interacting Dark Matter, which behaves like a collisionless gas. In the collision of the two clusters the Dark Matter halos intersect each other without any significant interactions, and thereby keep their gravitational potential, while the gas clouds are left behind because of their decelerating interactions (ram pressure).

4.1.3 Cosmic Microwave Background

The currently widely accepted model for the origin of our universe is the Big Bang Model [Kol90]. It explains the formation of the universe out of an extremely hot and dense state,

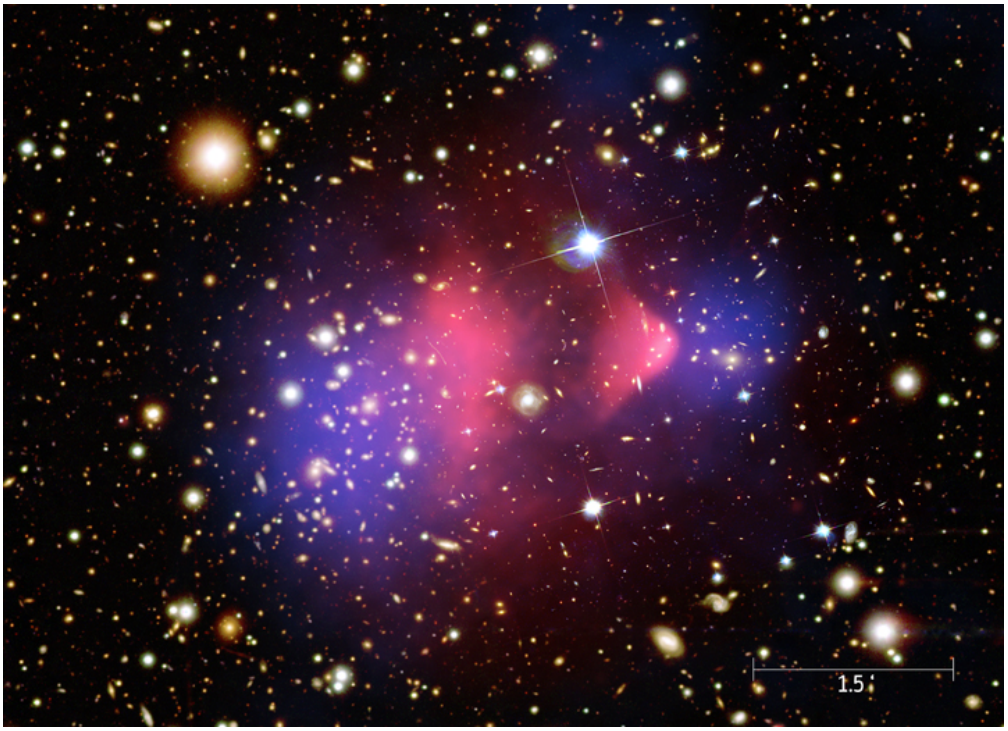

Figure 4.2: *Picture of the Bullet Cluster 1E 0657-558 in the Carina constellation. The optical image of the two galaxy clusters is overlaid by a pseudo-colour image of the NASA Chandra X-Ray Observatory to depict the X-ray emission of the intergalactic plasma (red). The blue-coloured areas indicate the mass distributions as derived from a microlensing analysis. Obviously, the centres of the plasma do not coincide with the centres of mass, but the plasma is left behind in the collision of the clusters due to the ram pressure. Both clusters seem to consist to a major part of a collisionless component, the Dark Matter. The whitish bar in the lower right corner depicts the scale of 1.5'. Courtesy of NASA/CXC/SAO.*

the so-called Big Bang, which happened around 13.7 Gyr ago [Ber04]. One of the features of this model is the existence of the Cosmic Microwave Background (CMB), which consists of thermal photons from the early phase of the universe and was firstly detected by Arno Penzias and Robert Wilson in 1965 [Dic65, Pen65]. The CMB is nearly perfect black-body radiation [Fix96, Smo97] with a current temperature of 2.73 K, however, it shows tiny anisotropies of the order of $\pm 200\,\mu$K [Ber04] (fig. 4.3), which contain lots of information on the energy content of the universe, both for ordinary baryonic matter as well as for Dark Matter [Lar11, Spe07].

The precise analysis of the angular power spectrum of the CMB (fig. 4.4) as recorded by the WMAP satellite project [Ben03] lead to the best fit values of $\Omega_{\mathrm{DM}} = 0.222 \pm 0.026$ and $\Omega_{\mathrm{bar}} = 0.0449 \pm 0.0028$ [Jar11]. This inevitably shows that cosmology also prefers a Dark Matter content of the universe which is more than four times bigger than the energy density of the baryonic matter as contained within the standard model.

In addition, there is still more experimental evidence, not discussed in detail here, like the mass determination of galaxy clusters by gravitational lensing or the structure formation in the universe [Ber04]. Altogether, these observations clearly indicate that most of the matter in the universe is non-luminous, i.e. not interacting electromagnetically, and even non-baryonic,

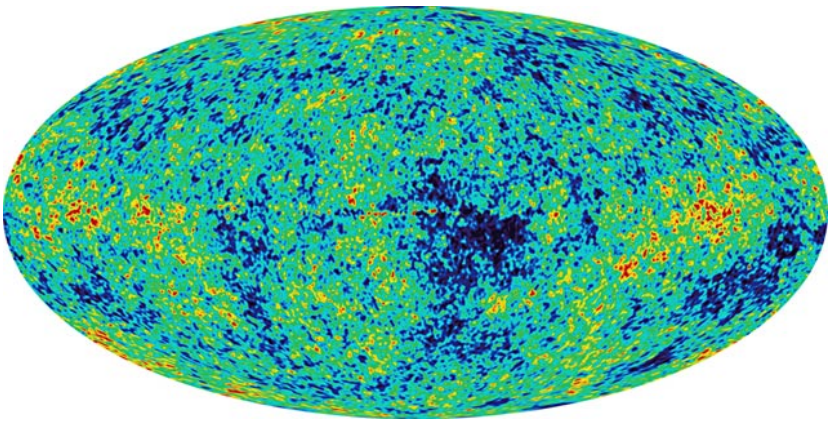

Figure 4.3: *All sky map of the temperature anisotropies of the Cosmic Microwave Background Radiation (CMB) as measured by WMAP. Effects from the Doppler shift due to Earth's motion and the galactic foreground are subtracted [Ben03]. The CMB is a nearly perfect black-body radiation with a temperature of 2.73 K and rather homogeneous, however, it shows tiny anisotropies. The colour coding depicts the deviations from the black-body radiation and ranges from dark blue (-200 μK) to red (+200 μK). Courtesy of NASA Goddard Space Flight Center.*

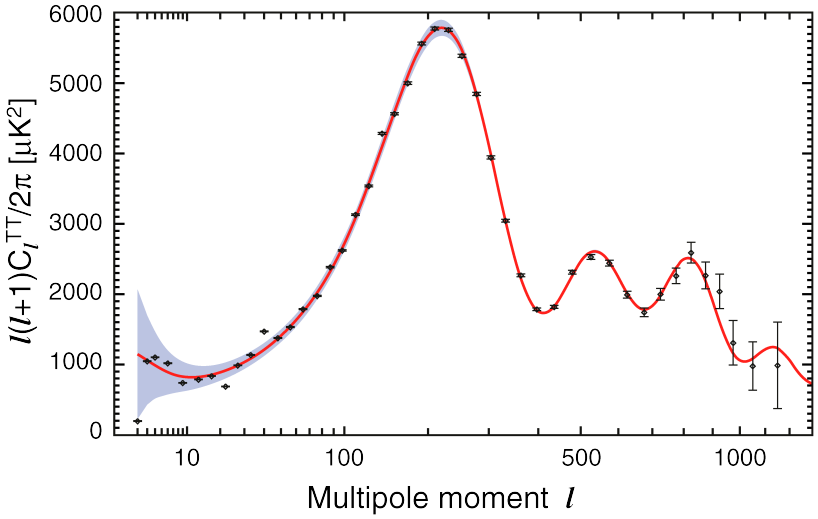

Figure 4.4: *Angular power spectrum of the CMB as measured by WMAP [Lar11] (7-years observation) with the best fit ΛCDM model [Ber04]. The y-axis shows the coefficients C_l of the multipole series of the power spectrum multiplied by l(l+1), where l is the multipole moment. The height and the centre multipole moment of the peaks also contain information on the energy density Ω_{bar} of baryonic matter and Ω_{DM} of Dark Matter [Lar11, Spe07]. Courtesy of NASA / WMAP Science Team.*

and that this Dark Matter can be found on all length scales.

4.2 Possible Explanations and Particle Candidates

As was deduced above, Dark Matter is totally non-luminous and collisionless and, therefore, can not interact with electromagnetic radiation[3], neither absorb it nor radiate itself. In astrophysics, there are very dense and compact objects known which fulfill this requirement, among them neutron stars, brown dwarfs, or black holes. Being part of the galactic halo these objects are referred to as MACHOs, **MA**ssive **C**ompact **H**alo **O**bjects [Ber04]. However, these MACHOs cannot explain the greater part of Dark Matter, as their number density in the galactic halos is much too small [Med09]. This was proven by microlensing experiments[4], which are searching for the short-time increase in the light intensity from a background star when one of these compact object is passing by in the foreground. Such events were found, yet, their small number shows that MACHOs can only account for about 8% of the Dark Matter in the halo of the Milky Way [Tis07]. Furthermore, the MACHOs consist of baryonic matter (or, in the case of black holes, the progenitor stars did), hence, the cosmological bounds for Ω_{DM} and Ω_{bar} rule out this explanation, too.

For the sake of completeness, another theory that might explain at least the observed rotation curves shall be mentioned: the so-called MOND (**MO**dified **N**ewtonian **D**ynamics), which assumes deviations from the Newtonian laws on length scales of parsec or more [Beg91]. By modifying the gravitational force, one does not need any additional matter content in the galaxy in order to explain the rotation curves. However, this theory completely fails in explaining Dark Matter evidence like the Bullet Cluster or the anisotropies of the CMB, and is therefore most likely ruled out.

The probably most appealing explanation for Dark Matter[5] is that it consists of particles. This theory is able to explain all the experimental evidence given above, however, it demands the Dark Matter particles to have some specific properties, thereby excluding all standard model particles[6]:

1. Because of the non-luminosity of the Dark Matter, its particles must not interact with photons, i.e. they must be electrically neutral and have no or only vanishingly small magnetic moments. This excludes all charged particles from the standard model, e.g. the charged leptons and most of the baryons and mesons including the proton.

2. The Dark Matter particles must be stable or, at least, their lifetimes must be of the order of the age of the universe, as we still observe Dark Matter today. By this, all baryons from figure 1.1 on page 6 are ruled out (except for the proton), because they are too short-lived [Pov04].

[3] At least, the cross sections for any interaction processes with photons must be extremely tiny. This could apply, for example, to sterile neutrinos (see below), which might have a small magnetic moment (sec. 2.2), but still are Dark Matter particle candidates.

[4] An overview of the experiments and a summary of their results can be found in [Med09] and references therein.

[5] Any exotic models beyond well-established physics shall not be regarded here.

[6] As was deduced above, the analysis of the CMB anisotropies already excluded baryonic Dark Matter. However, it is worth showing that standard model particles, including neutrinos, cannot make up the Dark Matter content of the universe for more than one experimental observation.

3. Cosmological observations like the CMB anisotropies highly favour Dark Matter particles which have already been non-relativistic in the very early stages of the universe ("Cold Dark Matter") [Ber04]. For particles which have been in thermal equilibrium this implies a particle mass of greater than at least a few GeV [7] [Kol90, Nan84]. Structure formation, however, favours somewhat lighter particles ("Warm Dark Matter") with masses in the keV-range [Veg10]. In chapter 2 it was concluded that neutrinos do posses a mass, however, experiments for the direct neutrino mass search as well as cosmology constrain the neutrino mass to values that are far too small to explain the Dark Matter content of the universe [PDG12, Spe07], both Cold and Warm Dark Matter (sterile neutrinos might be an exception, see below).

4. Laboratory experiments for the direct search for Dark Matter (see sec. 4.3.2) have shown that the Dark Matter particles' cross sections for the interaction with standard model matter need to be on the scale of the weak interaction, or even below.

Altogether, it can be derived that none of the particles contained in the standard model (chapter 1) is a viable candidate for the explanation of Dark Matter, hence, new and up to now unknown particles have to be considered. These Dark Matter candidates are often referred to as WIMPs (**W**eakly **I**nteracting **M**assive **P**articles), because of the requirements given above.

Some extensions to the minimal standard model contain possible WIMPs; the first to be mentioned here are right-handed (=sterile) Dirac neutrinos, which automatically occur for massive neutrinos in the Dirac case. They are Dark Matter particle candidates, as they are electrically neutral, possibly long-lived[8] and do not participate in the weak interaction at all (see ch. 1), but only in gravitation. Furthermore, if not produced thermally, sterile neutrinos could also be Cold Dark Matter [Shi99]. Since the mass of sterile neutrinos is most likely in the keV-range [Boy09], they are a good candidate for Warm Dark Matter, too [Li11].

Another Dark Matter particle candidate, highly favoured by some theories, is the lightest supersymmetric particle, or short LSP [Ber05]. In case R-parity, which distinguishes ordinary from supersymmetric matter, is conserved, the LSP is stable. If this particle was uncharged (e.g. the neutralino) it would be perfectly matching all requirements. However, supersymmetry has not been observed so far, thus, it is totally unclear if such particles exist at all.

An example for a possible lighter Dark Matter particle is the axion [Ber05], a particle originally introduced to solve the strong CP-problem[9] [Ros00]. Axions, if existing, would have masses of the order of 10^{-5} eV, but they would have been already non-relativistic at the decoupling of the CMB, as they never were in thermal equilibrium. Thus, they also fulfill the needs for a Dark Matter candidate. Axions have been searched for with dedicated experiments using the Primakoff effect [Raf06, Ros00], however, up to now no experimental evidence has been found [Raf12].

[7] Note that for particles which have not been in thermal equilibrium, no bounds for the mass can be derived from this argument.

[8] Sterile neutrinos are candidates for decaying Dark Matter, however, under certain circumstances their lifetimes are longer than the age of the universe [Boy09].

[9] However, it was pointed out recently that tuning the axion parameter space in such a manner that it is still compatible with observations might create a new fine tuning problem, which is even worse than the strong CP-problem [Mac09, Mac09a].

Besides these Dark Matter candidate particles, there are plenty of theories predicting a plethora of more or less fitting WIMP candidates, ranging in mass from the light axions up to greater than 10^{10} GeV for superheavy Dark Matter [Ber05].

4.3 Direct and Indirect Search for Dark Matter

The fact that the universe contains at least four times more Dark Matter than baryonic matter immediately makes clear that the experimental search for it nowadays is one of the most important issues in astrophysics and astroparticle physics. Besides astronomical observations, which have lead to the first evidence for the existence of Dark Matter, laboratory experiments here on Earth are performed in order to clarify the nature of Dark Matter. Assuming the latter is made up of particles, two major types of experiments for Dark Matter detection can be performed: the direct search for Dark Matter, which is trying to detect some of the omnipresent particles directly in a terrestrial setup, and the indirect search, looking for decay or annihilation products of WIMPs.

4.3.1 Experiments for the Indirect Search

Some of the above mentioned theories for Dark Matter particles predict WIMPs to be unstable (like the sterile neutrinos [Boy09]) or to be able to co-annihilate (e.g. for the LSP, which would be of Majorana type [Ber05]). In both cases, one could search for the decay or annihilation products of such processes, which could be high-energetic photons or leptons, including neutrinos. Furthermore, charged leptons from the decay or co-annihilation of WIMPs could lead to the subsequent emission of synchrotron radiation in galactic magnetic fields, which would be a bright astrophysical source in the radio or the microwave band [For12, Hoo12].

The WIMP decays or co-annihilations will mainly occur in space regions with an increased WIMP density. This is the case for the centre of the Milky Way itself; but also the centres of massive objects traveling through the galactic Dark Matter halo are possible regions for such a WIMP excess, as there is a small probability for the WIMPs to scatter off some nucleus in the massive object and, thereby, get bound to the object gravitationally by losing enough energy. Subsequently, the WIMPs can undergo further scattering processes and finally end up at the object's centre [Kra86, Pre95].

As neutrinos are the only possible secondary products which are able to escape from the centre of a massive object, indirect search for Dark Matter can be performed with neutrino detectors which have a directional sensitivity, like Super-Kamiokande [Fuk03] or IceCube [Hal10]. These detectors can look for an excess of high-energetic neutrinos[10] from the direction of a possible region of WIMP aggregation. However, up to now, no significant indication for a WIMP signal has been found in such neutrino-based searches [Abb11, Tan11]. In this context, it is worth mentioning that the experimental data from other indirect Dark Matter searches (see below), and data from three direct search experiments (sec. 4.3.2) possibly prefer light WIMPs with a mass around 10 GeV [Ang12, Hoo12, Kel11]. Assuming that case, the present lower energy threshold of IceCube, including its low-energy extension DeepCore, of ~ 10 GeV

[10] For a WIMP nearly at rest the summed neutrinos' kinetic energies equal the rest mass of the WIMP. As was explained above, for thermally produced WIMPs, masses below several GeV are already excluded by cosmology. Therefore, the neutrinos from the decay or co-annihilation are expected to be high-energetic. However, this is not the case for light Dark Matter particles like axions. In addition, low-energetic neutrinos are hardly distinguishable from the omnipresent neutrino background anyway.

[Gra09] might be too high to detect any Dark Matter related neutrinos at all. However, the envisaged extension to DeepCore called PINGU is intended to reach an energy threshold of $\sim 1\,\mathrm{GeV}$ [Kat12], which would allow to search for neutrinos from 10 GeV-WIMP decays or co-annihilations.

The indirect Dark Matter search with electromagnetic radiation shows some excess of events which cannot easily be assigned to astrophysical origin. In particular, gamma-rays from the galactic centre measured by the Fermi Gamma-Ray Space Telescope (FGST) [Hoo11, Vit09][11], synchrotron emission from the inner galaxy's radio filaments [Lin11], and the synchrotron emission from the inner galaxy (the so-called "WMAP haze") [Hoo11a] might be explained with the annihilation products of WIMPs with a mass around 10 GeV [Hoo12]. This interpretation of the experimental data could be in good agreement with the event excess found in the direct search experiments DAMA/LIBRA, CoGeNT, and CRESST-II (sec. 4.3.2) and is not excluded by other astrophysical measurements [Hoo12]. However, the proposed light mass of the WIMP does not allow a confirmation or a falsification of this theory by ground-based gamma-ray telescopes, as these have a too high energy threshold. Further measurement with increased statistics are needed, both in the neutrino and the electromagnetic sector, in order to clarify the situation.

4.3.2 Direct Search for Dark Matter with Underground Detectors

If Dark Matter is made up of heavy WIMPs, and if these participate not only in gravitation, but also in weak interaction, there is the possibility to measure them directly in a laboratory experiment[12]. The simplest case of interaction between a WIMP and ordinary matter is the elastic recoil off some target nucleus[13] by means of a Z^0-exchange; fig. 4.5.

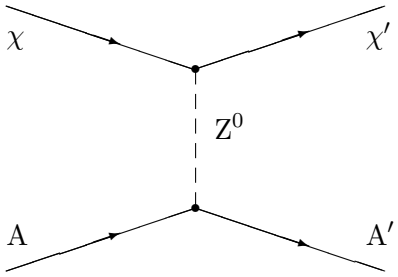

Figure 4.5: *Graph for the scattering of a WIMP (denoted by χ) off a nucleus with A nucleons via a neutral current weak interaction (Z^0-exchange). The primed quantities denote the recoiling particles. For low transferred momenta the de-Broglie-wavelength of the Z^0 is big enough that the WIMP interacts with all nucleons coherently.*

The experimental task now is to detect the tiny recoil energies of the target nucleus, and, more challenging, to distinguish them from any kind of (omnipresent) background, which

[11] However, the interpretation of FGST's results is still under discussion [Boy11].

[12] If WIMPs interacted only gravitationally, the cross sections for scattering reactions would become too small to be measured in any realistic experiment.

[13] In principle, also the recoil off an electron is possible, however, for a WIMP with a mass of some tens of GeV the recoil energy is for kinematic reasons too tiny to be measured in that case.

is mostly induced by radioactivity or cosmic muons. Because of the latter, all experiments for the direct Dark Matter search have to be in deep underground, to reduce the muon flux to a possible minimum, and select only very radiopure materials for the experimental setups. Apart from that, the background reduction can be achieved on an event-by-event basis by measuring two quantities at the same time [Cen11, Rau11], as is done by most of the leading experiments; see fig. 4.6. By this method, electron recoils as well as α-particles can be discriminated well from nuclear recoils as induced by WIMPs. However, the serious neutron background still remains, even after applying this discrimination cut, as neutrons also mainly scatter off nuclei. This kind of background has to be handled by each of the direct search experiments, mainly by a passive or active neutron shielding, but also by means of a dedicated analysis, for example by Monte-Carlo methods to determine the estimated number of remaining neutrons, or by looking for multiple scattering events, which are extremely unlikely for WIMPs, but not for neutrons [Sto11].

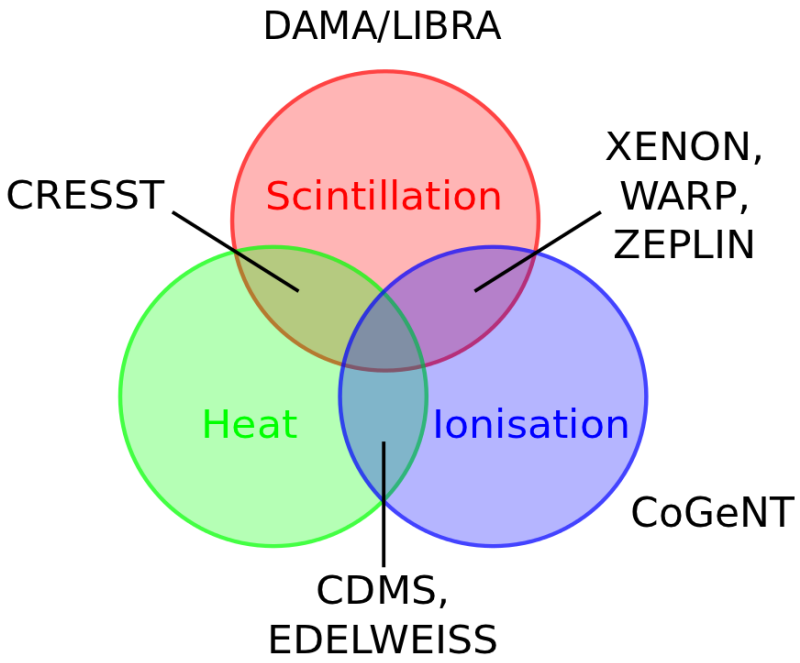

Figure 4.6: *Measured quantities in selected experiments for direct Dark Matter search. The simultaneous determination of two signals allows an enhanced background reduction (see text) [Rau11].*

Some of the experiments for direct Dark Matter search use liquefied rare gases (argon or xenon; in case of MiniCLEAN also neon) as detector materials, either only as scintillators (XMASS [Min10], MiniCLEAN [Him11], DEAP-3600 [Ols09]), or as two-phase time projection chambers (ZEPLIN-III [Aki07], LUX [McK10], XENON [Apr05], ArDM [Mar11], WARP [Ben08], DarkSide [Wri11]) for the simultaneous measurement of the scintillation and the ionisation signal. The ionisation is thereby determined by applying an electric field to the detector material to drift the ionisation electrons from the liquid phase to the gas phase, where they again produce scintillation light. Hence, by measuring the ratio of the scintillation signals in the liquid and the gas phase the ratio of the scintillation and the ionisation signal is

determined, allowing an event-by-event discrimination between electron and nuclear recoils. Obviously, a good knowledge of the underlying rare gas scintillation mechanisms, both for the gas and the liquid phase, is mandatory for the full understanding of this kind of experiments.

Already running experiments, e.g. XENON10 and ZEPLIN-III, have the two-phase time projection chamber (TPC) technique proven to be successful, however, two-phase detectors with an applied high voltage are technically much more challenging than single-phase liquid rare gas scintillation detectors. Within the scope of the present thesis experiments are presented (ch. 11) that will help to improve our knowledge on the light emission mechanisms in liquefied argon and to investigate if the precise measurement of only the scintillation signal in a single-phase liquid rare gas detector could be sufficient, too, to discriminate between electron and nuclear recoils, e.g. by means of pulse-shape discrimination or by measurements in different wavelength regions.

Of all the experiments for direct Dark Matter search, only DAMA/LIBRA [Ber10], CoGeNT [Aal11], and CRESST-II [Ang12] have published a possibly positive signal so far. While CRESST-II reports only an excess of events in the WIMP window, both DAMA/LIBRA and CoGeNT observe, in addition, seasonal variations [Aal11a, Ber10] of the signal, which are well in agreement and, furthermore, have the right phase to be a Dark Matter signal [Hoo12]. At present, these observed modulations cannot easily be explained by any kind of background [Ber09], and thus, maybe, hint for Dark Matter detection, although the modulation amplitudes seem to be too high (by a factor of 3 to 10) compared to the WIMP scattering cross sections derived from the CoGeNT and CRESST-II results [Hoo12, Kel11]. All three experimental data might be explained with WIMPs with masses in the 10-20 GeV range and a scattering cross section on nuclei of about (1-3)$\cdot 10^{-41}$ cm^2. However, these results are in conflict with the exclusion limits on the WIMP scattering cross-sections set by other experiments, especially XENON-10 and XENON-100 [Cen11, Hoo12, Kel11]. Therefore, the experimental searches have to go on in order to finally resolve the Dark Matter puzzle, and, in case of a positive evidence for WIMPs, decide about their nature.

Part II

The Double Chooz Reactor Antineutrino Disappearance Experiment: Radiopurity in a Liquid Scintillator-Based Experiment

Chapter 5

Detector Concept and Design of Double Chooz

5.1 The Idea of Two Detectors

After the discovery of a non-vanishing value for the mixing angle ϑ_{13} [PDG12], one of the most important tasks in neutrino physics for the next years is the precise determination of its value, see section 2.4, which can be performed with reactor antineutrino disappearance experiments. The first project of the second-generation experiments of this type [Cao07, Las05] that published an indication for a non-zero mixing angle ϑ_{13} is Double Chooz [Abe12, Abe12a, And04, Ard04, Ard06, Ber04a, Obe06], which is located in the North of the French Ardennes, see map in fig. 5.1. It is placed at the river Meuse close to the Chooz commercial nuclear power plant, which has two reactor cores with a thermal energy output of 4.25 GW each [Abe12]. Double Chooz measures ϑ_{13} by using electron antineutrinos emitted from these reactor cores to study neutrino-oscillation properties. As was already shown in section 2.4.2 this measurement is free from parameter correlations or matter effects, and in the end only limited by systematic uncertainties. Because of the latter, the concept of Double Chooz foresees two identical detectors in different distances to the reactor cores: one near detector, which is meant to monitor the antineutrino flux and its spectral shape without (or with only minor) oscillation effects, and one far detector measuring the oscillating antineutrino spectrum. By the comparison between the two detectors most of the systematic uncertainties like the detailed shape of the reactor antineutrino spectrum, the cross-section of the inverse beta decay, or the current reactor power cancel out [Ard04].

Figure 5.1: *Map of France indicating the location of the Double Chooz experiment (red star).*

The Double Chooz far detector has an averaged distance of $\sim 1050\,\mathrm{m}$ to the two reactor cores [Abe12]. There, a maximal effect due to neutrino oscillations is expected, because this distance covers the first minimum of the survival probability of electron antineutrinos (fig. 5.2).

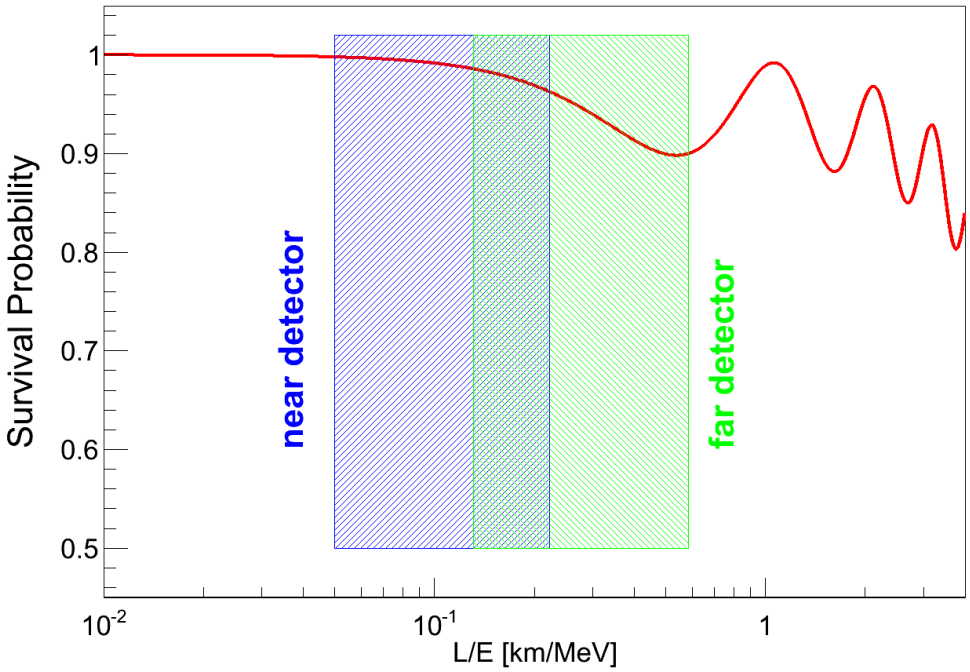

Figure 5.2: *Survival probability of reactor electron antineutrinos as a function of the flight distance L over neutrino energy E on a logarithmic scale. It is plotted with the following parameters:* $\Delta m^2_{32} = 2.32 \cdot 10^{-3}\,eV^2$, $\Delta m^2_{21} = 7.50 \cdot 10^{-5}\,eV^2$, $sin^2(2\vartheta_{12}) = 0.857$, *and* $sin^2(2\vartheta_{13}) = 0.098$. *The shaded areas correspond to the positions of the two Double Chooz detectors, covering antineutrino energies from 1.8 MeV (threshold of the Inverse Beta Decay) to 8 MeV. Obviously, any neutrino oscillation effects based on* ϑ_{13} *are maximal at the far detector site (L = 1050 m), while they affect the spectrum only little at the near detector site (L = 410 m), except for small neutrino energies (*$\lesssim 3$ *MeV), which is, however, the most interesting region.*

The averaged distance of the near detector to the reactor cores is about 410 m [Pal09]. At this position, effects stemming from neutrino oscillations cannot be fully neglected, cf. fig. 5.2, but are still small compared to the effects at the far site. In principle, a near detector position closer to the reactor cores would have been better, but in the end it had to be defined at a technically possible location and in agreement with the power plant authorities. Nevertheless, as there is only one free parameter in the final fits, ϑ_{13}, this does not pose problems to the analysis - the ratio of the survival probabilities of electron antineutrinos at the different distances to the reactor cores for far and near site is always fixed. Therefore, the near detector distance still allows a determination of the reactor neutrino output, and thereby of the current reactor power, as a normalisation for the neutrino oscillation measurement with the far detector. The whole Double Chooz detector site can be seen in fig. 5.3.

At present, only the far detector is taking data, the near detector is still under construction. As soon as both detectors will be online (which is expected for the end of 2013/ beginning of 2014), the systematic uncertainties in Double Chooz will be dominated by background, which is consequently the limiting factor for the reachable sensitivity. Concerning this point, a great

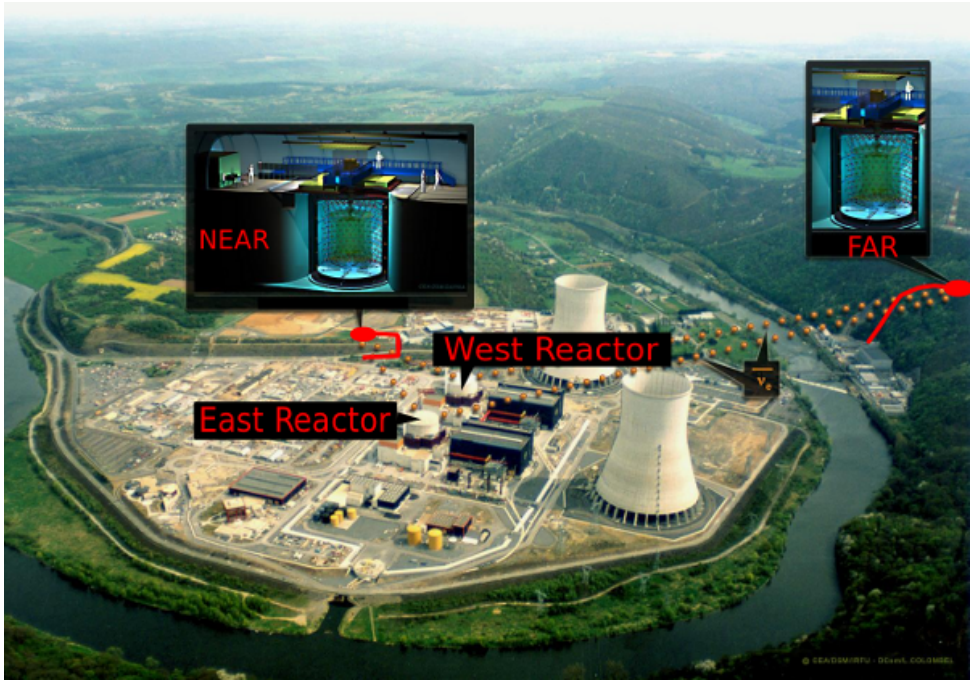

Figure 5.3: *Photograph of the Chooz nuclear power plant and the Double Chooz detector site. The positions of the near and the far detector are depicted. The red lines indicate the access tunnels to the laboratories. In the middle the two reactor buildings can be seen (white containments), as well as the corresponding machinery halls (black buildings). Based on [DC11].*

advantage of Double Chooz compared to other reactor neutrino experiments [Cao07, Las05] like Reno [Ahn12] or Daya Bay [An12] is that the Chooz reactor plant has only two cores, therefore, there is a non-negligible chance of having data with both reactors off[1]. This allows the ultimate measurement of the background not correlated to the power plant (see sec. 6.2).

In addition, the spectral analysis becomes easier with only two reactor cores contributing to the neutrino flux. Of all the reactor antineutrino disappearance experiments Double Chooz is at present the only one which performed an analysis of the oscillation signal not only by means of the measured neutrino rate, but additionally takes into account the shape of the measured spectrum (see sec. 8.4). This rate+shape analysis is more robust in identifying a neutrino-oscillation signal than a rate only analysis: any overestimation of background in the far detector's signal, or any misidentified background contribution in the near detector might lead to a fake oscillation signal at a rate only analysis, while the rate+shape analysis can identify such an error by the spectral shape. Hence, the ultimate measurement of the mixing angle ϑ_{13} should always rely on the shape of the measured antineutrino spectrum, too.

5.2 The Double Chooz Detector

The main part of each Double Chooz detector [Ard06] consists of four cylindrically shaped vessels, which are built-up concentrically (see fig. 5.4). The innermost of these vessels, the

[1]Since the beginning of data taking both cores were off simultaneously for in total $\sim$7.5 days.

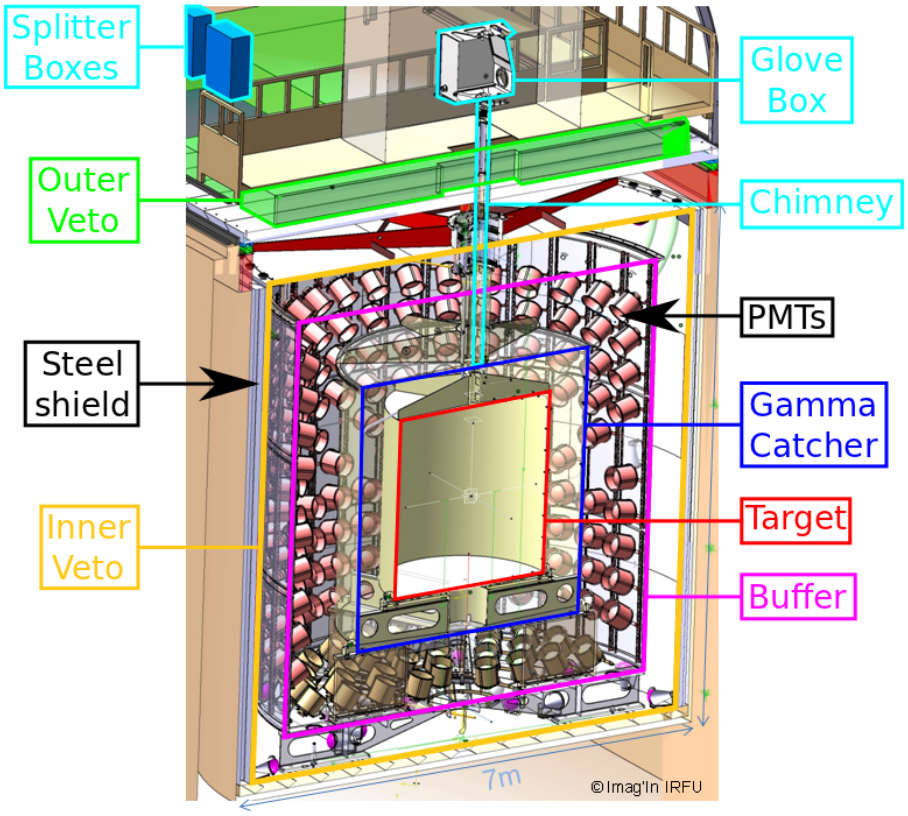

Figure 5.4: *Schematic view of the Double Chooz far detector. In the center, the acrylic vessel containing the Target liquid is shown (red). This vessel stands on six acrylic feet and has additionally six stiffeners on top, which are made of acrylic, too. The Target is surrounded by another acrylic vessel, which is filled with the GammaCatcher liquid (blue). Both vessels are fully contained in the stainless steel Buffer tank (pink), which holds the non-scintillating Buffer liquid (acting as a shielding against radioactivity from the PMTs) and furthermore serves as support structure for the 390 PMTs (black) looking at the inner parts of the detector. The outermost steel cylinder, the InnerVeto (yellow), is again filled with a scintillating liquid, which is monitored by 78 additional PMTs directly mounted to the tank walls. The detector is surrounded by a 15 cm thick steel shielding (black) at the side walls, on bottom, and on top to reduce the background stemming from radioactivity of the rock. Above the cylindrically shaped detector the plastic scintillator panels (green), the OuterVeto is made up of, can be seen. Additional supplementary structures (light blue), like the high voltage splitter boxes or the Glove Box, which is connected to the Target volume through the detector chimney for source deployment, are also indicated. Based on [DC11].*

so-called *Target*, has a capacity of 10.3 m^3 and is built of UV-transparent acrylic with a wall thickness of 8 mm. On top, this vessel has six acrylic stiffeners, on bottom six acrylic feet. It is filled with a liquid scintillator based on PXE as solvent, with PPO (7 $\frac{g}{l}$) and bisMSB (20 $\frac{mg}{l}$) as primary and secondary fluor, respectively (see sec. 5.3). This scintillator is additionally doped with 1 $\frac{g}{l}$ of gadolinium. The Target is the fiducial volume of Double Chooz, where the neutrino interactions are detected by means of the Inverse Beta Decay (cf. chapter 6). Hereby, the discrimination of neutrino events from background is simplified by the added gadolinium, as some isotopes of this element have a rather huge cross section for the capture of thermal neutrons, see tab. 6.1 on page 48, and the gamma energy released after this neutron capture, in total about 8 MeV [Fir96], is far above any energy deposit by radioactivity.

The Target is surrounded by another acrylic vessel, the so-called *GammaCatcher*. This vessel has a wall thickness of 12 mm and contains 22.3 m^3 non-Gd-loaded liquid scintillator, again based on PXE with a concentration of 2 $\frac{g}{l}$ PPO and 20 $\frac{mg}{l}$ bisMSB. This scintillator matches the Target scintillator in density and photoelectron light yield (about 230 p.e. per MeV [Abe12a]). The GammaCatcher ensures a homogeneous energy response of the detector all over the Target, as it captures gamma quanta which are emitted after a thermal neutron capture on gadolinium, but escape the Target volume. Therefore, the visible energy of the event does not depend on whether it took place at the center of the Target, or its border.

Both the Target and the GammaCatcher are fully contained within a stainless steel tank, the *Buffer*, which holds 110 m^3 of a non-scintillating mineral oil and serves as support structure for the 390 10" PMTs looking at the inside[2]. The Buffer shields Target and GammaCatcher from the radioactivity of the PMTs. All three vessels of the inner detector parts (Target, GammaCatcher, and Buffer) can be seen on the photograph in fig. 5.5.

The outermost vessel, the so-called *InnerVeto*, is again a steel tank, but filled with a LAB-based[3] liquid scintillator (90 m^3), which is directly monitored by 78 8" PMTs. Its main purpose is to detect incoming muons and muon secondaries, which might enter the Target region and mimic an electron antineutrino event. The InnerVeto is optically decoupled from the inner detector parts by the stainless steel Buffer tank. The scintillator of the InnerVeto also contains the wavelength shifters PPO (2 $\frac{g}{l}$) and bisMSB (20 $\frac{mg}{l}$).

The whole setup is additionally shielded against external radioactivity e.g. from the rock by 15 cm of steel[4]. On top, the whole detector is covered by the *OuterVeto*, which consists of plastic scintillator strips and provides further information on the incoming cosmic muons: on the one hand, the muon tracking is improved, and on the other hand, the area covered by the OuterVeto is larger than the detector vessels, therefore, it can also detect muons entering the chimney or passing nearby the detector. While the former directly deposit some energy in the detector, the latter muons may create fast neutrons in the rock material, which can subsequently enter the detector. Hence, both reactions pose a source of background; see section 6.2. However, in the first phase of data taking the outer veto was not fully operational, especially the part above the detector chimney was still missing. Therefore, stopping muons have still been a severe background which needs to be taken into account; see sec. 6.2.3.

Both Double Chooz detectors are identical, except for the shielding and the overburden: the far detector laboratory has an overburden of about 300 m.w.e. in a hill topology, while the near detector laboratory is covered by 120 m.w.e. with a flat topology [Pal09]. However,

[2]However, 14 PMTs have been switched off, since their bases generated too much light flashes [Abe12a]; see also sec. 8.2.1.

[3]See sec. 5.3.

[4]The near detector will have a ~ 1 m thick water shielding instead.

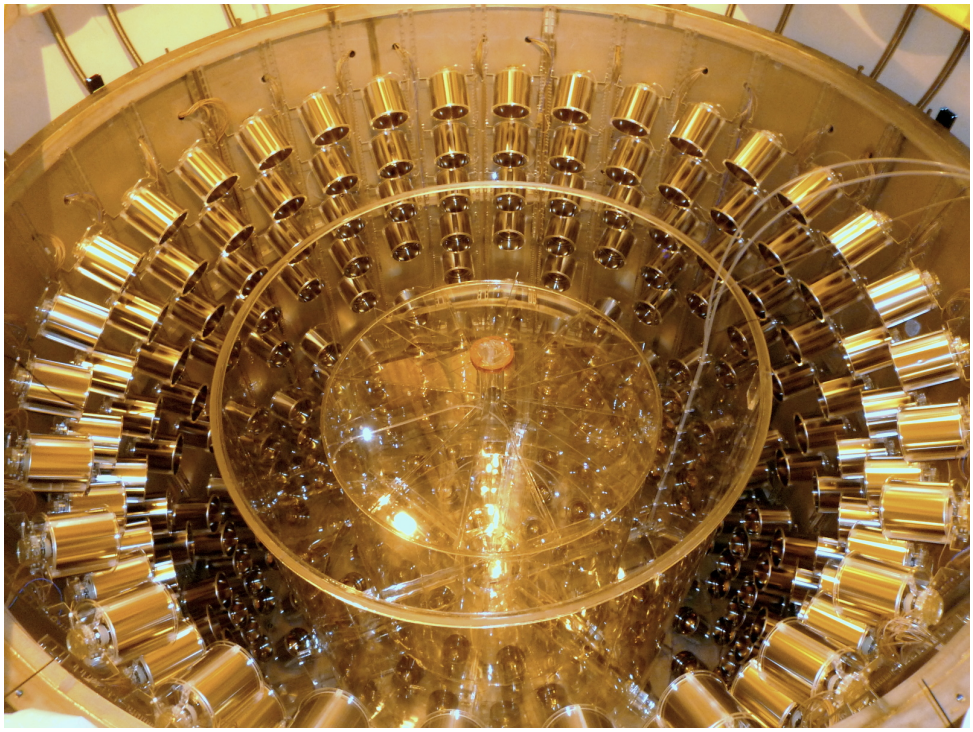

Figure 5.5: *Photograph of the far detector during the construction phase. The acrylic vessels of the Target (innermost part) and the GammaCatcher can be seen in the middle of the picture. Both are surrounded by the Buffer tank, which also holds the PMTs. GammaCatcher and Buffer top lid were not yet installed at that time. Taken from [DC11].*

due to its closer distance to the reactor cores the near detector will measure a higher neutrino rate of ~ 350 per day (compared to about 43 neutrino interactions detected per day at the far detector after all cuts [Abe12]), and therefore still has a signal to background ratio of 100:1 (compared to 20:1 for the far detector) [Pal09].

The construction and filling of the Double Chooz far detector has been finished in December 2010, the commissioning has been performed in the following four months, and the data taking of the first phase (far detector only) started on April, 13$^{\text{th}}$, 2011. The laboratory for the near detector is currently being excavated; the near detector itself will start data taking presumably in 2014.

5.3 Scintillation Mechanism and Quenching

A charged particle traveling through a liquid scintillator deposits kinetic energy along its path and, thus, produces luminescence light, whose intensity is to good approximation proportional to the deposited energy[5] [Leo87]. The interaction between the incident particle and the liquid scintillator medium is electromagnetic and leads to ionised[6] and electronically and/or vibra-

[5]Deviations from a linear dependence of the light output on the deposited energy are described by the semi-empirical Birks formula (5.4), see below.

[6]In principle, in a liquid an ionisation process creates an electron-hole pair. However, for simplicity, in the following always the term "ionised molecule" will be used instead.

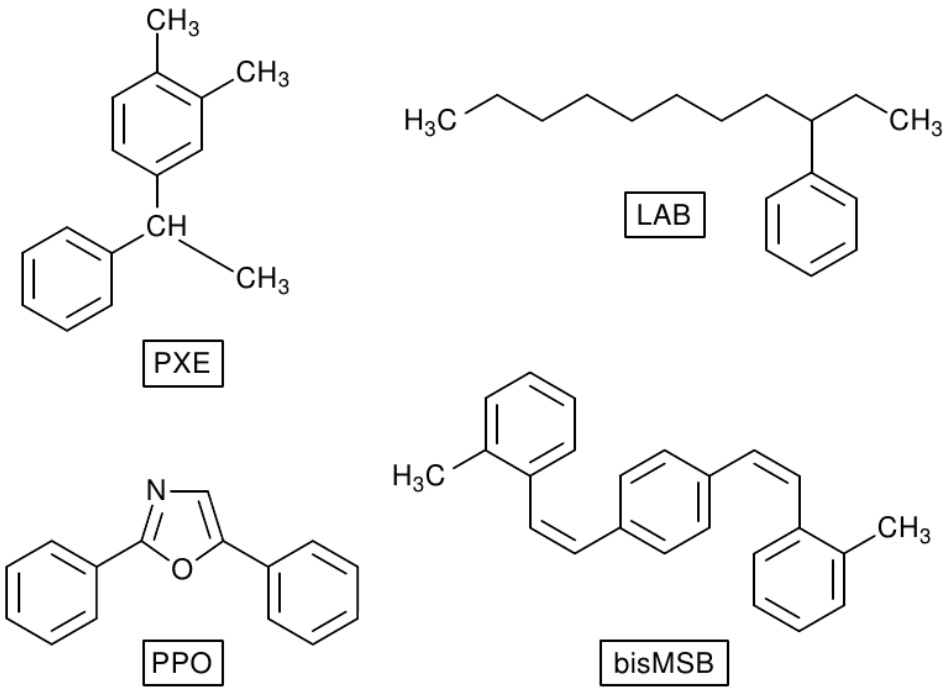

Figure 5.6: *Chemical structures of the solvents Phenyl-o-Xylylethan (PXE) and linear Alkyl-Benzene (LAB), as well as of the fluors 2,5-Diphenyl-Oxazole (PPO) and 1,4-bis-(o-Methylstyryl)-Benzene (bisMSB) [Mar08]. The liquid scintillators of Target and GammaCatcher are based on PXE, while the InnerVeto liquid contains LAB as scintillating solvent. In all cases, the wavelength shifters PPO and bisMSB are added in small concentrations.*

tionally excited scintillator molecules. In addition, absorption of electromagnetic radiation can also lead to excited molecules.

In a typical liquid scintillator, like that in Double Chooz, the scintillator molecules have one or more benzene rings [For51, Leo87], cf. fig. 5.6. These contain a delocalised system of π-electrons, which can easily be excited. Although also the more tightly bound σ-electrons of the interatomic bonds can be excited to higher electronic states, the latter process is highly suppressed due to the much larger excitation energies [Leo87, Mor10].

After a molecule of the liquid scintillator has been excited or even ionised it will return to the ground state or recombine either by emitting luminescence photons or - competing to photon emission - by non-radiative processes, where the energy finally ends up in heat. Therefore, not all of the energy originally deposited by the incident particle is converted into photons, but only a fraction. This is denoted by the term "quenching". The quenching factor QF is defined as the ratio of the deposited energy E of the exciting particle and the energy L converted into detectable light:

$$QF = \frac{E}{L} \quad . \tag{5.1}$$

For a given species of incident particles, chemical composition, and temperature of the liquid scintillator, the quenching factor is only a function of the particle's energy E [Jag06,

Leo87]. In this context, it is important to note that quenching even occurs for a scintillator free of any impurities. However, the latter can give rise to additional light-loss processes [Kno10].

In a simplified model, the excitation energy which is transferred to the scintillator molecules brings the molecule to an electronically and vibrationally higher state, see schematic drawing (Jablonski diagram) in fig. 5.7.

At first, the energy of the vibrational excitation is transferred into heat by collisions with other molecules of the liquid scintillator. This vibrational relaxation happens very fast, on time scales of a few picoseconds [Kno10]. The subsequent decay of the higher electronical states into lower ones also happens non-radiatively in collisions, and is referred to as electronic relaxation. Both vibrational and electronic relaxation lead to energy losses in the visible channels. The lowest electronically excited states can decay into the ground state S_0 by the emission of luminescence light. As this transition can also go into vibrational subexcitations of the ground state which de-excite non-radiatively, again some energy might be lost for scintillation light emission, giving rise to the so-called Stokes shift [Bir53], i.e. the emission band of a liquid scintillator molecule is shifted towards longer wavelengths compared to its absorption band.

Depending on the relative orientation of the spin of the excited electron with respect to the unpaired electron in the ground state, the lowest excited state can either be a singlet (S_1) or a triplet (T_1) state [Bir53]. According to the selection rules for photon emission ($\Delta S = 0,\pm 1$; $\Delta J = 0,\pm 1$, but not $J = 0 \rightarrow J = 0$), the decay $S_1 \rightarrow S_0$ is an allowed transition and, consequently, happens fast on timescales of tens of nanoseconds (fluorescence) [Mar08]. The transition $T_1 \rightarrow S_0$ (phosphorescence), however, is highly forbidden [Leo87] and thus happens on much slower timescales of microseconds [Mar08]. Actually, phosphorescence is so unlikely that a big part of the decays of triplet states happens by forming at first a singlet state, e.g. via the reaction

$$T_1 + T_1 \rightarrow S_i + S_0 \quad , \tag{5.2}$$

which then leads to the delayed emission of fluorescence photons [Leo87, Mar08]. In addition, an excited molecule in the lowest triplet state can also gain energy in collisions with other molecules, unless it has enough energy to return to the S_1 state by a spin flip.

But the radiative decay of the lowest electronically excited states is not the only possibility for de-excitation. Especially for high excitation densities in the liquid scintillator the collision of two excited molecules in some state S_i can happen, leading to non-radiative processes like

$$S_i + S_j \rightarrow S^+ + e^- + S_0 \quad (i, j > 0) \quad , \tag{5.3}$$

which cause additional losses of luminescence photons [Mar08]. Therefore, the quenching factor as defined in (5.1) depends on the density of the excited scintillator molecules and, thus, on the specific energy deposition per track length of the incident particle. For low excitation densities, as is the case for fast electrons, collisions between two excited molecules are very unlikely and the specific light output rises linearly with the particle's deposited energy. The quenching factors are small. On the other hand, for highly ionising particles like α's, the excitation densities can reach such high values that the quenching interactions cause the quenching factors to reach values of 10 or even higher [Abe11a].

A semi-empirical formula describing rather well the light-loss processes due to quenching interactions between scintillator molecules excited along the path of an incident particle is

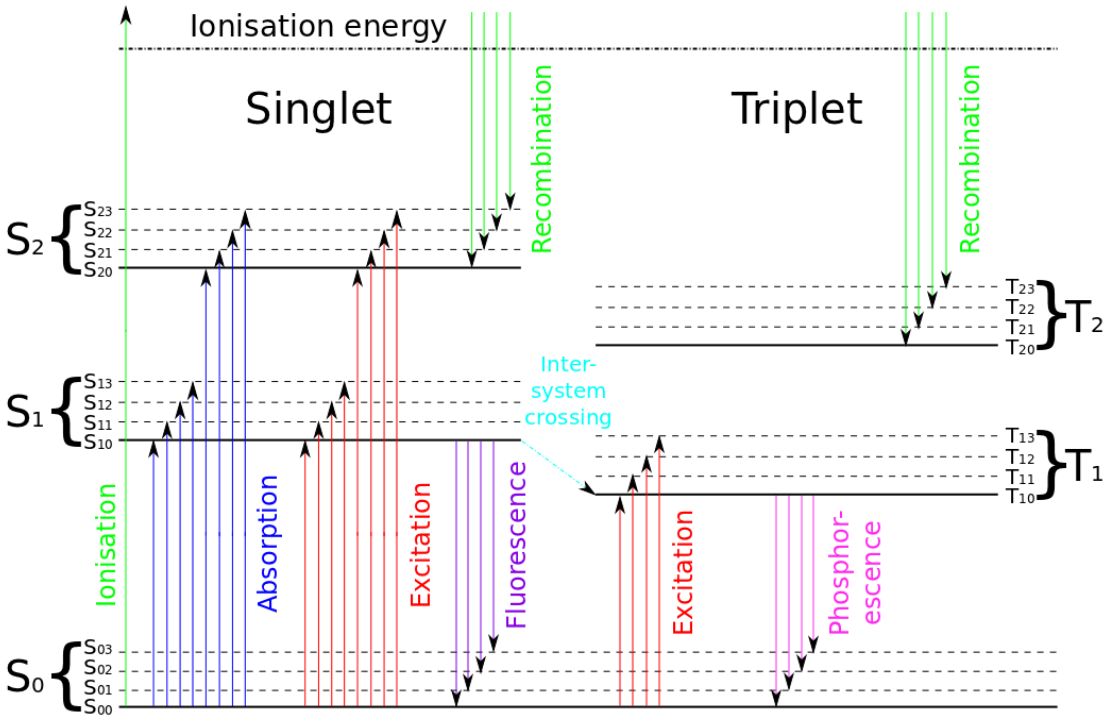

Figure 5.7: *Jablonski diagram [Jab35] showing schematically the excitation levels and possible transitions of a liquid scintillator molecule. The thick black horizontal lines indicate the ground state (S_0) and the electronically excited states (S_1, S_2, T_1, ..), the dashed lines the vibrational subexcitations (S_{00}, S_{01}, ..). Depending on the spin orientation of the excited electron relative to the unpaired electron of the ground state, singlet and triplet states are distinguished [Bir53]. The excitation by a charged particle (red arrows) leads to higher levels of both singlet and triplet states. In contrast, the absorption of electromagnetic radiation (blue) only excites the molecule to singlet states because of the selection rules. Recombination after ionisation (green) can again reach both singlet and triplet states, however, in about 75% a triplet states is formed [Bir64]. The highly excited vibrational and electronical states decay non-radiatively in collisions with other scintillator molecules [Kno10, Leo87], leading to non-visible energy losses into heat (not shown in the diagram). The lowest singlet and triplet states, respectively, can decay into the ground state by photon emission (fluorescence depicted in purple and phosphorescence in pink). While the transition S_1 to S_0 is allowed and, therefore, happens quite fast ($\tau \approx 10^{-8}$ s), the decay of T_1 is forbidden and, consequently, leads to a delayed photon emission [Mar08] (see text). Collisions with other molecules also allow spin flips leading to intersystem crossing, i.e. for example the decay S_1 into T_1 (light blue).*

the Birks equation [Bir51, Bir53, Leo87], which connects the specific light output $\frac{\mathrm{dL}}{\mathrm{dx}}$ to the energy deposition $\frac{\mathrm{dE}}{\mathrm{dx}}$ per unit path length:

$$\frac{dL}{dx} = \frac{S \cdot \frac{dE}{dx}}{1 + kB \cdot \frac{dE}{dx}} \quad . \tag{5.4}$$

Here, S denotes the absolute scintillation efficiency [Leo87], i.e. the produced light per deposited energy, and kB the Birks constant, both being material properties. To first approximation, kB is roughly the same for all kinds of incident particles, however, a better matching between Birks' theory and the experimental results is achieved when kB is adjusted for each particle separately [Abe11a]. The energy deposition per track length, $\frac{\mathrm{dE}}{\mathrm{dx}}$, can be calculated with Bethe's stopping power formula [Ahl80, Bet30] for heavy charged particles like protons or α-particles, or the Berger-Seltzer formula [Sel82] for electrons, respectively.

Two special cases shall be regarded: firstly, the case of no (or only very small) quenching interactions, which is, for example, the case for minimally ionising particles like electrons with only a very small energy deposition per track length ($\mathrm{kB} \cdot \frac{\mathrm{dE}}{\mathrm{dx}} \ll 1$). Here, the specific light output becomes proportional to the energy deposition, i.e. the light per energy is in a linear regime:

$$\left.\frac{dL}{dx}\right|_e \approx S \cdot \frac{dE}{dx} \quad \stackrel{\int dx}{\Longrightarrow} \quad L \approx S \cdot E \quad . \tag{5.5}$$

Secondly, for highly ionising particles like α-particles or heavy ions, the approximation

$$kB \cdot \frac{dE}{dx} \gg 1 \quad \Rightarrow \quad \frac{dL}{dx} \approx \frac{S}{kB} \Leftrightarrow L \approx \frac{S}{kB} \cdot R \tag{5.6}$$

can be made, as typical energy depositions here are of the order of 500 $\frac{\mathrm{MeV}}{\mathrm{cm}}$, while kB takes values of about 0.02 $\frac{\mathrm{cm}}{\mathrm{MeV}}$ [Abe11a]. In (5.6), R is the range of the particle passing through the scintillator. For particles with a high energy deposition per track length the specific light output $\frac{\mathrm{dL}}{\mathrm{dx}}$ is, according to Birks' theory, in saturation ($\frac{\mathrm{dL}}{\mathrm{dx}} \propto \mathrm{S}$).

The differences in the time behaviour of the luminescence photon emission of singlet and triplet states can be used for a particle discrimination by means of the pulse shape. Different incident particles with different specific energy losses $\frac{\mathrm{dE}}{\mathrm{dx}}$ produce different proportions of excited scintillator molecules in the singlet and the triplet state [Leo87], hence, the ratio of fluorescence and phosphorescence transitions changes. High energy depositions per unit track length lead to increased interactions between excited molecules, which increases the relative intensity of the delayed component of photon emission [Leo87]. Therefore, the scintillation light pulses have a more prominent tail for highly ionising particles like α's than for electrons.

Chapter 6

The Inverse Beta Decay as Detection Reaction and Possible Backgrounds

6.1 Inverse Beta Decay

In the Double Chooz detectors the electron antineutrinos from the reactors undergo an Inverse Beta Decay (IBD) reaction on the protons of the liquid scintillator, releasing a positron and a neutron:

$$\bar{\nu}_e + p^+ \rightarrow e^+ + n \quad . \tag{6.1}$$

The newly formed positron deposits its kinetic energy E_{e^+} in the liquid scintillator, giving rise to a fast scintillation signal proportional to E_{e^+} [Leo87]. After being stopped[1] the positron annihilates with an electron, releasing two 511 keV gamma quanta. As the detector volumes are big enough to fully contain the whole energy of these gammas, the visible energy of the fast signal is E_{e^+} plus 1022 keV.

The neutron from the IBD is thermalised and then eventually captured on gadolinium, hydrogen, or, seldomly, carbon. For neutrons interacting in the Target region the capture on gadolinium is highly favoured, as some isotopes of this element have a very high cross section for thermal neutron capture, see table 6.1, while for neutrons in the GammaCatcher scintillator the capture on hydrogen with a cross section of 0.332 barn [Fir96] dominates.

The neutron capture leads to a highly excited state of the daughter nucleus, which de-excites by the emission of one or more gamma quanta

$$n + {}^{A}X \rightarrow {}^{A+1}X^* \rightarrow {}^{A+1}X + \sum_i \gamma_i \quad , \tag{6.2}$$

where the summed gamma energy is around 8 MeV in the case of gadolinium and 2.2 MeV in the case of hydrogen. The seldom capture on carbon releases 4.9 MeV [Fir96]. This gamma

[1] The probability for a positron with an energy of a few MeV to annihilate in flight is below $\sim 15\%$ [LBL12, Sch12]. In case of Double Chooz the fiducial volume is restricted to the Target region, but gamma quanta escaping the Target because of an interaction at its rim are detected in the GammaCatcher. As this volume is big enough to even fully contain the more energetic gamma quanta resulting from an annihilation in flight, the latter is no problem anyway; the full energy of the positron event is detected in that case, too.

Gd isotope	***Natural abundance*** [%]	***Capture cross section*** σ_n [barn]
^{152}Gd	0.20	700
^{154}Gd	2.18	60
^{155}Gd	14.80	61000
^{156}Gd	20.47	2.0
^{157}Gd	15.65	254000
^{158}Gd	24.84	2.3
^{160}Gd	21.86	1.5

Table 6.1: *Cross sections of the stable gadolinium isotopes for the capture of a thermal neutron. Note that ^{152}Gd can, in principle, undergo an α-decay, but its half-life is longer than 10^{14} years. Therefore, it is considered to be stable, too. All data taken from [Fir96].*

emission is seen by the detector as a delayed signal coincident spatially and in time with the prompt positron signal. Hereby, the time delay comes from the thermalisation time of the neutron and is expected to be around 30 µs in the Target fiducial volume [Abe12]. By adding gadolinium to the Target scintillator two aims are achieved: firstly, the energy release of 8 MeV is above natural radioactivity (see also appendix A), thus, the neutron capture on Gd can be tagged nearly background-free. And secondly, the time delay between prompt and delayed event is minimised because of the huge capture cross sections. This again reduces the background, especially the accidental one (sec. 6.3).

In summary, the event signature of an antineutrino candidate is a signal with a visible energy greater than $\sim$1 MeV followed by a delayed signal with a visible energy of $\sim$8 MeV or $\sim$2.2 MeV for Gd or H, respectively. A schematic view of this signature is given in fig. 6.1.

For reasons of momentum conservation the recoil energy of the neutron released in reaction (6.1) is rather small (of the order of a few keV) and can be neglected. Therefore, the information on the antineutrino energy can be derived from the kinetic energy of the positron. The IBD (6.1) has an energy threshold of 1.8 MeV [PDG12], but the subsequent annihilation of the positron with an electron releases about 1 MeV. Hence, in total, the energy of the electron antineutrino is given by the visible energy $E_{vis} = E_{e^+} + 1\,MeV$ of the prompt signal plus 0.8 MeV:

$$E_{\bar{\nu}_e} \approx E_{vis} + 0.8\,MeV \quad . \tag{6.3}$$

The spectrum obtained for the antineutrinos in the detector is the convolution of the antineutrino spectrum emitted by the reactor cores [Haa12, Mue11] and the cross section of the IBD; see fig. 6.2. It starts at the reaction threshold of 1.8 MeV and goes up to more than 8 MeV.

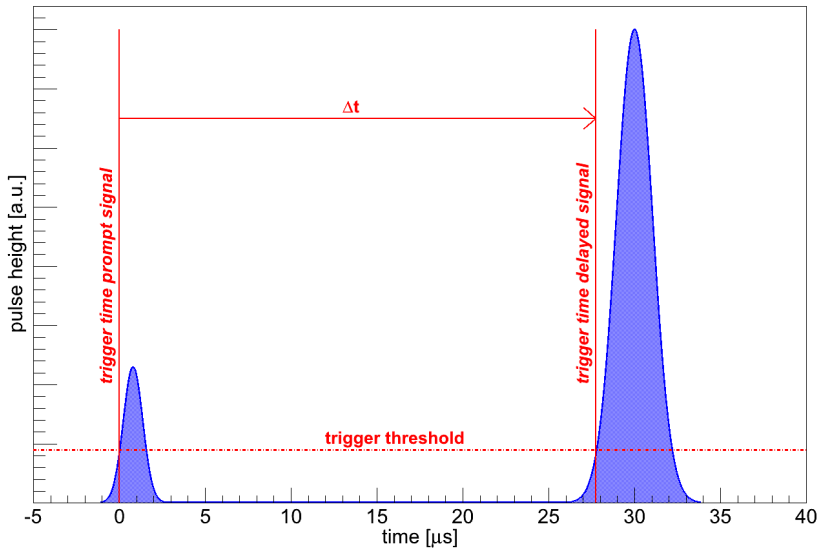

Figure 6.1: *Schematic view of the event signature of an antineutrino candidate event. The Gaussians (blue) illustrate the prompt and the delayed signal, where the energy of each signal is given by the peak area in each case. The prompt signal with a minimal energy of about 1 MeV is followed by a delayed signal, whose energy and temporal delay depend on the nucleus the neutron is captured on. Here, an example event in the case of neutron capture on gadolinium is shown.*

6.2 Correlated Background to the Antineutrino Signal

The search for the coincident signal of the prompt and the delayed event helps to greatly suppress background events, which mainly consist of single radioactive events in the detector. However, the above mentioned event signature for electron antineutrinos can, nevertheless, be mimicked by special background events [Ard06]. Principally speaking, there are two classes of these background events, the accidental ones (see section 6.3), and the correlated ones. The latter are events which have a signature like the antineutrino events with physically correlated prompt and delayed events in space and time. By means of their physical origin the correlated background events can be subdivided into four major classes: fast neutrons, cosmogenically produced isotopes, stopping muons, and nuclear reactions after an α-particle emission.

6.2.1 Fast Neutrons

One main source of correlated background events in the Double Chooz detectors are fast neutrons [Abe12]. These neutrons are released by cosmic muons either in the detector itself or in the surrounding material, e.g. the steel shield or the rock. The latter are the important ones in terms of background, as muons entering the detector or the OuterVeto can be tagged with a very high efficiency and, thus, the subsequent fast neutrons can be cut out in the recorded data. However, fast neutrons released by a muon not recognized by any active detector part can enter the detector and also reach the GammaCatcher or even the Target region without being detected by one of the veto systems. There, these neutrons can scatter

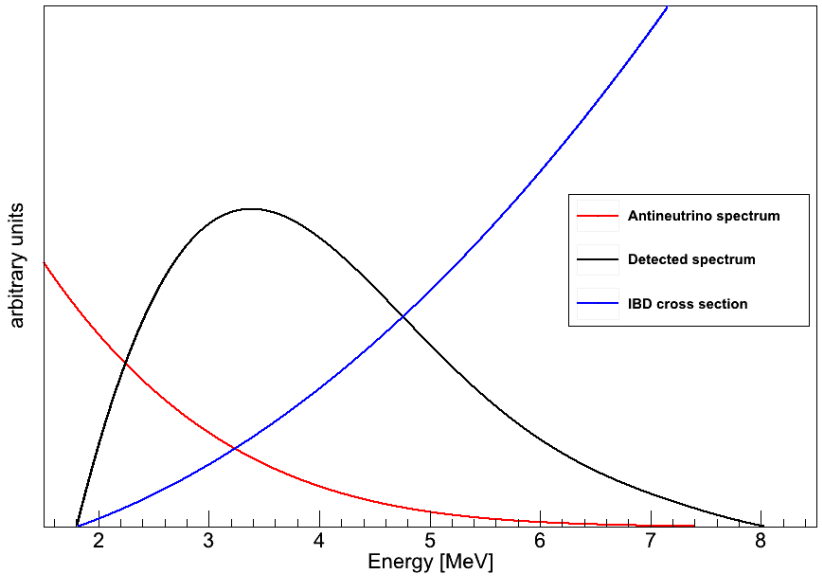

Figure 6.2: *Schematic drawing of the spectrum of the reactor electron antineutrinos (red) without any oscillation effects, convoluted with the cross section of the IBD (blue). The resulting spectrum (black) is the detected antineutrino spectrum in Double Chooz. The y-axis depicts the antineutrino flux and the cross section, respectively, in arbitrary units; the x-axis shows the energy in MeV.*

off a proton, giving rise to an event which might have a visible energy above the 1 MeV-threshold, and, after being thermalised, be captured on gadolinium or hydrogen, which leads to a valid delayed event.

6.2.2 Cosmogenic Radioisotopes: ^{9}Li and ^{8}He

Another important source of correlated background are cosmogenically produced radioisotopes [Abe12]. Cosmic muons or their high-energetic secondary particles can shatter a carbon nucleus of the liquid scintillator by spallation processes. In some cases the unstable isotopes ^{9}Li or ^{8}He are produced, e.g.:

$$\mu + {}^{12}C \rightarrow \mu' + {}^{9}Li + 3p^{+} \quad . \tag{6.4}$$

Here, μ' denotes the scattering muon after the nuclear photoreaction. Both ^{9}Li and ^{8}He are unstable to β^--decay, which is followed by the emission of a neutron in some branchings with a non-negligible probability [Fir96]:

$$^{9}Li \rightarrow e^{-} + \bar{\nu}_e + n + 2\alpha \tag{6.5}$$

$$^{8}He \rightarrow e^{-} + \bar{\nu}_e + n + {}^{7}Li \quad . \tag{6.6}$$

The decay schemes of both isotopes are depicted in figs. 6.3 and 6.4.

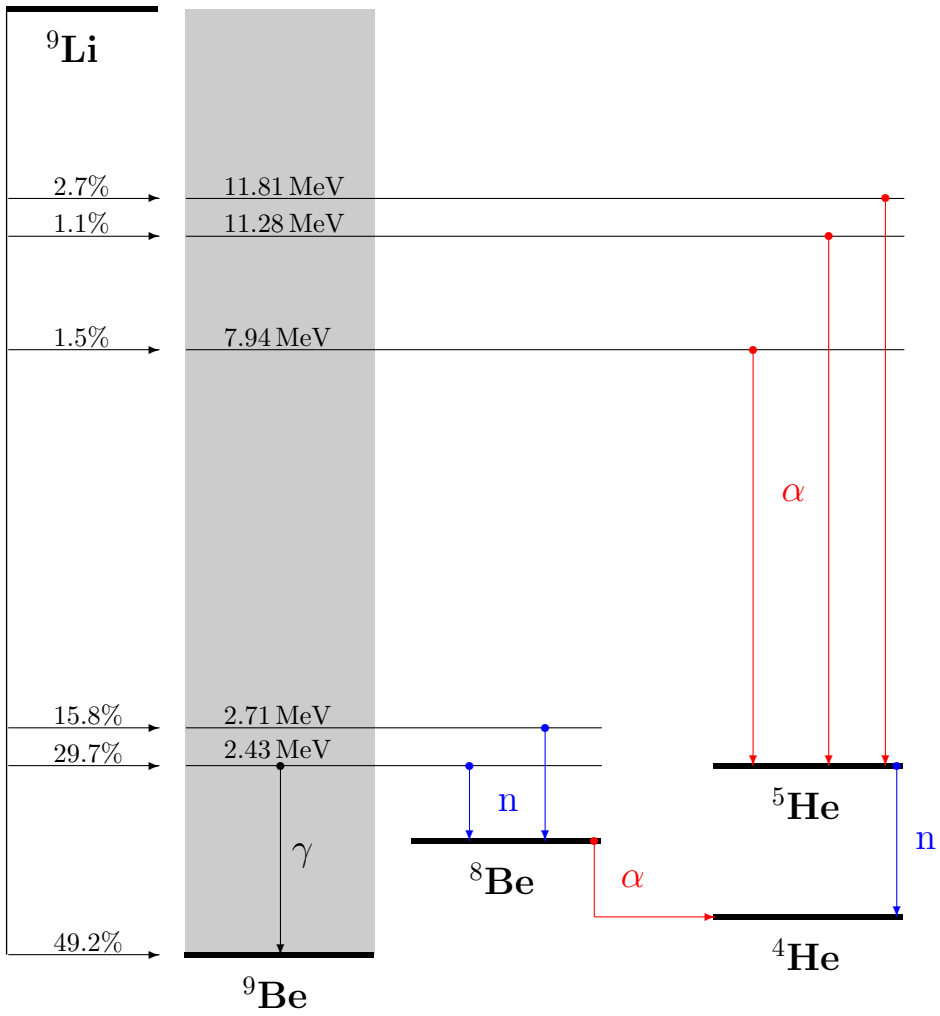

Figure 6.3: *Simplified decay scheme of the β-n emitting isotope ^{9}Li. In nearly 50% of all cases ^{9}Li decays directly into the stable ground state of ^{9}Be by means of a β^--decay, all other branchings lead to a highly excited state of ^{9}Be (greyish shaded box) with energies above the neutron separation threshold; the excitation energies are indicated, too. The states at 2.71 MeV and 2.43 MeV decay by neutron emission into ^{8}Be, which subsequently splits up into two alpha particles. Of all the excited states of ^{9}Be only that at 2.43 MeV has a non-vanishing probability to de-excite by gamma emission before neutron separation. The higher excited states of ^{9}Be are unstable to α-decay, which leads to ^{5}He. This isotope also emits a neutron; therefore, all decay modes, except for the direct decay into the ground state (and the gamma transition from the 2.43 MeV level), have the net reaction $^9Li \rightarrow e^- + \bar{\nu}_e + n + 2\alpha$. Data taken from [Fir96, TUN04].*

The electron from the β^--decay gives rise to a prompt signal, while the capture of the emitted neutron on gadolinium or hydrogen causes the correlated delayed event. In principle, the muon entering the detector can be tagged with a high efficiency, but the half-lives of both ^{9}Li and ^{8}He are too long (178.3 ms and 119 ms, respectively [Fir96]) to fully veto the whole

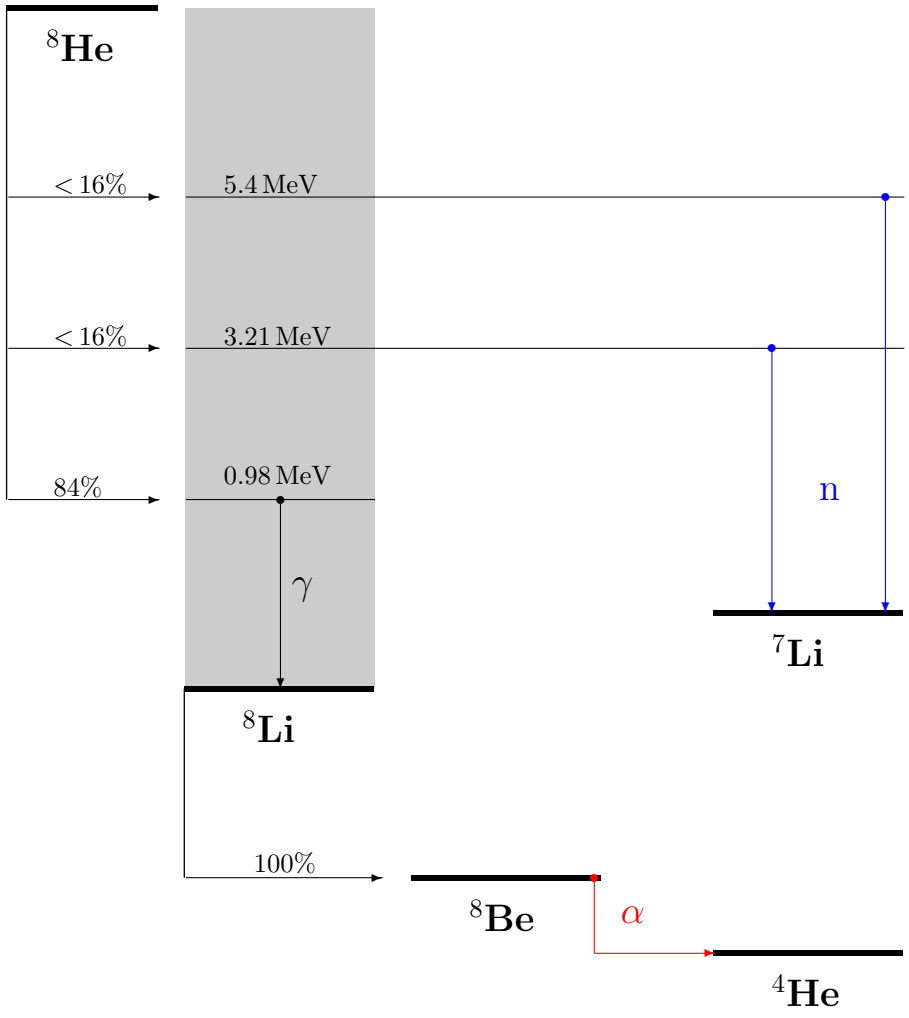

Figure 6.4: *Simplified decay scheme of the β-n emitting isotope ^{8}He. In 84% of all cases ^{8}He decays into a low excited state (0.98 MeV) of ^{8}Li, which de-excites by gamma emission. ^{8}Li is itself unstable to β^--decay, with ^{8}Be being the daughter nucleus, which eventually splits up into two α-particles. Thus, in total this branch of the decay has the reaction equation $^8He \rightarrow 2\alpha + 2e^- + 2\bar{\nu}_e + \gamma$. In less than 16% of all cases the β^--decay of ^{8}He leads to a highly excited state of ^{8}Li, which decays by neutron emission into the stable isotope ^{7}Li. The greyish shaded box indicates the excitation levels of ^{8}Li; the excitation energies are given, too. Note that not all levels are shown, therefore, the decay probabilities do not add up to 100%. Data taken from [Fir96, TUN04].*

detector after a showering muon: for instance, a veto time of one second after each suspicious muon event, which is still less than ten times the half-lives quoted, would lead to a detector dead-time of 100%, given the muon rate of around 46 Hz at the far detector site [Abe12]. Therefore, a more sophisticated discrimination method has to be applied. In addition, due

to the high muon rate the unambiguous allocation of the decay of a cosmogenically produced isotope and the corresponding muon is rather difficult, too.

6.2.3 Stopping Muons

The third contribution to the correlated background in Double Chooz are stopping muons. These were especially problematic as long as the OuterVeto was not fully installed and had still a "hole" in the middle directly above the detector chimney (cf. sec. 5.2). Here, muons could enter the inner detector parts like the Target without being identified by any veto system. In case these muons deposited only a small amount of energy of the order of a few MeV before being stopped, which means a track length of only a few centimeters in the liquid scintillator, they could be misidentified as neutrino candidate event: the direct energy deposition of the muon by means of ionisation and excitation of the liquid scintillator looks like a prompt positron signal, while the delayed signal (the half-life of μ^-, μ^+ is $\sim 2.2\,\mu s$ [PDG12]) is mimicked by the electron or the positron from the muon decay:

$$\begin{aligned} \mu^- &\longrightarrow e^- + \nu_\mu + \bar{\nu}_e \\ \mu^+ &\longrightarrow e^+ + \bar{\nu}_\mu + \nu_e \quad . \end{aligned} \tag{6.7}$$

This kind of correlated background, however, could only happen close to the detector chimney and is nearly completely eradicated since the OuterVeto is fully completed.

6.2.4 (α,n)-Reactions on Carbon Nuclei

In addition to the above given sources of correlated background, which are all caused by cosmic muons, also radioactivity, in particular α-particles, can mimic electron antineutrino events. This happens by a nuclear reaction on ^{13}C, which releases a neutron:

$$\alpha + {}^{13}C \longrightarrow {}^{16}O + n \quad . \tag{6.8}$$

Hereby, the energy deposition by the neutron recoiling off some protons in the liquid scintillator forms the prompt signal; its capture on Gd or H the delayed one. Due to the high quenching of the α-events in the Double Chooz liquids (see sec. 8.2.3) the α-decays themselves have a visible energy far below the 1 MeV-threshold [Abe11a] for positron identification and are, consequently, only visible in a dedicated search below the prompt-signal threshold. The (α,n) background is dominantly induced by the α-emitting isotope ^{210}Po with an α-energy of 5.3 MeV [Fir96], which might be present in the liquid scintillator in a rather high concentration[2], as it is part of the ^{238}U decay chain and, hence, may be introduced either with ^{222}Rn or with the long-lived isotope ^{210}Pb. Therefore, it is potentially dangerous for the precise determination of the neutrino interaction rate. The amount of radioactivity present in the detector thus needs to be measured with high precision, which can, in principle, be performed by an analysis of the bismuth-polonium coincidences[3]; ch. 8.

[2] In case the radioactive equilibrium in the uranium decay chain is broken, e.g. by the production process of the material, the activity of ^{210}Po can easily exceed the activity of ^{238}U.

[3] However, if ^{210}Po is introduced with ^{210}Pb, this methods fails to determine the whole amount of ^{210}Po present in the detector; sec. 8.3.

6.3 Radioactivity in the Detector and Resulting Accidental Background

Besides the correlated background also accidental background has to be regarded for the antineutrino measurement [Abe12]. This class of background events originates in random coincidences between a prompt-like event and a neutron-like delayed event. Such a delayed event could, for example, be a fast neutron entering the detector from outside or some high-energetic gamma quantum produced by a muon in the surrounding rock material.

Every event depositing more than 1 MeV of visible energy in the Target volume can be misidentified as a positron event as induced by an electron antineutrino from the reactor. To a large extend this class of events is due to radioactivity, either β^-- or γ-decays with energies above the 1 MeV-threshold, or α-emission with particle energies above ~ 10 MeV. The latter threshold originates from the quenching factors for α-particles in the Double Chooz scintillators, which have typically values of 10 [Abe11a], or even higher. The α- and β^--decays have to take place directly in the liquid scintillator, as the range of the particles emitted is rather short. Single events from γ-radiation, however, can also be induced by radioactive decays outside the sensitive detector volumes. High-energetic gamma quanta with energies above 1 MeV, as are emitted by ^{40}K, ^{214}Bi, or ^{208}Tl, are even able to penetrate the whole buffer volume. Therefore, also the level of radioactivity of the outer detector parts, like the shielding steel or the PMTs, has to be kept on a low level. The original design goal for Double Chooz aims for a radiopurity level that gives rise to not more than ~ 0.8 accidental coincidence in the antineutrino window per day [Ard06]. Hence, all parts which are meant to be finally installed in the detectors have to be investigated regarding their level of radioactivity. Furthermore, dedicated Monte-Carlo simulation studies have to be performed, in order to predict the singles rates and thus the rate of accidental background in the Double Chooz detectors.

6.4 Background Measurements in Situ

Both the correlated and the accidental background can be measured with the data stemming from the running detector(s). As accidental background originates from random coincidences, it can be measured online by delaying the time window for the antineutrino candidate search by a certain amount of time. Concretely, Double Chooz uses for the antineutrino coincidences a time window of 98 µs which starts 2 µs after the prompt event [Abe12a]. If this window is now shifted, for example to $[102, 200]$ µs (or even later) after the prompt event, most of the delayed events which are physically connected to the prompt event will not be identified any more, but only (new) random coincidences are found. Therefore, the shifted time window gives a direct measure for the number of accidental coincidences, which can then in the end be subtracted statistically from the antineutrino-like events found.

Correlated background, on the other hand, cannot be tagged by this method, as its delayed events are connected to the prompt ones in time. However, the number of correlated background events can be ultimately measured during a period with both reactor cores off[4] ("off-off data"). Even a few days with reactor-off-off data significantly decrease the uncertainties in the antineutrino spectrum coming from correlated background.

[4] Of course, correlated background induced by the reactor cores can not be tagged. However, as was explained above, the most important sources for correlated background are due to cosmic radiation and radioactivity, and thus not correlated to the reactors.

Chapter 7

Radiopurity in Double Chooz: Material Screening Measurements, Neutron Activation Analysis and Monte-Carlo Simulations of the Singles Rate

The background present in the measurement of reactor electron antineutrinos in Double Chooz is partly induced by radioactivity in the materials within and around the detector (secs. 6.2 and 6.3). Therefore, it is an important task to keep the amount of radioimpurities in the detector setup as low as possible. In most cases this means to thoroughly screen all detector parts and materials, and, eventually, select only those materials fulfilling the requirements of radiopurity for the final detector configuration. Only in a few cases, e.g. for the detector liquids, it is possible at all to reduce the intrinsic radioactivity by some purification process.

However, even after carefully selecting the materials to be used, a certain amount of radioactivity cannot be avoided in the detector. In order to be able to calculate the resulting accidental and correlated background, it is important to precisely determine the mass concentrations of the long-lived radioisotopes brought in. With the help of dedicated Monte-Carlo simulations, where the full geometry of the Double Chooz detector is included, the resulting energy spectra and count rates induced by these radioimpurities in the final detector setup can be determined. The comparison of the simulated spectra to the real detector data furthermore allows an additional energy calibration[1] and, in some cases, an allocation of the sources of radioactivity-induced background.

[1]The actual energy calibration in Double Chooz is done with calibration sources as well as the neutron capture peak on hydrogen [Abe12a]. In addition, especially high-energetic gamma quanta as emitted by ^{40}K and ^{208}Tl contain feasible information on the energy scale (see sec. 8.1).

7.1 The Germanium Detector System: Setup, Efficiency Calibration and Data Analysis

7.1.1 Detector Setup with Active and Passive Shielding

Some of the radiopurity measurements for Double Chooz have been performed in the Garching underground laboratory with a dedicated germanium detector setup. This laboratory has an overburden of about 15 m.w.e. [Hen99] in all directions, which is sufficient to completely shield the hadronic component of the cosmic rays. In addition, the muon flux is reduced by roughly a factor of three [Hen99]. In this underground laboratory a low-level germanium detector setup has been installed [Hof07] for gamma spectroscopy; fig. 7.1.

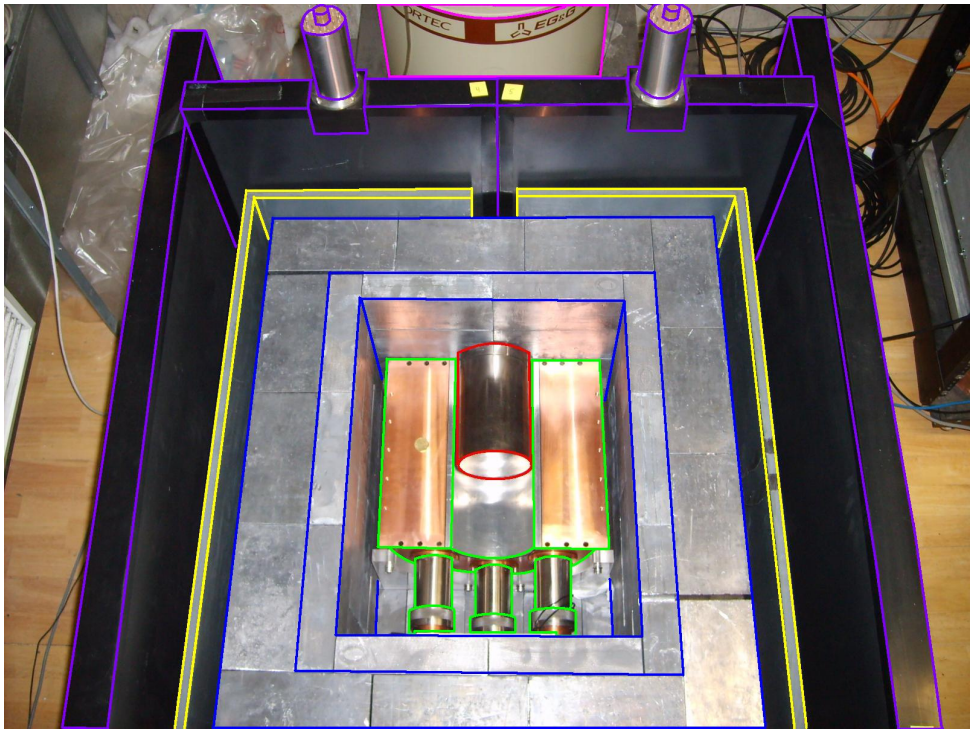

Figure 7.1: *Picture of the germanium detector setup with removed top cover. In the middle the germanium detector in its magnesium housing (marked in red) can be seen. It is surrounded by the anti-Compton veto system (green) in its copper and aluminium housing, and with the attached PMTs. Both the germanium detector and the anti-Compton veto are fully surrounded by the lead shielding (blue), where the innermost 5 cm are made of ultrapure lead. The muon veto system (purple) encloses all inner detector parts, including the PVC box (yellow), which is flushed with nitrogen evaporating from the liquid nitrogen dewar (pink) during operation to expel any traces of radon. To get an impression of the size a 50-Eurocent coin was placed on the left of the anti-Compton veto.*

The central part of this detector system is a high-purity germanium semi-conductor detector with a relative counting efficiency[2] of 150.5% [Hof07]. It is operated at liquid nitrogen

[2] A cylindrically shaped NaI-crystal with a diameter of 3" and a length of 3" has per definition 100% counting efficiency [Kno10]. The efficiency of germanium detectors is often quoted with respect to such a crystal.

temperature and mounted in an evacuated magnesium housing. At its frontside this housing has a thickness of 1.5 mm, which consequently leads to a lower detection threshold of about 15 keV, as for incoming gamma rays with energies well below this threshold the penetration probability drops below 5%. With the germanium detector an energy resolution of 955 eV at 122 keV (gamma line from a ^{57}Co-source) and 1.764 keV at 1.33 MeV (^{60}Co) [Hof07] is obtained. Due to its high counting efficiency this germanium detector is well suited for the measurement of high-energetic gamma rays, which is, in particular, important for materials to be used in Double Chooz, as high-energetic gamma quanta are highly penetrating and, hence, can reach the Target region even from outside the detector. The energy calibration of the germanium detector was carried out using calibration sources and gamma lines from the activity of omnipresent natural radioisotopes. This was done for each measurement separately to correct for any drifts in the energy scale.

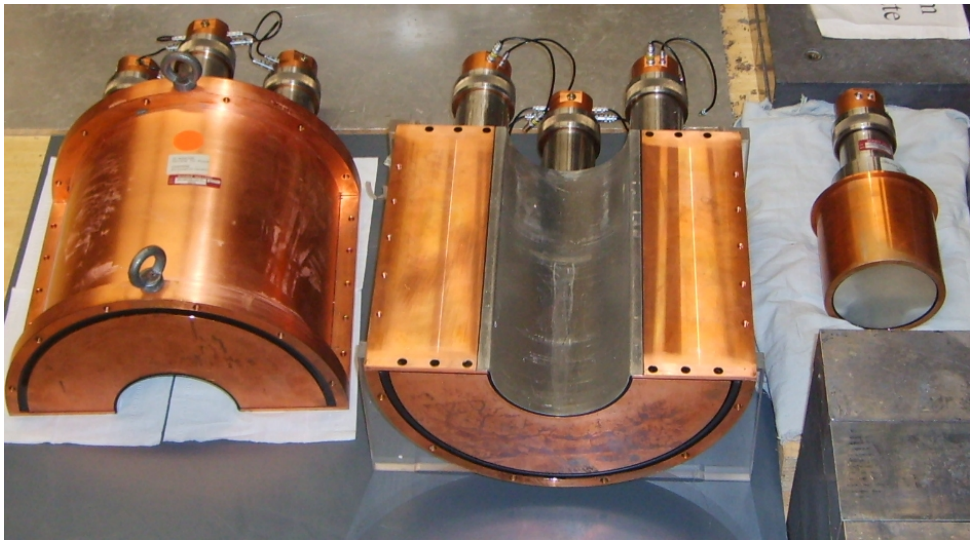

Figure 7.2: *Photograph of the three parts of the anti-Compton veto system. In the middle the lower half shell can be seen, which is also visible in fig. 7.1; at its left the upper half shell is placed, and at the right the endcap. This veto system consists of copper-housed sodium-iodide scintillation counters, read out by photomultiplier tubes (three 2" PMTs at each half shell, one 3" PMT at the endcap). All inner sides of the housing which are facing towards the germanium detector have 0.8 mm thin aluminium entrance windows for incoming gamma rays to allow a low detection threshold.*

The germanium detector is surrounded by Tl-doped sodium-iodide scintillation counters (fig. 7.2), which are read out by in total seven PMTs and serve as anti-Compton veto. These crystals cover nearly 4π solid angle around the germanium detector, only the detector's backside stays unmonitored. If a gamma quantum interacts in the germanium crystal via Compton scattering and escapes afterwards, there is a high probability for this scattering photon to deposit some energy in the anti-Compton veto system, too. In this way, gamma quanta not depositing their full energy in the germanium detector can be rejected from the recorded data on an event-by-event basis, thus greatly reducing the continuous background in the energy spectra. Hence, the signal-to-background ratio of the gamma spectroscopy system is greatly increased (cf. fig. 7.4).

The anti-Compton veto system is divided into three parts: an upper and a lower half shell, and an endcap, fig. 7.2. While both half shells are always used, the endcap can be removed for measurements of bigger samples, which, of course, slightly reduces the veto's efficiency.

However, in measurements recorded with running anti-Compton veto gamma quanta emitted as part of a gamma cascade cannot be used for the determination of the activity of some radioisotope, as one gamma of such a cascade may be detected in the germanium counter, while another gamma deposits some energy in the anti-Compton veto system and hereby leads to a veto signal. As a consequence, only gamma transitions from some excited state directly to the ground state of the daughter nucleus are taken for the analysis[3]. This is explained in more detail in sec. 7.1.3 and in appendix C.

Both the germanium detector and the anti-Compton veto system are fully enclosed by 15 cm thick lead layers, which shield a large fraction of all gamma rays from the laboratory. The innermost 5 cm of this lead shielding are built of ultrapure lead with a specific activity of the radioactive isotope ^{210}Pb of less than 5 $\frac{\text{Bq}}{\text{kg}}$ [Lan07]. The active detector parts and the lead are again fully contained within a plastic box, which is flushed during operation with the evaporating nitrogen from the dewar containing the liquid nitrogen supply for the germanium crystal. In this way, the air, and with it the radioactive rare gas radon, is expelled from the box. Hence, the activity of radon and its daughter isotopes is greatly reduced inside the lead shielding, further diminishing the background from ambient radionuclides.

The outermost part of the gamma spectroscopy system consists of six plastic scintillator panels serving as active muon veto. Except for the bottom side, the full detector setup is covered by these panels, see fig. 7.3. The energy threshold[4] of the muon veto system is set to 2-4 MeV. Each of these panels is 5 cm thick, therefore, a through-going muon will deposit at least ~ 10 MeV in the panels, which is far above the detection threshold. From measurements with and without running muon veto its efficiency for muon tagging could be determined to be $> 97.7\%$ [Hof07]. Again, the veto works on an event-by-event basis. The background suppression due to the active veto systems is depicted in fig. 7.4.

The scintillation signals of both veto systems, the anti-Compton sodium-iodide crystals and the muon veto panels, are converted into logic signals by the read-out electronics [Hof07] and fed into the gate input of the analogue-to-digital converter (ADC) of the germanium detector read-out. By this, every event which deposits enough energy in one of the veto systems to trigger it is rejected. Because of this hardware veto none of the rejected events is recorded, but the final spectra contain only those events which had only deposited energy in the germanium detector itself. The overall veto countrate is about 300 Hz. Combined with a length of the veto window of 20 µs this leads to a dead-time of 0.6%.

The germanium detector signals are read out with an analogue main amplifier and, in parallel, with the digital signal processing unit DSP 9660A from Canberra [DSP00]. All gamma spectroscopy results which will be shown in the following are recorded with the latter module, as it shows a considerably better energy resolution than an analogue main amplifier

[3] In principle, also gamma lines from gamma cascades could be taken for an analysis. This would require a precise determination of the probability of creating a veto signal, best performed by means of a Monte-Carlo simulation. However, there are enough gamma lines in each decay chain which stem from transitions directly to the ground state and thus can be analysed without any additional corrections.

[4] The exact threshold cannot be quoted, as it is strongly position dependent: an energy deposition of about 500 keV directly in front of one of the PMTs will trigger the veto, while for events close to the corners of the panels energy depositions of the order of 3-4 MeV are necessary for a valid signal. However, a through-going muon will always trigger the veto.

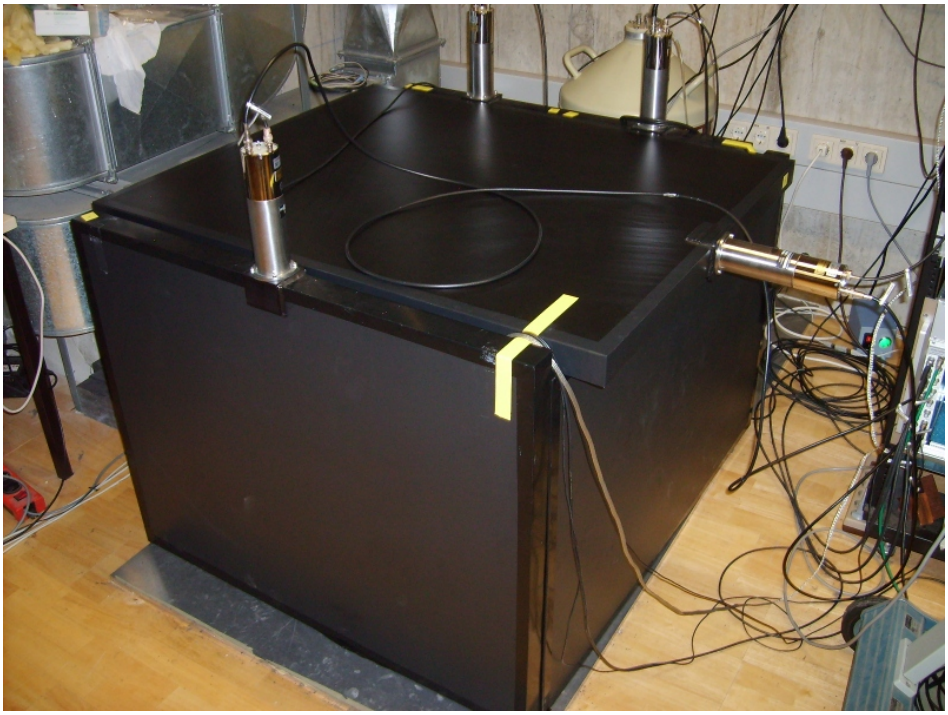

Figure 7.3: *The gamma spectroscopy system in its fully equipped state. The lead shielding and the plastic box are closed, and all six muon veto panels are in place and connected. Except for very tiny gaps between the panels and the bottom side the whole inner detector system is enclosed by the muon veto.*

[Hof07]. Nevertheless, the analogue chain was still running, too, to have an independent cross check. Therefore, one set of efficiency calibrations (sec. 7.1.2) was also carried out for both modules.

7.1.2 Efficiency Calibration of the Monte-Carlo Simulation

The number N(t) of remaining nuclei at time t in the decay of a radioactive isotope is given by an exponential function:

$$N(t) = N_0 \cdot e^{-\frac{t}{\tau}} \quad . \tag{7.1}$$

Hereby, τ denotes the life time of the radioisotope and N_0 the number of nuclei at $t = 0$. The activity A(t) of the isotope at a given time t is the negative time derivative of the number of remaining nuclei:

$$A(t) = -\dot{N}(t) = \frac{N(t)}{\tau} \quad . \tag{7.2}$$

From that the number of radioactive decays ΔN in a given time interval Δt, e.g. the measuring time, can be calculated by integration. For the special case of very long life times of the isotope ($\tau \gg \Delta t$), or for isotopes which are in a radioactive equilibrium (i.e. the number of decays is equal to the number of nuclei produced in the decay of some mother isotope), the activity can be approximated to be constant over the time interval and becomes

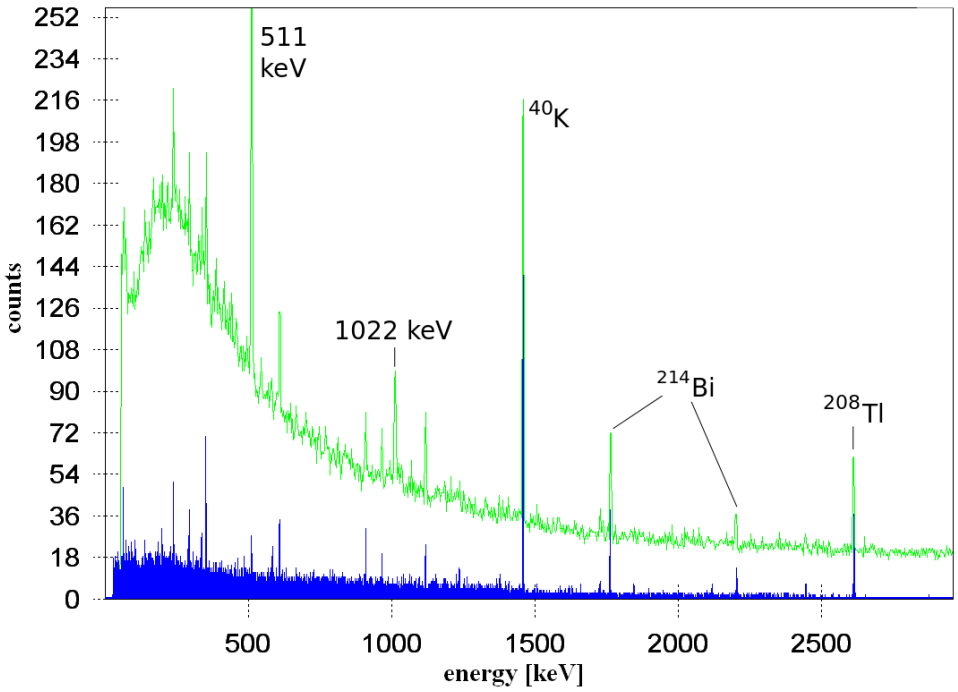

Figure 7.4: *Energy spectrum of the ambient radioactivity recorded with the germanium detector, once with (blue data) and once without (green data) running active veto systems. The measuring time was ∼ 230,000 s in both cases; all passive shieldings are fully set up. The most prominent lines in the spectrum are marked with the isotopes emitting them. The great suppression of the positron annihilation lines (511 keV and 1022 keV, respectively) is remarkable, indicating a very good muon identification. Positrons are mainly produced by pair production processes of muons in the surrounding lead shielding. Besides this, at low energies (not indicated here) also the X-ray fluorescence lines of lead and the lines of excited germanium isotopes (both again induced by muons or muon secondaries) vanish completely. The prominent gamma line from ^{40}K is identified to stem from the PMTs of the anti-Compton veto system [Hof07]. A complete list of all gamma lines is given in appendix B.*

$$A \approx \frac{\Delta N}{\Delta t} \quad . \tag{7.3}$$

If the decay of the isotope is now measured with the germanium detector, not all of the decays ΔN which emit a gamma quantum with a certain emission probability P ($0 < P \leqslant 1$) will lead to a full energy deposition of that gamma in the detector, but only the fraction

$$N_{meas} = \Delta N \cdot P \cdot \varepsilon \quad . \tag{7.4}$$

The detector efficiency ε specifies the probability for a full energy deposition in the detector and thus takes into account all effects like the solid angle covered by the detector, the absorption of gammas in the source itself, and the probability for energy losses in the detector. The latter can happen, for example, if the gamma quantum only Compton scatters in the detector and subsequently escapes, or if a pair production process takes place with one of the 511 keV annihilation quanta leaving the detector. Therefore, the efficiency ε depends on the

geometrical setup as well as the gamma energy, as the latter determines the cross sections for the interaction processes photoeffect, Compton scattering, and, if energetically possible, pair production. Its determination can best be performed by means of a Monte-Carlo simulation which accounts for the correct geometry and energy-dependent interaction cross sections.

The Monte-Carlo simulation used in the present thesis to analyse the gamma energy spectra recorded with the germanium detector [Hof07] is based on the toolkit program GEANT4 [Ago03, All06, CER12a], version 4.9.2.p02. It contains all active and passive detector parts (fig. 7.5), including the muon veto panels, and is able to simulate all relevant interactions between photons and matter, namely photoeffect, nuclear photoeffect, Compton scattering, and pair production. The subsequent emission of X-rays and Auger-electrons, respectively, is included, too.

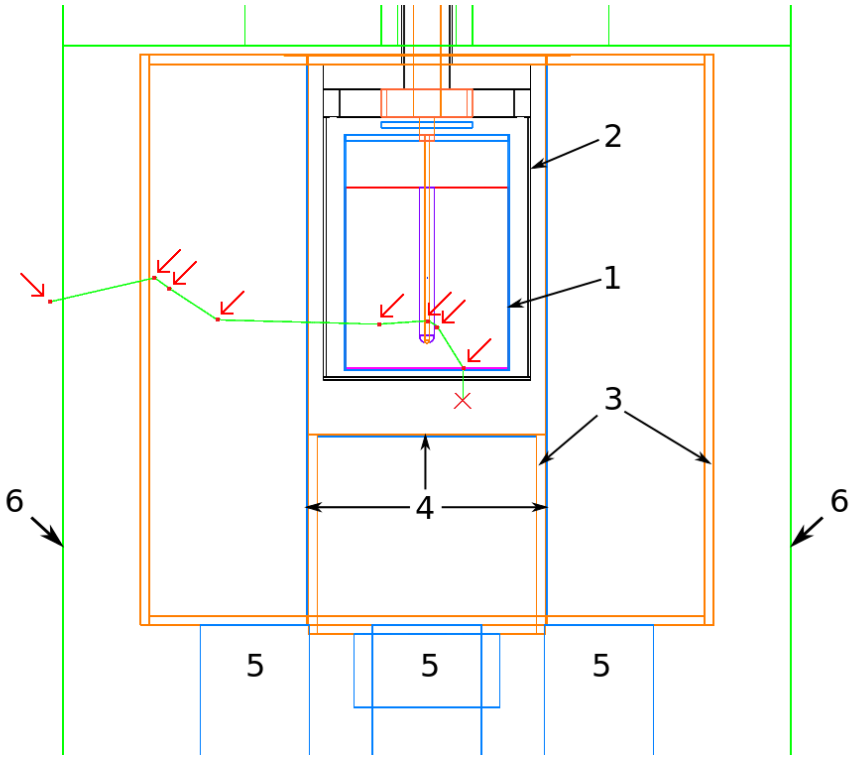

Figure 7.5: *Gamma event simulation performed with the detector Monte-Carlo program. This cross-sectional view shows the different parts of the inner detector, with the germanium crystal in its inner aluminium (blue; 1) and outer magnesium housing (black; 2). On top the cooling rod which connects the germanium detector with the liquid nitrogen dewar can be seen. The sodium-iodide scintillation crystals in their copper (amber; 3) and aluminium housing (light-blue; 4) with the attached PMTs (light-blue; 5) can be seen as well as the inner borders of the lead shield (green; 6). A gamma quantum with an energy of 1.33 MeV is generated at point "X" and tracked through the detector system (green path). Each interaction vertex is marked with a red dot and a red arrow. The gamma undergoes four Compton scattering processes in the germanium detector, then scatters off three times in the anti-Compton veto, and is finally absorbed in the lead by photoeffect [Hof07].*

However, the Monte-Carlo simulation needs to be calibrated in efficiency. Details on the

method of this calibration can be found in appendix D. The calibration was carried out using radioactive calibration sources with well-known activities and geometries, which cover the whole energy range up to nearly 2 MeV (cf. tab. D.1). The results from the measurements were then compared to the simulated efficiencies. In this way, an energy-dependent calibration curve (correction function) can be obtained for the simulation. For the determination of the detector efficiency for an investigated sample the Monte-Carlo program is used later-on to simulate this efficiency (including the correct geometry of the sample), and the correction function which was gained in the measurements with the calibration sources is applied to these data. This method accounts for any systematic deviations of the simulation and corrects them.

The radioactive calibration sources were used to record gamma spectra for three different source positions: directly in front of the entrance window of the germanium detector, and 10 cm and 20 cm away from it. As was shown in a previous calibration campaign [Hof07], moving the source to a position off the symmetry axis of the detector has only little impact on the detector efficiency and is, furthermore, handled correctly by the simulation. Therefore, all source positions chosen to be investigated in the present thesis are on-axis. In addition, only few of the later-on performed gamma spectroscopy measurements have an asymmetric sample geometry. The efficiency calibration was carried out twice, once in advance of all gamma spectroscopy measurements presented in sec. 7.2, and once after it. The first calibration campaign was performed both for the analogue and the digital read-out, the second one only for the digital DSP 9660A.

In order to obtain the efficiency calibration curves for the Monte-Carlo simulation the ratio of the measured detector efficiencies $\varepsilon_{\mathrm{meas}}$ to the simulated efficiencies $\varepsilon_{\mathrm{sim}}$ has been calculated. A fit to these data (fig. 7.6) yields the energy-dependent correction factors for the simulation, for each of the three geometrical setups.

For energies above ~ 300 keV the ratio of $\varepsilon_{\mathrm{meas}}$ to $\varepsilon_{\mathrm{sim}}$ is constant for all three geometrical setups and both for the analogue and the digital read-out. For the latter, the correction factors to the simulated efficiencies are (0.672 ± 0.002), (0.6969 ± 0.0002), and (0.688 ± 0.005) for 0 cm, 10 cm, and 20 cm distance to the entrance window, respectively; for the analogue system correction factors of (0.742 ± 0.003), (0.7452 ± 0.0003), and (0.7524 ± 0.0001) are obtained. The fitted efficiency ratios for the digital system for the first and second calibration campaign match perfectly, indicating a very stable detector performance over the whole period of gamma spectroscopy measurements (about 4 years). As can be seen from fig. 7.6 and tab. D.3 the analogue read-out system has a slightly higher efficiency; the reason for this is unknown, but the effect was already observed in a previous measurement [Hof07].

Towards lower energies the simulation clearly overestimates the photopeak efficiency of the detector. The efficiency ratio is therefore fitted with an exponential fit to account for these systematics:

$$\frac{\varepsilon_{meas}}{\varepsilon_{sim}} = a_0 - e^{a_1 \cdot E + a_2} \quad , \tag{7.5}$$

with the gamma energy E. The coefficients a_i ($i = 0,1,2$) of this fit for the different setups and read-out systems are summarised in tab. D.6 in appendix D.4.

The growing deviation between simulation and measurement towards smaller energies is most likely due to a dead layer at the front end of the germanium crystal which is not properly taken into account in the simulation. The front end of the crystal is doped with lithium for electric contacting. In the simulation this inactive layer is assumed to be 0.7 mm

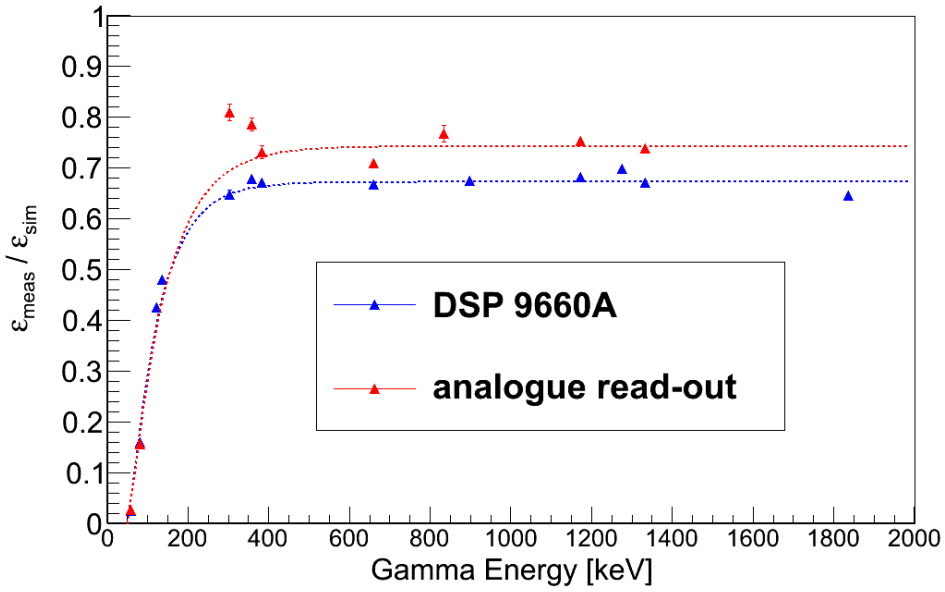

Figure 7.6: *Ratio of measured ε_{meas} to simulated detector efficiencies ε_{sim} for the source position directly at the entrance window for the analogue read-out system (first calibration campaign; red data points) and the DSP 9660A (second calibration campaign; blue). The ratios obtained for the digital system in the first calibration are not shown here, as they match perfectly with the values of the second calibration. Both data are fitted with an exponential function plus a constant (see eq. (7.5); dashed lines). The error bars are calculated by linear error propagation from the errors quoted in tabs. D.3 through D.5. In most cases the error bars (1σ) are smaller than the symbol used. For the gamma spectroscopy results presented in sec. 7.1.3 only the DSP 9660A was used.*

thick (the value quoted in the data sheet of the germanium detector), however, in the real detector it seems to be slightly thicker. This does not seriously affect high-energetic gamma rays, as these easily penetrate through this layer, but has a major impact on the detection efficiency at lower gamma energies. The observed over-estimation of the detector efficiency in the simulation also at higher energies might have several reasons: the simulation does not include effects like charge collection inefficiencies, thermal noise, or count rate losses due to pile-up. Besides this, also the geometry of the detector itself could be implemented somehow incorrectly or imprecisely into the simulation, causing the simulated efficiencies to be higher than the measured ones. The latter could be corrected in the future by taking an X-ray picture of the detector and comparing the true geometry to the simulated one. This is, however, a big effort and has not been performed so far.

The simulated detector efficiencies for the samples investigated with direct gamma spectroscopy are corrected with the above-quoted correction functions: the detector efficiency is simulated for each gamma energy to be analysed with the correct geometry; the outcome of the simulation is multiplied with the value of the correction function at the respective energy. In this way, the systematic deviations of $\varepsilon_{\mathrm{sim}}$ from $\varepsilon_{\mathrm{meas}}$ are cancelled out and do not affect the obtained results for the mass concentrations of the radioimpurities in the investigated samples.

7.1.3 Analysis of the Recorded Spectra

The first step in the analysis of the gamma spectra recorded for a certain sample is the comparison to the respective blank run. For each of the detector configurations used (e.g. with or without the endcap of the anti-Compton veto system, or different sample holders) a dedicated blank run was recorded under exactly the same conditions as the actual measurement with the sample to be investigated. In particular, the same flushing time with the evaporating nitrogen and the same measuring time were used. The comparison of the spectra with and without sample happens peak by peak.

Three different cases are distinguished here: in case a certain gamma peak only appears in the run with the sample but not in the blank run, its peak area (as calculated by the automatic peak fit routine of the program Genie2000 [GEN02]), already corrected for the underlying continuous background, gives the number of counts N_{meas} in the photopeak. The uncertainty of the number of counts, ΔN_{meas}, is hereby given by the uncertainty of the peak area only.

In case the gamma peak appears both in the spectrum with sample and in the blank run, the other two cases are checked: if the peak area in the recorded spectrum exceeds the peak area in the blank spectrum by at least 1.64 standard deviations (90% C.L.) as calculated by quadratic error propagation from the single uncertainties of the Gaussian peak fits, the number of counts allocated to the sample is simply the difference of the two peak areas.

In the last case, the number of counts found in a certain gamma photopeak in the spectrum recorded with the sample is compatible with or even less than the number of counts in the corresponding peak in the blank run (which can happen due to statistical fluctuations), only an upper limit for the number of counts from the sample is calculated. A Gaussian shaped function G(x) is set up around the difference in counts (sample minus blank) having a width equal to the combined uncertainties of the single peak fits [Hof07]. The upper limit for N_{meas} is found by integrating this Gaussian curve so that

$$\frac{\int_0^{N_{meas}} G(x) \cdot dx}{\int_0^{\infty} G(x) \cdot dx} = 0.90 \quad , \tag{7.6}$$

see also fig. 7.7. This method assumes that the number of counts with sample can only be greater than in the blank run, i.e. the sample does not absorb any gamma rays stemming from the ambient background[5]. An advantage of this calculation method is that it passes continuously into the method applied to Gaussian distributed measurands for the calculation of upper limits for a given confidence level, when the difference in counts approaches zero [PDG12].

Given the number of counts in a certain gamma photopeak (or, at least, its upper limit) the corresponding activity of the emitting radioisotope can be calculated by dividing N_{meas} by the measuring time t, the gamma emission probability P, and the detector efficiency ε:

[5]This is a very good assumption for most of the samples, as these are either very tiny (for example the welding electrodes; see below) or not very dense (any organic material). The bigger and dense samples (like the samples of the shielding steel) were measured without the endcap of the anti-Compton veto, which is known to be the biggest source of background inside the lead layers [Hof07]. Any background originating from outside the lead nearly comes from 4π solid angle, and the absorption by the sample can be neglected just for geometrical reasons.

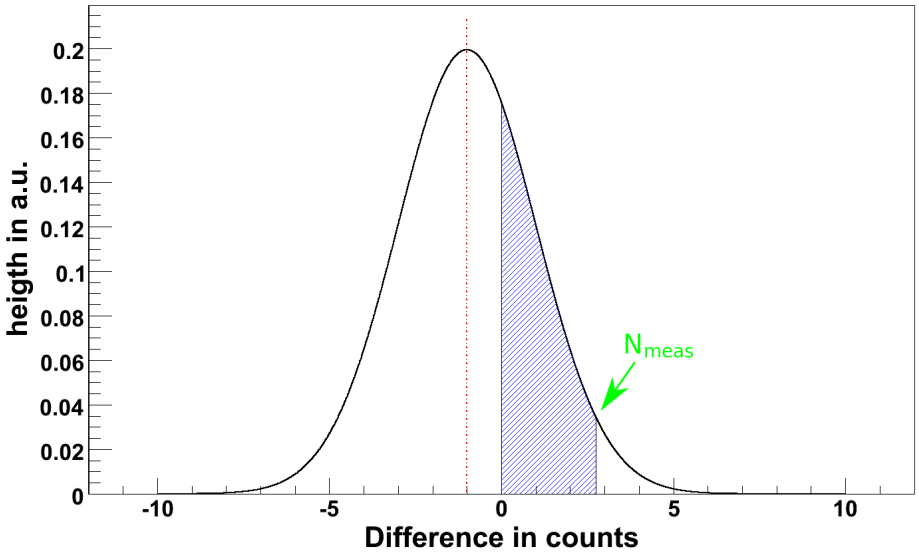

Figure 7.7: *Schematic drawing explaining the integration method of finding the upper limit for the number of gamma counts stemming from the sample: a Gaussian curve is set up around the difference in counts with and without sample (red dotted line); its width is the combined uncertainty of the two single errors of the peak areas. The upper count limit N_{meas} (indicated in green) is calculated so that the area ranging from zero the N_{meas} (blue shaded) covers 90% of the area of the Gaussian above zero (physically allowed region).*

$$A = \frac{N_{meas}}{t \cdot P \cdot \varepsilon} \quad . \tag{7.7}$$

This calculation assumes a constant activity over the measuring time, which is equivalent to the assumption of radioactive equilibrium, at least for all short-lived isotopes investigated (see sec. 7.1.2). The detector efficiency including all geometry related effects is hereby determined using the Monte-Carlo simulation. The gamma rays to be analysed are simulated for each sample with the correct geometry; the results of these simulation are corrected with the energy-dependent correction functions given in sec. 7.1.2.

In total, 17 different gamma lines from the decay chains of ^{238}U and ^{232}Th as well as the long-lived radionuclide ^{40}K are analysed for each sample; for selected samples like steel samples (sec. 7.2) also the concentration of ^{60}Co is calculated. The gamma lines chosen for the analysis have to fulfill certain criteria: as the anti-Compton veto was running during the measurements and vetoing any events which happened simultaneously with an event in the germanium detector, the gamma lines to be analysed must not be part of a gamma cascade, but represent direct transitions to the ground state of the daughter nucleus. Otherwise there is a non-negligible chance for another gamma quantum of the cascade to deposit some energy in the anti-Compton veto system, rejecting the whole event. In addition, for the same reasons the excited states emitting the gamma rays used in the analysis shall not be populated by transitions from higher excited states. Appendix C shows three different examples (^{212}Pb, where any effects of gamma cascades can be neglected, ^{214}Bi, have only some suitable transitions from highly excited states, and ^{208}Tl, having no viable transition at all) explaining the

selection criteria in more detail. The two gamma lines of ^{60}Co at 1173.2 keV and 1332.5 keV, however, do not match the criteria given above, as they are emitted together in 99.97% of all decays [Fir96]. This makes cascade vetoing rather likely, therefore, for ^{60}Co the Monte-Carlo simulation has to be used to determine this veto probability, and to correct the obtained results for this effect. In case of the decay chains of ^{238}U and ^{232}Th, respectively, the number of gamma lines which can be analysed without any cascade corrections is big enough, hence all lines which would need such corrections are set aside.

For some radioisotopes more than one gamma transition fulfills the requirements. In that case the activity of this isotope is calculated as the weighted average of the single activities of the gamma lines [Bev69, Hof07]. The advantage of the weighted average is that the single results with the highest precision have the biggest contribution to the combined result. In case only upper limits can be quoted, the lowest limit (= best constraint) again has the biggest contribution to the combined limit. In general, gamma lines with a high emission probability P lead to more precise results, as the number of counts N in the respective gamma peak is high, and its relative error (approximately given by $\frac{1}{\sqrt{N}}$) becomes small. This also applies to the calculation of upper limits (in case no enhancement of the gamma line over the background can be seen), as the width of the Gaussian G(x) in eq. (7.6) scales like the uncertainty of N. Therefore, gamma lines with a big peak area, i.e. with a high emission probability P, lead to smaller upper limits[6], too.

In sec. 7.2 the quoted activities for the decay chains of uranium and thorium (appendix A) are again the weighted averages of the activities of the single isotopes, assuming radioactive equilibrium. The latter assumption is most likely always valid for the thorium decay chain, as it contains no long-lived isotopes (the radioisotope with the longest half-life is ^{228}Ra with 5.75 a [Fir96]). However, radioactive equilibrium might be broken for the uranium chain, since especially ^{226}Ra and its two mother isotopes are long-lived. ^{210}Pb has a long half-life (22.3 a [Fir96]), too, and is another possible isotope for breaking the equilibrium. In principle, radioactive equilibrium can be tested by comparing the activity of some isotope above ^{234}U with the activity of some isotope below ^{226}Ra (and analogously for ^{210}Pb). However, the only gamma lines viable for such a comparison are the 1001.0 keV line of ^{234m}Pa and the 46.5 keV line of ^{210}Pb, and both lines have only small emission probabilities (0.83% and 4.25%, respectively [Fir96]). In addition, for gamma quanta with an energy of 46.5 keV the efficiency of the germanium detector is already less than 1% (see sec. 7.1.2), mostly because of the thickness of the entrance window and the detector's dead layer. Therefore, reliable tests of the radioactive equilibrium are difficult.

Nevertheless, the absence of prominent gamma emissions with high energies from any isotope above ^{226}Ra and below ^{210}Pb, respectively, also prevents these isotopes to deposit energy in the Target and GammaCatcher region of Double Chooz as long as they are not located directly there; α- and β^--particles have a much too short range to reach the inner detector parts from outside. In that sense the quoted values for the uranium chain (weighted averages under the assumption of radioactive equilibrium) can be considered to be equivalent concentrations, i.e. they depict the amount of uranium which would be needed to generate the observed activities of relevant isotopes like ^{214}Bi in case the chain was in equilibrium rather than the true concentration of uranium. Only in the case that samples of the inner

[6]The error of the number of counts N in the respective photopeak determines the width of the Gaussian distribution G(x) and with it the upper limit N_{meas} (eq. (7.6)). If the error of N is again taken to be $\sqrt{N}$ the upper limits of the activities A are expected to scale like $\frac{1}{\sqrt{P}}$, as $A \propto \frac{N_{meas}}{P} \propto \frac{\sqrt{N}}{P} \propto \frac{\sqrt{P}}{P}$.

detector parts (e.g. the liquids) are investigated the difference becomes important, as then α- and β^--activities play an important role, too.

The measured activities A of radioimpurities in the samples are finally also converted into mass concentrations c:

$$c = \frac{A \cdot \tau \cdot M}{m_{sample}} \quad , \tag{7.8}$$

where τ denotes the life time of the respective isotope, M its molecular mass, and m_{sample} the mass of the investigated sample. The mass concentrations are given in units of $\frac{g}{g}$.

The quoted uncertainties for the activity A (at 90% C.L.) are combined by error propagation from the single uncertainties of the measuring time t (recorded by the gamma spectroscopy program Genie2000 with a precision of 0.01 s), the gamma emission probability P (errors taken from [Fir96]), the peak area N_{meas} in the spectrum ($1.64\,\sigma$-error as calculated by Genie2000), the sample mass m_{sample} (measured with an uncertainty of 0.01 g), and the detector efficiency ε (as given by the correction function in sec. 7.1.2). The percental uncertainty of the mass concentration c is the same as for the activity A; the life time τ and the molecular mass M are considered to be exact. In case the number of counts N_{meas} has only an upper limit (which is already at 90% C.L.; see above), ΔN_{meas} is taken to be zero.

7.2 Results of Direct Gamma Spectroscopy

For the Double Chooz far detector several material samples have been screened for radioimpurities with the germanium detector system. As was discussed above, the germanium detector is well suited for the measurement of high-energetic gamma quanta, therefore mainly samples from the outer parts of the Double Chooz far detector have been investigated, like samples from the shielding steel, the InnerVeto (amongst others PMT-bases, -glass, and -cables), and samples from the filling system. These parts of the detector can only induce singles events in the Target region by emitting highly penetrating gamma rays; α- and β^--particles (including the bremsstrahlung emitted by the latter) do not play a role. Following the gamma spectroscopy measurements (direct measurements and neutron activation analysis (sec. 7.3)) Monte-Carlo simulations were carried out to investigate the rate and energy spectrum of the singles events induced by the identified radioimpurities (sec. 7.4). The results finally provide direct input parameters for the determination of the accidental neutrino background in Double Chooz.

All the samples were investigated for their content of ^{238}U, ^{232}Th, and ^{40}K; in some cases like the shielding steel samples also ^{60}Co is of interest. In principle, also radioimpurities from the decay chain of ^{235}U can be looked for, however, the natural abundance of ^{235}U is only 0.73% [Fir96] making gamma emissions from this chain less important as they occur only rarely. In addition, the decay chain of ^{235}U does not contain prominent gamma emissions with energies above ~ 830 keV. These energies are too low to reach the Target region from outside parts of the detector.

The recorded gamma spectra of all samples showed no gamma lines beyond the decay chains of ^{238}U and ^{232}Th, respectively, or ^{40}K and ^{60}Co. This lead to good constraints[7] for the

[7] The exact limit depends on the sample mass and the energy of the gamma line in question. In general, the bigger the sample mass and the higher the gamma energy, i.e. the lower the continuous background, the better the limit on the activity per mass for the respective isotope in the investigated sample.

activities of all other radioisotopes of the order of 10^{-2} to 10^{-3} $\frac{\text{Bq}}{\text{kg}}$. The only exception were the welding electrodes which contained (9.26 ± 1.30) $\frac{\text{Bq}}{\text{kg}}$ ^{138}La, or, given as mass concentration, $(1.01 \pm 0.10) \cdot 10^{-5}$ $\frac{\text{g}}{\text{g}}$.

The maximally allowed mass concentrations for radioimpurities strongly depend on the position of the investigated detector part (the closer to the Target region, the higher the required radiopurity) and its mass (small detector parts can have a higher activity per mass without introducing too much background); no general upper limit can be given. The design goal for the Double Chooz far detector is no more than ~ 0.8 accidental antineutrino-like coincidences per day in the Target[8] [Ard06], which translates into a singles rate below ~ 20 Hz in the energy window for the positron-like event (0.7 MeV to 12.2 MeV, [Abe12a]).

Shielding Steel

The Double Chooz far detector is surrounded by a 15 cm thick steel shield (cf. ch. 5) with a total mass of ~ 290 t to prevent gamma rays from the surrounding rock material to enter the detector. Although this shielding is rather far away from the inner detector parts (Target and GammaCatcher), its content of radioactivity emitting high-energetic gammas (^{60}Co, ^{208}Tl, ^{214}Bi) needs to be under control, too, especially because of its huge mass.

Figure 7.8: *Three of the four investigated samples of the Double Chooz shielding steel.*

Four different steel samples have been investigated, fig. 7.8, which have been taken directly from the steel melt at the manufacturer. Their identification numbers are 86638-4, 86665-6, 933993, and 86638. The results of the gamma spectroscopy measurements are summarised in tab. 7.1, indicating that two of the samples (86638-4 and 86665-6) have a rather high content of radioisotopes, especially thorium, compared to the other samples and are rejected for this reason. The other two samples, however, show no measurable radioimpurities, i.e. their concentrations are well below the sensitivity of the germanium detector system. These steels are fine for Double Chooz; in the final setup, the steel 933993 with a total activity of less than 80 $\frac{\text{mBq}}{\text{kg}}$ is used.

InnerVeto Parts

The InnerVeto of the Double Chooz detectors is predominantly meant to identify cosmic muons with the highest efficiency possible. As most of the muon-induced events are rather high-energetic[9] they can be easily distinguished from radioactivity events, which range up to a few MeV only. The radiopurity requirements for the components of the InnerVeto are therefore less stringent than for the inner detector. However, high-energetic gamma quanta

[8] The accidental background induced by all detector parts but inner phototubes is required to be smaller than 1% of the signal rate [Ard06], i.e. $\lesssim 0.4\,\text{d}^{-1}$. This corresponds to a singles trigger rate in the Target of $\lesssim 10$ Hz. The contribution of the inner detector PMTs was expected to be of the same order of magnitude, leading to an aspired total accidental background rate of about $0.8\,\text{d}^{-1}$.

[9] A high-energetic muon is a minimal ionising particle and thus deposits about 2 MeV per cm track length in the liquid scintillator.

Results for the Steel Samples (90% C.L.)		
isotope	***86638-4***	***86665-6***
K-40	$<$ (0.412±0.038) Bq/kg $<$ (1.59±0.15)·10^{-9} g/g	$<$ (0.387±0.035) Bq/kg $<$ (1.49±0.14)·10^{-9} g/g
Th-232 chain	(0.068±0.028) Bq/kg (16.8±6.9)·10^{-9} g/g	(0.039±0.016) Bq/kg (9.64±4.05)·10^{-9} g/g
U-238 chain	$<$ (0.027±0.002) Bq/kg $<$ (2.17±0.13)·10^{-9} g/g	(0.060±0.010) Bq/kg (4.82±0.79)·10^{-9} g/g
Co-60	$<$ (9.48±0.56) mBq/kg $<$ (2.28±1.36)·10^{-19} g/g	(3.36±2.32) mBq/kg (8.08±5.59)·10^{-20} g/g
isotope	***933993***	***86638***
K-40	$<$ (76.6±7.4) mBq/kg $<$ (2.96±0.29)·10^{-10} g/g	$<$ (75.8±8.4) mBq/kg $<$ (2.93±0.32)·10^{-10} g/g
Th-232 chain	$<$ (0.935±0.065) mBq/kg $<$ (2.31±0.16)·10^{-10} g/g	$<$ (31.1±1.9) mBq/kg $<$ (7.68±0.47)·10^{-9} g/g
U-238 chain	$<$ (1.55±0.08) mBq/kg $<$ (1.25±0.06)·10^{-10} g/g	$<$ (59.4±3.0) mBq/kg $<$ (4.77±0.24)·10^{-9} g/g
Co-60	$<$ (0.76±0.05) mBq/kg $<$ (1.83±0.12)·10^{-20} g/g	$<$ (9.08±0.64) mBq/kg $<$ (2.18±0.15)·10^{-19} g/g

Table 7.1: *Results on the activities (given in Bq/kg as well as in g/g) of the four steel samples for the uranium and thorium decay chains, as well as for ^{40}K and ^{60}Co. Upper limits are quoted in black, activities above the detector's sensitivity threshold in red. The numbers given for the whole decay chains are the weighted averages of the activities of the single isotopes analysed. The two steel samples 86638-4 and 86665-6 are rejected mainly due to their contamination with thorium. The other two samples, on the other hand, show no measurable radioimpurities.*

originating from the veto region can also penetrate into the Target and increase the singles rate there. Besides this, a low activity in the InnerVeto also allows a low energy threshold, which increases the efficiency in detecting muon secondaries like fast neutrons from the surrounding rock, recoiling off in the veto scintillator.

Different material samples meant to be used in the InnerVeto are investigated here: stainless steel rails and bolts for mounting and holding the VM2000 reflecting foil at the inside of the InnerVeto (fig. 7.9), the welding electrodes for welding the InnerVeto and the Buffer tank (fig. 7.9), and some rubber material for sealing the tanks.

Figure 7.9: *Photograph of different material samples from the InnerVeto. From left to right: steel rails, steel bolts (both for holding the VM2000-foil), and the welding electrodes (including its blue plastic wrapping).*

The rubber sample contains $(8.1 \pm 4.2)\,\frac{\text{Bq}}{\text{kg}}$ ^{40}K, $(4.1 \pm 0.7)\,\frac{\text{Bq}}{\text{kg}}$ Th, and $(10.8 \pm 1.2)\,\frac{\text{Bq}}{\text{kg}}$ U. Hence, it is found to be very active, therefore, it is rejected to be used in Double Chooz. Both steel samples, the rails and the bolts, are found to be rather clean (total activity $\sim 1\,\frac{\text{Bq}}{\text{kg}}$ and $\sim 0.45\,\frac{\text{Bq}}{\text{kg}}$, respectively) and match the requirements of the InnerVeto perfectly. The welding electrode especially contains thorium[10] in a quite big concentration ($(6.2 \pm 1.0)\,\frac{\text{Bq}}{\text{kg}}$). However, the mass of the welding seams is so small in the final detector (compared to the mass of the tanks themselves) that the welding electrodes are used nevertheless. The results of the direct gamma spectroscopy measurements of these four samples are summarised in tab. 7.2.

The Double Chooz InnerVeto also contains 78 8" PMTs. In general, photomultipliers (especially their glass) are known to contain a large amount of radioactivity, particularly ^{40}K. To get an idea of their activity, and to localise possible hot spots in their structure, two parts of the PMTs, the glass and the dynode structure, were investigated separately using the Garching germanium detector setup. Both for the glass and the dynode structure the concentrations of the radioimpurities uranium, thorium, and ^{40}K are far above the sensitivity threshold of the germanium detector system, tab. 7.3. Summed activities of $5.7\,\frac{\text{Bq}}{\text{kg}}$ for the glass and $51.3\,\frac{\text{Bq}}{\text{kg}}$ for the dynodes were found. However, the total mass of all InnerVeto PMTs

[10]Thorium is often deliberately added to welding electrodes, as its α-activity ionises the air around the electrode, making the ignition of the welding arc much easier.

Results for the InnerVeto material samples I (90% C.L.)		
isotope	***steel rails***	***steel bolts***
K-40	$<$ (0.469±0.044) Bq/kg $<$ (1.82±0.17)·10^{-9} g/g	$<$ (15.9±1.46) mBq/kg $<$ (6.14±0.57)·10^{-11} g/g
Th-232 chain	(0.125±0.108) Bq/kg (3.09±2.66)·10^{-8} g/g	$<$ (5.24±0.73) mBq/kg $<$ (1.29±0.11)·10^{-9} g/g
U-238 chain	(0.743±0.171) Bq/kg (5.97±1.36)·10^{-8} g/g	(0.450±0.016) Bq/kg (3.34±1.25)·10^{-9} g/g
isotope	***welding electrode***	***rubber***
K-40	$<$ (4.81±0.44) Bq/kg $<$ (1.86±0.17)·10^{-8} g/g	(8.41±4.20) Bq/kg (3.24±1.62)·10^{-8} g/g
Th-232 chain	(6.21±1.03) Bq/kg (1.53±0.25)·10^{-6} g/g	(4.14±0.69) Bq/kg (1.02±0.16)·10^{-6} g/g
U-238 chain	(4.64±1.20) Bq/kg (3.44±0.89)·10^{-7} g/g	(10.84±1.21) Bq/kg (8.70±0.97)·10^{-7} g/g
Co-60	$<$ (0.281±0.016) Bq/kg $<$ (6.76±3.96)·10^{-18} g/g	-

Table 7.2: *Results on the activities (given in Bq/kg as well as in g/g) of the four different material samples of the InnerVeto for the uranium and thorium decay chain, as well as for ^{40}K and ^{60}Co. Upper limits are quoted in black, activities above the detector's sensitivity threshold in red. The numbers given for the whole decay chains are the weighted averages of the activities of the single isotopes analysed. The rubber material is not used in Double Chooz due to its high content of radioactivity; the other materials are installed although they show a non-vanishing content of radioimpurities. Especially the welding electrode is active, however, its mass in the final detector setup is so low that it can safely be used.*

in the final detector setup is small, and their spacing to the Target region is big, hence higher concentrations of radioimpurities are tolerable (see also sec. 7.4).

Besides this, samples of supplementary materials were screened. This includes a sample from the stainless steel intended to be used to manufacture holding structures within the PMTs, a sample from the polyurethane material used to seal the PMT cable feed-throughs, and the PMT cablings. The gamma spectroscopy results for these samples are summarised in tab. 7.4.

Both the PMT holders and the cables easily fulfill the requirements on radiopurity. In contrast, the polyurethane contains a rather large amount of radioactive isotopes, particularly $(19.4 \pm 3.1)\ \frac{\text{Bq}}{\text{kg}}$ of ^{40}K and $(5.8 \pm 0.4)\ \frac{\text{Bq}}{\text{kg}}$ of uranium. However, just as for the InnerVeto PMTs

RESULTS FOR THE INNERVETO MATERIAL SAMPLES II (90% C.L.)		
isotope	***PMT glass***	***PMT dynode structure***
K-40	(1.29±0.74) Bq/kg (4.98±2.85)·10^{-9} g/g	(45.66±7.64) Bq/kg (1.76±0.30)·10^{-7} g/g
Th-232 chain	(0.540±0.107) Bq/kg (1.33±0.26)·10^{-7} g/g	(0.679±0.138) Bq/kg (1.68±0.34)·10^{-7} g/g
U-238 chain	(3.86±0.37) Bq/kg (3.10±0.78)·10^{-7} g/g	(5.01±0.43) Bq/kg (3.72±0.35)·10^{-7} g/g

Table 7.3: *Results on the activities (given in Bq/kg as well as in g/g) of the InnerVeto PMT glass and PMT dynode structure for the uranium and thorium decay chain, as well as for ^{40}K. The numbers given for the whole decay chains are the weighted averages of the activities of the single isotopes analysed. Both the PMT glass and the dynodes are highly active. However, their mass is small enough and their position in the detector far away from the Target, hence, the radioactivity is still tolerable (see sec. 7.4).*

and the welding electrode, mass and spacing to the Target still allow to use this material, see sec. 7.4.

Finally, also a sample of the mixed InnerVeto liquid scintillator as used in the Double Chooz experiment (taken directly from the storage area) was screened. The requirement of Double Chooz on the radiopurity of this liquid, however, is about $10^{-10}\,\frac{g}{g}$ [Ard06] and thus below the reachable sensitivity of the detector system for the sample mass used (80 g). The gamma spectroscopy measurement was in that sense only performed to check for any bigger contaminations, which could potentially have happened during the processing of the liquid in the different systems at Chooz. However, as can be seen from tab. 7.5, this has not happened. On the contrary, no enhancement of the gamma activity above background was observed. The concentrations of all radioimpurities in the InnerVeto scintillator were below the detection threshold, i.e. the purity of the liquid was kept during processing, or, at least, the mass concentration of any impurities newly brought in is very low. Therefore, no further purification of this liquid, for example by filtering or distillation, was necessary.

Filling System

Besides the samples for the InnerVeto also materials to be used in the filling system were investigated. The two acrylic vessels for Target and GammaCatcher liquid do not withstand big pressure differences. Therefore, all volumes of the Double Chooz far detector had to be filled simultaneously, with level differences smaller than 30 mm [Pfa12]. In order to precisely monitor the liquid levels and to have the possibility to cross-check the obtained results different monitoring systems were installed in the detector: a laser distance measurement system, measuring the distance from the top lid of the detector to a floater in dedicated stainless steel tubes mounted to the walls of the InnerVeto tank, hydrostatic pressure sensors (type ATM/T from STS [STS12]) at the detector bottom, and for the Target an intelligent tank

Results for the InnerVeto material samples III (90% C.L.)		
isotope	***PMT holders***	***PU sample***
K-40	$< (33.6 \pm 3.1)$ mBq/kg $< (1.30 \pm 0.12) \cdot 10^{-10}$ g/g	(19.36 ± 3.10) Bq/kg $(7.49 \pm 1.20) \cdot 10^{-8}$ g/g
Th-232 chain	$< (12.3 \pm 0.8)$ mBq/kg $< (3.03 \pm 0.20) \cdot 10^{-9}$ g/g	(1.91 ± 0.18) Bq/kg $(4.71 \pm 0.44) \cdot 10^{-7}$ g/g
U-238 chain	$< (27.6 \pm 1.2)$ mBq/kg $< (2.05 \pm 0.09) \cdot 10^{-9}$ g/g	(5.79 ± 0.38) Bq/kg $(4.30 \pm 0.28) \cdot 10^{-7}$ g/g
Co-60	$< (6.32 \pm 0.36)$ mBq/kg $< (15.16 \pm 0.88) \cdot 10^{-20}$ g/g	-
isotope	***PMT cables***	
K-40	$< (0.345 \pm 0.032)$ Bq/kg $< (1.34 \pm 0.12) \cdot 10^{-9}$ g/g	
Th-232 chain	$< (12.5 \pm 1.0)$ mBq/kg $< (3.08 \pm 0.25) \cdot 10^{-9}$ g/g	
U-238 chain	$< (46.9 \pm 2.1)$ mBq/kg $< (3.48 \pm 0.16) \cdot 10^{-9}$ g/g	

Table 7.4: *Results on the activities (given in Bq/kg as well as in g/g) of the InnerVeto PMT holders, the polyurethane sample and the PMT cables for the uranium and thorium decay chain, as well as for ^{40}K and ^{60}Co. Upper limits are quoted in black, activities above the detector's sensitivity threshold in red. The numbers given for the whole decay chains are the weighted averages of the activities of the single isotopes analysed. Both the holders and the cables are rather clean; the polyurethane material is highly active. But again, its mass in the final configuration and its position in the detector allow a higher content of radioimpurities.*

gauge ("Tamago"; Proservo NMS from Endress+Hauser [Tam12]). Within the present thesis, samples of the steel tubes (fig. 7.10(a)), the pressure sensors (fig. 7.10(b)), and some glass floaters were measured. The former two were finally installed in the Double Chooz far detector, while the glass floaters were not used, but floaters made of teflon instead. The results of the measurements are given in table 7.6.

The level measurement tube only contains a little amount of uranium, (18.5 ± 3.1) ppb, while the pressure sensor is much more active. As one of these sensors is placed in the middle of the GammaCatcher bottom lid it creates a hot spot there (sec. 7.4). However, other constraints of the filling and detector monitoring system make the use of this sensor necessary [Pfa12]. Two additional pressure sensors (for the Buffer and the InnerVeto liquid) are placed within the level measurement tubes which are mounted to the InnerVeto vessel

RESULTS FOR THE INNERVETO LIQUID (90% C.L.)	
isotope	***InnerVeto liquid***
K-40	$< (0.192 \pm 0.01)$ Bq/kg $< (6.42 \pm 0.34) \cdot 10^{-10}$ g/g
Th-232 chain	$< (30.1 \pm 15.9)$ mBq/kg $< (7.42 \pm 3.92) \cdot 10^{-9}$ g/g
U-238 chain	$< (0.567 \pm 0.332)$ Bq/kg $< (4.57 \pm 2.68) \cdot 10^{-8}$ g/g

Table 7.5: *Limits on the activities (given in Bq/kg as well as in g/g) of the InnerVeto liquid for the uranium and thorium decay chain, as well as for ^{40}K. The limits given for the whole decay chains are the weighted averages of the activities of the single isotopes analysed. As expected, no concentrations of radioisotopes above the germanium detector's sensitivity threshold could be seen, i.e. the liquid was not severely contaminated during processing.*

(a) Level measurement tube (b) Pressure sensor

Figure 7.10: *Samples of the filling system investigated in the gamma spectroscopy measurements: a) the level measurement tubes which guide the floaters for the laser distance measurement system; b) the hydrostatic pressure sensors which measure the pressure directly at the bottom of the detector.*

walls, and thus have a greater spacing to the Target.

For most of the investigated samples only upper limits on their content of radioimpurities can be given, i.e. the true mass concentration of the respective isotopes is below the detector's sensitivity threshold. To improve the results bigger sample masses or longer measuring times are needed. However, as both are limited the only possibility to raise the sensitivity of the detector system for direct gamma spectroscopy would be to lower the background. Especially at higher energies (above ~ 1 MeV) the remaining continuous background is induced by cosmic muons and their secondary particles, therefore, the method of choice would be to go deeper underground to have a better shielding against cosmic radiation. For comparison: the GeMPI-detector [Heu06] operated at the Gran-Sasso laboratory with an overburden of 3800 m.w.e.

Results for the Samples of the Filling System (90% C.L.)		
isotope	***glass floaters***	***pressure sensor***
K-40	(79.5±15.7) Bq/kg (3.07±0.61)·10^{-7} g/g	(2.64±1.71) Bq/kg (1.02±0.66)·10^{-8} g/g
Th-232 chain	(3.49±0.57) Bq/kg (8.61±1.41)·10^{-7} g/g	(2.44±0.64) Bq/kg (6.01±1.57)·10^{-7} g/g
U-238 chain	(5.10±0.67) Bq/kg (3.78±0.49)·10^{-7} g/g	(8.08±6.72) Bq/kg (6.49±5.40)·10^{-7} g/g
isotope	***level measurement tubes***	
K-40	< (48.4±4.5) mBq/kg < (1.87±0.17)·10^{-10} g/g	
Th-232 chain	< (22.5±1.8) mBq/kg < (5.54±0.44)·10^{-9} g/g	
U-238 chain	(0.230±0.039) Bq/kg (1.85±0.31)·10^{-8} g/g	

Table 7.6: *Results on the activities (given in Bq/kg as well as in g/g) of the glass floaters, the pressure sensor, and the level measurement tubes for the uranium and thorium decay chain, as well as for ^{40}K and ^{60}Co. Upper limits are quoted in black, activities above the detector's sensitivity threshold in red. The numbers given for the whole decay chains are the weighted averages of the activities of the single isotopes analysed. The glass floaters are not used in the final detector setup. While the steel tubes contain only little uranium, the pressure sensor creates a hot spot in the GammaCatcher volume. However, to fulfill other constraints of the filling system the utilisation of this sensor is necessary [Pfa12].*

reaches a sensitivity of $\lesssim 10\,\frac{\mu Bq}{kg}$ in ^{238}U and ^{232}Th, while for the detector system presented in sec. 7.1.1 the continuous background is still ~ 8 counts per keV and day, limiting the sensitivity to $\sim 1\,\frac{mBq}{kg}$. However, the sensitivities reached with the current setup are by far sufficient for most purposes. For the case of outer detector parts of Double Chooz the sensitivity is high enough to either have detector components rejected which are found to contain a too high amount of radioactivity, or to have them installed in the far detector with the certainty that they match with the concept of a high-purity detector.

7.3 Neutron Activation Analysis

In the preceding section the results for the concentrations of radioimpurities in the investigated samples obtained by direct gamma spectroscopy were presented. However, the sensitivity of

these direct measurements is limited, mainly because of the omnipresent ambient radioactivity and the geometrical limitations for the sample mass. Especially for the components of the inner detector of Double Chooz the required radiopurity is very much higher than the limits which could be reached by the measurements with the germanium detector, therefore, an improvement of the sensitivity is needed. For some isotopes, and for dedicated samples, this improvement can be achieved by neutron activation analysis. The basic idea hereby is to greatly enhance the activity of the impurities in the sample by irradiating it with thermal neutrons and to perform a gamma spectroscopy measurement afterwards.

The inner detector of Double Chooz (Target and GammaCatcher; ch. 5) consists of two liquid scintillator filled acrylic vessels. Besides the liquid components, these scintillators also contain PPO and bisMSB as wavelength-shifting materials, which are purchased as powders, as well as - in the case of the Target - gadolinium. All of these materials had to be investigated for their radiopurity prior to their utilisation in the final detector. Within the scope of the present thesis neutron activation analyses for different samples of PPO and the acrylic have therefore been performed. The secondary fluor bisMSB is added in only so small concentrations to the scintillators ($20\,\frac{\mathrm{mg}}{\mathrm{l}}$) that the limits obtained in direct gamma spectroscopy already fulfill the requirements. The liquids themselves, however, cannot be activated with the method described in the following, as the pneumatic delivery system of the irradiation facility (see below) can only carry solid samples, but no liquids. Hence, no neutron activation analysis could be performed in that particular case.

The investigated samples were irradiated at the Forschungs-Neutronenquelle Heinz Maier-Leibnitz (FRM2) in Garching in the pneumatic delivery system, which brings the samples (contained in a special encapsulation) very close to the reactor core. There, the thermal neutron flux of $(1.63 \pm 0.05)\cdot 10^{13}\,\mathrm{cm}^{-2}\mathrm{s}^{-1}$ [Li08] activates the sample for a certain irradiation time. After being retrieved from the delivery system the activated sample was screened with the detector system described in sec. 7.1.1.

For Double Chooz mainly the concentrations of uranium and thorium, and long-lived radioisotopes like ^{40}K are of interest. The decay chains of thorium and uranium, however, do not contain an isotope with a rather large cross-section for thermal neutron capture and a viable gamma-emitting decay afterwards [Fir96]. Therefore, with the short irradiation times used here (typically 10 min) no major improvement for the sensitivity in the determination of the concentrations of these isotopes is achieved compared to direct low-background gamma spectroscopy. Much longer irradiation times are impossible for radiation security issues. However, the sensitivity for measuring ^{40}K is greatly enhanced; the results of these studies will be presented in the following.

The investigated samples contain natural potassium, consisting to 6.73% of the stable isotope ^{41}K [Fir96]. This isotope has a cross-section for thermal neutron capture of 1.46 barn [Fir96]. By neutron activation unstable ^{42}K is produced, which decays into stable ^{42}Ca with a half-life of 12.36 h and under emission of gamma quanta with an energy of 1525 keV [Fir96] (fig. 7.11).

From the results of the gamma spectroscopy of this decay line the concentration of ^{41}K in the sample can be calculated. Under the assumption that the natural abundances of the different potassium isotopes are not broken for the investigated sample, the concentration c(^{40}K) of radioactive ^{40}K can be calculated, too:

$$c(^{40}K) = \frac{40\,\frac{g}{mol}}{N_A \cdot m} \cdot \frac{N_{peak}}{\varepsilon \cdot P} \cdot \frac{exp(\frac{t_1}{\tau})}{1 - exp(-\frac{t}{\tau})} \cdot \frac{1}{\Phi_n \cdot \sigma_{th} \cdot t_{irr}} \cdot \frac{R(40)}{R(41)} \quad . \tag{7.9}$$

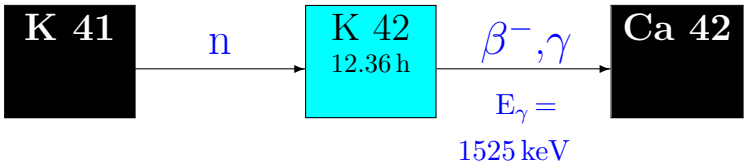

Figure 7.11: *Neutron activation and decay scheme of ^{41}K. Stable ^{41}K is activated by thermal neutron capture. The subsequent β^--decay of ^{42}K with a half-life of 12.36 h into stable ^{42}Ca also releases (with an emission probability of 18.1%) 1525 keV-gamma quanta, which are measurable with the germanium detector. Data taken from [Fir96].*

N_A denotes Avogadro's constant, m the mass of the sample, N_{peak} the number of counts in the photopeak of the 1525 keV-gamma line, ε the detector efficiency of the germanium detector (determined by the Monte-Carlo simulation; sec. 7.1.2), P the emission probability of the 1525 keV-gamma line (18.1% [Fir96]), t_1 the time span between end of the irradiation and the start of the gamma spectroscopy measurement, t the measuring time, τ the half-life of ^{42}K, Φ_n the thermal neutron flux, σ_{th} the thermal neutron capture cross-section of ^{41}K, t_{irr} the irradiation time (typically 10 min), and R(X) the natural abundance of the respective potassium isotopes ^{40}K and ^{41}K (0.0117% and 6.73% [Fir96]). Unlike the analysis of the gamma spectroscopy measurements presented in secs. 7.1.2 and 7.1.3, ^{42}K is neither in radioactive equilibrium nor has a half-life much longer than the measuring time. Therefore, its activity has to be calculated by integration over the measuring time, and effects like the loss of nuclei by decay in the time between end of the irradiation and start of the measurement have to be taken into account, too. Although the thermal neutron flux is rather high the probability for neutron capture on an already produced ^{42}K-nucleus is negligibly small[11]. Hence, in the following it is always assumed to have maximal one neutron capture per target nucleus.

PPO

The neutron activation analyses of PPO were divided into two separate measuring campaigns. In the first campaign four different samples of the manufacturers Sigma-Aldrich[12] and PerkinElmer[13] were investigated to pre-select a viable candidate, and the final measuring procedure to be applied in the second campaign was developed. In the second campaign, finally, three different samples of the PPO "Neutrino Grade" from PerkinElmer were investigated in more detail, as these turned out to be best-fitting for Double Chooz. Table 7.7 again summarises all measurements performed for PPO.

During the irradiation the powdery PPO samples, each about 0.25 g to 0.6 g in weight, were enclosed in a small plastic bag made of polyethylene (PE). For the first measuring campaign this bag was not removed during the gamma spectroscopy not to spill any neutron-activated powder in the germanium detector setup. However, in a blank run with the PE bag only it has been found out that the plastics contains trace elements (mainly halogenides, but also potassium), which become activated, too (tab. 7.8).

[11] The probability for a neutron capture on an already activated nucleus is calculated to be less than $2 \cdot 10^{-6}$%.
[12] Sigma-Aldrich Chemie GmbH, Riedstrasse 2, 89555 Steinheim, Germany
[13] PerkinElmer, Rigaweg 22, Groningen, 9723 TH, Netherlands

First Campaign	
PPO	Sigma-Aldrich
PPO (Standard)	PerkinElmer
PPO (Neutrino Grade)	PerkinElmer
PPO (Neutrino Grade 2)	PerkinElmer
Second Campaign	
PPO LOT 26-1003	PerkinElmer
PPO LOT 26-1005	PerkinElmer
PPO LOT 26-1007	PerkinElmer

Table 7.7: *Overview of the PPO samples investigated in the neutron activation analysis including the manufacturer. The three samples for the second measuring campaign are all "Neutrino Grade" from PerkinElmer, as this turned out to be most suitable for Double Chooz in the first campaign.*

ACTIVITIES IN THE BLANK MEASUREMENTS		
Isotope	***blank 1***	***blank 2***
^{82}Br	12.2±0.8 $\frac{\text{kBq}}{\text{kg}}$	14.0±0.8 $\frac{\text{kBq}}{\text{kg}}$
^{56}Mn	9.58±0.53 $\frac{\text{MBq}}{\text{kg}}$	1.07±0.08 $\frac{\text{MBq}}{\text{kg}}$
^{41}Ar	140.5±16.6 $\frac{\text{kBq}}{\text{kg}}$	189.5±19.6 $\frac{\text{MBq}}{\text{kg}}$
^{24}Na	421.3±32.0 $\frac{\text{kBq}}{\text{kg}}$	722.5±58.5 $\frac{\text{kBq}}{\text{kg}}$
^{38}Cl	10.5±1.7 $\frac{\text{MBq}}{\text{kg}}$	-
^{42}K	230.6±32.4 $\frac{\text{kBq}}{\text{kg}}$	93.2±15.7 $\frac{\text{kBq}}{\text{kg}}$

Table 7.8: *Activities of two different plastic bags directly after the neutron irradiation. The bags contain some traces of halogenides as well as potassium. ^{41}Ar is produced from ^{40}Ar in the air and adsorbed at the sample's surface. This explains the huge deviation between the two blank measurements. ^{38}Cl, however, has a very short half-life of 37.18 min [Fir96] only, and was therefore not detectable any more in the second sample because of a bigger time delay between irradiation and measurement. In case one isotope emits more than one gamma line, the quoted activity is the weighted average of the single activities obtained from the respective gamma emissions; cf. appendix E.*

The potassium contained within the plastic bags severely interferes with the potassium measurement of the PPO sample. Therefore, the measuring procedure was changed for the second campaign; the irradiated samples were re-filled into another plastic container after activation (fig. 7.12). Open radioactivity was hereby avoided by sealing the containers before the gamma measurement. In addition, a smear test of the container's outside was performed.

Figure 7.12: *Samples of PPO (left, refilled) and acrylic (right) for the NAA.*

The four PPO samples investigated in the first measuring campaign all showed a positive signal for potassium, tab. 7.9. The number of counts in the 1525 keV-gamma peak stemming from the plastic bag as expected from the blank run (blank run N°1) was hereby subtracted from the total ^{42}K-peak in the spectrum; the remaining number of counts was allocated to the PPO.

In this pre-selection stage, the second PPO "Neutrino Grade" from PerkinElmer showed the smallest concentration of potassium (and also other trace elements; see tab. E.1 in appendix E) and is therefore used in Double Chooz.

PPO Sample	***c(^{40}K)***
Sigma-Aldrich	$(2.52 \pm 1.87)\cdot 10^{-11}\ \frac{g}{g}$
PerkinElmer Standard	$(1.54 \pm 0.49)\cdot 10^{-10}\ \frac{g}{g}$
PerkinElmer Neutrino Grade	$(2.58 \pm 1.38)\cdot 10^{-11}\ \frac{g}{g}$
PerkinElmer Neutrino Grade (2)	$(1.36 \pm 1.32)\cdot 10^{-11}\ \frac{g}{g}$

Table 7.9: *Mass concentration of ^{40}K in the PPO samples investigated in the first measuring campaign (pre-selection stage). The effect of the plastic bags is subtracted statistically (see text), however, this subtraction introduces huge errors to the calculation. In total, the second PPO sample "Neutrino Grade" from PerkinElmer turned out to be best-fitting for Double Chooz, as it has the lowest content of ^{40}K.*

For the final analysis three different samples of this PPO type, PPO LOT 26-1003, PPO LOT 26-1005, and PPO LOT 26-1007, were irradiated for 10 min each, re-filled into sealed plastic containers directly after the irradiation and finally screened in the germanium detector. The gamma measurement was hereby divided into several distinct time segments[14], the concentration of ^{40}K was calculated for each time segment separately using eq. (7.9). At the last time bins, when most of the total activity of the sample had already decayed[15], the

[14] A detailed time line of the measurements can be found in appendix E.

[15] Nearly all of the radioisotopes produced by thermal neutron activation have only short half-lives of the order of minutes to hours. Switching on the anti-Compton veto system already at the beginning of the measurements would create a too big dead-time due to the very high activity of the sample.

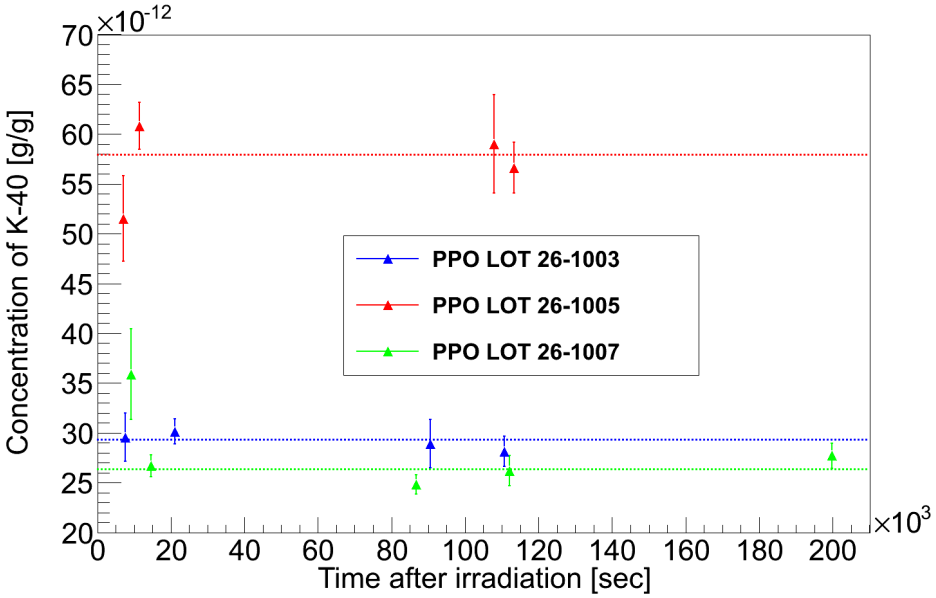

Figure 7.13: *Mass concentration of ^{40}K in the three different samples of PPO "Neutrino Grade", as calculated for different time segments and corrected for dead-time effects. The weighted average values over all time bins are depicted, too, by the dashed lines. Mass concentrations of $(2.93 \pm 0.09) \cdot 10^{-11} \frac{g}{g}$ (PPO LOT 26-1003), $(5.79 \pm 0.15) \cdot 10^{-11} \frac{g}{g}$ (PPO LOT 26-1005), and $(2.63 \pm 0.06) \cdot 10^{-11} \frac{g}{g}$ (PPO LOT 26-1007) are obtained. The data points are plotted at the time of the start of the respective time segment.*

anti-Compton veto was switched on. By this, the continuous background was greatly reduced for the last measurement of the ^{42}K gamma emission, increasing the sensitivity. With this method all data points can be cross-checked with the other ones, and the calculation of the concentration of ^{40}K as the weighted average of all single data points diminishes possible errors. Fig. 7.13 depicts the results of these calculations, corrected for dead-time effects. The single values obtained for the different time segments are in rather good agreement for one sample, proving the reliability of the method. The final results for the mass concentration of ^{40}K in the three different samples are calculated as weighted averages of the single data points. These averages are depicted in fig. 7.13 by the dashed lines.

The final values for the mass concentration of ^{40}K in the PPO samples LOT 26-1003, $(2.93 \pm 0.09) \cdot 10^{-11} \frac{g}{g}$, and LOT 26-1007, $(2.63 \pm 0.06) \cdot 10^{-11} \frac{g}{g}$, are in good agreement, however, the value obtained for PPO LOT 26-1007, $(5.79 \pm 0.15) \cdot 10^{-11} \frac{g}{g}$, is about a factor of two higher. This might hint to a systematic error in the measurement (for example an erroneous irradiation time[16] of 20 min instead of the desired 10 min). However, the resulting mass concentrations for other trace elements identified in the sample[17] do not show a significant

[16]The neutron irradiation was carried out by the technical staff of the FRM II and can therefore not be checked any more.

[17]The results on all other elements in the PPO samples which also get activated by thermal neutrons can be found in appendix E. These elements, however, are not of any particular interest in Double Chooz, as they do not have long-lived radioactive isotopes which could contribute to the background for the neutrino measurement.

enhancement for the sample LOT 26-1005. In particular, the mass concentration of ^{23}Na, which is an alkali metal like potassium and therefore a good indicator for the concentration of the latter as it has similar chemical properties, is found to be $(7.87 \pm 0.40) \cdot 10^{-7} \frac{\mathrm{g}}{\mathrm{g}}$ for PPO LOT 26-1005, while it has similar values of $(8.53 \pm 0.38) \cdot 10^{-7} \frac{\mathrm{g}}{\mathrm{g}}$ for PPO LOT 26-1003 and $(9.87 \pm 0.41) \cdot 10^{-7} \frac{\mathrm{g}}{\mathrm{g}}$ for PPO LOT 26-1007, respectively. This disfavours systematic errors in the measurement, but makes deviations in the concentration of ^{40}K in the different samples likely. Such variations in the mass concentrations of trace elements can also be found for other isotopes; see appendix E.

Table 7.10 lists the final mass concentration of ^{40}K in the three different PPO samples, calculated as weighted average of the single data points. In addition, the results of an atomic absorption spectroscopy measurement (AAS) performed at MPIK Heidelberg [Buc09, Abe12b] are quoted, showing the good agreement between the two measuring methods for the samples LOT 26-1003 and LOT 26-1007. For PPO LOT 26-1005, however, no enhancement in the mass concentration of ^{40}K is found in the AAS.

Final results on the concentration of ^{40}K		
	NAA	***AAS***
PPO LOT 26-1003	2.93 ± 0.09	2.7
PPO LOT 26-1005	5.79 ± 0.15	2.3
PPO LOT 26-1007	2.63 ± 0.06	2.3
Weighted Average	3.03 ± 0.05	2.5 ± 0.4

Table 7.10: *Mass concentration of ^{40}K in the three investigated final PPO samples in units of $10^{-11} \frac{g}{g}$. The values quoted for the NAA are the weighted averages from the single values obtained for the different time segments; the values quoted for the AAS are taken from [Abe12b, Buc09].*

Acrylic

The neutron activation analysis of the acrylic GS0Z18 for Target and GammaCatcher vessel (fig. 7.12) was again carried out in two separate steps. At first, a 1 g test sample of the material was irradiated for 10 min to get an impression on its concentration of ^{40}K and the total count rate induced by all activated isotopes in the germanium detector. The latter turned out to be well manageable, i.e. the dead time of the detector system was below 10% directly at the start of the measurement; the content of ^{40}K was found to be $7.8 \cdot 10^{-11} \frac{\mathrm{g}}{\mathrm{g}}$, and thus clearly above the detector's sensitivity threshold. As acrylic is a solid material no plastic bag is needed to hold the sample during irradiation. Hence, big changes in the irradiation

procedure were unnecessary here, only sample mass and irradiation time were doubled for the second measurement to lessen the errors by increasing the count rate in the 1525 keV-gamma peak. Thoroughly wiping the acrylic sample after the neutron activation furthermore removed most of the radioactive ^{41}Ar deposited on its surface, greatly decreasing the total activity, and with it the measurement dead-time of the sample.

For the second measurement consequently 2 g of the final material were irradiated for 20 min; the analysis performed is the same as for the final PPO samples (see above; measurement timeline and results for the other trace elements can be found again in appendix E). Figure 7.14 depicts the mass concentration of ^{40}K, again calculated independently for several time segments and corrected for dead-time effects.

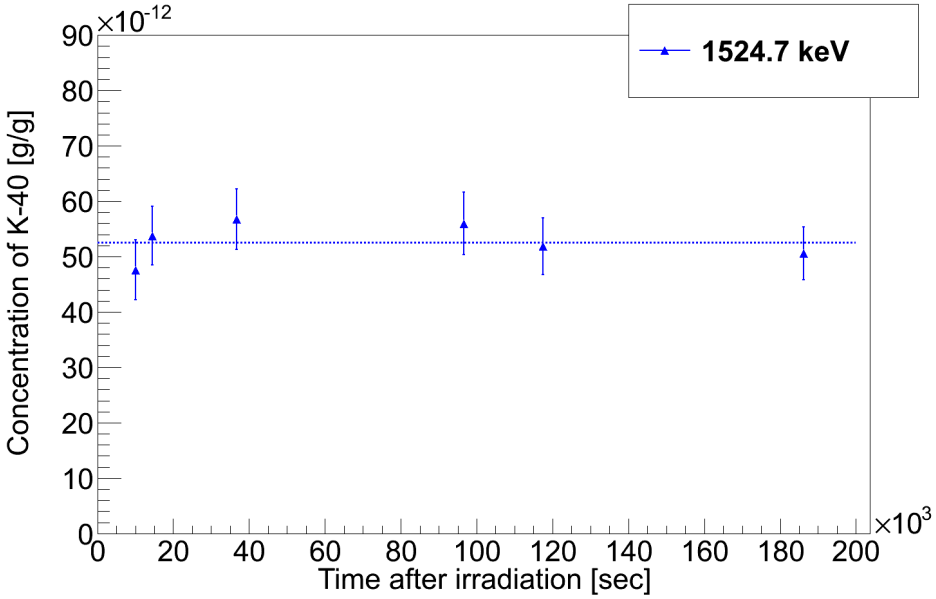

Figure 7.14: *Mass concentration of ^{40}K in the investigated acrylic sample, as calculated for different time segments and corrected for dead-time effects. The blue dashed line depicts the weighted average value of $(5.26 \pm 0.21) \cdot 10^{-11} \frac{g}{g}$. The data points are plotted at the time of the start of the respective time segment.*

As for the PPO the single mass concentrations match each other very well, indicating the absence of big systematic errors. The resulting final mass concentration of ^{40}K in the acrylic is $(5.26 \pm 0.21) \cdot 10^{-11} \frac{g}{g}$, calculated as weighted average of the single results.

7.4 Monte-Carlo Simulation of Radioactivity in Double Chooz

The results for the radiopurity measurements presented in secs. 7.2 and 7.3 were used as input parameters for the simulation of the resulting trigger rates in the Target region of the Double Chooz far detector. The determination of these trigger rates prior to the installation of the respective detector part was crucial, as they contribute to the rate of single physical events in the detector and thus to the accidental background for the antineutrino measurement. The design goal of Double Chooz is no more than ~ 0.8 accidental antineutrino-like events in the Target per day [Ard06] (see above), which translates into a maximum singles trigger rate of

$\sim 20\,\mathrm{Hz}$ in the energy window for the positron search (0.7 MeV to 12.2 MeV [Abe12a]), given a singles rate in the energy window of the delayed event of about $18\,\mathrm{h}^{-1}$ [Abe12a]. Therefore, for each of the investigated detector parts a GEANT4-based Monte-Carlo simulation[18] [Ter11] was used to determine the respective trigger rate.

This simulation includes all relevant components of the Double Chooz far detector, and is able to fully take into account effects like quenching, propagation of optical photons in the detector liquids and acrylic, and behaviour of the read-out electronics. For the simulation of ^{40}K in the inner parts of the detector (Target and GammaCatcher liquid, as well as acrylic) the full spectrum of decay particles was considered, including the branching ratios of β^-- and EC-decay; for the simulation of the effect of radioimpurities in the outer parts of the detector (like the shielding steel or components of the InnerVeto) on the Target only high-energetic gamma quanta were simulated, as neither α- and β-particles nor low-energetic radiation are able to reach the Target and induce events there. The rates obtained for the decay chains of uranium and thorium are consequently dominated by the high-energetic gamma lines of ^{214}Bi (1120.3 keV and 1764.5 keV) and ^{208}Tl (2614.5 keV), respectively. All other gamma emissions play a subdominant role, as either their energy or their branching ratio is too low; see also appendix A. The decays of ^{40}K and ^{60}Co release only one and two gamma quanta, respectively, anyway.

The quoted trigger rates are calculated for a trigger threshold of 700 keV [Abe12a]. In case the gamma spectroscopy measurements yield only an upper limit for the concentration of a certain radioisotope in some detector part also upper limits for the trigger rate are given. Typically, for each gamma energy and for each detector part to be investigated 10,000,000 gamma quanta were simulated; in case the resulting rate in the Target was still too low to allow definite conclusions, statistics were notably increased by simulating another 30,000,000 quanta. For the InnerVeto PMTs (including glass, dynode structure, steel holders, PU sealing of the cable feed-throughs, as well as the cables themselves) not each part was simulated separately but instead an "effective" PMT was investigated, i.e. a PMT with a total activity which is calculated from the single activities of its components weighted with the mass of the respective component. Hence, only results for the full PMTs are quoted below, not for the single components. The same procedure is applied to the steel rails and bolts which are used in the Double Chooz far detector to hold the reflecting VM2000 foil at the outside walls of the Buffer vessel in the InnerVeto.

In addition, the trigger rates quoted for the InnerVeto PMTs are weighted sums calculated from the trigger rates induced by the different positions of the PMTs within the InnerVeto. The 78 PMTs are arranged in five different positions: an inner and and outer ring in the top part of the InnerVeto (12 PMTs each), at the sidewalls of the InnerVeto (12 PMTs), and again an inner and an outer ring in the bottom part of the InnerVeto (18 PMTs and 24 PMTs). For each of these five positions the singles trigger rate induced in the Target by one PMT was simulated (which is enough due to the rotational symmetry of the detector); the total trigger rate of the InnerVeto PMTs is calculated as a sum of these rates, each multiplied with the number of PMTs at the respective position.

All other samples investigated in direct gamma spectroscopy or neutron activation analysis, respectively, were simulated and analysed separately including the full geometry, except for samples which were excluded during the screening phase, like the rubber material or the glass floaters. These were not simulated here. In addition, the total mass of the welding elec-

[18] DOGS version PROD-07-03 was used.

trode material in the final detector setup is so low[19] compared to other detector parts that its contribution to the total radioactivity is small, although its activity per mass is rather high. Therefore, no explicit simulations taking into account the very complex geometrical distribution of the welding seams in the Double Chooz far detector were carried out, but only a simplified one[20]. For all simulations a homogeneous distribution of the radioactivity all over the respective detector part was assumed.

Tables 7.11 and 7.12 summarise the singles trigger rates induced in the Target of the Double Chooz far detector as obtained from the simulation of the radioactivity of the detector parts investigated in secs. 7.2 and 7.3. In addition, sums of the trigger rates from all parts related to the filling system, parts of the InnerVeto, and activity of ^{40}K in the inner detector (PPO and acrylic) are quoted.

The by far dominant contribution to the singles trigger rate in the Target region of all samples investigated here comes from the ^{40}K-activity of the PPO in the inner detector liquids, especially in the Target liquid itself, and the acrylic. In total, this activity induces a trigger rate of (295 ± 7) mHz above the 0.7 MeV-threshold. However, this rate is still small compared to the allowed singles rate of ~ 20 Hz. This is mainly due to the high purity of the used materials, see sec. 7.3, and additionally the small concentration of PPO in the final liquid ($7\,\frac{\mathrm{g}}{\mathrm{l}}$ for the Target and $2\,\frac{\mathrm{g}}{\mathrm{l}}$ for the GammaCatcher).

All other detector parts, the parts of the filling system and the InnerVeto as well as the shielding steel and the welding seams, have a big distance to the Target and, therefore, the induced rates are extremely small. The total trigger rate induced by the parts of the filling system (a pressure sensor each for the GammaCatcher, the Buffer, and the InnerVeto, as well as five level measurement tubes) summed over all isotopes is $(1.45 \pm 0.83) \cdot 10^{-2}$ Hz. It is dominated by the contribution from the pressure sensor in the GammaCatcher vessel, just because of its smallest distance to the Target.

The InnerVeto parts, holders for the reflecting VM2000-foil mounted to the outside of the Buffer tank and the PMTs, contribute only $(1.77 \pm 0.48) \cdot 10^{-3}$ Hz to the trigger rate in the Target (sum over the two decay chains and ^{40}K). The contribution from the PMTs is hereby about twice as high as the rate induced by the holders. The total trigger rate (again summing over the two decay chains and the contribution from ^{40}K) stemming from the welding seams is somewhat higher, $(2.7 \pm 0.5) \cdot 10^{-2}$ Hz, and comes mainly from the thorium content of the welding electrodes. The decays of thorium give rise to the highly penetrating 2614.5 keV-gamma line of ^{208}Tl, which causes the thorium-induced rate to be one order of magnitude higher than the uranium-induced rate, although the mass concentrations of Th and U are nearly equal in the electrodes, see tab. 7.2. However, due to the simplified simulation (see above) this rate should be considered as an upper limit only.

For the steel shield only upper limits for the trigger rates above 700 keV in the Target can

[19] Both the Buffer and the InnerVeto tank are assembled from big bent steel plates and welded with only few seams. Per metre of such a seam typically about 12 electrodes of the type used (2.4 mm diameter, 150 mm length) are consumed [Iso12]; thereof $\sim$55-60% of the welding electrode material are deposited in the seam [Boe12], the rest is lost in welding cinder, sparks, and the electrode stub. The total length of all welding seams in the Double Chooz far detector is estimated to be 200 m, which leads to a total mass of the deposited electrode material in the final detector of about 17 kg.

[20] A point-like source of radioactivity at the sidewalls of the Buffer tank at height of the Target's centre was investigated. The activity of this source was set to the activity per mass of the welding electrode times the estimated mass of all welding seams together. As all other parts of the Buffer tank, and the whole InnerVeto vessel, have a bigger spacing to the Target region than this point-source this simplified simulation delivers an upper limit for the contribution of the welding electrode to the total trigger rate in the Target.

Sample	***U-chain*** $[Hz]$	***Th-chain*** $[Hz]$	^{40}K $[Hz]$
PPO Target Liquid			0.181 ± 0.003
PPO GC Liquid			$(2.64 \pm 0.04) \cdot 10^{-3}$
Acrylic			0.111 ± 0.004
Σ Inner Detector			$\mathbf{0.295 \pm 0.007}$
Pressure Sensor GC	$(7.1 \pm 6.0) \cdot 10^{-3}$	$(6.6 \pm 1.8) \cdot 10^{-3}$	$(8.3 \pm 5.4) \cdot 10^{-4}$
Pressure Sensor BF/IV	$(3.1 \pm 0.3) \cdot 10^{-8}$	$(2.8 \pm 0.8) \cdot 10^{-7}$	$< 2.3 \cdot 10^{-9}$
Level Measurement Tube	$(6.6 \pm 1.1) \cdot 10^{-6}$	$< 8.1 \cdot 10^{-6}$	$< 3.1 \cdot 10^{-7}$
Σ Filling System	$\mathbf{(7.1 \pm 6.0) \cdot 10^{-3}}$	$\mathbf{(6.6 \pm 1.8) \cdot 10^{-3}}$	$\mathbf{(8.3 \pm 5.4) \cdot 10^{-4}}$

Table 7.11: *Radioactivity-induced singles trigger rates (at 90% C.L.) in the Target for detector parts measured in the present thesis: PPO in the Target and GammaCatcher liquid, acrylic, and the parts of the filling system. For each investigated sample the rate is quoted separately for events from the U- and the Th-chain, as well as ^{40}K. In addition, the summed rates for the parts of the inner detector and the filling system are given. Note that the values quoted for pressure sensor in the Buffer / InnerVeto and the level measurement tube denote the trigger rate induced by one sensor or tube.*

be quoted, because the gamma spectroscopy measurements yield only upper limits, too, see tab. 7.1. These limits, however, already indicate that the radioactivity of the shielding steel is no problem at all for the antineutrino measurement in Double Chooz.

Summing up, the trigger rates in the Target region induced by all samples investigated in the course of the present thesis are very small compared to the allowed rate of $\sim 20\,\mathrm{Hz}$ (design goal). The main sources of gamma ray induced background in the Double Chooz far detector are the inner detector PMTs, in particular their glass, and radioactivity from the surrounding rock [Abe12a]. However, the design goal of Double Chooz is no more than ~ 0.8 accidental antineutrino-like coincidences per day [Ard06]. Due to the high purity reached in the detector, which is also an achievement of the thorough material screening in advance to

Sample	***U-chain*** $[Hz]$	***Th-chain*** $[Hz]$	^{40}K $[Hz]$	^{60}Co $[Hz]$
VM2000 Holders	$(1.9 \pm 0.6) \cdot 10^{-4}$	$(2.5 \pm 2.1) \cdot 10^{-4}$	$< 3.4 \cdot 10^{-5}$	
InnerVeto PMTs	$(3.6 \pm 0.3) \cdot 10^{-4}$	$(6.3 \pm 1.2) \cdot 10^{-4}$	$(3.4 \pm 0.6) \cdot 10^{-4}$	
Σ InnerVeto Parts	$\mathbf{(5.5 \pm 0.9) \cdot 10^{-4}}$	$\mathbf{(8.8 \pm 3.3) \cdot 10^{-4}}$	$\mathbf{(3.4 \pm 0.6) \cdot 10^{-4}}$	
Shielding Steel	$< 6.3 \cdot 10^{-4}$	$< 1.4 \cdot 10^{-3}$	$< 1.0 \cdot 10^{-2}$	$< 1.4 \cdot 10^{-3}$
Welding Electrode	$(2.2 \pm 0.6) \cdot 10^{-3}$	$(2.5 \pm 0.4) \cdot 10^{-2}$	$< 6.9 \cdot 10^{-4}$	$< 3.7 \cdot 10^{-4}$

Table 7.12: *Radioactivity-induced singles trigger rates (at 90% C.L.) in the Target for detector parts measured in the present thesis: the holders for the reflecting VM2000-foil mounted to the outside of the Buffer tank, the InnerVeto PMTs, the shielding steel, and the welding electrodes. For each investigated sample the rate is quoted separately for events from the U- and the Th-chain, as well as ^{40}K. In addition, the summed rate for the parts of the InnerVeto is given.*

the installation of all detector parts, Double Chooz encounters a singles rate of 8.2 Hz in the prompt energy window for the antineutrino search (0.7 MeV - 12.2 MeV) and, consequently, an accidental background of only (0.261 ± 0.002) events per day [Abe12a], which is more than three times less than the design goal.

Chapter 8

Analysis of the First Double Chooz Far Detector Data

On April 13$^{\text{th}}$, 2011, Double Chooz started data taking with the fully commissioned far detector. Until 18$^{\text{th}}$ of September, 101.5 days of data had been taken, distributed over 2594 physics runs. The full run list of all these physics runs is given in appendix F; all analyses presented in the following are based on this data set. Data taking of physics runs has only been interrupted by calibration runs, either with the light injection system (daily) or with artificial radioactive calibration sources in dedicated calibration campaigns. During most of the period of data taking the OuterVeto was still under construction and commissioning, therefore, no data from this detector part is used.

8.1 Spectrum of the Single Events

The Double Chooz far detector records data with a total trigger rate of about 120 Hz, including events after a preceding cosmic muon (~ 46 Hz) and light of glowing PMT bases (~ 60 Hz). Rejecting both muon induced events and instrumental light[1] the spectrum of all single physical events can be obtained. Fig. 8.1 depicts this singles spectrum in an energy window[2] from zero to 10 MeV; the most remarkable features are the gamma lines of ^{40}K ($E_\gamma = 1460.8$ keV [Fir96]) and ^{208}Tl ($E_\gamma = 2614.5$ keV [Fir96]), which are indicated, too.

Except for distinct features like the gamma photopeaks, the singles spectrum is smooth and continuously rises towards lower energies, mainly because of radioactivity-induced events. In the energy window for the prompt positron-like events ranging from 0.7 MeV to 12.2 MeV the singles trigger rate in the Target is ~ 8.2 Hz [Abe12a]. The singles rate in the energy window for the delayed events, from 6 MeV to 12 MeV, is $\sim 18\,\text{h}^{-1}$ [Abe12a], which leads in combination with a 98 µs-long time window after each trigger to a calculated rate of accidental antineutrino coincidences of $0.35\,\text{d}^{-1}$.

Comparing the number of singles events contained in the detector data to the expected singles count rates obtained in the simulations in ch. 7.4 the conclusion can be drawn that a major part of all singles events is induced by radioimpurities (mainly uranium, thorium, and their daughter isotopes) diluted directly in the liquid scintillator and not coming from outside. However, the photopeaks of ^{40}K and ^{208}Tl indicate gamma events not originating

[1] The method of rejecting both types of events is thoroughly explained in sec. 8.2.1.

[2] Here and in the following all energy scales refer to calibrated energy.

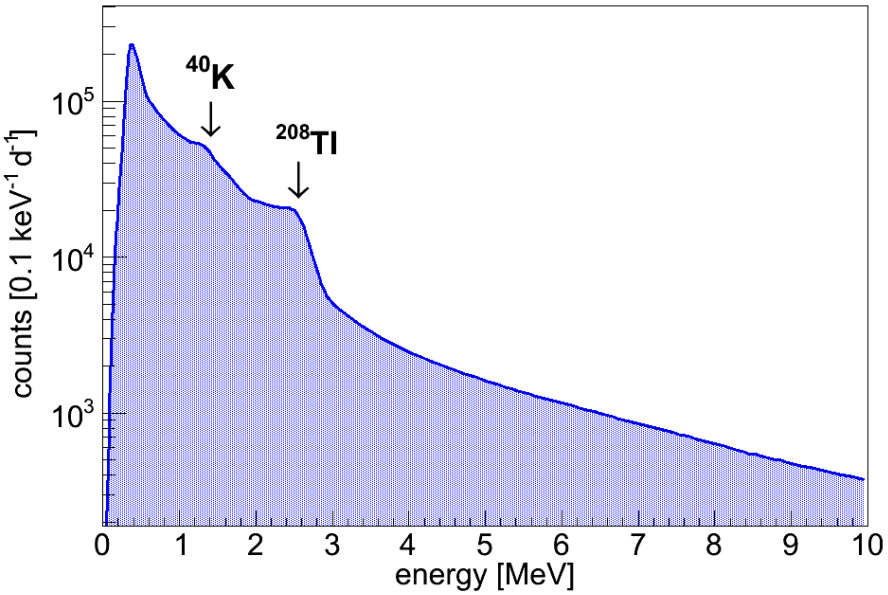

Figure 8.1: *Logarithmically scaled spectrum of all single physics events in the Double Chooz far detector in an energy range from zero to 10 MeV. Below ∼ 0.5 MeV the trigger efficiency fades, cf. fig. 8.7. Muon induced events and instrumental light, respectively, are cut out. The singles spectrum is dominated by radioactivity and falls smoothly towards higher energies. The most remarkable spectral features are the two gamma lines of ^{40}K at 1460.8 keV and ^{208}Tl at 2614.5 keV, respectively, which are indicated.*

from the active detector parts themselves: the β^--decay of a ^{40}K-nucleus in the Target would, for example, deposit the full energy corresponding to its Q-value in the liquid scintillator, leading to an event with an energy far above the gamma energy only. The gamma lines stem from decays outside the active parts, e.g. at the inner detector phototubes or the surrounding rock, with the emitted gamma entering the inner detector and being detected there.

As the singles events are by far the main source for accidental antineutrino events, a determination of the radioactive background in the inner liquids is desired. The low mass concentrations can, however, not be measured by direct gamma spectroscopy (see, for example, tab. 7.5), but the detector data itself contains a handle to determine the concentration of uranium and thorium in Target and GammaCatcher: the bismuth-polonium coincidences.

8.2 Bismuth-Polonium Coincidences

The natural decay chains of ^{238}U and ^{232}Th (see appendix A) both contain a short-lived polonium isotope, ^{214}Po in the case of uranium and ^{212}Po in the case of thorium. These polonium isotopes are both fed by the β^--decay of a bismuth isotope (^{214}Bi and ^{212}Bi, respectively) and unstable against α-decay, see decay schemes in figs. 8.2 and 8.3. Because of the short time difference between the two decays, the decay of bismuth followed by the decay of polonium is usually referred to as bismuth-polonium coincidence, or short BiPo coincidence.

The fast decay of the polonium isotopes provides the possibility to extract these coinci-

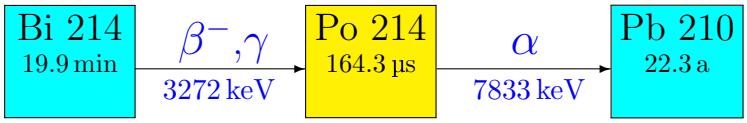

Figure 8.2: *Decay scheme of the β^--decay of ^{214}Bi into ^{214}Po and the subsequent α-decay into ^{210}Pb. The half-life of ^{214}Po is only 164.3 µs, while its daughter isotope ^{210}Pb can be considered to be stable on the fast timescales of interest here. The Q-values of the decays are given, too. Data taken from [Fir96].*

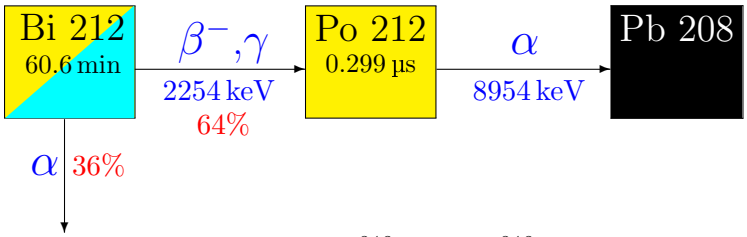

Figure 8.3: *Decay scheme of the β^--decay of ^{212}Bi into ^{212}Po and the subsequent α-decay into stable ^{208}Pb. Note that ^{212}Bi can also undergo an α-decay in 36% of all cases. This branching ratio has to be taken into account when calculating the concentration of thorium in the detector. The half-life of ^{212}Po is 299 ns, and thus even much shorter than the half-life of ^{214}Po; cf. fig. 8.2. The Q-values of the decays are given, too. Data taken from [Fir96].*

dences from the recorded data with a very high efficiency by searching for two events with the right energy which are correlated in space and time. By this, the number of uranium and thorium decays in the active parts of the inner detector (Target and GammaCatcher) can be measured in-situ, and a handle is provided to precisely determine the amount of radioactivity in the detector. This is an useful cross-check for the determination of the radiopurity with other methods (like the analysis of the singles spectrum) and an important input parameter for the calculation of the accidental background in the reactor antineutrino search. For the detector liquids, whose content of radioactivity can barely be measured with direct gamma spectroscopy, the search for BiPo coincidences is the most sensitive method to tag radioimpurities. In addition, the outcome of this search provides a clean sample of β^-- and α-events, which allows to study quenching factors (see sec. 8.2.3) and the pulse-shapes for different exciting particles[3].

However, in the case of uranium some care has to be taken, as the radioactive equilibrium of its decay chain might be broken at some long-lived isotope, e.g. ^{226}Ra with a half-life of 1600 years [Fir96]. Therefore, the determination of the number of BiPo-214 coincidences only depicts the number of ^{222}Rn decays and its daughter isotopes all of which have much shorter half-lives (see appendix A). The decay chain of ^{232}Th on the other hand contains no long-lived isotope (the longest half-life is that of ^{226}Ra with 5.8 a [Fir96]), hence, the number of thorium decays can be tagged using the BiPo-212 coincidences.

[3]The pulse-shape analysis is not part of the present thesis, but studied elsewhere [Jol12, Wag12].

8.2.1 Data Reduction and Optimisation of Applied Cuts

The data recorded with the Double Chooz far detector contains several classes of events:

- Reactor electron antineutrinos
- Events induced by radioimpurities
- Cosmic muons and muon secondaries
- Instrumental light (glowing) of the PMTs

In order to extract the BiPo coincidences, distinct selection cuts are applied to these data.

Veto on Cosmic Muons

Muons, produced by processes of cosmic rays in the Earth's atmosphere, are partly able to traverse the rock overburden of the detector (depending on their energy) and induce signals in the active detector parts. Although direct hits by a muon deposit so much energy in the detector that these events can be easily rejected, secondary particles produced by spallation processes of muons in or closeby to the detector might have the right energy to mimic BiPo events. Therefore, after each event which is identified as muon[4], a 1 ms time veto (2 ms in the case of BiPo-214) is cut out. Of course, this method rejects only muons hitting the detector directly; muons passing nearby cannot be tagged. The efficiency of detecting the latter rises with the OuterVeto online. However, OuterVeto data was only available since end of July, 2011 and not for the full data set used in the present thesis. Therefore, data from this detector subsystem was not used. An analysis of more recent data, on the other hand, can make use of the OuterVeto data and therefore increase the tagging efficiency for close-by muons.

The average muon rate in the Double Chooz far detector is about 46 Hz or $\sim$3,975,000 muons per day (see fig. 8.4). This consequently leads to a total veto time[5] of about 4.6% (9.7% for BiPo-214). This muon veto time has to be accounted for in all calculations of the BiPo rate.

The efficiency of this cut[6] was tested with a subsample of 750 physics runs: the number of BiPo-214 coincidences found was studied as a function of the muon veto time applied, ranging from zero to 4 ms in steps of 0.1 ms. Fig. 8.5 depicts the outcome of this study: the results of an exponential fit to the time difference between prompt and delayed event yield constant life times (which match the literature value of 164.3 µs) for muon veto times longer than 1 ms. In addition, for veto times longer than 2 ms the number of BiPo-214 coincidences found, and corrected for the live time, is constant, too. From that it is concluded that the data contains no more muon secondaries. Hence, a veto time of 2 ms is applied for the BiPo-214 search, which is a conservative approach to get rid of muon induced events in this search.

[4]Each event with an energy deposition of more than 10,000 DUQ (digital units of charge) in the InnerVeto or $\approx$30 MeV in the inner detector is flagged to be a muon.

[5]The quoted veto times are calculated such that neither the prompt event nor the subsequent delayed events falls into the veto time window after an identified muon. Therefore, the veto times are slightly bigger than just the muon rate multiplied with the length of the veto window.

[6]Here and in the following the term "cut efficiency" always refers to the percentage of true events passing the respective selection cut. The efficiency of the cuts for false events (background) being rejected can hardly be determined and is consequently not quoted. However, the background still contained in the data sample is studied separately (sec. 8.2.8) and properly taken into account in all conclusions.

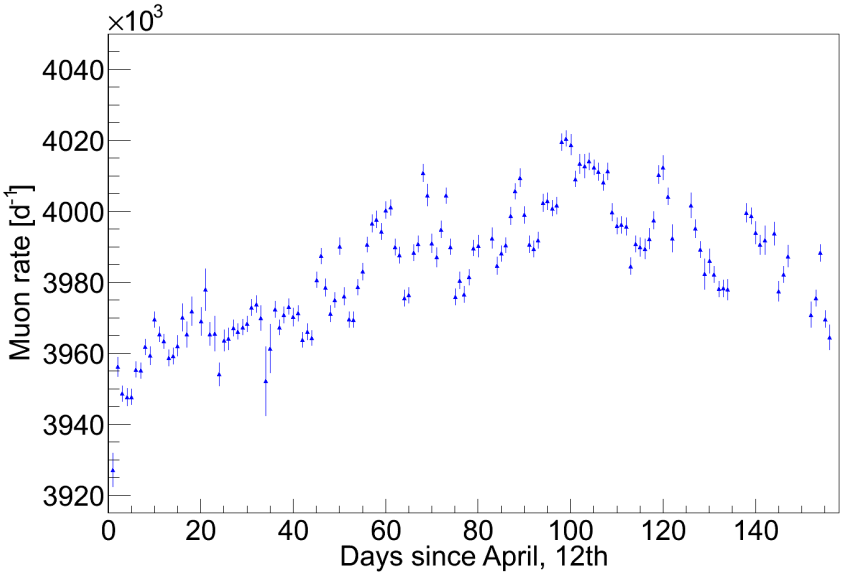

Figure 8.4: *Daily muon rate at the Double Chooz far detector as a function of days after start of the official data taking. Every event with an energy deposition of more than ∼ 30 MeV in the inner detector or 10,000 DUQ in the InnerVeto, respectively, is hereby considered to be a muon. The slight rise in the muon rate of ∼ 1.1% over the first 100 days and the dropping afterwards is related to changes in the atmospheric pressure over time and well understood [Die11]. On average, the muon rate is ∼ 3,984,000 d^{-1}, or 46 Hz. Error bars are statistical only.*

The maximum time difference between prompt and delayed event is also 2 ms (see tab. 8.2 on page 96), therefore, a 2 ms muon veto time window corresponds to the requirement of no muon event in the whole time window. However, as for the BiPo-212 search a maximum time difference of only 5 µs between the prompt and the delayed event is chosen (because of the much shorter half-live of ^{212}Po; tab. 8.2), the veto time after each muon is set to 1 ms here. A similar study showed that for this choice again no more muon induced events are expected in the extracted data sample.

Besides the veto-time cut an additional multiplicity cut is applied to the data. Only BiPo coincidences with no additional valid prompt or delayed event in the time window are stored. This cut removes all fake events from the data sample, which are generated by particles recoiling off several times in the detector, e.g. fast neutrons stemming from an unidentified muon or an (α,n)-reaction on a carbon nucleus. Furthermore, this multiplicity cut prevents the time distribution between prompt and delayed event to be spoiled by accidental coincidences: for example, any event fulfilling the criteria for a delayed event (see tab. 8.2) occurring between the correctly identified prompt event (Bi decay) and the "true" delayed event (Po decay) would lead to a shorter time difference obtained for this event. However, the multiplicity cut rejects also true BiPo coincidences, where some additional accidental prompt (delayed) event occurs in the time window preceding the delayed event (after the prompt event). To gain the number of true BiPo coincidences this has to be corrected for. The number of coincidences rejected by the multiplicity cut as well as the number of coincidences accepted are given in table 8.1.

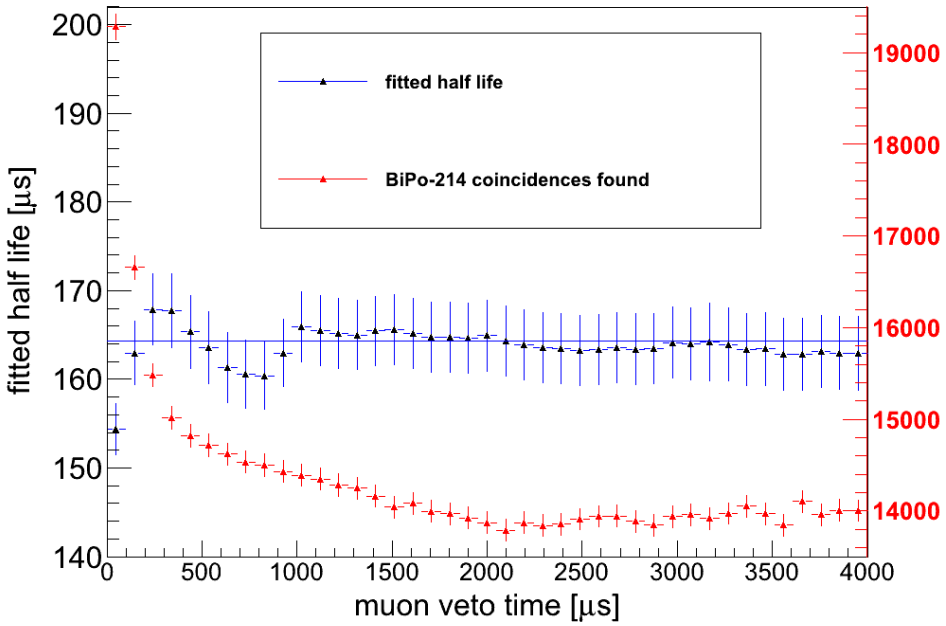

Figure 8.5: *Number of BiPo-214 coincidences found and half-life obtained from data in a subsample of 750 physics runs as a function of the muon veto time ranging from 0 ms to 4 ms. The black data with the blue error bars shows the fitted half-life of ^{214}Po (see text), the horizontal blue line depicts the literature value of 164.3 µs [Fir96]. For muon veto times longer than ∼ 1 ms the data is stable. The red data and the red y-axis (right) show the number of BiPo-214 coincidences corrected for the live time. For muon veto times longer than 2 ms (i.e. no muon in the time window of the coincidence search, see below) the number of BiPo coincidences stays constant, hence, all muon induced events are surely cut out of the data. Error bars are statistical only.*

	number of coincidences rejected N_r	number of coincidences accepted N_{acc}	fraction $\frac{N_r}{N_r+N_{acc}}$
BiPo-214	42	42182	0.10%
BiPo-212	16	10659	0.15%

Table 8.1: *Number of BiPo coincidences accepted and rejected by the multiplicity cut, as well as the fraction of rejected events of all coincidences found. This percental deviation is corrected for in the rate calculations later-on, although it is very small.*

Rejecting Instrumental Light

The bases of some PMTs of the Double Chooz far detector spontaneously emit some instrumental light by glowing [Abe12a]. The events caused by this light emission are strongly

localised at the glowing PMT (fig. 8.6) and spread out in time. As the energy distribution of these glowing events covers also the energy windows for the BiPo search (see below) two additional quality cuts have to be applied to the data in advance of the BiPo coincidences search: a homogeneity cut rejects all events which are localised to a few PMTs only, and a cut on the width of the distribution of first hit times at the PMTs (T_s) selects all events for their time spread.

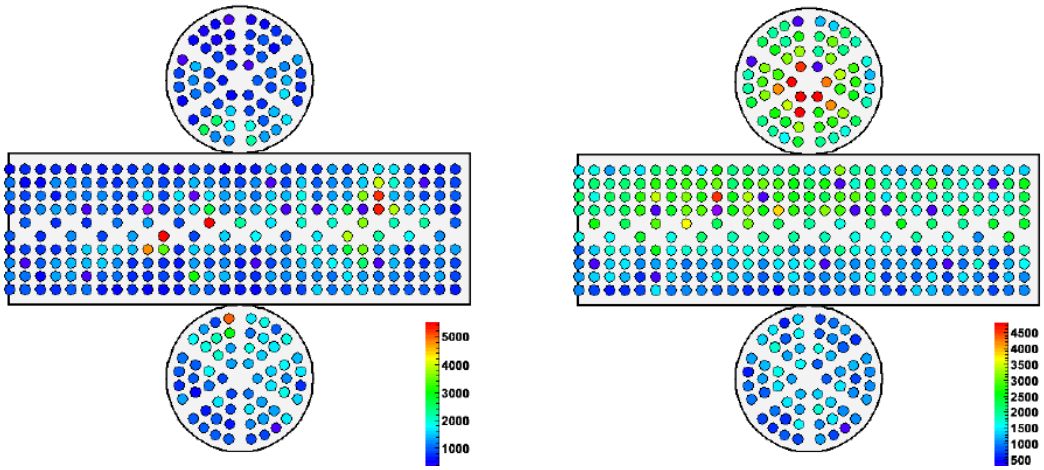

Figure 8.6: *Event display of the Double Chooz far detector showing a strongly localised glowing event (left) and a more homogeneously distributed physics event (right). The cylindrically shaped detector is rolled out; each small circle corresponds to one PMT of the Inner Detector. The colour coding depicts the charge seen by the PMTs, ranging from dark blue (little charge) to red (high charge). The charge distribution of the instrumental light is much more inhomogeneous, most of the charge is localised to a single PMT, its close-by neighbours and the PMTs facing it.*

The homogeneity cut is performed as cut on the ratio of the charge of the single PMT with the maximum charge (MQ) for a certain event to the sum of all PMT charges (total charge; TQ). Values of this ratio, referred to by MQTQ in the following, below 0.09 hereby mainly belong to physics events, while all events with MQTQ > 0.09 are rejected as instrumental light candidates [Abe12a].

The time spread cut is set to $\mathrm{RMS}(T_s) < 40\,\mathrm{ns}$, where $\mathrm{RMS}(T_s)$ is the standard deviation of the first hit times of all 390 PMTs in the inner detector for each event. The value for this cut was also optimised in dedicated studies concerning instrumental light: the outcome of these studies proves that the fraction of physics events rejected by the combination of both quality cuts is negligibly small, however, some instrumental light survives the cuts and enters the data sample [Pal12]. The fraction of the latter of all events is very hard to determine, even statistically, as no "radioactivity-off" data can be purchased. For the studies presented in this thesis the cut efficiency is therefore assumed to be 100%. This is a conservative approach, as for the rate calculations all events passing the reduction cuts are taken to be physics events, and thus an upper limit for the true number of BiPo coincidences is provided.

Separation from Other Physics Events

After the removal of cosmogenically induced events and instrumental light from the data sample the BiPo coincidences have to be selected out of the remaining physics events. Therefore, four additional cuts are applied to the data:

1. Energy cut for the bismuth event (prompt event)
2. Energy cut for the polonium event (delayed event)
3. Cut on the time difference between prompt and delayed event
4. Spatial cut on the vertex displacement of prompt and delayed event

1. The cut on the energy of the prompt event is related to the Q-value of the β^--decay of the bismuth isotope. The Double Chooz far detector is big enough to fully contain the energy released in these decays, i.e. it acts like a calorimeter. As the quenching effect both for electrons and gamma quanta is small [Abe11a] the upper limit of the energy window of the prompt event is chosen to be bigger than the Q-value, i.e. 3.5 MeV for ^{214}Bi (Q-value: 3.27 MeV) and 3.0 MeV for ^{212}Bi (Q-value: 2.25 MeV). The lower energy threshold is set to 1.0 MeV in the case of ^{214}Bi and 0.5 MeV in the case of ^{212}Bi, respectively. Both β^--decays can reach the ground state of the daughter nucleus (for ^{214}Bi see appendix C) with a non-negligible probability [Fir96], hence, both β-energy spectra go down to zero. However, the trigger efficiency steeply drops to zero for energies smaller than $\sim$0.5 MeV [Stu12] (fig. 8.7), therefore, these events are excluded from the analysis, diminishing the efficiency of this energy cut (see below).

The time window opened after a prompt event is much larger for the BiPo-214 coincidences than for the BiPo-212 coincidences (2 ms compared to 5 µs). Therefore, the number of accidental coincidences will be much higher, too. In order to reduce the number of accidentals in the BiPo-214 analysis the lower energy threshold for the prompt event is set to 1 MeV, as the energy spectrum of all single events (fig. 8.1) quickly rises towards lower energies. Hence, the number of rejected prompt-like events is disproportionately high by increasing the lower energy threshold, compared to the number of true ^{214}Bi-events excluded. For the same reason the upper cut value for the prompt energy cut is much closer to the Q-value of the β^--decay for ^{214}Bi than for ^{212}Bi, although at energies around 3 MeV the singles count rate is more than one order of magnitude lower than at $\sim$1 MeV (fig. 8.1).

Using the Double Chooz Monte-Carlo simulation[7] [Hor05, Mot05] the cut efficiencies of the energy cuts on the prompt event could be determined to be (84.3 ± 1.3)% for ^{214}Bi and (74.1 ± 1.5)% for ^{212}Bi. For each of these isotopes 10,000 events have been simulated in the Target and GammaCatcher region, taking fully into account all effects like quenching, energy resolution of the detector and possible energy losses.

2. Unlike the continuous energy distribution of the prompt event the α-decays of the polonium isotopes (delayed events) have a well-defined energy deposition, which is only smeared out by the energy resolution of the detector. Therefore, the energy window for the delayed events can be chosen to be more narrow. However, due to the big quenching factors for α-particles in the detector liquids of the order of 10 [Abe11a] the visible energies are rather low, and the energy cut for the delayed events has the following values: [0.2; 0.9] MeV for ^{214}Po

[7] DOGS version PROD-07-03.

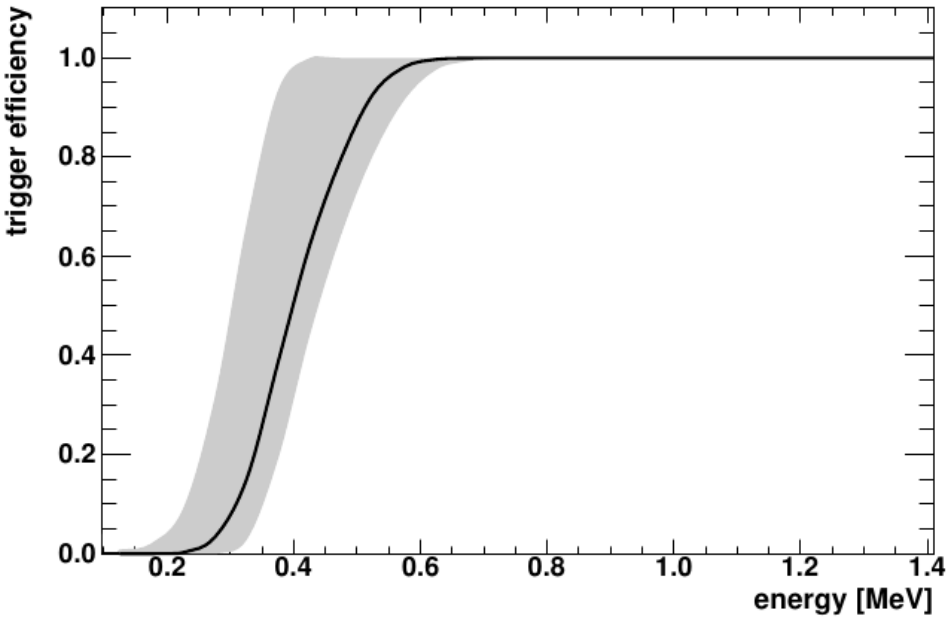

Figure 8.7: *Efficiency curve of the Double Chooz trigger at center position (including energy map correction) [Stu12]. The shaded area depicts the total systematic uncertainty. For energies below ∼ 0.5 MeV the efficiency steeply drops to zero. This effect has to be considered for any studies in the low-energy regime.*

(α-energy: 7.69 MeV) and [0.35; 1.2] MeV for ^{212}Po (α-energy: 8.78 MeV). Furthermore, the α-quenching factors are slightly different for Target and GammaCatcher, however, the energy windows are chosen big enough to fully contain the α-peaks for both detector liquids.

For the Target region the cut efficiency of the α-energy cut was found to be $> 96.2\%$ for ^{214}Po and $> 99.8\%$ for ^{212}Po at 68% C.L., while for the GammaCatcher the efficiencies are 100% and $> 98.0\%$, respectively.

3. The selected time differences between prompt and delayed event are [6; 2000] µs for BiPo-214 and [0.5; 5] µs for BiPo-212. The 500 ns lower time cut threshold eliminates most of the afterpulse events in the PMTs and correlated noise. In principle, a 2 µs veto time after each event is favourable [Abe12a], however, this would correspond to nearly seven times the half-life of ^{212}Po rejecting more than 99% of all BiPo-212 coincidences. The 500 ns cut threshold is thus a compromise between the efficiency in gathering as much true BiPo events and coincidentally rejecting as much correlated noise as possible. The 5 µs upper time limit, which corresponds to nearly 17 half-lives of ^{212}Po, ensures no additional losses due to the timing cut and, furthermore, allows a determination of the accidental background in the BiPo sample. The latter is not correlated in time, i.e. it has a flat timing distribution, and thus can be determined from the tail of the distribution of the time difference between prompt and delayed event at late times, where no true BiPo events can be found anymore (see sec. 8.2.8). In the BiPo-212 search a part of the background entering the selected sample comes from BiPo-214 events due to the overlaps in the energy windows. This has to be accounted for in the rate calculations, too. The time window for the BiPo-214 search starts only at 6 µs, excluding all events from correlated noise as well as any contamination from BiPo-212 coincidences. The upper time cut is chosen to be bigger than 12 half-lives of ^{214}Po, allowing

	BiPo-214	BiPo-212
muon veto time	2 ms	1 ms
multiplicity cut	no further valid trigger in time window	
instrumental light cut	MQTQ < 0.09 and RMS(T_s) < 40 ns	
E(prompt)	[1.0; 3.5] MeV	[0.5; 3.0] MeV
E(delayed)	[0.2; 0.9] MeV	[0.35; 1.2] MeV
Δt	[6; 2000] µs	[500; 5000] ns
$\Delta\rho$	< 50 cm	
vertex	no badly reconstructed events	

Table 8.2: *Selection cuts applied to the detector raw data for the analysis of BiPo-214 and BiPo-212 coincidences, respectively.*

again a determination of the accidental background.

An analytical calculation yields the cut efficiencies of the time difference cut, using the literature values for the half-lives of the polonium isotopes. Within the first 0.5 µs, 68.6% of all ^{212}Po atoms decay, and 2.5% of the ^{214}Po nuclei within the first 6 µs. The cuts at late times do not affect the cut efficiency, as the time windows are chosen to be much larger than the half-lives of the respective polonium isotopes.

4. The last cut to be applied to the data is a spatial cut on the reconstructed vertices of prompt and delayed event. As the time difference between these two is rather short, and no big convection happens within the Double Chooz far detector, the true positions of both decays are expected to be the same. However, as the spatial resolution of the reconstruction algorithm[8] is of the order of 20 cm [Sta11] (depending on the energy), the displacement between the reconstructed vertices of prompt and delayed event is restricted to be smaller than 50 cm in this analysis. This cut has quite a high acceptance for spatially correlated events like BiPo coincidences ($\gtrsim 99.7\%$), but it also rejects lots of accidental coincidences ($\sim 99.8\%$), as these are not correlated in space, too. In addition, the BiPo analysis excludes all badly reconstructed events.

Table 8.2 summarises all cuts applied to the raw data in order to extract the BiPo-214 and BiPo-212 coincidences; table 8.3 gives an overview of the cut efficiencies as determined above.

[8] In this case the algorithm RecoBAMA was used.

	BiPo-214	BiPo-212
muon cut	100%	
multiplicity cut	99.9%	99.85%
instrumental light cut	100%	
E(prompt)	$(84.3 \pm 1.3)\%$	$(74.1 \pm 1.5)\%$
E(delayed) NT	$> 96.2\%$	$> 99.8\%$
E(delayed) GC	100%	$> 98.0\%$
Δt	97.5%	31.4%
$\Delta\rho$	$> 99.7\%$	

Table 8.3: *Efficiencies of the selection cuts for the acceptance of true events for the BiPo search at 68% C.L. as explained in the text. For the delayed energy cut the values for the Target ("NT") and the GammaCatcher ("GC") are quoted separately. The analytic calculation of the efficiency of the time difference cut is assumed to be exact. Both in case of the instrumental light cut as well as the multiplicity cut the worst-case scenario is assumed: all events passing the instrumental light cut and all events rejected by the multiplicity cut are assumed to be caused by true BiPo coincidences. In this way, the rate calculations give the upper limits for the concentration of radioimpurities in the detector.*

8.2.2 Energy Distribution of Prompt and Delayed Events

After having applied the above mentioned cuts, the energy spectrum of the prompt events both for ^{214}Bi and ^{212}Bi shows the continuous energy distribution of the β^--decay; fig. 8.8. These spectra are a sum of the single e^--spectra due to the decay of the mother isotope to different excited states (or the ground state) of the daughter isotope plus the energy of the subsequently emitted gamma quanta in the fast de-excitation processes of the daughter nucleus. The active parts of the Double Chooz far detector are hereby big enough to fully contain these gamma quanta; only minor losses at the edges of the GammaCatcher are expected. The analysis of the remaining background in the data sample (sec. 8.2.8) shows that for ^{214}Bi the number of background events is not negligible (more than 20%), therefore, the energy spectrum of background events gained by the offtime-window method is subtracted statistically from the spectrum of all events. For ^{212}Bi, however, the background contribution is negligibly small ($< 0.5\%$), thus no subtraction is performed.

The monoenergetic α-decays of the polonium isotopes cause the energy spectra of the delayed events to be rather narrow Gaussian-shaped distributions. The widths of these peaks reflect the energy resolution of the Double Chooz far detector (see below). As the quenching factors for α-particles are quite different for Target and GammaCatcher liquid [Abe11a], the

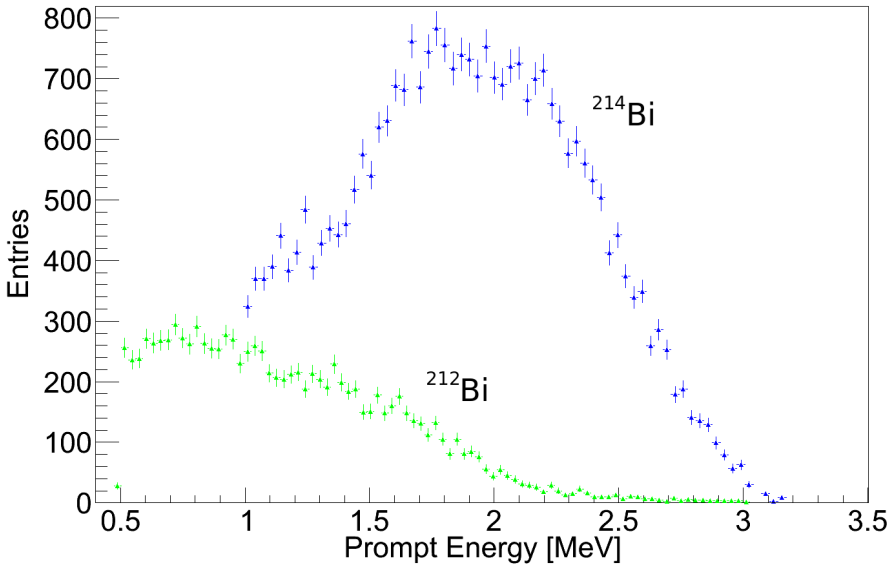

Figure 8.8: *Visible energy spectrum of the prompt ^{214}Bi (blue) and ^{212}Bi events (green) in an energy range from 0.4 MeV to 3.5 MeV. The energy spectrum of background events (sec. 8.2.8) is subtracted statistically from the ^{214}Bi sample; bins with negative entries are not shown. For the case of ^{212}Bi no background correction needs to be applied. The continuous energy distribution reflects the underlying β^--decay with Q-values of 3272 keV (^{214}Bi) and 2254 keV (^{212}Bi) [Fir96], respectively, and is the sum of all spectra emitted in the decay of the bismuth nuclei to the various excited states of the daughter polonium isotopes (for ^{214}Bi cf. appendix C). The decay energy is distributed to the emitted electron, gamma quanta stemming from the de-excitation of the daughter nucleus in case an excited state was populated, and an electron antineutrino causing a part of the Q-value to be lost for scintillation light production. Error bars are statistical only.*

energy distributions are plotted separately for the two active detector volumes; figs. 8.9 and 8.10. In all four cases a Gaussian fit to the data is shown, too. Again, for ^{214}Po the energy spectrum of background events as gained by the offtime-window method is subtracted statistically; the energy spectra of ^{212}Po are not corrected.

In order to avoid a diminished energy resolution and a wrongly fitted peak position of the Target distributions by GammaCatcher events falsely reconstructed into the Target region (and vice versa), the depicted events are restricted to a fiducial volume. In case of the Target, only events with a vertex (ρ, |z|) < (85 cm, 92.9 cm) are taken[9], in case of the GammaCatcher the vertices for the fiducial volume[10] are restricted to 145 cm < ρ unified with 152.9 cm < |z|.

From the Gaussian fits to the data both the energy resolution and the α-quenching factors of the detector at the respective α-particle energy can be derived. The energy resolution (1 σ-

[9] ρ denotes the displacement from the detector's symmetry axis (z-axis). Hence, the Target fiducial volume vertices correspond to a cylindrically shaped volume in the centre of the detector which has a spacing of 30 cm to all Target vessel walls.

[10] Again, these are all vertices within the GammaCatcher which have at least a spacing of 30 cm to the Target vessel walls. A separation to the GammaCatcher vessel walls is not needed, as the Buffer is not scintillating and, therefore, no events from the Buffer can be falsely reconstructed into the GammaCatcher.

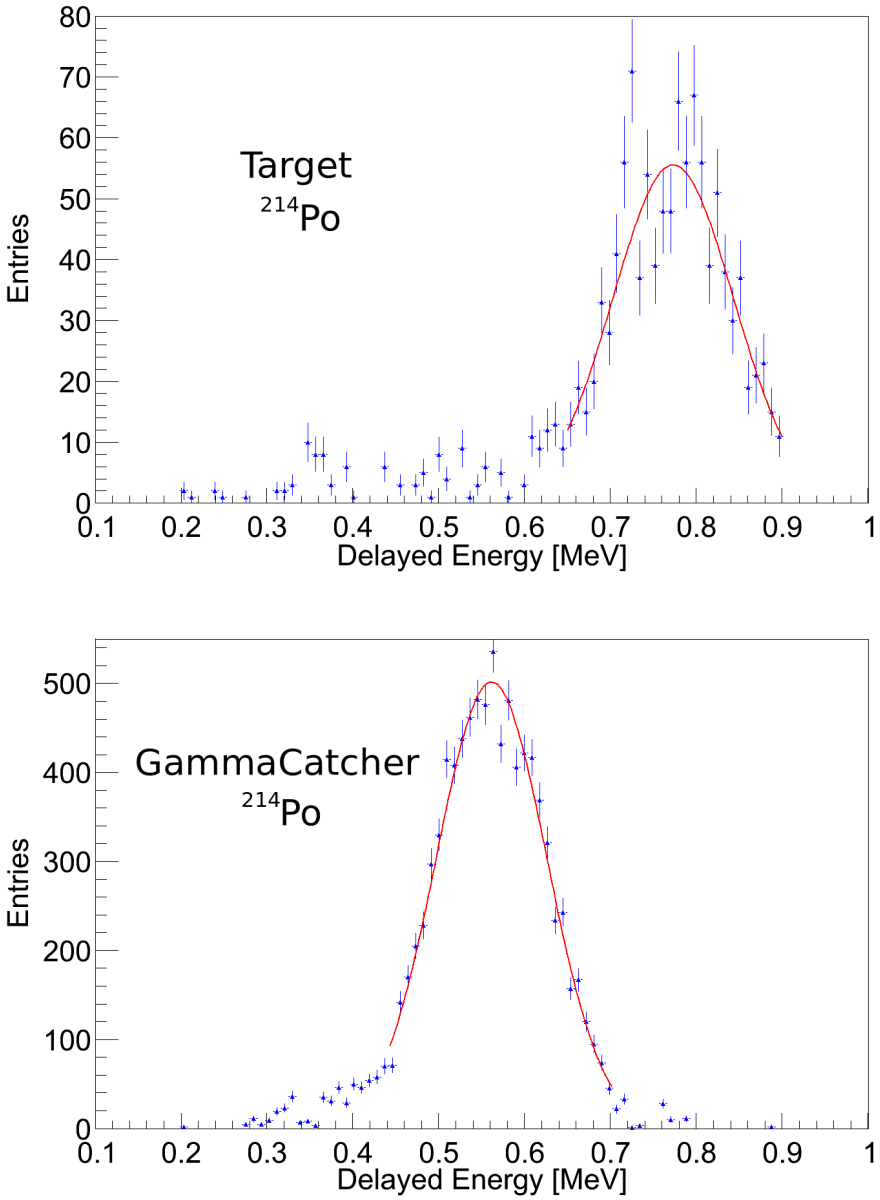

Figure 8.9: *Energy spectrum of the delayed ^{214}Po events in an energy range from 0.1 MeV to 1 MeV, restricted to events in the Target (top panel) and GammaCatcher (bottom) fiducial volume. The energy spectrum of background events (sec. 8.2.8) is subtracted statistically in both cases. The physical energy of the α-particle is 7.69 MeV [Fir96]. A Gaussian fit is applied to the data in both cases; its width reflects the energy resolution of the Double Chooz far detector of 9.1% (Target) and 11.5% (GammaCatcher) for this energy (1 σ), its peak position the α-quenching factor of 9.94 ± 0.04 for the Target liquid and 13.69 ± 0.02 for the GammaCatcher liquid for this α-energy. Error bars are statistical only.*

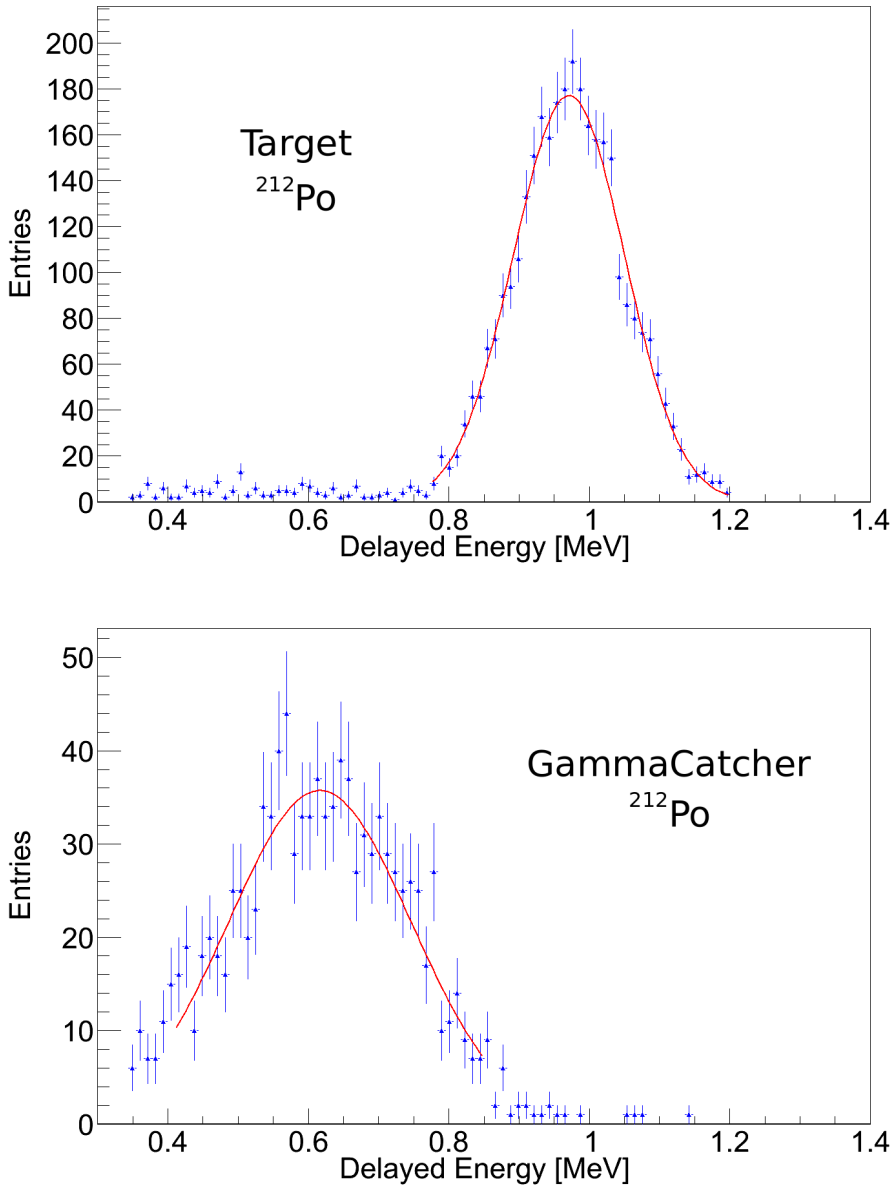

Figure 8.10: *Energy spectrum of the delayed ^{212}Po events in an energy range from 0.35 MeV to 1.2 MeV, restricted to events in the Target (top panel) and GammaCatcher (bottom) fiducial volume. The physical energy of the α-particle is 8.78 MeV [Fir96]. Again, a Gaussian fit is applied to the data in both cases; energy resolutions of the Double Chooz far detector of 8.2% (Target) and 21.1% (GammaCatcher) for this energy (1σ) are found, the α-quenching factors are 9.046 ± 0.014 for the Target liquid and 14.25 ± 0.12 for the GammaCatcher liquid for this α-energy. Error bars are statistical only.*

width of the Gaussian fit) of the detector at the low visible energies is found to be 9.1% (^{214}Po at Target; 773 keV visible energy), 11.5% (^{214}Po at GammaCatcher; 564 keV), 8.2% (^{212}Po at Target; 936 keV), and 21.1% (^{212}Po at GammaCatcher; 615 keV). In both cases the resolution is considerably better in the Target region than in the GammaCatcher, which reflects that the Double Chooz detector design was tuned to achieve the highest resolution at its fiducial volume for the antineutrino search, which is the Target. By this, the spectral information on the positron spectrum is most precise, allowing shape analyses of the neutrino oscillation signal.

The energy resolution is expected to be slightly better for α-particles from ^{212}Po-decays because of their slightly higher energy. This is indeed observed for the Target liquid, however, the energy resolution obtained from the ^{212}Po-α-peak in the GammaCatcher liquid is much worse (21.1%) than that obtained for ^{214}Po (11.5%). At present, this behaviour is not understood. The energy spectrum (fig. 8.10) is fitted quite well with a single Gaussian distribution, although statistics is less than for the Target region and for the BiPo-214 coincidences. This issue needs to be investigated in further studies, possibly with considerably increased statistics.

8.2.3 Quenching Factors Obtained from the α-Peaks

The α-quenching factors[11] are obtained from the peak position of the Gaussian fit. These quenching factors for ^{214}Po were also determined in some laboratory experiment [Abe11a] using a radioactive α-source. Tab. 8.4 lists the peak positions for the different α-energies and the different detector parts, and the quenching factors calculated from that. In addition, the results of the laboratory experiment are given, showing good agreement.

	peak position [keV]	quenching factor	laboratory measurement
Po-214 (7687 keV)			
Target	773.0 ± 3.0	9.94 ± 0.04	9.8 ± 0.4
GammaCatcher	561.5 ± 0.8	13.69 ± 0.02	12.6 ± 0.6
Po-212 (8784 keV)			
Target	971.0 ± 1.5	9.05 ± 0.02	-
GammaCatcher	616.5 ± 5.4	14.2 ± 0.1	-

Table 8.4: *Fitted peak positions of the α-peaks of ^{214}Po and ^{212}Po in the detector data, and the α-quenching factors calculated from it. The results of the laboratory measurements for ^{214}Po [Abe11a] are given, too, showing good agreement. For ^{212}Po no laboratory measurements were performed.*

8.2.4 Time Difference between Prompt and Delayed Event

The time differences between prompt and delayed event of the BiPo coincidence obtained in the data analysis are plotted in fig. 8.11 for BiPo-214 and BiPo-212.

In both cases a single exponential function plus a constant c are fitted to the data:

[11] A detailed discussion of the quenching mechanisms can be found in section 5.3.

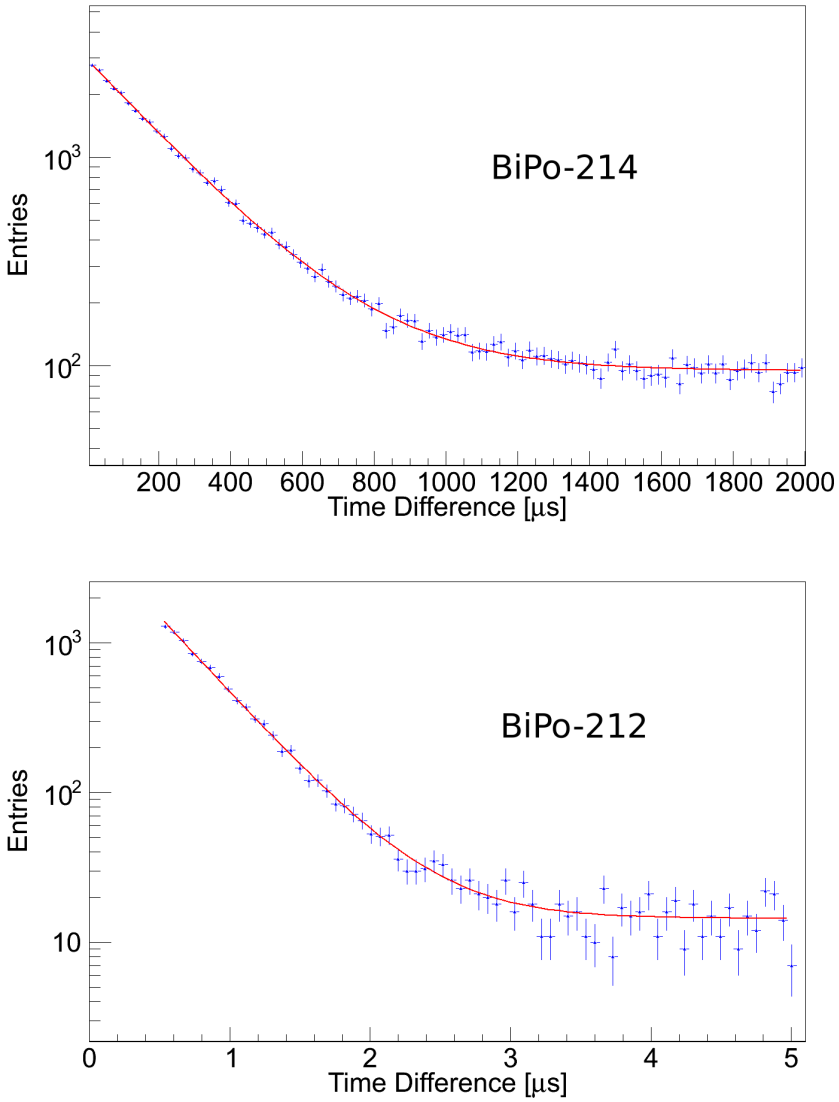

Figure 8.11: *Time difference between prompt and delayed event for BiPo-214 (top panel) and BiPo-212 (bottom panel), plotted on a logarithmic scale. An exponential plus a constant are fitted to the data (red line) in both cases. From these fits half-lives of (163.4 ± 1.4) µs (^{214}Po) and (295.0 ± 3.9) ns (^{212}Po) are obtained. Error bars are statistical only.*

$$f(t) = exp\left\{-\frac{t}{\tau}\right\} + c \quad . \tag{8.1}$$

From the exponential the life time of the coincidences can be derived. For the BiPo-214 data a half-life for ^{214}Po of (163.4 ± 1.4) µs is found, the literature value is (164.3 ± 2.0) µs [Fir96]. The fit to the BiPo-212 data yields a half-life for ^{212}Po of (295.0 ± 3.9) ns (literature value: (299 ± 2) ns [Fir96]). Both values agree rather well with the expectation and thus clearly indicate the absence of a remaining dominant correlated background, which would

spoil the distribution of the time differences.

However, some accidental BiPo-like coincidences still survive the cuts given in sec. 8.2.1, which can be seen from the constant tail of the data at time differences far above ten times the half-life of the polonium isotope. Accidental coincidences are not correlated in time, i.e. they have a flat distribution of the time difference, hence, their number can be estimated from the constant term to the fit (see also below in sec. 8.2.8 on background determination). The best fit values for the constants c_{212} (for BiPo-212) and c_{214} (for BiPo-214) are

$$\begin{aligned} c_{212} &= (226.1 \pm 10.5)\,\mu s^{-1} \\ c_{214} &= (4.73 \pm 0.08)\,\mu s^{-1} \quad . \end{aligned} \tag{8.2}$$

As already mentioned above, the background for the BiPo-212 search partly consists of BiPo-214 coincidences, as the energy windows considerably overlap.

8.2.5 Spatial Distribution of the BiPo Coincidences

Fig. 8.12 shows the spatial displacement between prompt and delayed event for the BiPo coincidences. This displacement ϱ is calculated as

$$\varrho = \sqrt{(x_p - x_d)^2 + (y_p - y_d)^2 + (z_p - z_d)^2} \quad , \tag{8.3}$$

where $(\mathrm{x_p}, \mathrm{y_p}, \mathrm{z_p})$ and $(\mathrm{x_d}, \mathrm{y_d}, \mathrm{z_d})$ denote the reconstructed vertices for prompt and delayed event, respectively. As was deduced above, the true vertex displacement is expected to be close to zero. However, the resolution of the vertex reconstruction algorithm introduces an additional uncertainty of about 20 cm, which is also reflected in the depicted distributions of ϱ. According to the calculation of ϱ the resolution of the spatial reconstruction in 3D is given by the mean value of the distribution of ϱ.

For a perfectly uncorrelated sample the distribution of the vertex displacements is expected to follow a ϱ^2-distribution. This is because the volume of the spherical shells between some radius ϱ and $\varrho + \Delta\varrho$ scales like ϱ^2. The green data in fig. 8.12 shows the calculated values of ϱ corrected for this volume effect (blue data divided by ϱ^2). This distribution clearly shows the spatial correlation between prompt and delayed event in the BiPo data, as it reaches its maximum towards zero in both cases. In contrast, for an uncorrelated sample a flat distribution would be expected after correcting for volume effects.

The distribution of the BiPo-214 event vertices in the Double Chooz far detector is shown in figs. 8.13 and 8.14, once as xy-plot, i.e. a projection of all event vertices on the detector's lid and once as rz-plot, where $\mathrm{r} = \sqrt{\mathrm{x}^2 + \mathrm{y}^2}$. To correct the vertex density for volume effects the abscissa is not linear in r, but rises quadratically.

The rz-projection of the event vertices shows an excess of BiPo-214 coincidences in the GammaCatcher liquid in comparison to the Target liquid. This directly leads to the conclusion that the GammaCatcher scintillator contains more ^{222}Rn, or, in case the radioactive equilibrium is not broken, more uranium than the Target scintillator. These radioimpurities were most likely introduced during manufacturing or preparation of the liquid, or during the filling process. Any doping through radon emanation from a localised source would - in absence of big convection processes - lead to big inhomogeneities in the BiPo-214 vertex distribution, which are, however, not observed.

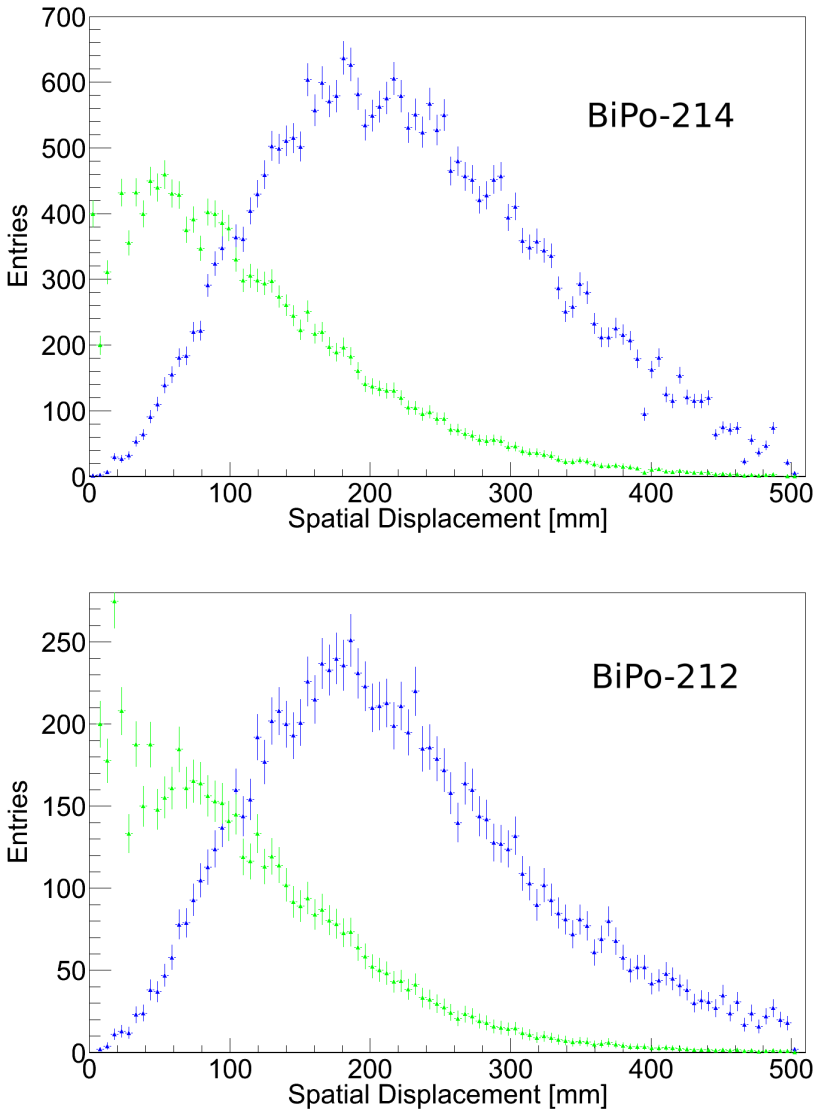

Figure 8.12: *Spatial displacement ϱ between prompt and delayed event for the BiPo-214 coincidences (blue data points, top) and the BiPo-212 coincidences (blue data points, bottom). In both cases, the green data points show the displacements corrected for the volume effect (see text), and indicate clearly the spatial correlation of the two events. For the BiPo-214 coincidences the accidental background is once again subtracted statistically. Error bars are statistical only.*

However, the vertex plots 8.13 and 8.14 are not fully homogeneous but shows also a clear excess of events in the middle of the detector, both on top and less prominent on the bottom. Both excesses are also seen in the vertex distribution of the accidental coincidences (see below, fig. 8.29), hinting to an excess of radioactivity at these locations. The event excess in the middle of the GammaCatcher bottom is most likely connected to the pressure sensor placed there, which contains a considerably higher amount of activity than the liquid (see sec. 7.2).

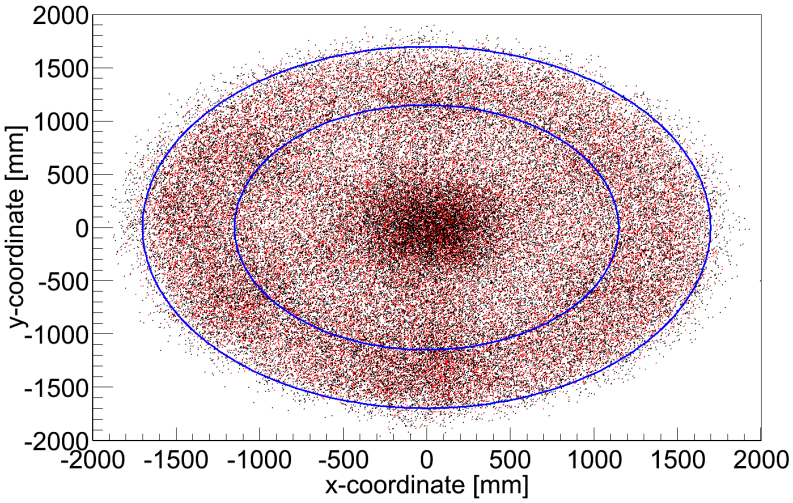

Figure 8.13: *xy-projection of the reconstructed event vertices of the BiPo-214 coincidences. The vertices of the prompt events are depicted in red, the vertices of the delayed events in black. The blue ellipses indicate the positions of the Target and GammaCatcher acrylic vessels, respectively. A clear excess of BiPo-214 events in the middle can be seen, which is due to events close to the chimney; see figs. 8.14 and 8.15.*

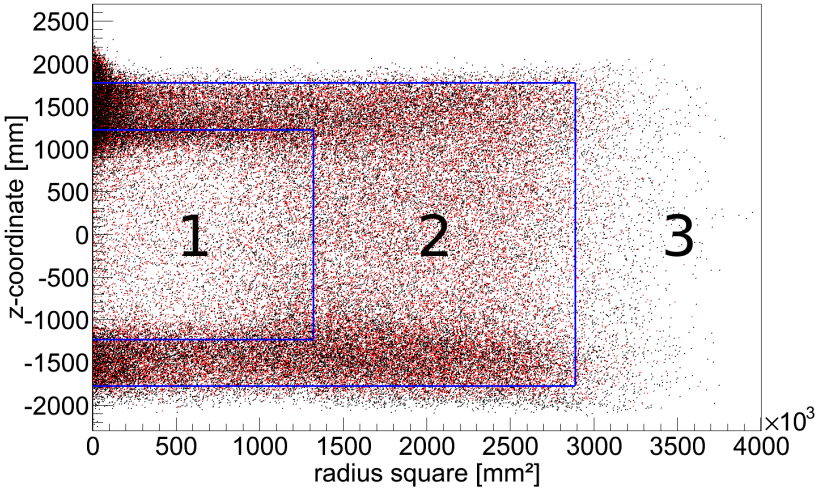

Figure 8.14: *rz-projection of the reconstructed event vertices of the BiPo-214 coincidences. The vertices of the prompt events are depicted in red, the vertices of the delayed events in black. The abscissa is scaled quadratically to correct the vertex density for volume effects. The blue lines indicate the positions of the Target and GammaCatcher acrylic vessels, respectively. Obviously, the GammaCatcher liquid (2) contains more BiPo-214 events, i.e. more ^{222}Rn and its daughters, than the Target liquid (1). An excess of events at the chimney ($r^2 < 100\,\mathrm{mm}^2$) can be seen, too, which is partly due to higher accidental background there (cf. fig. 8.29). All events reconstructed to the Buffer region (3) can be explained with the finite resolution of the reconstruction algorithm; no leakage of liquid scintillator is observed.*

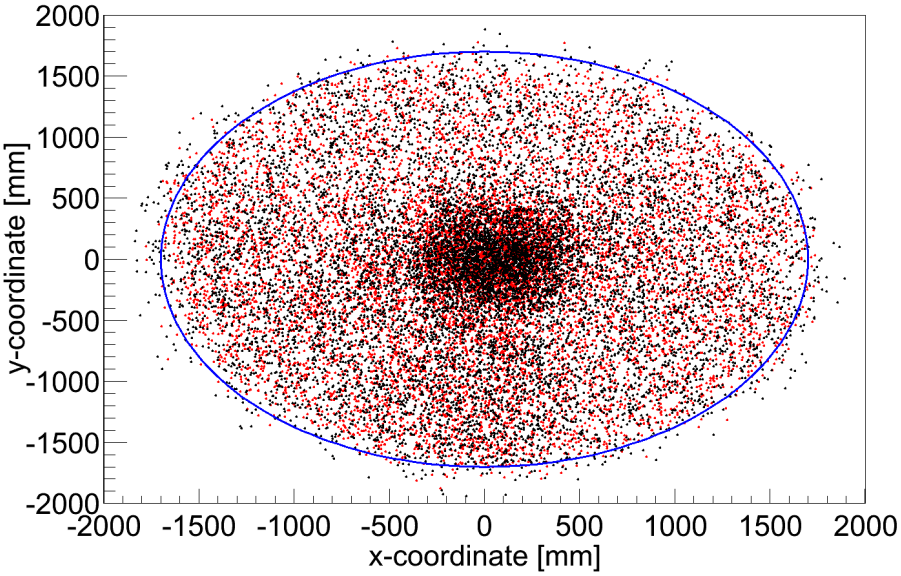

Figure 8.15: *xy-projection of the reconstructed event vertices of the BiPo-214 coincidences for events above the Target vessel top lid. The vertices of the prompt events are depicted in red, the vertices of the delayed events in black. The blue ellipse indicates the position of the GammaCatcher acrylic vessel. The excess of BiPo-214 events in the middle is still seen, depicting events close to the chimney which might be due to the higher rate of external gamma rays there.*

The excess on top can be explained by the absence of any steel shielding here (the steel shield has a hole for the chimney feed-through), which allows external gamma rays to enter the detector and increase the background there. Fig. 8.15 shows a xy-distribution, but only for events with vertices restricted to z-coordinates greater than 1229 mm, i.e. above the top lid of the Target vessel. This confirms an excess of BiPo-214 events close to the chimney. Besides the excess in the middle no further structures can be seen.

However, not all excess events can be explained with accidental coincidences, which are less in rate. In addition, both the top and the bottom part of the GammaCatcher contain more BiPo-214 events than its sides. To investigate the origin for this, the vertices of BiPo-214 events at the GammaCatcher bottom are shown in fig. 8.16.

The event excess in the middle of the detector is seen again, however, also an aggregation of BiPo-214 events at the positions of the Target vessel feet is observed. This excess causes the GammaCatcher bottom to seemingly contain more BiPo-214 events in fig. 8.14, although their concentration in the liquid is not enhanced. The aggregation of radioimpurity-induced events at the vessel feet could happen for several reasons: firstly, the vertex plots all show the reconstructed event vertices, not the true ones. Therefore, any systematic shifts in the vertex reconstruction might mimic such an event excess, although the true vertices are homogeneously distributed all over the respective liquid. Such a shift could, e.g., be due to optical photons reflected at the acrylic's surfaces of the feet structure and thus leading to falsely reconstructed vertices. However, the reconstructed event vertices from a Monte-Carlo simulation, where the simulated vertices were homogeneously distributed all over the Gam-

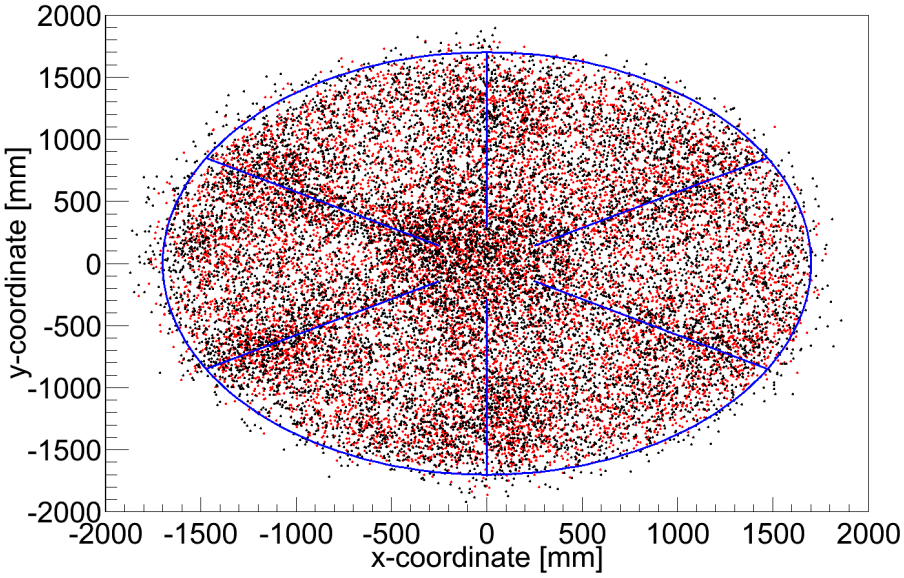

Figure 8.16: *xy-projection of the reconstructed event vertices of the BiPo-214 coincidences for events below the Target vessel bottom lid. The vertices of the prompt events are depicted in red, the vertices of the delayed events in black. The blue ellipse indicates the position of the GammaCatcher acrylic vessel, the blue lines the positions of the Target vessel feet. At the feet positions an excess of BiPo-214 events is seen.*

maCatcher liquid, did not show this aggregation. In addition, for the accidental coincidences (fig. 8.30) also no event aggregation at the feet positions is observed.

Secondly, the acrylic, or one of its components, might be the source of some radon emanation, leading to localised aggregation of BiPo coincidences close to it. At the sidewalls of the acrylic vessels, however, no excess of BiPo-214 events is found (see also fig. 8.17), making radon emanation from the acrylic itself rather unlikely. Fig. 8.17 shows the radial distribution of BiPo-214 coincidences with a z-component of the event vertex which lies between top and bottom lid of the Target vessel. Besides the continuous rise of the event rate towards greater radii (which is expected from volume effects), and the excess of BiPo-214 events in the GammaCatcher liquid over the Target liquid, no further aggregation of event vertices at the position of the walls of the acrylic vessels is observed. Nevertheless, another component of the vessel, like the glue which was used to connect the feet to the vessel, could be the source for impurities. Such an emanation could also explain a part of the observed huge event excess in the top middle of the detector (here, the chimney is glued to the vessel) and the slight excess all over the GammaCatcher top (Target vessel stiffeners).

And thirdly, also radioimpurities from the liquid itself could cause the vertex distributions to be inhomogeneous in case they get adsorbed at the acrylic's surface. As acrylic is an insulator it can get electrically charged (e.g. during the filling process) and, hence, attract any ionic contaminants out of the scintillator. The deposition and subsequent decay of some mother isotope of ^{214}Bi would consequently lead to the aggregation observed. An inhomogeneous electrical charging of the acrylic, or a bigger adsorbing surface at the chimney, the vessel stiffeners and the vessel feet, could be the reason for the non-observation of aggregation

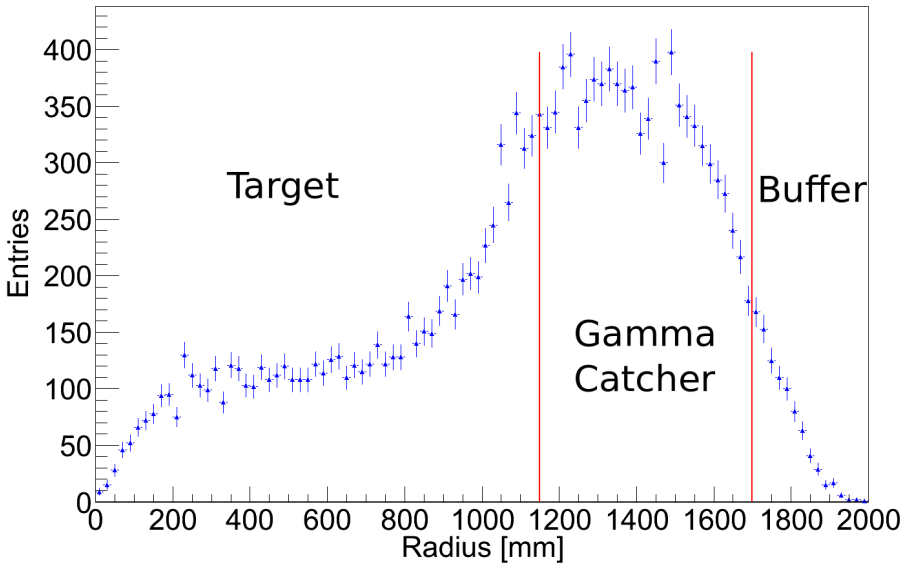

Figure 8.17: *Radial distribution of the BiPo-214 coincidences with a z-component of the event vertex greater than -1229 mm and smaller than 1229 mm (height of the Target vessel), not corrected for any volume effects. The positions of Target vessel wall and GammaCatcher vessel wall, respectively, are indicated by the two red lines. The Target liquid contains much less BiPo-214 events than the GammaCatcher. The rise in the event number close to the Target vessel and within the Buffer volume is due to the spatial resolution of the vertex reconstruction. No aggregation of events at the vessel walls is seen, i.e. a radon emanation by the acrylic itself is unlikely. Error bars are statistical only.*

of BiPo-214 events at both vessel walls.

The vertex distributions of the BiPo-212 events (figs. 8.18 and 8.19), however, show the opposite behaviour: much more events of this class are found in the Target region, only little in the GammaCatcher. As the thorium decay chain (appendix A) contains no long-lived isotopes, the conclusion can directly be drawn that the Target scintillator contains more thorium than the GammaCatcher scintillator. The quite homogeneous distribution of the reconstructed vertices shows that the radioimpurities are mainly contained in the liquid itself, and not, or at least only little, emanated from the acrylic or some other source. This is also shown in fig. 8.20, showing a linear rise of the event number per radius bin (as is expected for a perfectly homogeneous distribution in a cylinder) and a steep drop of the event rate at the Target vessel wall. No indications for an excess of events at the vessel walls are seen, too.

Although the number of BiPo-212 events in the GammaCatcher is quite low resulting in bad statistics, the same cumulative effect at the positions of the Target vessel feet as for the BiPo-214 coincidences can be seen (fig. 8.21), most likely for the same reasons as discussed above.

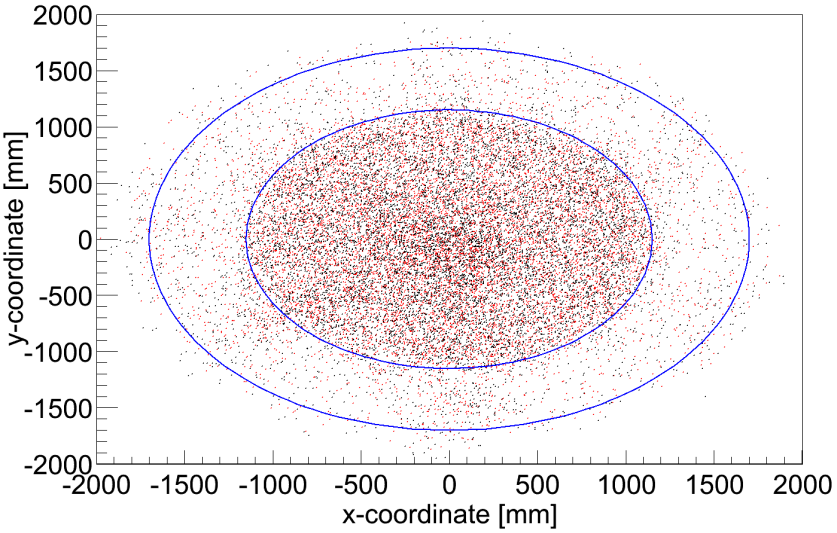

Figure 8.18: *xy-projection of the reconstructed event vertices of the BiPo-212 coincidences. The vertices of the prompt events are depicted in red, the vertices of the delayed events in black. The blue ellipses indicate the positions of the Target and GammaCatcher acrylic vessels, respectively. Unlike the BiPo-214 coincidences most of the events are located in the Target region; only little events are found in the GammaCatcher. The homogeneous vertex distribution indicates that the impurities are contained within the liquid itself.*

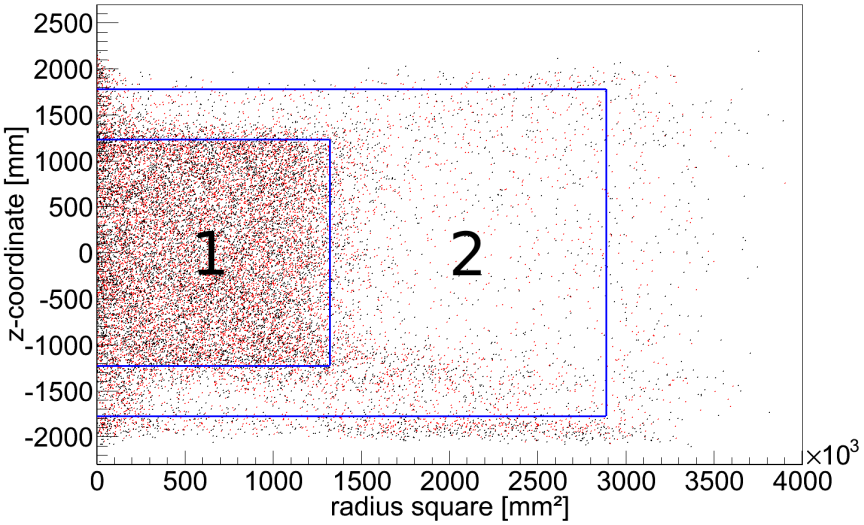

Figure 8.19: *rz-projection of the reconstructed event vertices of the BiPo-212 coincidences. The vertices of the prompt events are depicted in red, the vertices of the delayed events in black. The abscissa is scaled quadratically to correct the vertex density for volume effects. The blue lines indicate the positions of the Target and GammaCatcher acrylic vessels, respectively. Again, the higher concentration of thorium in the Target (1) than in the GammaCatcher (2) can be seen.*

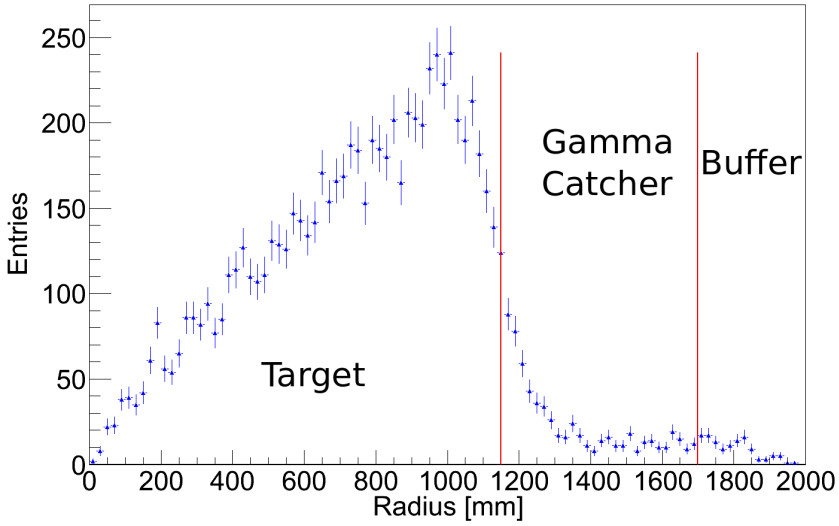

Figure 8.20: *Radial distribution of the BiPo-212 coincidences with a z-component of the event vertex greater than -1229 mm and smaller than 1229 mm (height of the Target vessel), not corrected for any volume effects. The positions of Target vessel wall and GammaCatcher vessel wall, respectively, are indicated by the two red lines. The linear rise of the event number in the Target region is expected for a cylindrically shaped volume. Obviously, the Target contains much more thorium than the GammaCatcher; no event excess at the positions of the vessel walls is seen, too. Error bars are statistical only.*

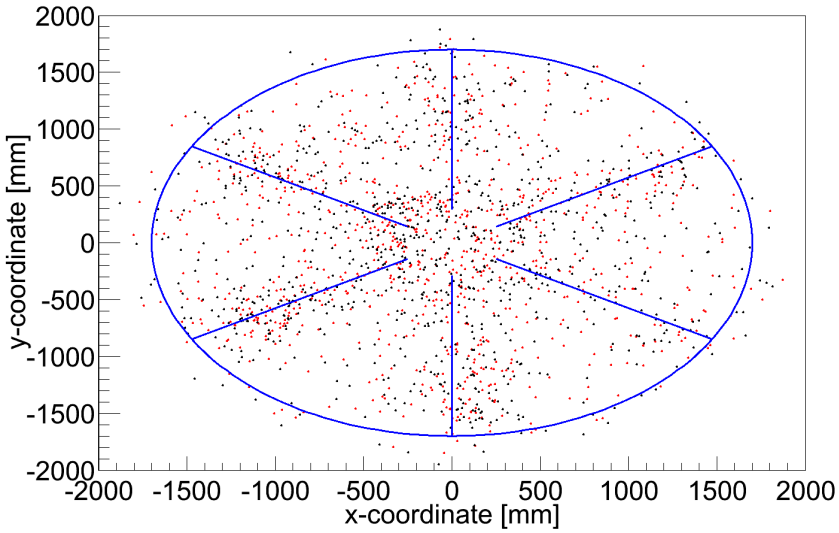

Figure 8.21: *xy-projection of the reconstructed event vertices of the BiPo-212 coincidences for events below the Target vessel bottom lid. The vertices of the prompt events are depicted in red, the vertices of the delayed events in black. The blue ellipse indicates the position of the GammaCatcher acrylic vessel, the blue lines the positions of the Target vessel feet. As for the BiPo-214 coincidences an excess of events is seen at the positions of the vessel feet, however, with much less statistics.*

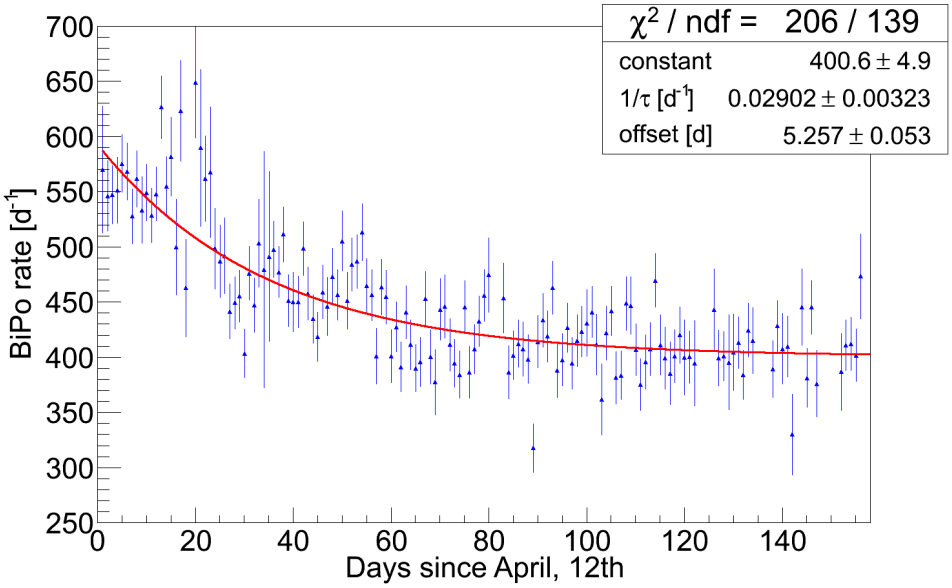

Figure 8.22: *Daily rate of the BiPo-214 coincidences (blue data points), fitted with an exponential function plus a constant (red line). In the beginning the rate drops with a time constant τ of ~ 34 days; after day ~ 100 it becomes stable at a level of 401 ± 5 events per day. The dropping event rate is not understood yet, but needs to be assigned to some process changing the BiPo-214 concentration in the detector, as the obtained life time of ~ 34 days does not match at all the life time of any mother isotope of ^{214}Bi. Error bars are statistical only.*

8.2.6 Rate of the BiPo Coincidences

A key question in the context of BiPo coincidences is the daily rate of events, as this directly provides information on possible changes in the amount of radioimpurities in the detector. Especially for the BiPo-214 coincidences, which are following the decays of ^{222}Rn, indications for air leaks or radon emanations could be found. In addition, in case the radioactive decay chains are not fully in equilibrium, the BiPo rate changes with time, possibly providing information on which mother isotope has an enhanced concentration in the detector. Figs. 8.22 and 8.23 depict the number of BiPo events found on a day-by-day basis, starting from April 12$^{\text{th}}$.

While the rate of BiPo-212 events is rather stable, indicating radioactive equilibrium in the thorium chain and the absence of any sources for this isotope, the rate of BiPo-214 events slowly drops over time at the beginning with a time constant of ~ 34 days (obtained by a single exponential fit to the data); after day ~ 100 it becomes stable. The time constant, however, does not correspond to any half-life of a mother isotope of ^{214}Bi at all. Therefore, it needs to be conditioned by the time constant of some feeding process of a short-lived mother isotope of ^{214}Bi. This could be, for example, radon diffusion into the detector or the radon emanation of some component of the acrylic. The stable rates of both the BiPo-212 coincidences (fig. 8.23) and the accidental BiPo-214 coincidences (see below; fig. 8.27) over time indicate that the dropping rate of the BiPo-214 coincidences is not caused by any detector related feature

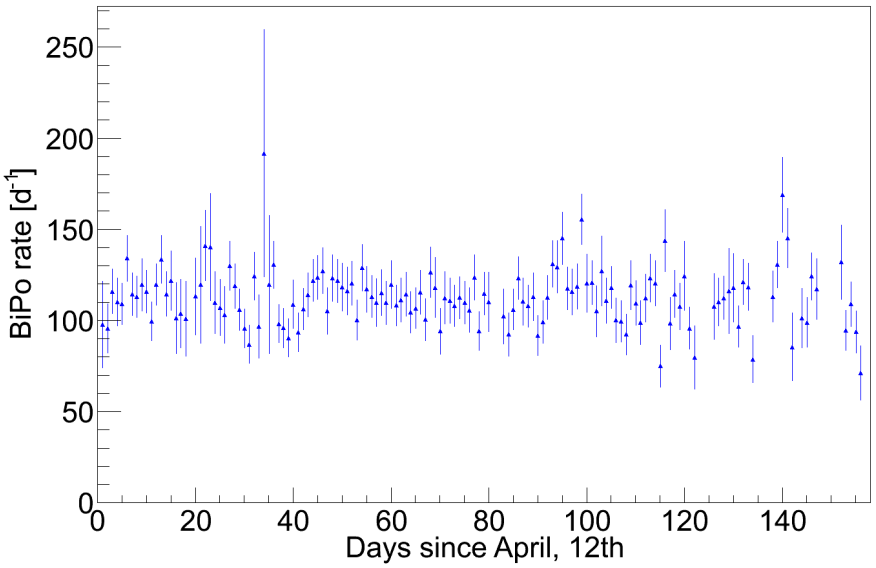

Figure 8.23: *Daily rate of the BiPo-212 coincidences. The rate is stable over the time analysed, indicating no sources for thorium insertion into the detector. Error bars are statistical only.*

like instrumental light. The stable rate at the end indicates that radioactive equilibrium is reached for the uranium decay chain (at least up to ^{226}Ra with 1600 years half-life), and that no further mother isotopes of ^{214}Bi (like ^{222}Ra) are introduced into the detector.

8.2.7 Detector Stability Obtained from the α-Peaks

Besides the daily rate also the peak position of the α-peaks can be monitored over time. This yields information on the stability of the detector in the regime of small visible energies, particularly the light yield of the liquid scintillator. Fig. 8.24 shows the peak position of the ^{214}Po α-peak in the Target scintillator as a function of time.

The fitted peak position of the α-peak stays constant over time; the slope of a linear fit to the data is very small and nearly compatible with zero within its error bars. Hence, the light yield of the scintillator is stable, which could also be confirmed for the first period of data taking by other methods, e.g. fitting the neutron capture peaks of hydrogen and gadolinium [Abe12a]. A stable detector is mandatory for the reactor antineutrino analysis, as a diminishing light yield would constantly decrease the detector's efficiency, and by this the measured antineutrino rate. In addition, also the measured positron spectrum would be distorted.

A stable position of the ^{214}Po α-peak indicates both the absence of chemical impurities like oxygen in the detector, which would cause the number of photons produced per unit energy of the incident particle to decrease by chemical degradation, as well as the absence of dissolving impurities in the detector's liquids (including the Buffer liquid), which would shorten the attenuation lengths and increase absorption for the scintillation light.

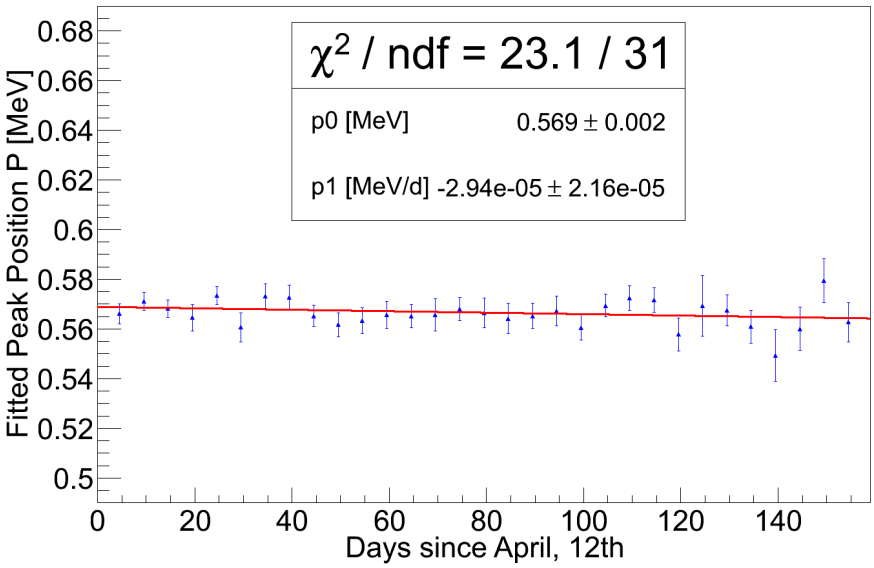

Figure 8.24: *Fitted peak position P of the ^{214}Po α-peak in the Target scintillator as a function of time, each data point is averaged over 5 days of data taking. A linear fit to the data, P = p0 + p1·t, including its fit parameters is shown, too, indicating a stable detector performance over time. Error bars are statistical only.*

8.2.8 Determination of the Accidental Background in the BiPo Data Sample

Not only true BiPo coincidences pass the selection cuts applied to the data (tab. 8.2), but also some background events. As is shown in fig. 8.11 the time difference distributions both for BiPo-214 and BiPo-212 events yield nearly perfectly the expected values for the half-lives of the respective polonium isotopes. Hence, most of the background still contained in the data sample is either uncorrelated in time (accidental coincidences) or, at least, has a time constant much larger than the respective BiPo coincidence (as is the case of BiPo-214 events in the BiPo-212 sample), which prevents the time difference distributions from being spoiled. This also excludes big contributions from correlated background, like particles recoiling off twice in the detector. Therefore, in the following the total background to the BiPo-analysis is assumed to be accidental, except for the BiPo-214 events in the BiPo-212 data sample.

Accidental background cannot be tagged on an event-by-event basis. However, its rate can be determined in a dedicated analysis and statistically subtracted from the BiPo sample later-on. For the determination of the accidental coincidences three different methods are used in the present analysis:

1. Fitting the distribution of the time difference between prompt and delayed event with an exponential (describing the data correlated in time) plus a constant (describing the uncorrelated data like the accidental coincidences). Hence, the constant yields the number of accidental coincidences per time bin, from which the total number of accidentals can be easily calculated. In case of the BiPo-214 coincidences this method delivers a rather good estimate for the number of accidental background events. However, for the

BiPo-212 coincidences, remaining BiPo-214 events have to be subtracted statistically. The latter enter the BiPo-212 sample as the energy cuts for both the prompt event (β^--decay of ^{212}Bi) and delayed event (α-decay of ^{212}Po) have a rather high acceptance for the decays of ^{214}Bi and ^{214}Po, respectively. This makes a correction necessary, introducing a large uncertainty.

2. Shifting the time window for the coincidences search backwards by 2 ms, i.e. the time differences of the delayed event with respect to the prompt event have to be in a window of [2006; 4000] µs in the case of BiPo-214, or [2000.5; 2005] µs in the case of BiPo-212. Any correlated events are cut out by this method, only accidental coincidences survive. As the shifted time windows have the same lengths as the not-shifted ones, the number of accidental coincidences is determined directly. Besides the shift of the time window, no other selection cut (tab. 8.2) is changed. With this method also the energy spectra of background events are determined which are subtracted statistically from the energy spectra of ^{214}Bi- and ^{214}Po-events (see sec. 8.2.2).

3. Shifting the window for the spatial coincidences search: after a valid prompt event is found its vertex is "mirrored" in the detector, i.e. the sign of its x-, y-, and z-coordinates is changed, and delayed events are looked for in the vicinity (50 cm radius) of this new position. Vertices of prompt events within a sphere of 50 cm radius around the detector's origin (0, 0, 0) are rejected, all other selection cuts for the BiPo search stay unaffected. This method excludes all spatially correlated events, and thus also allows a direct determination of the number of accidental coincidences. As was already deduced above more than 99.7% of all correlated events with zero physical displacement between prompt and delayed event have reconstructed vertices within the 50 cm radius; the remaining 0.3% are negligibly small. However, this method only works well for a homogeneous distribution of the event vertices of accidental BiPo coincidences. In case this distribution has cumulations the method with the spatially displaced window fails, as it gives too small a number of accidental coincidences. Unless the homogeneity of accidental coincidences is granted this method is the least reliable one.

In the following the results of the three methods of determining the accidental background are presented.

1. The calculation of the number of accidentals from the tail of the time difference distribution yields (9428.8 ± 152.8) accidental coincidences in the BiPo-214 sample, and (1272.0 ± 59.3) accidental coincidences in the BiPo-212 sample (see tab. 8.5 on page 120). However, the BiPo-212 data also contains BiPo-214 events (due to the overlapping energy windows), which appear in the "constant" of the fit to the time difference distribution and have to be subtracted. From the number of BiPo-214 coincidences found this number is calculated to be (750 ± 36), hence, the total number of accidental BiPo-212-like coincidences found in this analysis is (522 ± 95). Compared to the other two methods of determining the accidental background of the BiPo-212 coincidences (see below and tab. 8.5) the latter number is quite high. However, lots of corrections like the cut efficiencies of the BiPo-212 cuts for BiPo-214 events have to be applied here, while for example the offtime-window methods provides a rather clean background sample. In principle, also a sum of two exponential functions plus a constant could be fitted to the data, however, the half-life of ^{214}Po is much longer than the time window for the BiPo-212 search, causing such a fit not to converge. In

the following, the number of accidental BiPo-212 coincidences calculated from the tail of the time difference is not used for any further calculations.

2. The search for accidental BiPo coincidences with the offtime-window method yields a rather clean sample of uncorrelated events, both in space and time: the distribution of time differences between prompt and delayed event is flat (fig. 8.25). This can be seen even in the case of BiPo-212-like coincidences, although the number of events obtained is very small. The spatial displacement distribution (fig. 8.26) of BiPo-214-like coincidences rises like ϱ^2 as expected for an uncorrelated sample; the number of BiPo-212-like events is too small to draw any conclusions, hence, no plot is shown here.

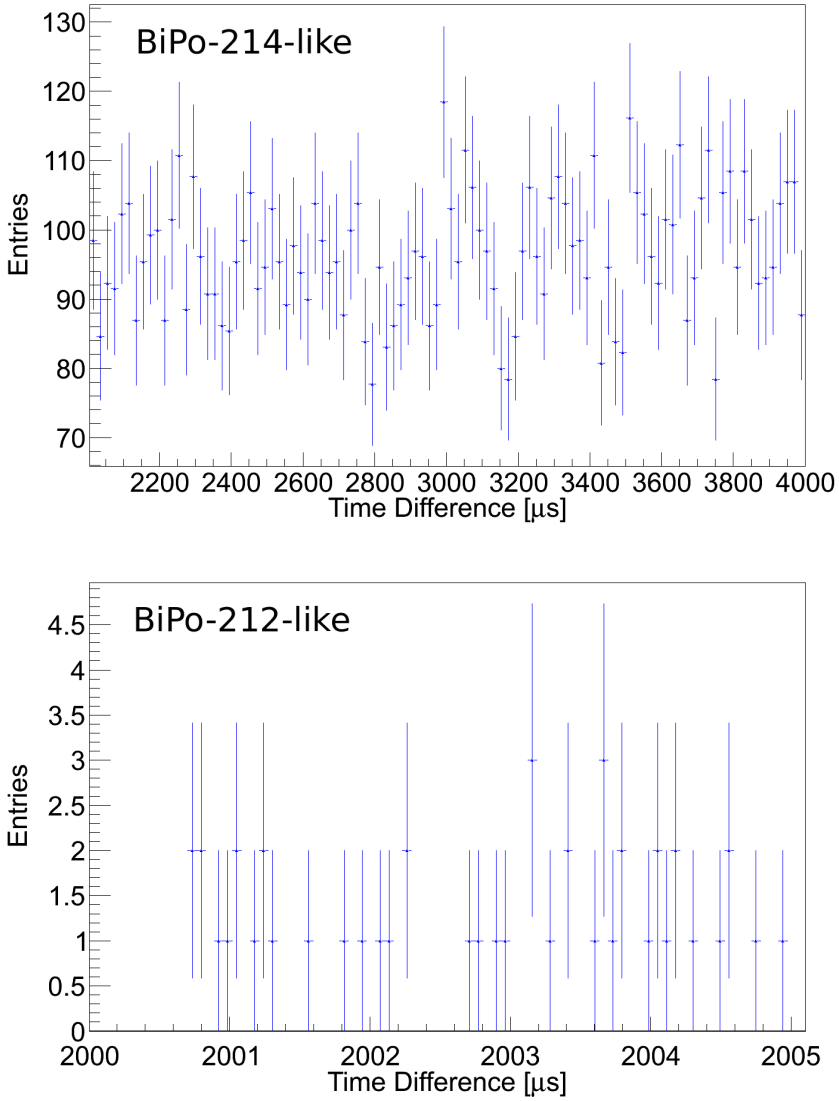

Figure 8.25: *Time difference between prompt and delayed event for the BiPo candidates in the offtime-window search. Top panel: BiPo-214-like events; bottom panel: BiPo-212-like events. In both cases no correlation in time between the two events can be seen, i.e. the distributions are flat. Error bars are statistical only.*

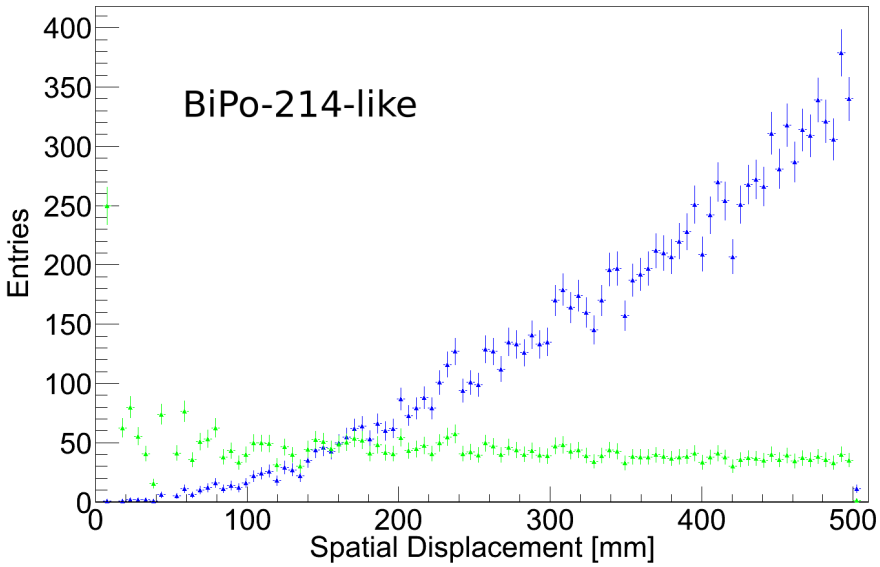

Figure 8.26: *Spatial displacement between prompt and delayed event for the BiPo-214 candidates in the offtime-window search. The data (blue) rises like ϱ^2 as is expected for a perfectly uncorrelated sample. The green data depicts the blue data corrected for volume effects, and is found to be flat. Error bars are statistical only.*

The number of accidental coincidences found with this method is (9632 ± 98) for BiPo-214 and (48 ± 7) for BiPo-212. While the latter number is too small to draw any unambiguous conclusions on the vertex distribution or the daily rate, the BiPo-214-like accidentals allow such studies. As is expected from the stability of the BiPo rates, showing a nearly constant level of radioactivity in the detector, also the rate of accidental coincidences, which are also mainly caused by radioactivity-induced events, is stable over time; fig. 8.27.

Interesting in that context is the vertex distribution of the accidental coincidences: a huge fraction of events of this class resides close to the chimney; figs. 8.28 and 8.29. This indicates that the singles rate is high (above-average) there, too, which is due to the missing top shielding in the middle of the detector. Therefore, external gamma rays can easily enter the detector there, raising the rate of single events and thus of accidental BiPo coincidences. The hole in the shielding is needed for the feed-through of the chimney to the glove-box above the detector for source deployment. The aggregation of accidental BiPo coincidences is, in addition, a reason for the excess of BiPo-214 events close to the chimney.

But also in the bottom (middle) of the GammaCatcher volume an event excess is found (fig. 8.30), which is most likely due to the radioactivity of the pressure sensor located there. The two streams seen in the vertex distribution of the accidental BiPo-214 coincidences on top and on bottom of the GammaCatcher (fig. 8.29) cannot easily be assigned to any source of radioactivity (neither external nor internal). These events might be caused by instrumental light not rejected by the quality cuts applied to the data.

Unlike the true BiPo-214 events, which are clustered at the position of the Target vessel feet, no such aggregation can be observed for the accidental coincidences (fig. 8.30). From that two conclusions are drawn: firstly, any event aggregation at the vessel feet is not caused

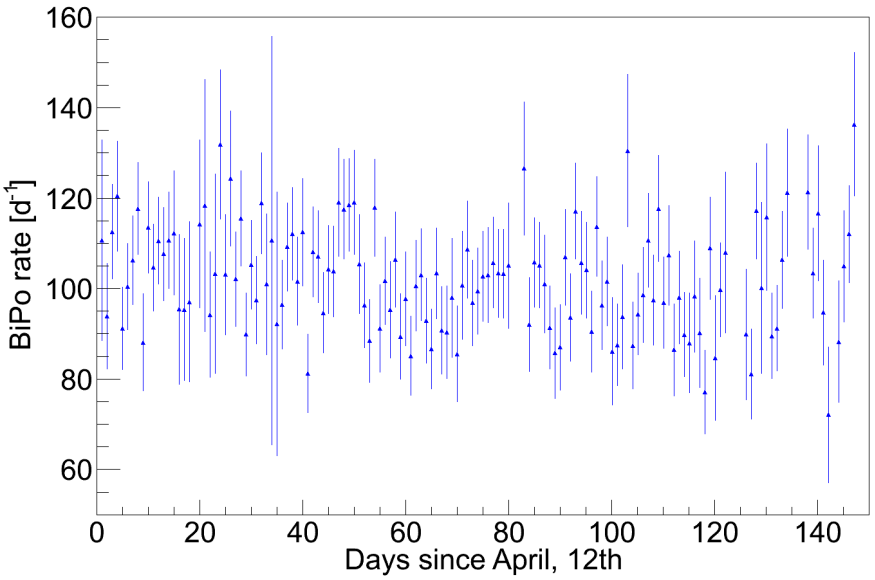

Figure 8.27: *Daily rate of the BiPo-214-like events found in the analysis with the offtime coincidence window. The rate is stable over time, indicating a constant level of radioactivity in the detector, the main source for accidental BiPo coincidences, and a stable detector performance. Error bars are statistical only.*

by the vertex reconstruction algorithm, as the same reconstruction is used in all cases. And secondly, the source of the accidental coincidences is either not aggregated at the acrylic feet at all, or its event vertices are smeared out. The latter would be the case if the accidental BiPo coincidences are caused to a great extend by gamma radiation, which has a non-negligible mean free path in the liquid, causing the point of scintillation light production to be displaced from the point of gamma production.

3. With the third method, the accidentals search with the displaced spatial coincidence window, in total (9343 ± 97) accidental BiPo-214 coincidences and (71 ± 8) accidental BiPo-212 events are found. However, as was already discussed above, these numbers could be too low in case of an inhomogeneous distribution of the event vertices of the accidental coincidences. For the BiPo-214 coincidences the latter is the case, and the resulting number of accidental coincidences is indeed slightly lower than the number obtained with the other two methods, but still in good agreement. For BiPo-212 coincidences, however, the vertex distribution especially in the Target region is rather homogeneous and the number of accidental coincidences obtained with the displaced spatial coincidence window is consequently quite reliable. For all events found with this method also no correlation in time is found, indicating a very clean sample, and the daily rate of the BiPo-214 accidental coincidences[12] found in this analysis is stable over time, too. However, especially due to the possible bias of this method of the spatial distribution of the event vertices the results on the number of accidental coincidences obtained with the displaced window is not used for further calculations.

Table 8.5 lists again the results of the three methods to determine the accidental back-

[12] Again, the number of BiPo-212 accidental coincidences is too low (less than one per day on average) to allow conclusions on the daily rate.

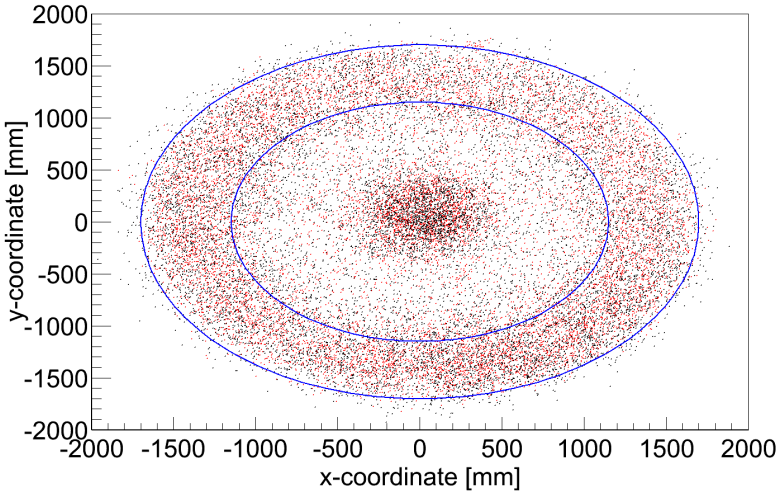

Figure 8.28: *xy-projection of the event vertices (black: delayed events, red: prompt events) of the accidental BiPo-214 coincidences found in the offtime-window analysis. The blue ellipses indicate the positions of Target and GammaCatcher acrylic vessel. Most of the vertices are located in the middle close to the chimney. There, no shielding against external radiation is present, which causes the singles rate and with it the BiPo-like coincidences to increase. Like for the true BiPo-214 coincidences more events are found in the GammaCatcher than in the Target, indicating a slightly higher rate of radioactivity-induced events there.*

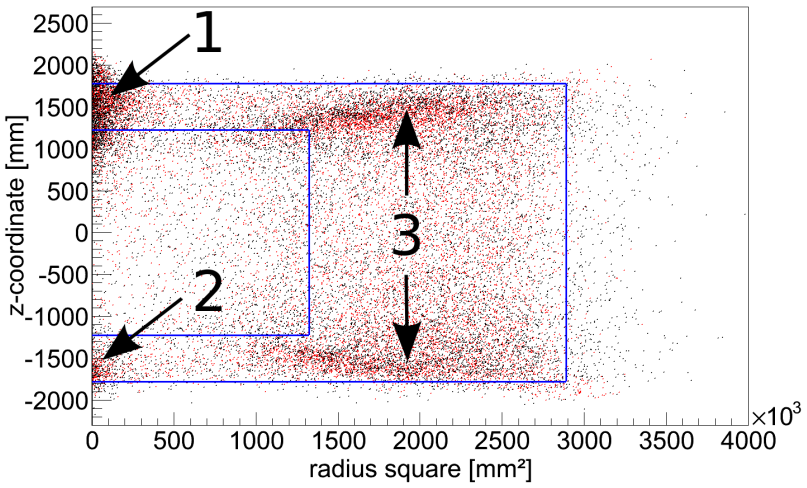

Figure 8.29: *rz- distribution of the event vertices (black: delayed events, red: prompt events) of the accidental BiPo-214 coincidences found in the offtime-window analysis. The blue lines indicate the acrylic vessels of Target and GammaCatcher, respectively. Again, most of the events are located close to the chimney (1) because of the above-average high singles rate there. The event excess due to radioactivity from the pressure sensor (2) can be seen, too, in the middle of the GammaCatcher bottom. The two vertex clusters on top and bottom of the GammaCatcher volume (3) cannot be easily attributed to a source of radioactivity, but are likely caused by residual instrumental light.*

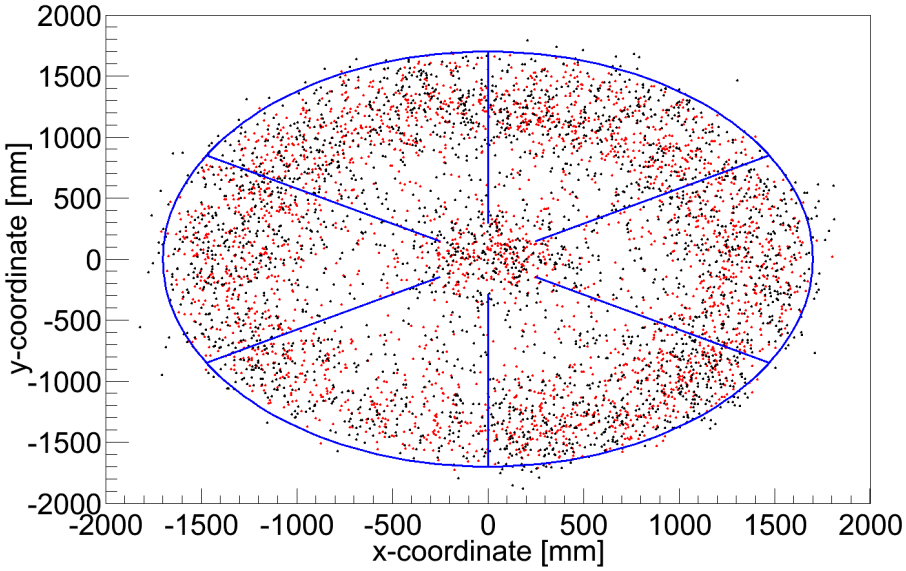

Figure 8.30: *xy-projection of the event vertices of the accidental BiPo-214 coincidences found in the offtime window search at the GammaCatcher bottom. Prompt events are depicted in red, delayed events in black. The GammaCatcher vessel is indicated by the blue ellipse, the Target vessel feet by the blue straight lines. No aggregation at the feet positions can be seen for the accidental coincidences. However, the event aggregation due to the pressure sensor in the middle is clearly visible.*

ground. The most reliable method, i.e. the method with least corrections to be applied and which is not affected by inhomogeneities, is the offtime-window search for accidental coincidences. Therefore, in the following all calculations will be performed using the results of this method.

8.2.9 Concentration of Radioimpurities in the Double Chooz Far Detector

Given the numbers for the BiPo coincidences found (tab. 8.5) the concentrations of uranium (assuming radioactive equilibrium) and thorium in the Double Chooz far detector can be calculated, analogously to equation (7.8) in sec. 7.1.3. The number of accidental events found with the offtime-window search (the only method to determine the background where no corrections have to be applied) is therefor subtracted from the number of coincidences found in total. The number of all BiPo coincidences N_{bipo} happening in the detector is then calculated by taking into account the (lower) cut efficiencies determined above (tab. 8.3). The resulting number thus represents the upper limit for the number of BiPo coincidences in the data sample and is finally converted into a mass concentration c of uranium and thorium, respectively, by dividing by the detector liquid's mass m and the live time t of the analysis[13],

[13]This division assumes a constant rate of BiPo coincidences over the measuring time. This does not hold for BiPo-214 (see above), as this rate drops in the time analysed. However, calculating an average BiPo-214 rate over the time analysed, and from that the uranium concentration, gives a slightly too big mass concentration and can therefore be regarded as a conservative approach. The final mass concentrations calculated represent upper limits in that sense.

	all events	tail of Δt	offtime window	displaced window
BiPo-214	42182 $\pm$ 205	9428.8 $\pm$ 152.8	9632 $\pm$ 98	9343 $\pm$ 97
BiPo-212	10659 $\pm$ 103	522 $\pm$ 95	48 $\pm$ 7	71 $\pm$ 8

Table 8.5: *Number of accidental BiPo coincidences found in the three different analyses: constant fit to the tail of the time-difference distribution, search with the offtime-window, and search with the spatially displaced coincidence window. The number of BiPo-212 accidental coincidences from the fit to Δt is corrected for BiPo-214 events (see text). The total number of all BiPo coincidences found is quoted, too. Especially in case of the BiPo-212 coincidences the signal-to-background-ratio is very high (> 200); in case of BiPo-214 it is still about 4.4.*

and multiplying with the molar mass M and the life time τ of ^{238}U and ^{232}Th, respectively:

$$c = \frac{N_{bipo} \cdot M \cdot \tau}{m \cdot t} \quad . \tag{8.4}$$

This calculation assumes radioactive equilibrium, i.e. the activity of uranium and thorium, respectively, is taken to be equal to the activity of the corresponding bismuth isotopes. As the half-lives of both U and Th are much longer than the measuring time, the activity is simply calculated by dividing the number of decays by the measuring time.

The resulting mass concentrations are $(1.71 \pm 0.08) \cdot 10^{-14} \frac{g}{g}$ for uranium and $(8.16 \pm 0.49) \cdot 10^{-14} \frac{g}{g}$ for thorium (corrected for BiPo-214 events). Both values are far below the design goal[14] of $2 \cdot 10^{-13} \frac{g}{g}$ for Double Chooz [Ard06], indicating the high level of radiopurity reached. However, as was shown above, the concentrations of radioimpurities are not equal for Target and GammaCatcher, therefore, they have been calculated for the respective volumes separately, too (tab. 8.6).

In the Double Chooz far detector the uranium concentration is dominated by its presence in the GammaCatcher liquid. As the GammaCatcher fiducial volume cut ($145\,\text{cm} < \rho$ unified with $152.9\,\text{cm} < |z|$) excludes not only the Target and the surrounding 30 cm, but also to a great extend the BiPo-214 events aggregated in the middle of the top of the GammaCatcher, the mass concentration obtained only for the GammaCatcher is below the concentration derived from an analysis of the full inner detector.

Thorium on the other hand is much more prominently present in the Target. This could be assigned to gadolinium-doping of this scintillator, which might have introduced some additional thorium.

Summing up, the concentrations of uranium and thorium in the Target and the GammaCatcher are in sum $9.87 \cdot 10^{-14} \frac{g}{g}$ and thus far below the desired $4 \cdot 10^{-13} \frac{g}{g}$. Only the thorium content of the Target is found to be above $10^{-13} \frac{g}{g}$, which is, however, no problem at all, as the sum of all concentrations, and by this the rate of singles events, is far below the

[14] The design goal is calculated from the requirement of Double Chooz not to have more than ~ 0.8 accidental antineutrino events per day [Ard06].

	all	Target	GammaCatcher
Uranium	1.71 ± 0.08	0.52 ± 0.04	1.41 ± 0.08
Thorium	8.16 ± 0.49	21.1 ± 1.4	1.86 ± 0.12

Table 8.6: *Mass concentrations of uranium (obtained from the BiPo-214 analysis under the assumption of radioactive equilibrium and a constant BiPo rate over time) and thorium (BiPo-212; corrected for BiPo-214 coincidences still present in the BiPo-212 data sample) in the Double Chooz far detector in units of $10^{-14}\,\frac{g}{g}$. The concentrations for the single active volumes of the inner detector, Target and GammaCatcher, are calculated separately, too. The design goal of Double Chooz not to have more than $4{\cdot}10^{-13}\,\frac{g}{g}$ for both isotopes in sum is matched well.*

intended goal. As a result of the BiPo coincidences studies the inner active parts of the Double Chooz far detector prove to be very clean in terms of radioimpurities, which also causes the rate of accidental antineutrino-like events to be a factor of three better than originally intended, $(0.261 \pm 0.002)\,\mathrm{d}^{-1}$ [Abe12a] instead of 0.8 per day [Ard06].

8.3 The Po-210 Background: (α,n)-Reactions

In ch. 6 the possible sources of background to the Inverse Beta Decay (IBD) have been given. Besides the accidental coincidences, radioactivity in the detector possibly also induces correlated background via (α,n)-reactions (sec. 6.2.4). From the experience of the reactor neutrino experiment KamLAND [Abe08] it is known that this kind of background is dominantly induced by decays of the α-emitter ^{210}Po.

^{210}Po is one of the daughter isotopes of ^{214}Bi and part of the uranium decay chain. Therefore, the amount of uranium quoted in tab. 8.6 together with the known cross-section for the reaction $^{13}\mathrm{C}(\alpha,\mathrm{n})^{16}\mathrm{O}$ can be used to calculate the daily rate of background events[15]. This is carried out for the Target and the GammaCatcher region separately; the results are summarised in tab. 8.7.

Daily rate of (α,n)-reactions	
Target	$(1.5 \pm 0.3){\cdot}10^{-6}$
GammaCatcher	$< (8.8 \pm 1.9){\cdot}10^{-6}$

Table 8.7: *Calculated daily rate of fake IBD events due to (α,n)-reactions on ^{13}C induced by the α-emitter ^{210}Po in the Double Chooz far detector. The uranium chain was assumed to be in radioactive equilibrium; the number of events was determined by scaling the (α,n)-results of KamLAND [Abe08] to the mass and radiopurity of Double Chooz. The number quoted for the GammaCatcher is only an upper limit, as by far not all produced neutrons reach the Target region.*

[15] Carbon-13 has a natural abundance of 1.07% and is therefore omnipresent in the liquid scintillator.

Both the background rates due to (α,n)-reactions in Target and GammaCatcher are extremely small (less than $10^{-5}\,\mathrm{d}^{-1}$) compared to the reactor antineutrino signal, hence, this kind of background does not play a significant role in the case of Double Chooz. For the far detector the signal (reactor antineutrinos) to background ((α,n)-reactions) ratio exceeds $4{\cdot}10^6$, even under the assumption that all fast neutrons produced by the (α,n)-reactions in the GammaCatcher enter the Target region and get captured on gadolinium, thus mimicking an IBD event.

However, in the decay chain between ^{214}Po and ^{210}Po one long-lived isotope is present, ^{210}Pb with a half-life of 22.3 a [Fir96]. There, the radioactive equilibrium could be broken, e.g. due to some processes during the preparation of the detector liquids or the filling. To check for equilibrium the detector raw data was analysed for the α-peak of ^{210}Po directly. The α-energy of the decay of ^{210}Po is 5.305 MeV [Fir96], and the quenching factors measured in the laboratory for this α-energy are 13.1 ± 0.2 for the Target scintillator and 17.4 ± 0.5 for the GammaCatcher scintillator, respectively [Abe11a]. Hence, the ^{210}Po α-peak is expected at $\sim$405 keV in the Target and at $\sim$305 keV in the GammaCatcher. These energies, however, are so low that the trigger efficiency of the detector is already significantly below 100% (fig. 8.7). This effect is taken into account by dividing the singles spectrum obtained at low energies by the trigger efficiency curve. The resulting spectrum for GammaCatcher events is shown in fig. 8.31.

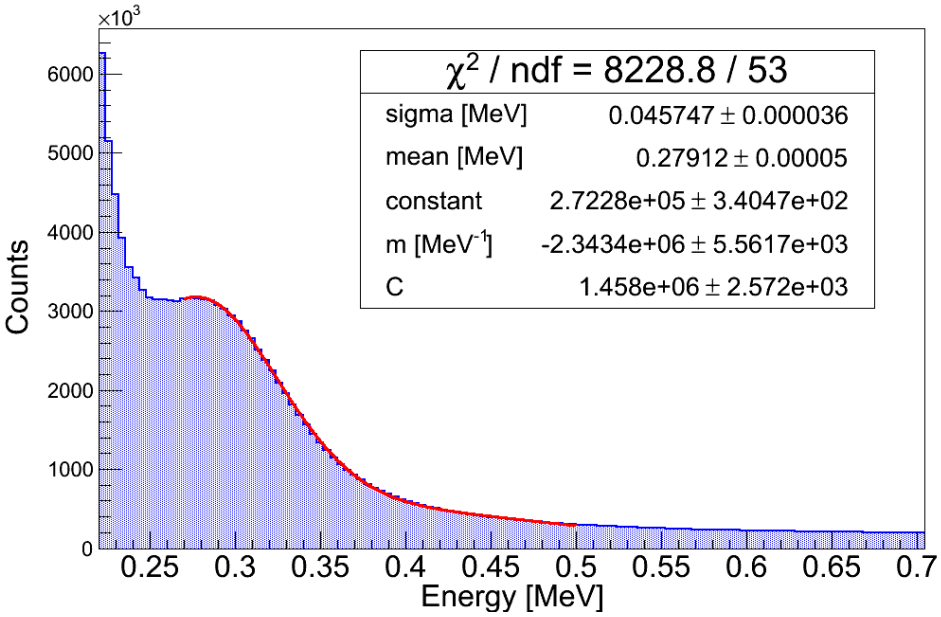

Figure 8.31: *Singles spectrum at low energies (0.22 MeV to 0.7 MeV) divided by the trigger efficiency curve (fig. 8.7) for GammaCatcher events only. The ^{210}Po α-peak is expected at $\sim$ 305 keV. The data is fitted with a Gaussian plus a straight line (m·E + C) representing the background. The best-fit values for the Gaussian are quoted, too. Its mean position is found at 0.279 MeV, its width is (45.75 ± 0.04) keV. The parameter denoted by "constant" is simply a scaling parameter and without any particular physical meaning. A peak structure which could stem from the ^{210}Po α-decay is found at 279 keV.*

Both for the Target and the GammaCatcher the α-peak of ^{210}Po can be fitted with a Gaussian plus a straight line (y = m·E + C), which is approximating the underlying continuous background. The fitted mean positions of the Gaussians are 345.2 keV for the Target and 279.1 keV for the GammaCatcher. Taking into account the systematic uncertainty of the trigger efficiency (see fig. 8.7) the quenching factors obtained from these fit values are (15.4 ± 1.3) for the Target and (19.0 ± 1.1) for the GammaCatcher, respectively. Both values are higher than the quenching factors obtained from the laboratory measurement, however, still in agreement due to the big errors. These big errors are mainly introduced by the rather big errors of the trigger efficiency curve (fig. 8.7), while the fitted peak positions of the Gaussians are very precisely determined, see inset in fig. 8.31.

The peak area of the fitted Gaussian distributions yields information on the rate of ^{210}Po-decays in the respective detector volumes. Assuming that all events in the corresponding Gaussian peak stem from the α-decay of ^{210}Po, (α,n)-background rates of $(1.47 \pm 0.25) \cdot 10^{-2}\,\mathrm{d}^{-1}$ for the Target and $(4.50 \pm 0.72) \cdot 10^{-2}\,\mathrm{d}^{-1}$ for the GammaCatcher are found. Both rates are still not a problem for the antineutrino measurement in Double Chooz, as they are much lower than the signal's rate: on average, Double Chooz measures ~ 40 electron antineutrinos from the reactor per day [Abe12], which translates into a signal-to-background-ratio of more than 1000. In addition, not all neutrons from the GammaCatcher reach the Target, thus this value is again only an upper limit.

However, the background rates obtained from the data differ significantly from the rates calculated from the BiPo-214 results. This could have two different reasons: either the radioactive equilibrium is indeed broken, and the detector contains much more ^{210}Po than expected from the BiPo-214 coincidences, or the peaks seen at low energies in the singles spectra do not stem from the α-decay of ^{210}Po, but have a different origin (e.g. an artefact from the division by the trigger efficiency curve). Besides these peaks no further α-peaks are seen in the energy spectra, although the decay chains of uranium and thorium contain lots of α-emitting isotopes (see appendix A). However, this does not allow a discrimination between the two hypotheses, but again emphasizes the much higher rate in the observed peak than in any other α-decay channel. The only method to really prove or refuse one of the hypotheses would be pulse shape discrimination, a future upgrade of the presented analysis [Jol12, Wag12].

8.4 First Results of Double Chooz on the Measurement of ϑ_{13}

In November 2011, Double Chooz was the first reactor neutrino experiment that published an indication for a non-zero value of the third mixing angle [Abe12]. In June 2012, an improved analysis has been presented by the collaboration [Abe12a], based on ~ 228 live days of data. The results of this analysis will be summarised in brief in this section. All data were obtained with the far detector only, as the near detector is not finished yet. Therefore, the reactor electron antineutrino spectrum of the two cores of the Chooz nuclear power plant was not directly measured, but calculated implying the MURE[16] [MUR12] and DRAGON [DRA12] reactor codes for calculating the reactor evolution. These calculations are based on the antineutrino spectra of ^{235}U, ^{239}Pu, and ^{241}Pu as measured at the ILL [Fei82, Hah89, Sch85], and the ab-initio calculated spectrum[17] of ^{238}U [Mue11], and include all relevant effects, e.g.

[16] **M**CNP **U**tility for **R**eactor **E**volution

[17] Results on the measurement of this spectrum will be published soon [Haa12].

burnup. However, the predicted spectrum was normalised to the antineutrino spectrum of the Bugey4 reactors, which are identical to the Chooz reactors. In this way, the reactor antineutrino anomaly reported in ch. 1 [Men11] does not affect the obtained results.

In total, the analysis covers a live time of 227.93 days, 88.66 days thereof with one reactor off and 22.5 hours[18] with both reactors off [Abe12a]. This live time already includes the veto times of both the InnerVeto, which triggers with a rate of $\sim 46\,\mathrm{Hz}$, and the OuterVeto, which was running for the last 68.9% of the data [Abe12a]. After each event which is identified as a muon a veto time of 1 ms is applied to the detector. The Double Chooz far detector has a total trigger rate of $\sim 120\,\mathrm{Hz}$ (including instrumental light) [Abe12]; the lower trigger threshold of the inner detector is set to 350 keV. The energy calibration was carried out by using the light injection system, radioactive calibration sources, cosmic muons, and natural radioactivity. The light yield found in these studies is 230 p.e. per MeV and is very stable over the measuring time [Abe12a].

In order to extract the events with a signature of the IBD, the $\bar{\nu}_e$-candidates, five selection cuts are applied to the events triggering the detector:

1. ***Instrumental light cut:*** MQTQ < 0.09 (0.055) for the prompt (delayed) event, and RMS(T_s) < 40 ns for both events (cf. also sec. 8.2.1).

2. ***Energy cut for the prompt event:*** $0.7\,\mathrm{MeV} < E_{prompt} < 12.2\,\mathrm{MeV}$. The lower energy threshold of the prompt events is 1.022 MeV (see sec. 6.1), however, the energy interval between 0.7 MeV and 1 MeV allows for a great reduction of threshold systematics. The upper threshold, on contrast, is related to the maximum energy of the reactor electron antineutrinos.

3. ***Energy cut for the delayed event:*** $6.0\,\mathrm{MeV} < E_{prompt} < 12.0\,\mathrm{MeV}$. By this cut only neutron capture on gadolinium is selected, therefore, the fiducial volume is restricted to the Target volume only[19]. In this context, it is worth mentioning that no further spatial cut is applied to the candidate events.

4. ***Time difference cut:*** $2\,\mu\mathrm{s} < \Delta t_{e^+n} < 100\,\mu\mathrm{s}$. The 2 µs-cut diminishes any effects from correlated noise; the 100 µs-time window is chosen because of the capture time of a neutron on Gd after IBD which is about 30 µs.

5. ***Multiplicity cut:*** no additional valid trigger in a time window of [-100 µs, 400 µs] around the prompt event.

In total, 9021 IBD candidate events are found after applying cuts 1) through 5). In order to further reduce remaining background, mainly muon-induced background, two additional selection cuts were applied: firstly, after each muon which has an energy deposition greater than $\sim 600\,\mathrm{MeV}$ in the inner detector a veto time of 0.5 s was cut out of the data, and secondly, all IBD candidates whose prompt event is in coincidence with an OuterVeto trigger were rejected, too.

[18] A separate publication presenting the results obtained with a larger data set with both reactors off is in preparation.

[19] However, there is still the effect of neutrons entering the Target after an IBD event in the GammaCatcher ("spill-in") or leaving the Target region after an IBD event in the Target ("spill-out"). This was studied in dedicated Monte-Carlo simulations, and the results take into account this effect.

With these additional cuts 8249 $\bar{\nu}_e$-candidates have been found, which are distributed homogeneously over the Target region. This corresponds to an average rate of (36.2 ± 0.4) events per day (43.7 events per day with both reactors on (139.27 live days), and 24.4 events per day with one reactor at less than 20% of its nominal thermal power (88.66 live days)) [Abe12a]. However, these events do not only contain electron antineutrinos from the reactor cores, but also some background survives the selection cuts. The accidental background in the data sample could be measured by using the shifted time window method[20] to be $(0.261 \pm 0.002)\,\mathrm{d}^{-1}$ [Abe12a]. Its energy spectrum of prompt events is in very good agreement with the singles spectrum of the detector. The number of accidental coincidences is kept fixed for the final fit and not allowed to vary.

The main contribution to the correlated background comes from cosmogenically produced isotopes. These were searched by a triple coincidence of a muon in the detector and a $\bar{\nu}_e$-like event following afterwards. The time difference between the parent muon and the IDB-like event was fitted with a constant plus an exponential. Out of this fit the background rate due to cosmogenics surviving the above listed selection cuts was determined to be $(1.25 \pm 0.54)\,\mathrm{d}^{-1}$ [Abe12a]. This number serves as input parameter for the final fit to the antineutrino spectrum.

The second contribution to the correlated background to be regarded are fast neutrons and stopping muons. These were looked for in the data by applying the above mentioned selection cuts, but with a prompt energy window of $12\,\mathrm{MeV} < \mathrm{E_{prompt}} < 30.0\,\mathrm{MeV}$. This window lies energetically above the search window for antineutrinos as well as the energy window for cosmogenics. By separating the data sample obtained with this method into events with a time difference Δt between prompt and delayed event of $\Delta t < 10\,\mu s$ (mainly stopping muons) and $\Delta t > 10\,\mu s$ (mainly fast neutrons), the rates of both events could be studied separately. In total, (0.34 ± 0.18) stopping muons per day and (0.30 ± 0.14) fast neutron events per day are expected; a combined analysis yields a rate estimation for fast neutrons and stopping muons in the energy window of the antineutrino search of $(0.67 \pm 0.20)\,\mathrm{d}^{-1}$ [Abe12a]. Again, this number is taken as input parameter for the final fit. All expected event numbers - signal and background - are summarised in tab. 8.8.

The final fit to the prompt energy spectrum is done over 18 variably sized energy bins, and carried out separately for the two integration periods, one period of 139.27 live days with both reactors on and one period of 88.66 live days with one reactor at below 20% of its nominal thermal power. This is done as the two periods have a different signal-to-background ratio, and additional information on the background behaviour is obtained. The total normalisation uncertainty of signal and background relative to the total prediction adds up to a total error of 2.66% [Abe12a].

Both the numbers of cosmogenics and fast neutrons/stopping muons in the data sample of IBD candidates were determined independently from the fit to the prompt energy spectrum obtained. The resulting rates of $(1.00 \pm 0.29)\,\mathrm{d}^{-1}$ and $(0.64 \pm 0.13)\,\mathrm{d}^{-1}$, respectively, are in good agreement with the rates measured independently from the isolated samples. In addition, in the 22.5 h of reactor off-off data (with an expected rate of residual antineutrino events of < 0.3) three IBD candidates were found, two of them likely attributed to ^{9}Li (one of them rejected by the 0.5 s veto time cut after a high-energetic muon; see above), and one accidental coincidence. This independently verifies the background rates obtained with the

[20] 198 time windows, each shifted by 500 µs with respect to the preceding one are used. The accidental background is given by averaging over all these windows. Besides the shift of the time window the same cuts as for the $\bar{\nu}_e$-search are applied.

event type	Event number
$\bar{\nu}_e$-candidates + background	8249
accidental background	59.5
fast neutrons + stopping muons	152.7
cosmogenics	284.9
No-oscillation expectation	8439.6
total expectation	8936.8

Table 8.8: *Event numbers of the IBD candidates ($\bar{\nu}_e$ plus background) observed in 227.93 days of detector live time, and the expected number of the most important sources of background (accidental coincidences, cosmogenic isotopes, and fast neutrons/stopping muons; numbers as obtained from the isolated data samples) as well as the expected number of antineutrino events from both reactor cores in case of no oscillations. The total number of expected events is quoted, too. The tables sums over both integration periods (both reactors on and one reactor below 20% thermal power) [Abe12a].*

other methods. Subdominant contributions to the background like the (α,n)-reactions on ^{13}C (see sec. 8.3) were not taken into account.

In the two-neutrino oscillation scenario the best fit value is $\sin^2(2\vartheta_{13}) = 0.109 \pm 0.030$ (stat.) ± 0.025 (syst.) at a mass-square difference of $|\Delta m^2_{31}| = 2.32 \cdot 10^{-3}\,\mathrm{eV}^2$ [Abe12a]. The measured prompt energy spectrum including the best-fit curve and the spectrum expected in case of no oscillations is shown in fig. 8.32. The no-oscillation hypothesis is hereby excluded at $2.9\,\sigma$. A rate-only analysis of the Double Chooz data gives $\sin^2(2\vartheta_{13}) = 0.170 \pm 0.052$ [Abe12a]. The analysis of Double Chooz gives the first result on the neutrino mixing angle ϑ_{13} in a combined rate + shape analysis.

Combining the findings of the first rate + shape analysis of Double Chooz [Abe12] with the results from the accelerator neutrino experiments T2K (rate only) [Abe11] and MINOS (rate + shape analysis) [Ada11], as well as the reactor neutrino experiments RENO (rate only) [Ahn12] and DayaBay (rate only) [An12], an interval of $0.070 < \sin^2(2\vartheta_{13}) < 0.122$ at 95% C.L. is found [Mac12], independent of the mass hierarchy. The no-oscillation hypothesis can be excluded at $7.7\,\sigma$. The best-fit points of the combined analysis of the three experiments are shown in fig. 8.33.

Currently, the best constraints on the mixing angle ϑ_{13} both for small and large values come from the reactor antineutrino disappearance experiments, although, in principle, appearance experiments are more sensitive in excluding small (or even vanishing) values for $\sin^2(2\vartheta_{13})$. The best fit points both for inverted and normal hierarchy hint on a non-vanishing CP-violating phase δ_{CP}, however, with very poor significance. To finally conclude on the value of δ_{CP} especially the accelerator experiments have to collect more statistics and improve the significance of their results.

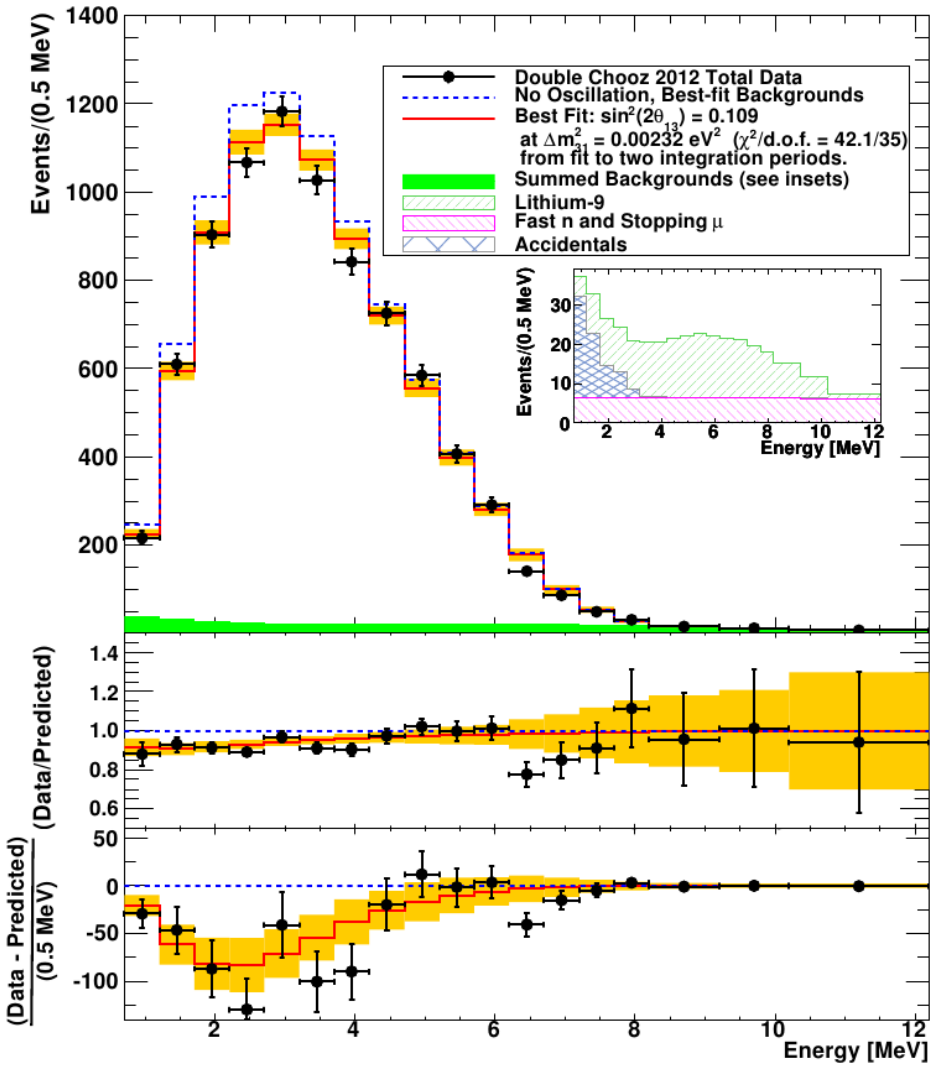

Figure 8.32: *Top: Measured positron spectrum of Double Chooz (black data points) summed over both integration periods, drawn together with the no-oscillation expectation (blue dashed spectrum), the best fit curve (red spectrum), and the background spectrum (green) [Abe12a]. The inset depicts a zoomed-in view on the background broken down into its various contributions. The best-fit value for the data is* $sin^2(2\vartheta_{13}) = 0.109 \pm 0.030$ *(stat.)* ± 0.025 *(syst.). Bottom: Differences between the data points and the no-oscillation curve (blue dashed line) and differences between the best-fit curve (red line) and the no-oscillation curve. Copyright (2012) by The American Physical Society.*

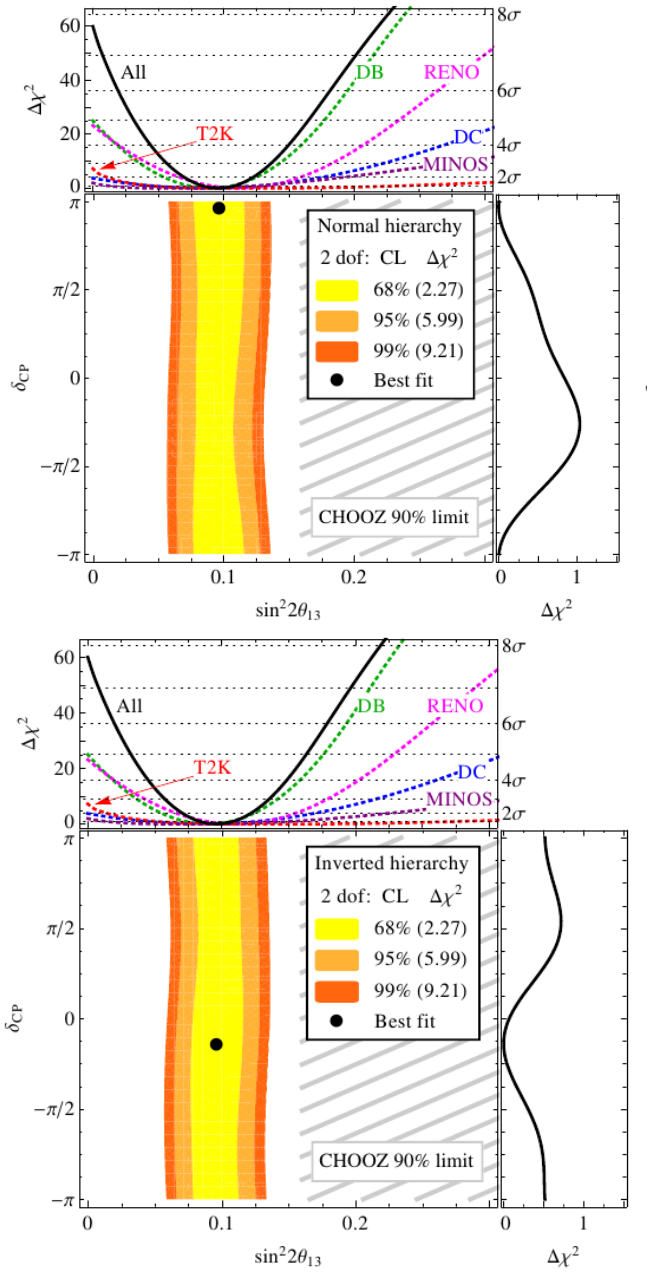

Figure 8.33: *Best-fit points for the combined analysis [Mac12] of Double Chooz, RENO, DayaBay, T2K, and MINOS. The upper panel shows the case of normal hierarchy, the lower one inverted hierarchy. The greyish shaded area depicts the 90% C.L. exclusion contours of the CHOOZ experiment [Apo03]. The $\Delta\chi^2$-distribution is shown in each case, too, once as a function of $sin^2(2\vartheta_{13})$ (top) and once as a function of δ_{CP} (right). At present, both for small and large values of $sin^2(2\vartheta_{13})$ reactor antineutrino disappearance experiments are more sensitive. For normal (inverted) hierarchy the best fit points are $sin^2(2\vartheta_{13}) = 0.096$ (0.096) and $\delta_{CP} = 0.97\pi$ (-0.14π).*

Part III

Liquefied Rare Gas Detectors: Wavelength- and Time-Resolved Studies on the Scintillation Properties of Liquid Argon

Chapter 9

The Scintillation of Rare Gases

In the recent decades liquefied rare gases have become more and more interesting as a detector medium in a variety of fields, amongst them the search for rare events, high energy particle physics, astroparticle physics, or medical applications [Apr06, Cur09, Lop02], not only because they have rather good scintillation properties with a high light yield, but also since liquid rare gas detectors are rather easily scalable, can be cleaned chemically to a high purification level, and provide the possibility to choose different detector media, like argon or xenon, which have different atomic mass numbers. All these properties are of particular interest for experiments in astroparticle physics, oftentimes searching for rare events at a low energy scale.

The high light yields[1] increase photon statistics notably at low energies and, therefore, allow low energy thresholds of the detectors. This is, for example, especially useful for the search for Dark Matter, where the energies deposited by the WIMP recoiling off in the detector are expected to be only of the order of a few keV.

The possibility of cleaning the detector media to a very high purification level is important in terms of background. The higher the radiopurity, the lower the background level and, thus, the better the reachable sensitivity. However, not only radioactivity needs to be removed from the detector liquid, but also impurities like oxygen or water, which lead to luminescence light losses because of additional quenching and absorption processes [Acc10] and deteriorate the timing and position reconstruction due to scattering. Some impurities alter the time constants of the scintillation light [Hei11], too, diminishing the potential for particle discrimination (sec. 11.3). In the case of TPC detectors (sec. 4.3.2), oxygen is, in addition, capturing free electrons and thereby diminishes the ionisation signal [Acc10].

The scalability of the detectors is a fundamental requirement for the next generation of detectors dealing with processes which have an exceedingly rare occurrence because of extremely tiny reaction cross sections or very long half-lives, as is the case in neutrino physics (e.g. ICARUS [Rub11] and GLACIER [Rub04] as detectors for neutrino experiments), the direct search for Dark Matter, and the search for the neutrinoless double β-decay, see chapters 2, 3, and 4.

The possibility of having different target media is, in particular, advantageous for the Dark Matter search: the energy transfer from the WIMP to a nucleus of the detector medium is for kinematic reasons maximal in case the atomic mass of this nucleus is of the order of the

[1] The light yield of pure liquid argon is about 40,000 photons per MeV (for an incident electron with an energy of $\sim$1 MeV and in absence of an electric field which would prevent argon ions and electrons to recombine and, consequently, to emit scintillation light; see below) [Dok88]. For comparison: the light yield of a typical PXE-based liquid scintillator is $\sim$10,000 photons per MeV [Moe12].

WIMP mass. Therefore, different detector media with different mass numbers allow to cover a wider mass range in the WIMP search. But also experiments looking for the $0\nu\beta\beta$-decay benefit from the possibility of probing several different isotopes to cross-check the results.

However, for practical reasons not all of the rare gases are well-fitting candidates for detector media. Helium and neon have boiling temperatures far below the temperature of liquid nitrogen (77 K) [Smi51], which makes cooling more difficult. In addition, their scintillation light is emitted to a great extent at wavelengths below 90 nm (see sec. 9.2), and it is therefore harder to work with. Krypton would, in principle, be viable for particle detectors, but it contains non-negligible amounts of radioactive ^{85}Kr [Lop02]. Consequently, most of the projects in particle and astroparticle physics focus on either argon[2] or xenon.

Within the scope of the present thesis, the scintillation of liquid argon with ion-beam excitation has been studied in a broad wavelength region of about 110 nm to 950 nm, both wavelength- and time-resolved. In this chapter the scintillation mechanisms of liquid rare gases will be explained; ch. 10 gives an overview of the experimental setup used for the present studies and the results will finally be presented in ch. 11.

9.1 Scintillation Mechanism of Liquid Rare Gases

The electromagnetic interaction between an incident particle and the liquefied rare gas leads to excited and ionised[3] rare gas atoms. The spectrum of the subsequently emitted scintillation light of the liquid rare gas has been found to be very similar to that of the gas phase in experiments with electron excitation [Bas70, Hei10, Hei11, Hei11a], synchrotron radiation [Mor89], and α-particles [Che72, Jor65], hence, the underlying gas kinetic processes seem to be similar[4]. Therefore, the liquid rare gases will be described in the following just as very dense gas, whose scintillation mechanism is well examined. One of the questions to be addressed with the experiments performed within this thesis is if the scintillation light emission following an excitation of liquid argon with heavy ions can be explained with the dense-gas model, too, or if new processes in the liquid come into play. The latter could be suspected especially due to the high specific energy loss of heavy ions and the resulting high excitation densities.

The experimental results presented in chapter 11 only concern liquid argon, therefore, all the equations and spectroscopic notations used below will refer to that special element. However, nearly all conclusions are still valid for other liquid rare gases, too.

Light incident particles like β-rays, gammas, and also protons, as well as high-energetic heavy ions (with kinetic energies much bigger than 250 keV), lose their energy mainly in interactions with the electron shells of the argon atoms ("electronic stopping"); energy losses

[2] However, for big detectors a depletion of the content of radioactive ^{39}Ar might also be mandatory [Lop02].

[3] In the liquid phase excited atoms correspond to a "free" exciton, ionised atoms to an electron-hole pair [Dok88]. However, in the following the terms "excited atom" and "ionised atom" will be used, analogous to the gas phase, as from the investigation of the scintillation properties (see sec. 9.3 and ch. 11) it turns out that the liquid phase behaves similar to the gas phase (see also [Mor89]).

[4] Absorption measurements with xenon-doped argon and krypton, both in the liquid and the solid state, showed that the atomic transitions of xenon observed for the gas phase can also be found as distinct absorption bands in liquid argon [Raz70], also pointing out a similarity. Compared to the atomic transitions these bands are, however, slightly redshifted and considerably broadened, which can be understood in the picture of excitons [Raz70]. The atomic states seem to be mildly disturbed by the surrounding argon matrix. In addition, it is reported that the conduction band states in liquid argon are free-electron-like, i.e. the electron-atom interactions are weak [Raz70].

in collisions with argon nuclei can be neglected. The interactions with the electron shells lead to highly excited (Ar^{**}) or singly ionised (Ar^{+}) atoms [Dok02]:

$$Ar + \chi \longrightarrow Ar^{**} + \chi' \tag{9.1}$$
$$Ar + \chi \longrightarrow Ar^{+} + \chi' + e^{-} \quad . \tag{9.2}$$

Here, χ denotes the incident particle and χ' the scattered particle. The probability for an ionisation process is hereby reported to be about four times larger than the probability for an excitation [Dok02]; theoretical calculations predict a ratio of ionised to excited atoms of 4.8:1 [Tak75], independently of the exciting particle. The probability of ionising argon atoms to higher charge states, however, is small with electron excitation.

The electron originating from the ionisation process most often has gained enough energy to excite or ionise further argon atoms before it is finally thermalised. This thermalisation typically happens on time scales of a few hundreds of picoseconds [Sow82].

The positively charged argon from reaction (9.2) ion collides with other (neutral) argon atoms of the surrounding liquid and forms an ionic excimer[5] molecule:

$$Ar^{+} + 2Ar \longrightarrow Ar_2^{+} + Ar \quad . \tag{9.3}$$

The additional argon atom is needed for momentum conservation. Process (9.3) is rather fast ($\sim$ ps), especially due to the high density of liquid argon [Hit84]. In case the thermalised electron is still close enough to the ionic excimer molecule, i.e. within the so-called Onsager radius, it "sees" its attracting electric field and a prompt recombination process takes place (typically on a timescale of nanoseconds [Hit84]):

$$Ar_2^{+} + e^{-} \longrightarrow Ar^{**} + Ar \quad , \tag{9.4}$$

which again produces a highly excited argon atom Ar^{**}, just like reaction (9.1). If the electron does not thermalise within the Onsager radius, which is 128.9 nm for liquid argon [Jas09], the prompt recombination is unlikely and the energy primarily transferred to this argon atom is lost for prompt (i.e. within the first few nanoseconds) light emitting processes, diminishing the prompt scintillation efficiency. However, the recombination (9.4) can, of course, also happen with a thermalised electron from another ionisation process, therefore, the number of electrons not recombining within the first nanoseconds depends not only on the energy spectrum of the electrons released in the ionisation processes, but also on the ionisation density of the incident particle in liquid argon. As different particle types have different specific energy losses, and therefore different ionisation densities, changes in the prompt recombination rate are expected here. Electrons which do not immediately recombine with an ionic excimer molecule, however, are not lost, but can recombine delayed.

The highly excited argon atoms Ar^{**} from reactions (9.1) and (9.4) undergo optical or non-radiative transitions (in collisions with atoms from the surrounding argon matrix) and, by this, de-excite to the lowest excited level $[Ne]3s^2 3p^5 4s^1$ [Dok02]. In the following, this state is always referred to by the symbol Ar^{*}. Depending on the relative orientation of the spin of the electron in the 4s-level and the core angular momentum [Len71] the four electronic

[5]Excimer stands for **exc**ited d**imer**, i.e. a two-atomic molecule which is only strongly bound in its excited state. In the liquid phase, this process is also known as "self-trapping" of the argon ion.

configurations $^1P_1$, $^3P_0$, $^3P_1$, and $^3P_2$ are possible[6]. These four configurations have slightly different excitation energies due to fine structure splitting; the state $^1P_1$ has the highest (11.8 eV), the state $^3P_2$ the lowest (11.5 eV) energy [NIS12]. These energies are so high that radiationless transitions to the ground state [Ne]$3s^2 3p^6$:$^1S_0$ are too slow and unlikely compared to photon emission. However, for the states $^1P_1$ and $^3P_1$ optical dipole transitions to the ground state by emission of a photon are possible, giving rise to the resonance lines of argon at wavelengths of 104.8 nm and 106.7 nm, respectively [NIS12]. The states $^3P_0$ and $^3P_2$ have no allowed optical dipole transition to the ground state because of the selection rules for electromagnetic radiation ($\Delta S = 0,\pm1$; $\Delta J = 0,\pm1$, but not $J = 0 \rightarrow J = 0$). The resonance lines can only be seen in the scintillation spectra of a very dilute gas [Fed04], as neutral argon atoms can reabsorb the resonance photons and get into the excited state themselves. Therefore, liquid argon - as well as the dense gas - is opaque for this kind of scintillation light[7], only the energetically lower photons emitted in the decays of argon excimer molecules (see below) are free to leave the liquid. This radiative trapping significantly slowes down the radiative decay of the resonance levels.

In radiationless dissipative collision processes the Ar^* atoms can change their electronic configuration and finally end up in the energetically lowest two, $^3P_1$ and $^3P_2$ [Lor76], of the four excitation levels, and subsequently form argon excimers[8] on a timescale of picoseconds [Hit84],

$$Ar^* + 2Ar \longrightarrow Ar_2^* + Ar \quad , \tag{9.5}$$

either in the triplet state $^3\Sigma_u^+$ (from $^3P_2$), or in the singlet state $^1\Sigma_u^+$ (from $^3P_1$). This is depicted in fig. 9.1. Finally, in the decay of the vibrationally relaxed states of the excimers to the ground state photons with a wavelength around 127 nm [Dok02] are emitted, either by an allowed fast singlet transition ($\tau \approx 4.4$ ns to 6 ns) or by a forbidden slow triplet transition ($\tau \approx 1.1$ µs to 1.7 µs) [Car79, Hit83, Pei08]. The energies of the two transitions are not exactly equal, but differ by ~ 75 meV [Mor89], however, the emitted molecular spectrum has a width of $\sim$7-10 nm (also depending on the temperature) [Hei11], therefore, singlet and triplet transitions cannot be resolved spectroscopically. The spectrum arising from these decays of argon excimer molecules is called *second excimer continuum* [McC84] (see below).

The ratio of the intensities of singlet and triplet transitions contributing to this continuum, I_s/I_t, is not fixed, but depends on the incident particle and the particle's energy [Car79, Hei11, Hit83, Lip08, Pei07, Pei08], and the density of excited atoms: the higher the excitation density, the more singlet photons are observed[9]. This is most likely due to a re-distribution of the excitation energy between the singlet and triplet states in collisions with hot electrons [Lor76], and the much faster decay of the singlet. In principle, this can be used for a particle discrimination by pulse shape analysis, as the decay-time constants of the two transitions are very different [Pei07, Pei08]. However, the fast scintillation light emitted at longer wavelengths

[6] Here and in the following the widely known Paschen notation is used. Without any deeper discussion it shall be noted that the electronic states of the rare gases are, however, best described with the Racah notation [Len71]. In this notation these states have the symbols $4s'[\frac{1}{2}]_1$ ($^1P_1$), $4s'[\frac{1}{2}]_0$ ($^3P_0$), $4s[\frac{3}{2}]_1$ ($^3P_1$), and $4s[\frac{3}{2}]_2$ ($^3P_2$).

[7] Photoabsorption in dense rare gases and rare gas liquids also extends to the red wings of the resonance lines [Ger74, Neu12, Neu12a].

[8] This process is also known as "self-trapping" of an argon exciton [Dok88].

[9] The singlet to triplet ratio for liquid argon for the undisturbed case (no mixing) is about 0.3. For high excitation densities values up to 3.5 are observed [Pei08].

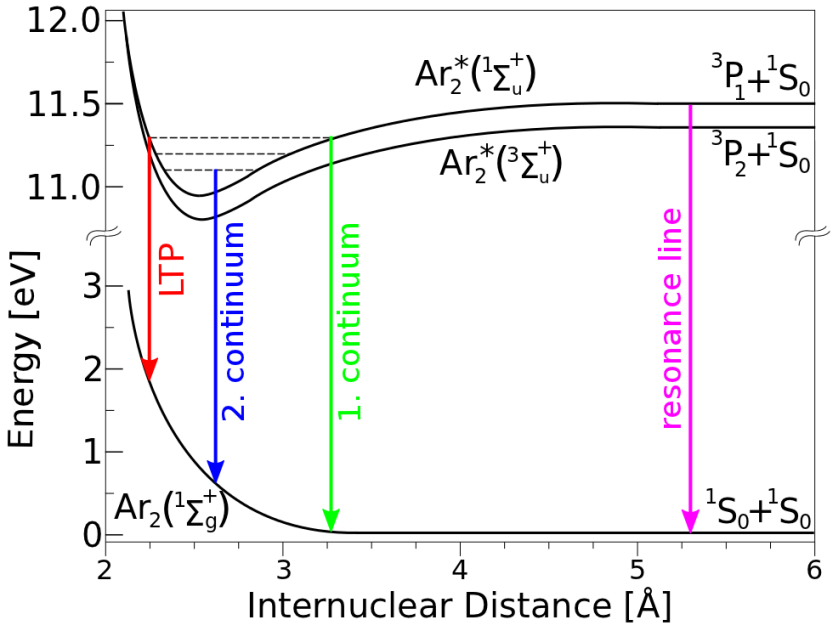

Figure 9.1: *Schematic potential diagram for the argon excimer molecules and the ground state as a function of the internuclear distance [Lor76]. The thick black lines represent the energy levels of the singlet ($^1\Sigma_u^+$) and the triplet ($^3\Sigma_u^+$) state of the argon excimer, which forms in the collision of an excited ($^3P_2$ and $^3P_1$, respectively) and a ground-state ($^1S_0$) argon atom, and the repulsive ground state ($^1\Sigma_g^+$). The tiny van-der-Waals minimum at 3.75 Å [Col76] is not shown. The horizontal dashed black lines schematically indicate the vibrationally excited states of the excimer. Colored arrows depict the possible transitions from the excited to the ground state: blue for the main emission feature, the 2nd excimer continuum stemming from the decay of vibrationally relaxed excimer molecules; red (left turning point, LTP, see text) and green (1st excimer continuum) for the decays of the vibrationally excited excimer states; pink for the resonant transitions of an excited argon atom to the ground state. According to the Franck-Condon principle [Con28, Fra26] the transitions happen vertically.*

[Wie00] (see below) might mimic the fast component of the second excimer continuum in not wavelength-resolved measurements (e.g. in case a wavelength shifter is used), and thus worsen the discrimination potential. Therefore, wavelength-resolved studies of the scintillation properties are mandatory.

But not only the vibrationally relaxed states of the argon excimer can decay into the ground state, but also the vibrationally excited ones. In a classical consideration the probability density for the two argon atoms in the excimer molecule is highest at the turning points of the vibrational mode. The decay of an argon excimer close to the turning point for large interatomic distance gives rise to a photon emission with higher energy than the photons from the second excimer continuum, as the energy distance to the ground state is bigger (fig. 9.1). This leads to the *first excimer continuum* at shorter wavelengths [Dan11].

The excimer decay for small interatomics distance emits photons with a lower energy and can be seen in the emission spectra as a distinct feature at longer wavelengths (in gaseous argon around 155 nm [Lan88]). This emission feature is commonly referred to as *"classical left turning point"*, or in short *LTP* [Kro91].

As the ground state for all these transitions from the decay of the excimer is not bound[10] it decays into two neutral argon atoms [Dok02]:

$$Ar_2^* \longrightarrow Ar_2 + \gamma \longrightarrow 2Ar + \gamma \quad . \tag{9.6}$$

Therefore, a resonant re-absorption of the photons of the first and second excimer continuum and the LTP is not possible; the scintillation photons are free to leave the argon liquid. An overview of all the processes described above is given in fig. 9.2.

Electronic stopping, as was described above, is, however, not the only interaction possibility between particles and argon atoms. Heavy ions with kinetic energies below $\sim 200\,\mathrm{keV}$ or WIMPs deposit most of their energy in collisions with nuclei of the liquid argon ("nuclear stopping"). As a consequence, fast recoil nuclei[11] are created, which again can excite or ionise further argon atoms. Because of the much higher energy loss per unit length in the case of low-energetic heavy ions, the excitation densities are much larger for nuclear stopping than for electronic stopping [Wil77]. Besides this, the probability for the creation of highly charged argon ions is much higher, which renders possible several additional light emission processes. As an example, the initial steps of the gas kinetic processes following the creation of an Ar^{2+}-ion, which were examined in an experiment at the Munich Accelerator Laboratory for gaseous argon at different pressures [Wie00], shall now be discussed in more detail.

The interpretation of the emission features which arise at longer wavelengths ($\gtrsim 170\,\mathrm{nm}$) than the second excimer continuum given in [Wie00] is as follows: the first step is again the formation of an ionic excimer:

$$Ar^{2+} + 2Ar \longrightarrow Ar_2^{2+} + Ar \quad . \tag{9.7}$$

This excimer molecule can either decay into two Ar^+ atoms, releasing photons with a wavelength of 188 nm, or form doubly charged Ar_3^{2+} molecules in collisions with other argon atoms. In the case of gaseous argon at room temperature, the 188 nm radiation is the dominant scintillation light emission in the first few nanoseconds [Wie00]. In particular, it exceeds the second excimer continuum in intensity; only the emission from the LTP, which stems from vibrationally excited argon excimers, has a comparable intensity at very early times. In the liquid phase, however, the density might be so high that the Ar_3^{2+} molecule formation dominates by far, and the photons from the Ar_2^{2+} decay are too rare to show up in the spectra recorded.

The Ar_3^{2+} molecules in turn can either decay, radiating at a wavelength of 199 nm, or form in collisions the excited ionic excimers Ar_2^{+*}. The decay of the latter releases photons of 177 nm, 212 nm, or 225 nm, however, it is once again in competition with another molecule formation, Ar_3^{+*}, which is the origin for scintillation light with a wavelength of 245 nm. All these emissions, and some more stemming from even more highly charged argon atoms not quoted here, form the *third excimer continuum*, which can be found at wavelengths above $\sim 170\,\mathrm{nm}$. Fig. 9.3 again depicts the single steps.

[10] More precisely, the ground state has an attracting van-der-Waals minimum, however, its depth is only 12 meV [Col76], which is of comparable size as the thermal energy of 7 meV at the boiling temperature of argon ($\sim 87\,\mathrm{K}$). Therefore, the ground state can be considered to be repulsive only.

[11] In the case of WIMPs the expected recoil energies are only few keV. Some experimental data hint to a further not yet understood stopping mechanism at these low energies, which again increases the scintillation efficiency [Gas10].

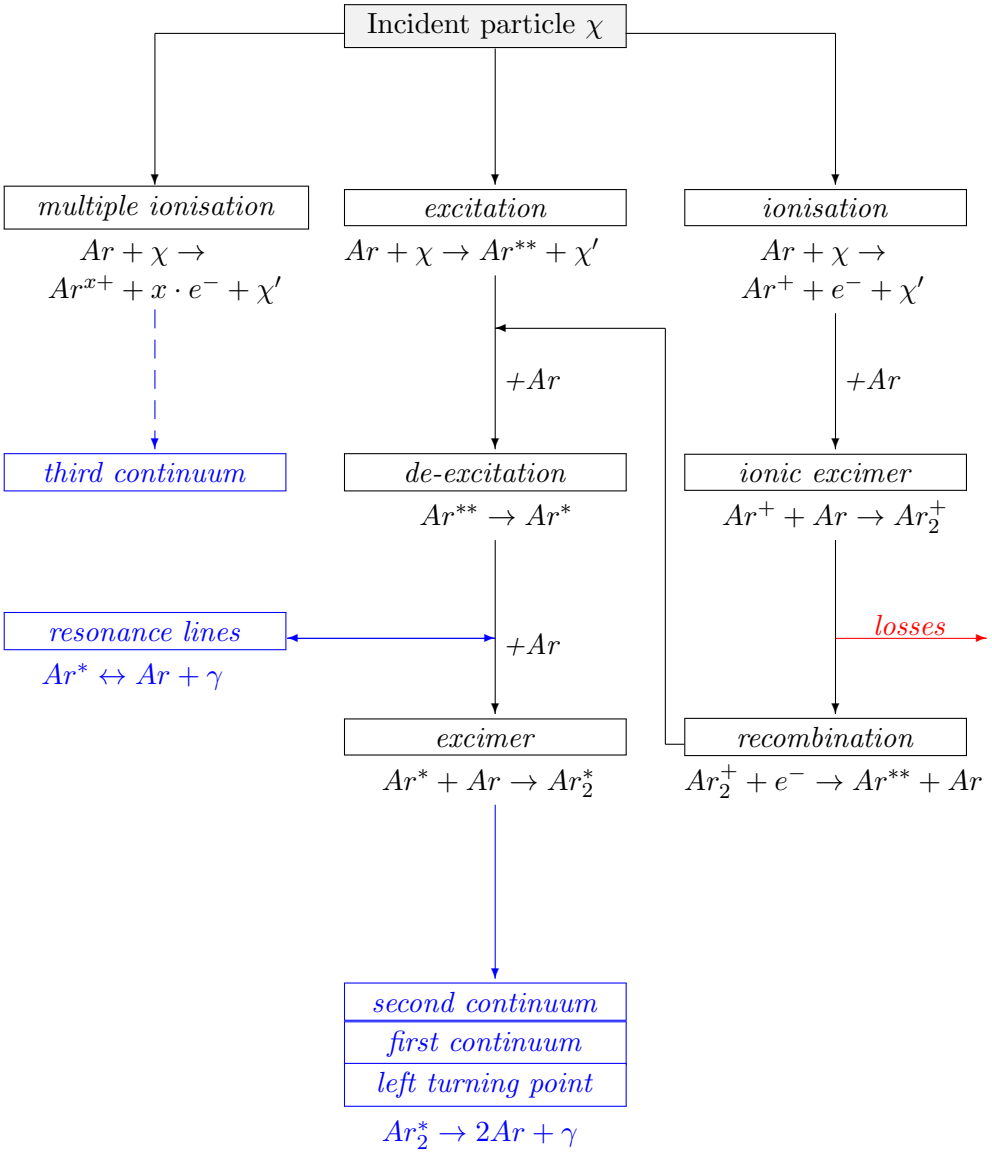

Figure 9.2: *The gas kinetic processes in argon and light emission mechanisms after excitation or single ionisation by an incident particle χ [Dok02]. The various processes leading to the emission of the third excimer continuum after multiple ionisation are not shown here, but the initial steps [Wie00] can be found in fig. 9.3. However, recombination processes of highly ionised atoms also lead to singly ionised or excited argon atoms, contributing to the processes leading to the emission of excimer light. The two- and three-body reaction steps need a collision with an additional argon atom for reasons of momentum conservation, which is indicated by "+Ar" at the respective arrows. Light emission processes are depicted in blue, the losses of fast scintillation light photons in the recombination process in red. For details see text.*

The multiple steps of the underlying gas kinetic processes define the time structure of the third excimer continuum. Within the present thesis, the analogue of the third excimer continuum of the gas phase was looked for in liquid argon, and the time structure of the emission features found in the corresponding wavelength region was investigated (sec. 11.3)

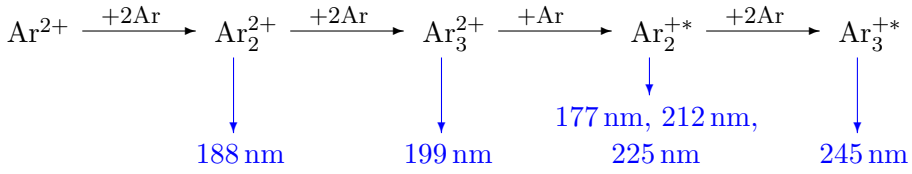

Figure 9.3: *Possible interpretation of the initial steps of the gas kinetic processes following the formation of an Ar^{2+}-ion [Wie00]; the newly formed excimer molecules can either decay radiatively (the photon wavelengths are given in blue) or lose energy in collision processes with other argon atoms, forming molecules with lower energy. For details see text.*

for a set of selected wavelengths. As will be shown below (sec. 9.2), in the gas phase differences in the scintillation light spectra are observed for different incident particles in the wavelength region of the third excimer continuum. An analogous behaviour of the liquid phase could possibly yield the potential for particle discrimination by means of the scintillation light only. This was one of the main motivations for the studies presented here (see ch. 11). In addition, the measurement of the decay time structure could help to identify the gas kinetic processes.

Analogous to liquid scintillators, high excitation densities (as are, for example, present at nuclear stopping) lead to quenching processes which are eventually reducing the scintillation efficiency [Dok02, Gas10]. For example, two excited argon atoms could form a single argon ion [Dok02]

$$Ar^* + Ar^* \longrightarrow Ar + Ar^+ + e^- \quad , \tag{9.8}$$

which leads to the emission of only one luminescence photon instead of two.

9.2 Emission Spectra in the Gaseous State

The scintillation-light emission spectra of the rare gases helium, neon, argon, krypton, and xenon at room temperature are well-known in a broad wavelength region [Mor08, Ulr87, Wie00], see fig. 9.4. The by far dominant scintillation feature is the second excimer continuum, stemming from the decay of neutral rare gas excimers, as was explained above for Ar_2^* (sec. 9.1). The width of the second excimer continuum exceeds by far the energy splitting of the singlet and triplet transitions [Mor89], hence, both transitions are not visible as distinct features in the spectrum. For all rare gases most of the scintillation light is emitted in the vacuum ultraviolet[12] (VUV) wavelength region.

Towards shorter wavelengths the first excimer continuum follows, which is emitted in the decay of vibrationally excited neutral excimers. At gas pressures of 1000 mbar (and for kinetic energies of the secondary particles, electrons and ions, much smaller than 1 eV [Dan11]) the intensity of the first excimer continuum is small compared to the second excimer continuum, as the gas density is high enough to enable fast non-radiative vibrational de-excitation in collisions with other atoms. The other spectral feature stemming from the decay of vibrationally excited excimers, the LTP, however, cannot be seen at all.

[12] Air is only transparent for photons down to ~ 185 nm [Ulr11]. Below this threshold absorption by oxygen prevents a free propagation of the scintillation light.

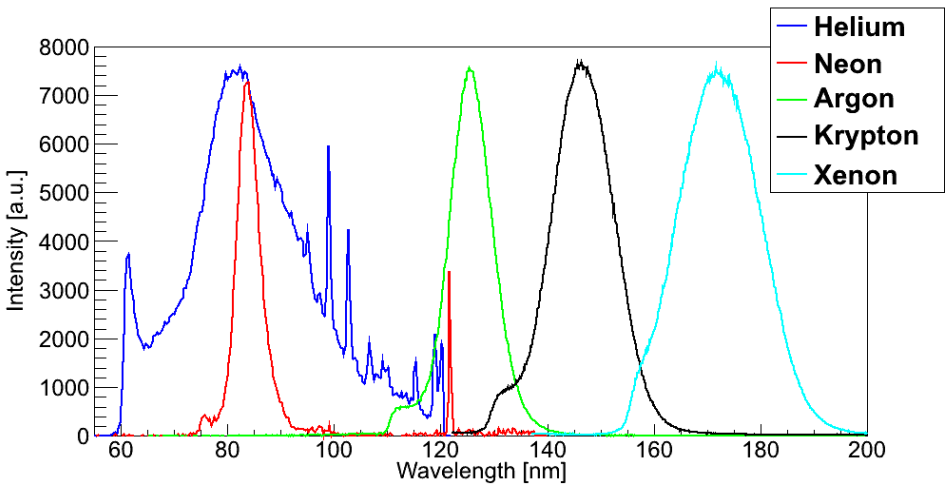

Figure 9.4: *Emission spectra of the various rare gases in gaseous state at ∼ 1000 mbar and room temperature when excited with electrons. The by far dominant emission feature that can be seen is the second excimer continuum, continuously shifted to longer wavelengths for the heavier rare gases. At its short-wavelength end the respective first excimer continuum is visible. The spectrum of neon additionally contains the Lyman-α line at 121.6 nm from a residual hydrogen impurity [Mor08].*

The probability for the creation of doubly charged rare gas ions is rather low with electrons as exciting particles, therefore, the third excimer continuum is also invisible on a linearly scaled scintillation light spectrum. This continuum, however, becomes more prominent for the excitation with heavy ions; fig. 9.5 [Ulr12].

9.3 Argon in Gaseous and Liquid State with Electron-Beam Excitation

The emission spectra of argon in gaseous and liquid state have recently been recorded wavelength-resolved with electrons as incident particles [Hei10, Hei11, Hei11a], both in a continuous and a pulsed beam mode. The energy of the electrons was about 10 keV when entering the argon. The results of these measurements confirmed the similarity between the emission spectra of both states of aggregation, see fig. 9.6, however, emission features which emerge from the decays of highly excited molecular states (like the LTP) are strongly suppressed in the liquid. This seems to be due to the much higher density of liquid argon, which strongly increases the collision rates and, therefore, enforces the probability for radiationless gas kinetic processes and de-excitations. In addition, the intensity and the spectral shape of the emission features in the wavelength region of the third excimer continuum are considerably different in the liquid phase (fig. 9.7). This might also be due to the huge difference in density compared to gaseous argon, which makes some processes leading to the emission of the third excimer continuum unlikely. However, it has to be clarified if the underlying scintillation mechanisms are still the same, or if different processes come into play.

Therefore, within the scope of the present thesis the scintillation-light spectrum of argon in gas and liquid phase has been recorded with different ion beams. The spectra arising for

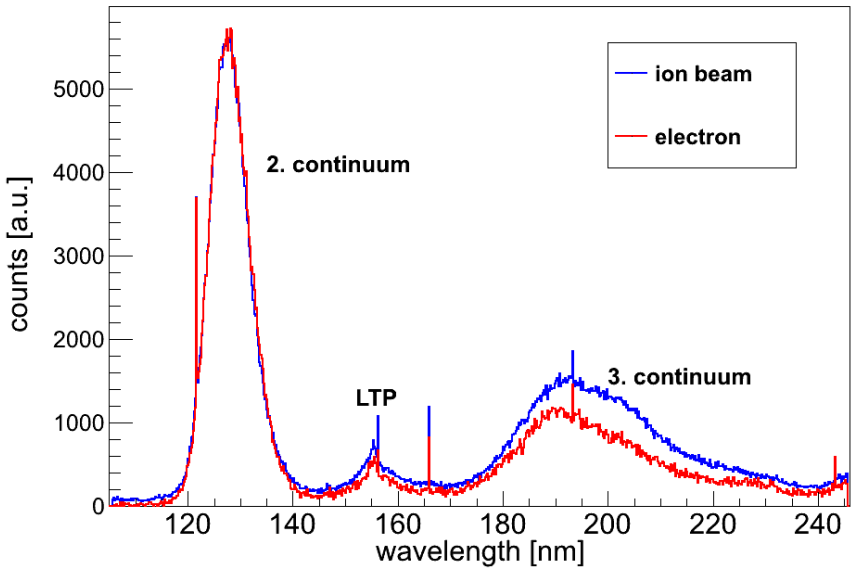

Figure 9.5: *Comparison of the emission spectra with electron-beam (red) and ion-beam (120 MeV sulfur beam; blue) excitation of gaseous argon at 300 mbar and room temperature [Ulr12]. The intensities of the second excimer continuum are scaled to match each other; the third excimer continuum above ∼ 170 nm is clearly enhanced with the ion beam. Due to the cut-off wavelength of MgF_2 used as window material the first excimer continuum cannot be seen here. The sharp emission lines at 121 nm, 156 nm, 166 nm, and 193 nm are due to a residual contamination with traces of hydrogen and carbon, respectively.*

the different states of aggregation are compared to each other (sec. 11.2.1), and differences are looked for which might give indications on the underlying physics processes. In addition, the spectra obtained with the different incident particles (different heavy-ion beams and electrons) are compared to each other to obtain experimental information on the particle discrimination potential in liquid argon by means of the scintillation light only.

Differences between the wavelength-resolved emission spectra with electron- and ion-beam excitation, respectively, are mainly expected due to the larger number of highly ionised argon atoms in case of heavy ions. Their subsequent light emission processes could enhance the third excimer continuum. However, not only the ionised atoms produce scintillation light, but also the electrons released in these ionisation processes, which can again excite and/or ionise further argon atoms. As the number of secondary electrons greatly exceeds the number of primary particles[13] the scintillation spectra recorded with the heavy ion beam are to a great extend also originating from electron interactions with argon. The energy of the secondary electrons produced by ion beams with energies of about 3 MeV per nucleon is known to range up to several keV [Rib94]. This corresponds to the energy of the electrons (∼ 10 keV) from the electron gun [Hei11], therefore, the results obtained with electron excitation can give an estimate of the influence of the secondary electrons on the scintillation spectra as recorded with the heavy ion beam.

[13] In argon the energy needed to create an electron-ion pair is only 23.6 eV [Dok02], therefore, up to ∼ 40 secondary electrons can be produced per keV energy of the primary particle.

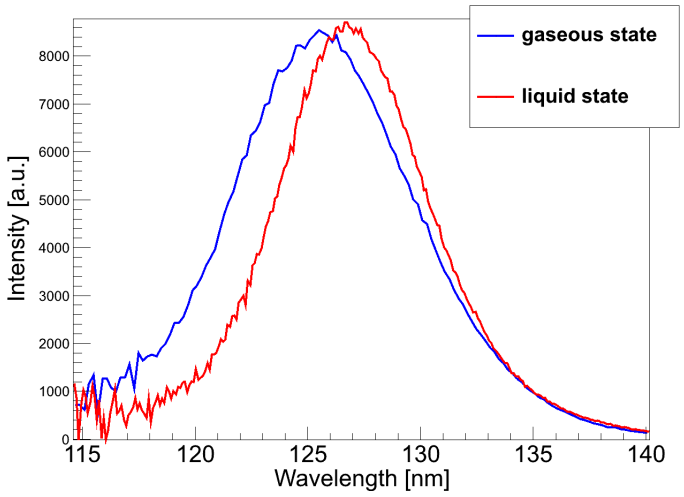

Figure 9.6: *The second excimer continuum of argon in the gas (blue) and the liquid (red) phase [Hei10, Hei11] with electron-beam excitation (raw data corrected for the detector response function). The gaseous argon was at room temperature and at a pressure of 300 mbar. The overall shape and the width of both continua are similar, however, the peak intensity is shifted from 125.7 nm in the gaseous state to 126.8 nm in the liquid. For the gas phase this shift is reported to be mainly due to different densities [Mor89] and temperatures [Pre94]. The similarity points out that the underlying scintillation mechanisms could be identical, i.e. the liquid rare gas behaves like a dense cold gas for excitation with electrons.*

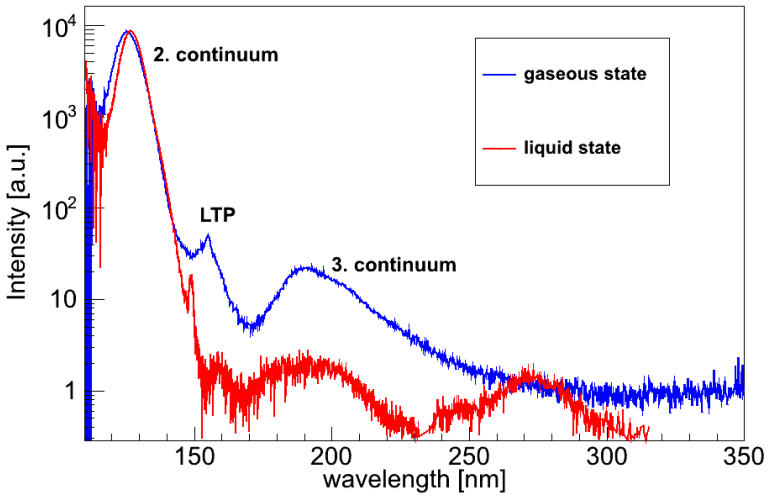

Figure 9.7: *Same plot as fig. 9.6, but on a logarithmic scale and for a wider wavelength range [Hei10, Hei11]. Besides the second excimer continuum which is dominating the spectrum, several distinct emission features can be seen: at about 155 nm the LTP shows up, but with an only very tiny intensity in the liquid phase. Beginning from ∼ 170 nm the third excimer continuum arises. In the liquid phase, the third excimer continuum is much more suppressed compared to the second excimer continuum and shows two maxima instead of one. The sharp peak at 148.9 nm in the liquid-state spectrum comes from a residual xenon impurity in the argon.*

Chapter 10

Experimental Setup at the Tandem Accelerator for Ion-Beam Excitation of Liquefied Argon

The measurement of scintillation light emitted by liquid argon when excited by heavy ions[1] required a new setup at the Munich Tandem Accelerator Laboratory (*Maier-Leibnitz-Laboratorium*, MLL). This setup consisted of a target cell, capable of cooling gaseous argon down to the liquid phase, with an entrance foil for the ion beam and an exit window for the scintillation light, and supplementary installations for beam monitoring, cooling, and gas handling. In three beam times the detection of VUV and UV scintillation-light was accomplished by a monochromator with an attached PMT. The read-out electronics allowed to record wavelength-resolved spectra as well as time-resolved measurements at a given wavelength. One additional beam time with an UV-Vis grating spectrometer was used for complementary measurements of the wavelength spectra in the longer wavelength region.

10.1 The Target Cell

The target cell for the scintillation-light measurements was made of copper and had a cylindrical shape with an outer diameter of 50 mm and a length of 60 mm; see figs. 10.1 and 10.2. Its inner borehole with a diameter of 12 mm provided the volume which was filled with liquid argon during operation. On the side of the cell, facing the light detector, another hole was drilled which was covered by an indium-sealed MgF_2-window to allow the scintillation light to exit the cell. This window was held by a steel plate. MgF_2 is transparent down to $\sim$110 nm [Kor12] and, therefore, the scintillation light of liquid argon can be recorded down to the short-wavelength end of the second excimer continuum. Both the exit window and its holding plate were 5 mm thick, which restricted the opening angle of the scintillation-light emission to $\sim 53°$ (fig. 10.1). This angle was large enough to fully illuminate the exit flange of the surrounding CF-100 cross piece, therefore, no light was lost by shadowing effects. In the setup with the Czerny-Turner monochromator (see sec. 10.3.1) a mirror optics was connected

[1] In principle, the scintillation light emission could have also been studied with a radioactive source (α-particles or fission fragments). However, with such a source time-resolved measurements are difficult. Furthermore, the power of radioactive sources is limited, which requires long measurement times and has a low signal-to-noise ratio.

to the CF-100 exit flange to collect the scintillation light and focus it onto the entrance slit of the monochromator.

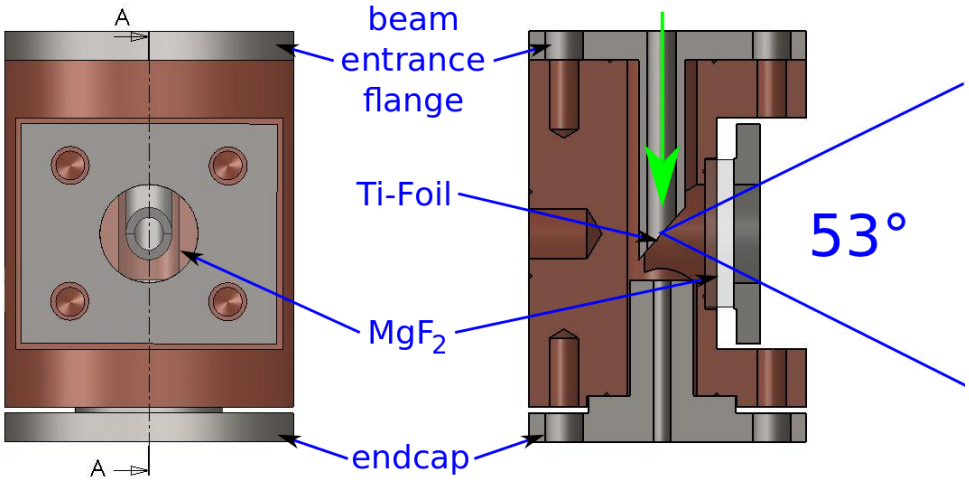

Figure 10.1: *CAD drawing of the target cell. The left view shows the cell from the direction of the light detector; the direction of the incoming ion beam is from top (green arrow). Through the MgF_2-window the inclinedly cut beam entrance flange can be seen, where the titanium entrance foil is glued on. The dashed-dotted line marked with "A" depicts the section plane for the cross-sectional view of the cell shown on the right. Here, also the MgF_2-window, held by a steel plate, can be seen. In this picture the beam entrance flange holding the titanium foil is seen on the top, while the endcap serving as Faraday cup is depicted on the bottom side (details see text). The opening angle of the cell of 53° is designed in such a manner that the full exit connector of the surrounding CF-100 cross piece is illuminated, hence, no scintillation light is lost by shadowing.*

Towards the incoming ion beam a beam entrance flange was screwed to the cell, extending into the latter up to the exit window. At this point, the beam entrance flange was cut inclinedly; a titanium foil with a thickness of $1.5\,\frac{\mathrm{mg}}{\mathrm{cm}^2}$ ($\approx 3\,\mu\mathrm{m}$) was glued onto the end of the beam entrance flange and served as entrance foil for the heavy ions. As the range of heavy ions with energies of some tens of MeV is only a few millimetres (or below; see fig. 10.7 in sec. 10.2) in liquid argon, nearly all scintillation light was produced directly at the Ti-entrance foil. The inclined cut of the beam entrance flange thus ensured a high light-detection efficiency, as the cross-section of the scintillating volume seen by the detector was maximised. In principle, the light detector could have been placed at the opposite side of the beam entrance, too, making an inclinedly cut beam entrance flange dispensable. However, this would have made measurements in the gas phase impossible, as then the ion beam would have passed the argon volume and deposited its energy in the MgF_2-exit window, possibly creating a blind spot. Furthermore, the sidewise arrangement of the light detector minimised the distance the scintillation light had to travel through argon. Hence, all effects of absorption and scattering were minimised, too, and the undisturbed scintillation light spectrum could be measured[2].

[2]The effective attenuation length of liquid argon for its own scintillation light is measured to be $\sim 1.6\,\mathrm{m}$ [Neu12a] for all wavelengths above 118 nm, and the Rayleigh scattering length is calculated to be $\sim 90\,\mathrm{cm}$ [Sei02], hence these effects can safely be neglected on the short distances of interest here.

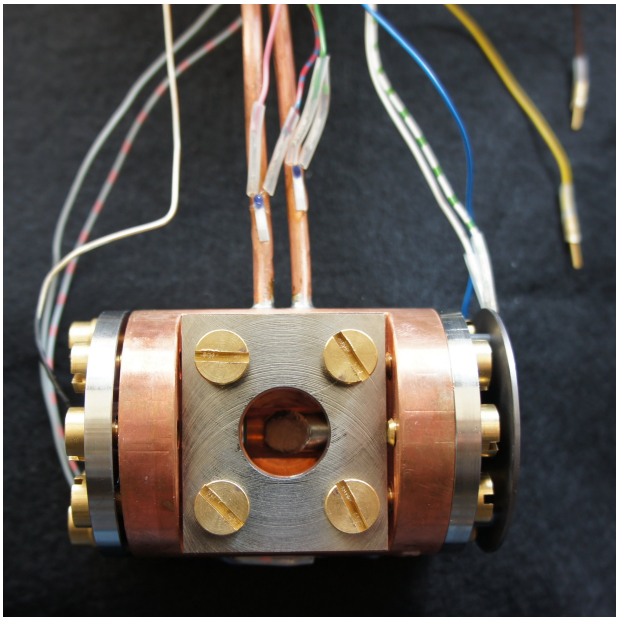

Figure 10.2: *Photograph of the fully assembled target cell. In the middle the MgF_2-exit window can be seen, which is held by a steel plate. Through the window the titanium entrance foil can be seen, which is glued to the beam entrance flange (from the right). On the very right, the tantalum aperture is visible. In the experiments the ion beam will come from the right, pass this aperture and enter the cell through the titanium foil. The tubes for gas inlet and outlet, respectively, are connected to the cell from the top. The various cables serve for read-out of the four PT-100 resistance thermometers and the electric charge of the endcap and the aperture. The two open cable heads in the top right corner are connected later-on to the heating resistor.*

In front of the beam entrance flange the cell had a tantalum aperture with an inner borehole of 3 mm diameter (see fig. 10.2). This aperture cut off the halo of the ion beam and was, furthermore, monitored in temperature and electric charge. Hence, the intensity of the beam halo could be measured, allowing an optimisation of the beam focus onto the cell. The backside of the target cell was closed with a stainless steel endcap, which had an electrically insulated copper plate at its inner end serving as a Faraday cup[3]. Thereby, the beam current entering the cell through the entrance foil could be measured for an evacuated cell. This was especially helpful in steering the beam, and, together with the beam halo measurement at the tantalum aperture, made it possible to find the optimal beam focus. All components of the target cell which were in contact with liquid argon were sealed with indium, except for the titanium entrance foil, which was glued to the beam entrance flange with an epoxy glue. With this technique, the impurities introduced into the argon were minimised, and cold leaks were avoided. In the final configuration the total volume of liquid argon in the cell was 5.6 cm^3. The fully assembled target cell is shown in fig. 10.2.

The target cell had two connections to the outside: firstly, opposite to the exit window, the cell was connected to a liquid nitrogen supply (in a 15 l dewar) through an adapter

[3]In fact, it was no real "cup" but only a plate. This is not the perfect configuration for a precise determination of the beam current as some charge is lost by knocked-out electrons, however, this setup worked quite well in finding the optimal beam focus.

piece and a solid copper rod. This connection simply served for cooling the cell below the condensation temperature of argon ($\sim 87\,\mathrm{K}$ at 1 bar [Smi51]). The adapter piece allowed a precise adjustment of the target cell in the beam-line setup. In addition, a $50\,\Omega$ heating resistor was soldered onto the copper adapter, and was used for fine tuning the cell's temperature by applying a low voltage.

Secondly, the target cell had two holes on its top, where two copper tubes were soldered in. These tubes served as gas inlet and outlet, respectively, as the argon was continuously condensed in and re-evaporated during operation. Both tubes had a length of about 300 cm and were in thermal contact to each other. This system served as heat exchanger for the gas. In order to save space, the tubes were bent into the shape of a coil.

Most of the components were screwed to the target cell with brass screws. The coefficient of thermal expansion of brass is larger than that of pure copper [Smi51], therefore, the screws even tightened the sealings during cool-down. The temperature of the system was monitored at four different positions with PT-100 resistance thermometers: one directly at the cell, one thermometer each at gas inlet and outlet, and one thermometer at the tantalum aperture.

The whole setup was mounted inside of a vacuum-tight CF-100 cross piece, which was connected directly to the beam line. All feed-throughs (gas inlet and outlet, electric feed-throughs) were vacuum-tight. The vacuum around the target cell served several purposes: firstly, both the ion beam and the VUV scintillation light would be absorbed by air[4]. Secondly, the target cell was cooled to very low temperatures, therefore, any residual gas in the system would condense on all cold surfaces, diminishing the transparency of the MgF_2-exit window. And thirdly, the vacuum thermally insulated the cell from the CF-100 cross piece, which was at room temperature. However, the temperature difference between the cell and the outside parts of the setup was so big that thermal radiation played an important role. Therefore, all parts of the target cell, except for the MgF_2-window and the tantalum aperture, were wrapped into several layers of superinsulating mylar foil. All other contributions to the heat input like the ion beam itself, the thermal conduction through the gas tubes, or the flowing gas are by far smaller than the heat input by thermal radiation. A test cool-down showed that the cooling power of liquid nitrogen was sufficient to bring the cell to temperatures below the condensation temperature of argon; a cooling curve recorded with the PT-100 thermometer at the cell is shown in fig. 10.3. The condensation temperature was reached ~ 100 minutes after the start of the cool-down.

For testing purposes the fully assembled system was installed at the beam line, but at first without any light detector. A viewport at the detector's connection flange allowed an observation of the cell during operation. A picture of the cell half-filled with liquid argon is shown in fig. 10.4.

10.2 Beam-Line Setup at the Accelerator Laboratory

The heavy ion beam used to excite the argon was provided by the Munich Tandem Accelerator Laboratory (figs. 10.5 and 10.6). The ion source of this accelerator is capable of injecting nearly all elements, ranging from protons to very heavy ions like iodine or lead. At first, the particles leave the ion source singly negatively charged and gain a relatively small amount of energy ($\sim 200\,\mathrm{keV}$) in a pre-accelerating stage. After that, they enter the main accelerator

[4] The light absorption by air is mainly due to oxygen, which is opaque for wavelengths shorter than $\sim 185\,\mathrm{nm}$ [Ulr11].

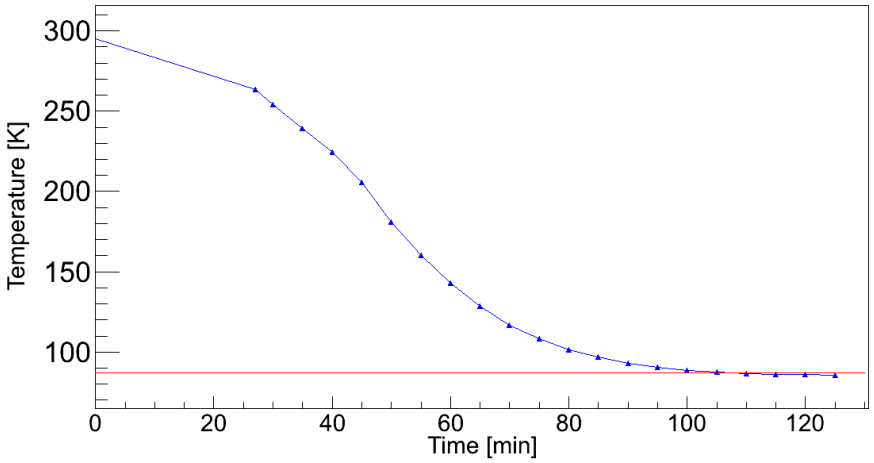

Figure 10.3: *Cooling curve of the target cell. The time (given in minutes) starts with the filling of the dewar with liquid nitrogen. The condensation temperature of argon (87 K; indicated by the red line) is reached about 100 min after start of the cool-down.*

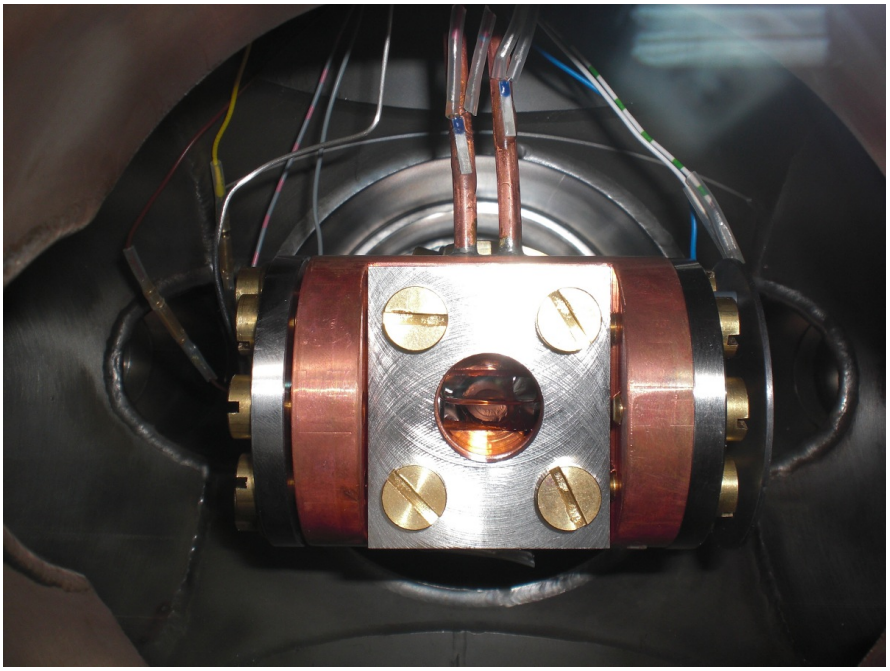

Figure 10.4: *Photograph of the fully assembled target cell half-filled with liquid argon in a test setup at the MLL beam line. The surface of liquid can be seen in the middle. The light detector was not yet installed at that time, but instead a viewport at its connector flange. The connection of the cell to the dewar is on the backside; the gas inlet and outlet can be seen on top. In the experiments the heavy-ion beam will come from the right, pass the tantalum aperture, and enter the liquid argon through the titanium foil.*

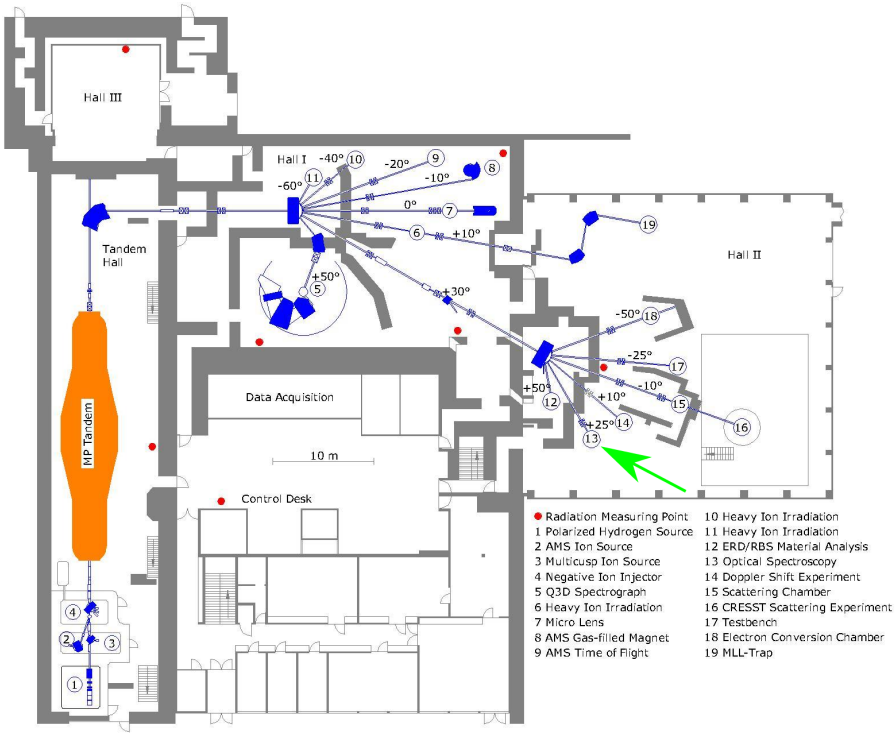

Figure 10.5: *Plan overview of the MLL Tandem Accelerator. The accelerator tank is depicted on the left side in orange colour, the beam lines to the single experiments and the magnets for steering the beam in blue. The experiments on scintillation spectroscopy were set up at the beam line +25° in hall II (no. 13; indicated by a green arrow).*

tank, where they gain energy by passing through the accelerating potential difference of about 12 MV, which is applied between the entrance point and the stripper foil in the middle of the tank. The stripper foil, a thin carbon foil, is hit by the particles and strips off electrons of the injected negatively charged ions. Hence, the ions are positively charged and can gain further energy by passing the potential difference once again. The final energy of the ion is consequently given by (z+1)·12 MeV, where z denotes the charge of the ion after the stripper foil. Typically, z has values up to 15 [Kos10]; the maximally reachable energy is thus limited to about 200 MeV per ion.

Figure 10.6: *Photograph of the Tandem Accelerator tank (orange) and the first deflecting magnet (blue).*

After being accelerated the ions are selected by their charge in the first deflecting magnet, which bends the beam by 90°. Thereafter, they are magnetically guided to the experiment through evacuated beam lines.

However, the Tandem Accelerator can produce not only direct current beams (DC beams), but also pulsed ones with a pulse duration down to a few nanoseconds. For this purpose two beam choppers, one at the low-energy side and one at the high-energy side of the accelerator tank, and one beam buncher at the low-energy side are installed [Cie11].

The choppers cut out selected parts of the beam, producing the pulsed beam and reducing also the time-averaged beam power. The buncher compresses the single beam packets and reduces their length. In addition, the beam choppers deliver a fast logic signal at the start of the beam bunch, which can be used to trigger the detector in time-resolved measurements.

As already mentioned above, the ions entered the target cell through a $1.5\,\frac{\mathrm{mg}}{\mathrm{cm}^2}$-thick titanium foil, which consequently lead to some energy loss prior to the energy deposition in argon. Especially for heavy ions these losses cannot be neglected; table 10.1 lists some values for ion beams used during the measurements for this thesis.

ion	energy [MeV]	energy loss [%]
p^{+}	10	1.3
O^{6+}	70	6.8
S^{9+}	115	14.5
S^{10+}	120	13.7
Au^{14+}	195	41.0

Table 10.1: *Energy loss in the titanium entrance foil of the liquid argon target cell of the different ion beams used. For the light ions the Bragg peak, i.e. the part of the track with the highest specific energy loss, lies behind the entrance foil, therefore, the energy losses are small. However, for the heavy ions the energy losses are not negligible. All values were calculated using the program LISE++ [Tar08].*

Finally, the ion beam deposited its remaining energy in the argon, typically on a track length of less than one millimetre (see plot in fig. 10.7).

Besides the target cell in its CF-100 cross piece the experimental setup at the beam line included a gas system, a photon detector (see sec. 10.3), and supplementary installations for pumping and beam monitoring (fig. 10.8). A closed cycle gas system was used[5], which was all metal-sealed. The system was used for circulating argon through the target cell with a metal-bellows pump; the cell was added as a bypass to the system. In addition, a rare gas purifier was installed in the main gas loop, which contained a hot titanium sponge as active medium and removed most of the impurities like oxygen, nitrogen, or water vapour from the circulating argon, but not other rare gases. The argon was continuously condensed into the target cell and re-evaporated; by this, its purity was kept on the highest possible level. A 10 l expansion volume was installed in the gas system to store purified argon, thus no unpurified argon from the bottle was needed to be refilled during cool-down and condensation.

The beam line was pumped to a vacuum of 10^{-7} mbar with a turbomolecular pump and an ion getter pump; the insulating vacuum around the target cell, which was not pumped directly but only connected to the beam line through a KF-40 metal bellows, reached hereby values of $\lesssim 10^{-5}$ mbar. During cooling of the target cell the cryo-getter materials in the insulating

[5] A schematic drawing of the gas system can be found in [Neu12a], figure 2.

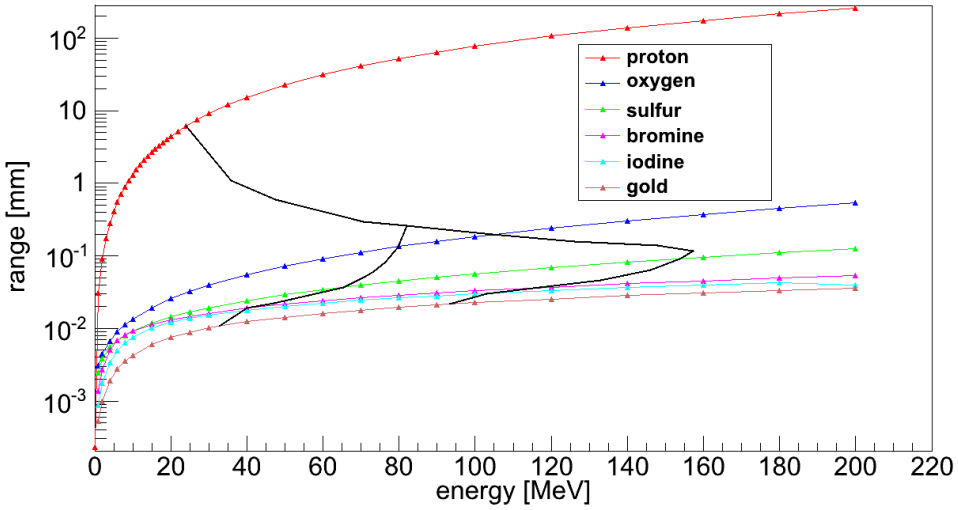

Figure 10.7: *Range of different ion beams in liquid argon as a function of the beam particle's energy. The black lines indicate the approximate energy limit of the Munich Tandem Accelerator minus the energy loss in the titanium foil, once for a maximal charge state of the ion of 6+ (left line) and once for the maximal charge state 14+ (right line). Except for very light ions like protons the energy deposition happens in a very small volume directly after the entrance foil. All data calculated with the program LISE++ [Tar08].*

vacuum of the liquid nitrogen dewar, which was connected directly to the vacuum around the target cell, improved the latter vacuum further by roughly one order of magnitude. Directly in front of the target cell a retractable Faraday cup was installed in the beam line to precisely measure the beam current. In addition, for measurements with a pulsed beam a capacitive probe ("pick-off") was installed, which delivered a fast trigger signal at each beam bunch passing. Besides the chopper signal from the accelerator, this fast signal could also be used to trigger the detector read-out for time-resolved measurements.

10.3 The Four Beam Times in Overview

The scintillation properties of gaseous and liquid argon were investigated in four beam times using two different detection techniques and different ion beams for argon excitation.

10.3.1 Experiments with the VUV-Reflection Grating Monochromator

Three beam times were performed with a VUV-reflection grating monochromator (McPherson model 218 [McP12]) with a focal length of 30 cm. This monochromator has a criss-cross Czerny-Turner design; the selected grating had 1200 lines per millimetre and a blaze wavelength of 150 nm. Fig. 10.9 shows the opened monochromator. It was evacuated during operation with a separate turbomolecular pump to be able to measure VUV-light. As already mentioned above, at the beam-line setup the scintillation light emitted by argon was at first collected by a mirror optics which is adapted to the aperture ratio of $\frac{D}{f} = \frac{1}{5}$ of the monochromator, and was subsequently focused onto the entrance slit of the monochromator.

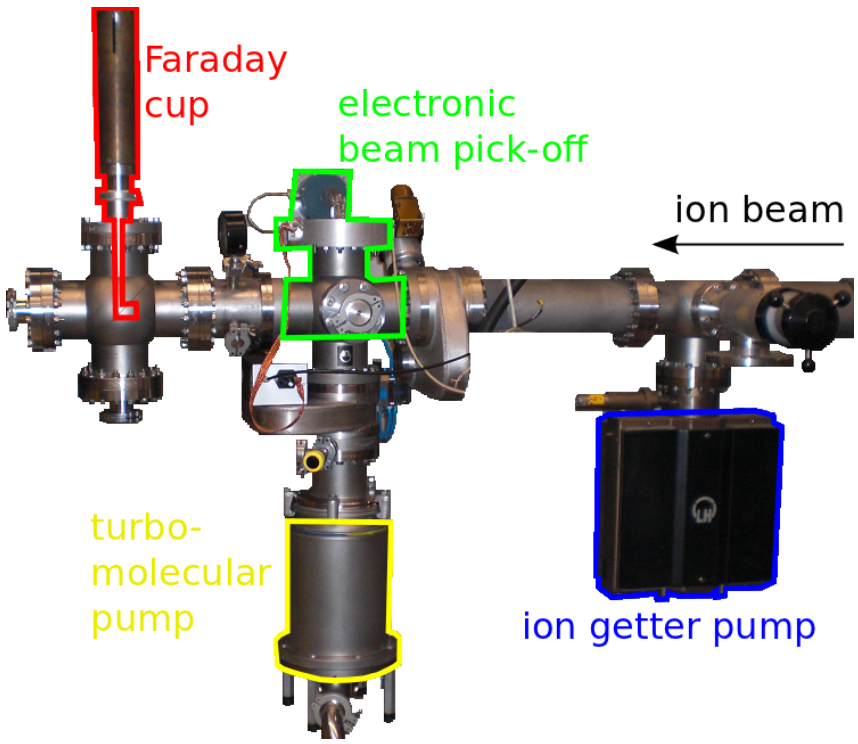

Figure 10.8: *Photograph of the experimental setup at the beam line in front of the target cell (to the left of the picture; not visible here). The ion beam comes from the right. In the middle, the turbomolecular pump (yellow) for pumping the beam line can be seen, to its right the ion getter pump (blue). The cross piece on top of the turbomolecular pump (green) contains the electronic beam pick-off, the cross piece on the left the Faraday cup (red).*

The adjustable mirror optics hereby allowed an optimal focus even for small displacements of the target cell by thermal contractions during the cool-down. In addition, for the experiments with a 10 MeV-proton beam, which has a range in liquid argon of ~ 1.2 mm, the scintillation light production can be scanned along the track.

Inside the monochromator the light is parallelised by a curved mirror and hits the reflection grating. There, it is split into its spectral components. The diffracted light from the grating is reflected by a second mirror onto the multi-alkali cathode of a VUV-sensitive PMT. By rotating the grating with a computer-controlled stepper motor the wavelength can be selected. The wavelength-resolved scintillation spectra were obtained by scanning a certain wavelength range in small steps and recording the count-rate of the PMT for each step. The PMT was hereby used in single photon counting mode, and the signal count-rate never exceeded ~ 100 kHz, where the PMT was still in a linear regime.

The wavelength resolution is determined by the widths of the slits, which are regulated with micrometre-screws. Typically, the scintillation spectra were recorded with a slit width of 100 µm, which translates into a resolution of $\Delta\lambda \approx 0.3$ nm for the grating used [Ulr11].

Between the mirror optics and the monochromator a turnable filter wheel was installed, which allowed a filter change without breaking the monochromator's vacuum. Four different positions of this wheel were used: no filter, a sapphire disc, a glass disc, and an aluminium plate. The sapphire and the glass filter were used to cut out the higher diffraction orders of the

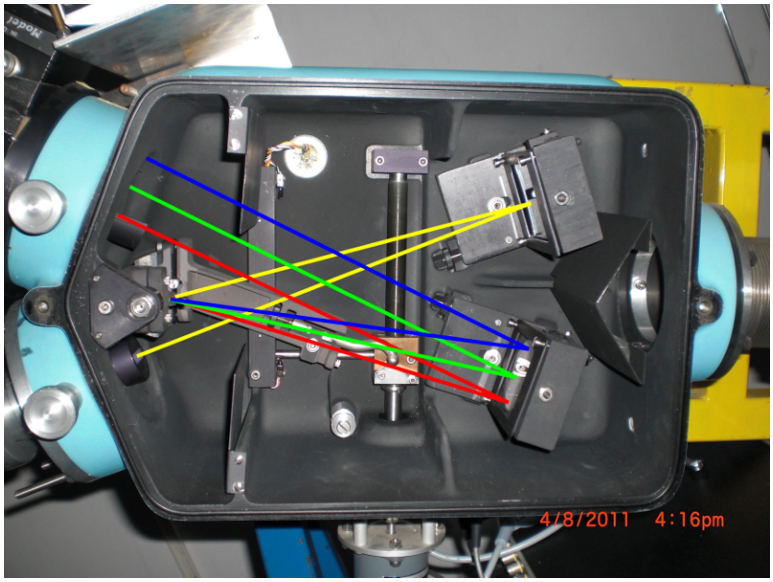

Figure 10.9: *Opened reflection grating monochromator. The scintillation light (indicated by the yellow line) enters the monochromator through an adjustable entrance slit (lower left corner) and is parallelised by the upper curved mirror. After being split up by the reflection grating (middle left) the light is reflected by the second mirror onto the PMT cathode, again through an adjustable slit. The reflection grating can be turned by a computer-controlled stepper motor to select the wavelength to be analysed.*

scintillation light when recording wavelength spectra at longer wavelengths; the aluminium plate allowed to determine the detector's dark count-rate. The cut-off wavelength of sapphire is at about 140 nm [Kor12a], and the glass used is transparent for wavelengths longer than $\sim$310 nm. Typically, the wavelength-resolved spectra were recorded in a wavelength region from 105 nm to 250 nm without any filter[6], from 230 nm to 350 nm with the sapphire filter, and for wavelengths above 320 nm with the glass filter. The overlap regions are used for an offline correction for the light attenuation by the filters.

In addition, this setup made time-resolved measurements possible. Hereby, the monochromator was set to a fixed but selectable wavelength. The time measurement was started by the PMT measuring the scintillation light; the stop signal came from either the capacitive probe of the electronic beam pick-off (fig 10.8), or in case this signal was too low, directly from the beam chopper. Physically the trigger signal from the pick-off or the chopper came first, however, to use it as a stop signal it was delayed with a precision gate generator. With this method, the time-resolved spectrum was recorded invertedly, however, this technique ensured a valid stop signal for each start signal. The light intensity was so small that the PMT was triggered only about every 100^{th} beam pulse, therefore, also time structures at longer times could be measured. It was hereby thoroughly checked that the emission time constants do not depend on the current of the ion beam used and the width of the entrance slit of the monochromator, i.e. the light intensity. The PMT trigger signal was generated from the

[6]In this case, the lower cut-off wavelength is simply given by the transmission curve of the MgF_2-window of the target cell, which is transparent down to $\sim$110 nm [Kor12]. The wavelengths below this cut-off are used to determine the background level (dark count-rate; $\sim$50 Hz noise).

PMT pulses by a constant fraction discriminator to minimise effects from the PMT jitter.

A time-to-amplitude converter (Ortec 566) in the read-out electronics with adjustable time range (500 ns or 5 µs) then converted the time difference between the two logic signals into an analogue signal, whose height is directly proportional to the time difference. This analogue signal was then converted into a digital one by a 13-bit ADC (Ortec AD413A), and fed into a personal computer via a CAMAC-to-PC interface. There, the voltage of the digital signal was stored in a histogram. Typically, 1,000,000 valid signals were recorded in such a histogram for each wavelength investigated. With this method the time structure of the scintillation light of liquid argon was measured for a set of selected wavelengths; sec. 11.3.

Three different beam times were carried out for a systematic investigation of the scintillation properties of argon with three different projectiles: protons were chosen as light incident particles, sulfur ions (S^{10+}) as particles with an intermediate mass[7], and gold ions (Au^{14+}) as heavy projectiles. For the sulfur and the gold beam the maximum possible energy of the Munich Tandem Accelerator was fully utilised (120 MeV and 195 MeV, respectively), however, for the proton beam the energy had to be lowered to 10 MeV (instead of the maximum possible 24 MeV) as otherwise the specific energy loss of the protons would have been too low to ensure a good signal-to-noise ratio. In addition, protons with only 10 MeV energy are fully stopped already within the liquid argon avoiding problems with a radioactive activation of the cell's endcap.

10.3.2 The Ultraviolet, Visible, and Near Infrared Grating Spectrometer

In order to study the scintillation light emission of argon near wavelengths beyond the third excimer continuum (> 350 nm) up to the infrared region a fourth beam time was performed using a grating spectrometer (OceanOptics model QE65000 [Oce12]) instead of the mirror optics, monochromator and PMT. This UV-Vis grating spectrometer covers a wavelength region from ~ 250 nm to ~ 950 nm with a measured optical resolution of ~ 1.4 nm at a wavelength of 700 nm (FWHM). It is capable of subtracting the dark count-rate online and can record the full wavelength-resolved spectrum at once. The read-out electronics is fully implemented in the spectrometer, for the offline analysis the data are transferred to a PC via an USB-interface. Higher diffraction orders of the spectral features are cut out by internally installed filters, which made the use of additional filters in an external filter wheel unnecessary. However, time-resolved measurements were not possible, and the main components of the scintillation light like the second excimer continuum, which are in the UV and VUV range, cannot be recorded, too.

The scintillation light emitted by argon was fed into the spectrometer via a lens in a vacuum feed-through and a glass fibre. For the measurements with the grating spectrometer again a filter wheel was installed between target cell and detector. Besides an empty position for measuring down to the shortest wavelengths possible, an aluminium plate (for measuring the dark count-rate) and a thin mylar foil were installed in the filter wheel. The latter was used for a measurement of the gamma-ray background, as it is opaque to photons from the VUV to the IR range, but can be passed easily by X-rays due to its low atomic number and its small thickness. The gamma-ray background would show up as a broad continuum underlying

[7] In principle, an argon beam would be desirable to study, as any particle recoiling off in some liquid argon bulk material (like WIMPs) produces fast argon nuclei. However, an argon beam is difficult to prepare at the Tandem Accelerator as argon atoms can hardly be charged negatively. Therefore, a sulfur beam is used instead, as the atomic mass of sulfur is close to the atomic mass of argon, but beam preparation is rather easy.

the scintillation light. The last two positions of the filter wheel contained two sapphire filters coated with sodium salicylate, a wavelength shifting material. At one filter the scintillating side faced the target cell, at the other filter position it faced the light detector; fig. 10.10.

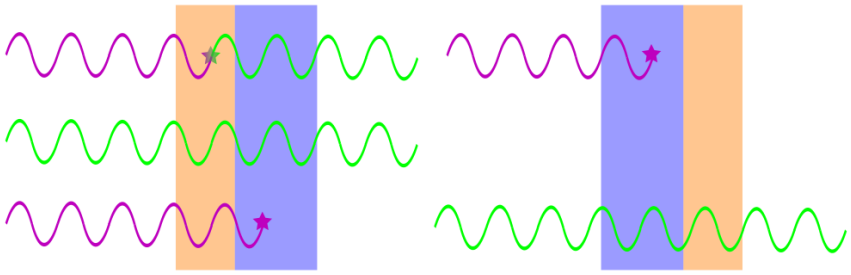

Figure 10.10: *Sapphire filters coated with sodium salicylate as used in the filter wheel for the grating spectrometer. At one filter position the scintillating material (light ochre) coated onto the sapphire (light blue) faces the target cell (left). There, the VUV photons (purple) emitted by argon can be converted into visible light (green) before they pass the sapphire (which is transparent for visible light, but not for VUV light) (upper case). Any residual VUV light (lower case) will eventually be blocked by the sapphire sheet. Optical photons can pass the filter combination unaffectedly (middle). At the second filter position the scintillating coating faces the light detector (right), hence, any VUV light will be absorbed by the sapphire (top). Optical photons can again pass (bottom).*

In case the scintillating coating faced the target cell VUV light emitted by argon could be converted into visible light ($\sim$400 nm to 500 nm [Sam67]), which is capable of passing the sapphire sheet. Sapphire is opaque to VUV light, but transparent for wavelengths above $\sim$140 nm. Any remaining VUV photons were consequently absorbed by the sapphire. Photons in the visible range, however, could pass the filter combination nearly unaffectedly, except for some attenuation. This orientation of the sodium salicylate-sapphire combination thus allowed to measure both the visible light and the wavelength-integrated intensity of the VUV component of the scintillation light of argon.

In case the scintillating coating faced the light detector any VUV components of the scintillation-light were absorbed by the sapphire. Only visible light could pass the filter and be detected in the grating spectrometer. The coating with sodium salicylate thereby ensured the same attenuation of this filter combination for visible photons as the orientation the other way round. Comparing the spectra recorded with the two orientations of the filter combination the integral light output in the VUV range could be monitored, and any time dependent processes which diminish the detectable light intensity (for example a decreasing transparency of the cell's MgF_2-window) could be discovered.

The studies of the long-wavelength components of the scintillation light of argon were performed with three different ion beams: protons (10 MeV), oxygen (O^{6+}; 70 MeV), and sulfur (S^{9+}; 115 MeV). Heavier nuclei than sulfur were not used for these studies as the experiments with the gold beam posed some problems due to the high energy deposition in the titanium entrance foil, which caused the foil to rupture twice during that beam time (cf. also sec. 11.1.4).

Chapter 11

Ion-Beam Excitation of Liquid Argon: Wavelength-Resolved Emission Spectra and Emission Time Constants

In the three beamtimes with the Czerny-Turner monochromator and the attached PMT and the single beamtime using the UV-Vis grating spectrometer, the luminescence-light spectra of liquefied argon have been recorded for different beam projectiles from the 110 nm cut-off wavelength of MgF_2 (VUV region) to about 950 nm in the near infrared. The read-out electronics of the monochromator setup furthermore allowed to perform time-resolved measurements at a given wavelength. Both data yields information on the underlying scintillation mechanisms. In addition, the comparison of the spectra obtained with different ion- and electron-beam excitation, respectively, provides information on the particle-discrimination potential in liquid-argon detectors by means of the scintillation light only. This is an important input parameter for the design and development of future experiments for the search for rare-event physics (ch. 2 through 4).

The present study focuses on the experimental aspect of measuring the scintillation light of liquefied argon both wavelength- and time-resolved with high resolution and best statistics, the results of these experimental studies are presented in this chapter. In most cases also an interpretation of the underlying physics processes is given; for this purpose the picture is taken that liquid argon behaves just like a dense gas. This interpretation of the data succeeds to explain most of the phenomena observed, however, some experimental results cannot be understood in this model. These issues might be understood describing the liquid in an energy-band model, which is, however, not tried within the scope of the present thesis.

In sec. 11.1 the procedure of gas preparation and the settings of the ion beam used are explained. In addition, the correction functions to be applied to the raw data (detector response functions and correction for the diminishing transmission of the MgF_2-window due to deposition of residual gas from the insulating vacuum) are calculated. In sec. 11.2 the wavelength-resolved scintillation-light spectra of liquid argon (from the VUV to the near IR range) are presented, recorded with different ion beams (protons, oxygen, sulfur, and gold), and compared to the spectra obtained for the cold gas and with electron-beam excitation. Sec. 11.3 finally shows the results for the emission time constants measured for a set of selected

wavelengths, and an assignment of the various emission features to gas kinetic processes is tried.

11.1 Gas Preparation, Beam Settings and Correction Functions

11.1.1 Gas Cleaning and Impurities

Measurements performed on the scintillation light of argon with electron beam excitation [Hei10, Hei11, Hei11a] clearly show that some impurities have a major impact on the spectrum (fig. 11.1) and the emission time constants. Therefore, a crucial point for the scintillation experiments is the purity of the gas. As was explained in ch. 10 a rare gas purifier was installed in the outer gas system, which is capable of removing chemical impurities, like water vapour, nitrogen, or oxygen from the argon, but no other rare gases. The gas purification takes several hours, therefore, the 557.7 nm emission line caused by oxygen impurities was continuously monitored during the purification process: oxygen is known to be a severe impurity in terms of distorting the scintillation spectrum [Acc10], and the line at 557.7 nm [McC84], which stems from the $2^1\Sigma^+ \rightarrow 1^1\Sigma^+$ transition of the argon-oxide excimer molecule [Bel00], is one of the dominant light emissions[1]. The desired purity of the argon gas had been reached as soon as the oxygen impurity emission had vanished completely, which was typically the case a few hours after the start of the gas purification process. For all measurements presented in the following the purification was completed before the start of the cool-down.

Traces of xenon (< 1 ppm) still present in the argon used (see below) do not significantly disturb the measurements [Hei10, Hei11]: except for an emission line additionally appearing in the scintillation spectra of gaseous argon at 147 nm, the scintillation features of argon stay unaffected, as well as the corresponding emission time constants. Only much higher concentrations of xenon give rise significant spectral changes (for example the xenon excimer continua become dominant) and lower the intensity of light emission of pure argon. From a comparison of the scintillation spectra in the present thesis with spectra obtained for gaseous argon where traces of xenon were deliberately added [Eft97] the xenon concentration in the present data can be estimated to be far below 3 ppm in the gas phase. In the liquid phase, however, the cold target cell acts like a cold-trap for xenon possibly increasing its concentration by about a factor of ten [Bal65]. Comparing the scintillation spectra obtained with the ion beam to those recorded with the electron beam [Hei10, Hei11] the xenon concentration in liquid argon was found to be not higher than 0.3 ppm, and thus small enough to have no major impacts on the measurements. Therefore, in the data presented here no further removal of the residual xenon impurity (e.g. by fractional distillation) was needed.

11.1.2 Monitoring the Beam-Current Stability

Unlike the electron beam in the table-top setup used for recording the scintillation spectra of liquid argon [Hei10, Hei11, Hei11a] the ion beam provided by the Tandem Accelerator is not always stable in terms of beam current. To avoid the scintillation spectra to be spoiled by effects of a varying intensity of the ion beam the beam current was monitored throughout

[1] The scintillation light of pure argon appears whitish to the eye because of the underlying broad continuum. However, already small oxygen impurities make it green-coloured [Hei11].

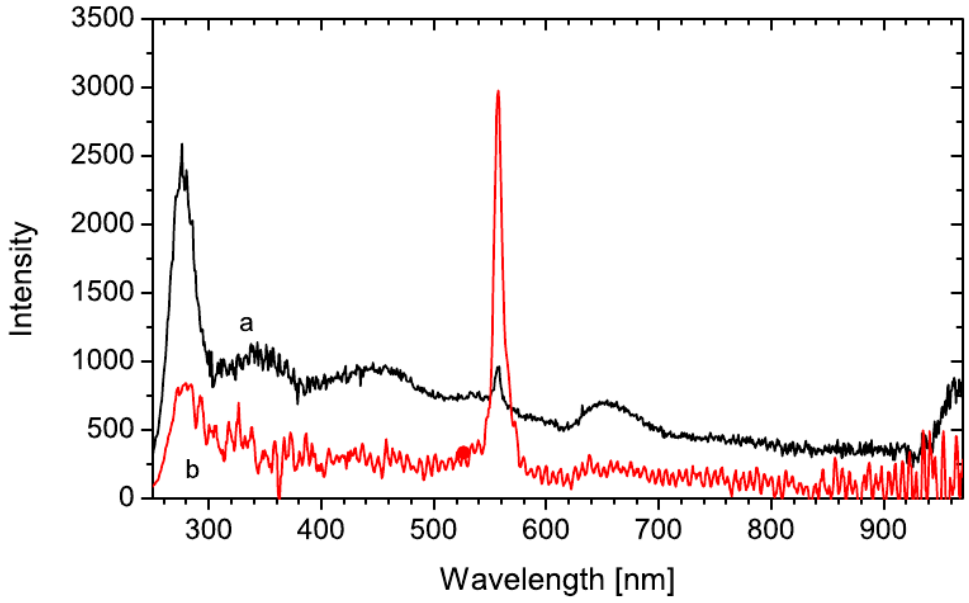

Figure 11.1: *Influence of an oxygen impurity on the scintillation-light spectrum of liquid argon: the unpurified spectrum (red; b) shows a very intense emission at ∼ 558 nm stemming from an argon-oxide excimer molecule (see text); all other spectral features lose significantly in intensity compared to purified argon (black data; a). Plot taken from [Hei11a]. Copyright by IOP Publishing Ltd (2011).*

the beam time. Immediately before and after recording wavelength-resolved spectra, which typically took one hour, the intensity of scintillation light at a certain wavelength (second excimer continuum) was recorded for several minutes to obtain information on the stability of the ion beam. Only if the beam current showed no variations beyond a ten-percent level the wavelength-resolved spectrum was taken for the analysis. In case the beam stability was not satisfying the recorded spectrum was rejected, the beam parameters were adjusted to achieve stable conditions, and the spectrum was recorded again. Typically, the beam current fluctuations are of the order of 5%, which adds to the total error margin of the scintillation spectra. As beam-current variations can also happen on a very short time-scale only spectral features which show up in more than one wavelength bin were taken to be true physics; all others were regarded as beam current instabilities. For the search for narrow emission lines this consequently urges an improved resolution, i.e. the width of the entrance slits of the monochromator and the step size of spectral recording had to be adjusted accordingly.

11.1.3 Determination of the Evaporation Threshold of Liquid Argon

Another important point in recording the scintillation-light spectra of liquefied argon is that the power density deposited by the ion beam must not exceed the threshold for evaporation. Otherwise small argon gas bubbles form along the particle beam track and, consequently, mainly the scintillation light of the gas phase is emitted. In the gas phase highly excited neutral argon atoms (ArI) can undergo radiative 4p-4s transitions [Lin88], radiating - amongst others - at a wavelength of 696.5 nm [NIS12]. These transitions, however, are suppressed in the liquid phase, as the competitive non-radiative de-excitations in collisions with other argon

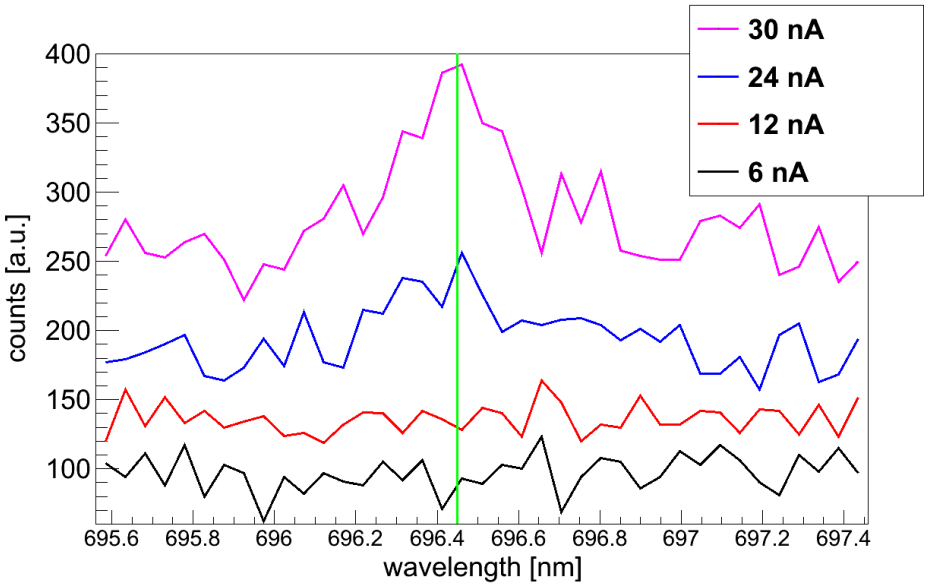

Figure 11.2: *The 4p-4s emission line of argon at 696.45 nm (position indicated by the green line) for different values of the beam current: black 6 nA, red 12 nA, blue 24 nA, and pink 30 nA. The different spectra are shifted along the y-axis to make the differences better visible. The 4p-4s line is invisible for beam currents of 6 nA and 12 nA, respectively, while it is indicated for a current of 24 nA and clearly visible for 30 nA. Hence, for this set of beam parameters the evaporation of the liquid argon starts at a beam current around 20 nA, and the beam current has to be kept at lower values for spectroscopy of liquid argon.*

atoms are favoured due to the high density, and the line widths are much broader than in the gas phase [Hei11]. Unlike photons of optical resonance transitions of excited atoms to the ground state the 4p-4s photons can travel freely even in the liquid phase, as their energy is not sufficient to excite argon atoms in the ground state, and the density of already excited atoms, which could absorb these photons, is much too small. Therefore, these emission lines are a good indicator for evaporation of the liquid.

Each time the settings of the ion beam are changed (different energy, particle, or charge state) the 696.5 nm emission line is looked for, and in case it appears the beam current is lowered to values corresponding to less than half of the evaporation threshold. Fig. 11.2 shows a set of dedicated measurements with a sulfur beam where the beam current is deliberately increased to make the liquid argon boil. The 4p-4s emission line is clearly visible for a beam current[2] above 24 nA, which corresponds to an average power density[3] of $1\,\frac{\mathrm{W}}{\mathrm{mm}^3}$. For the measurements with liquid argon the current of the sulfur beam, for example, is finally set to approximately 10 nA which corresponds to half the value where evaporation starts.

However, the energy deposition by the ion beam leads to a local heating of the liquefied

[2]Measured at a Faraday cup directly in front of the target cell.

[3]This power density is calculated by dividing the power of the beam by the volume of energy deposition. The latter is simply assumed as a cylinder with a length equal to the penetration depth of the ion beam in the liquid argon and a radius equal to the radius of the inner bore of the beam entrance flange. This calculation, however, does not take into account the inhomogeneous distribution of the energy deposition along the beam's track and is therefore only an estimate of the average value. For the electron beam, peak power densities up to 60 $\frac{\mathrm{W}}{\mathrm{mm}^3}$ have been reported [Hei11, Hei11a] before the liquid argon boils.

argon. Consequently, the exact temperature of the liquid volume emitting the luminescence light cannot be determined, but only the average temperature of the target cell, which is measured with the PT-100 resistance thermometers. Therefore, all temperature values quoted in the following are only approximate values. The only conclusion that can be drawn from the non-observation of the 4p-4s transition lines is that the local temperature does not exceed the boiling temperature of liquid argon at 970 mbar pressure. Most likely, all results of the present thesis are obtained for a state of liquid argon just below the evaporation threshold ($\sim$87 K).

The average energy to create an electron-ion pair in liquid argon is 23.6 eV [Dok02]. Using the power density of 1 $\frac{\mathrm{W}}{\mathrm{mm}^3}$ calculated above this leads to a production rate of $2.6{\cdot}10^{17}$ electron-ion pairs per second and mm^3. Most of the recombinations of these pairs happen rather fast on a timescale of nanoseconds (see ch. 9). Assuming that all these recombinations lead to an excimer state, equilibrium densities of $2.0{\cdot}10^{8}$ for excimer molecules in the singlet state (life time $\sim$3 ns) and $2.5{\cdot}10^{11}$ in the triplet state (1.3 µs) per mm^3 are obtained. These calculations are carried out for the data obtained with the proton beam[4], see tab. 11.2 on page 187. The density of liquid argon is 1.4 $\frac{\mathrm{g}}{\mathrm{cm}^3}$ [Var83], which translates into a particle density of $2.1{\cdot}10^{19}$ per mm^3. This is nearly eight orders of magnitude higher than the summed density of excited states. Therefore, the probability for an excitation of an already excited argon atom is negligibly small, even if the deposited power density is locally higher than 1 $\frac{\mathrm{W}}{\mathrm{mm}^3}$ estimated above. The excitation by the ion beam is consequently equal to an excitation by single particles; almost all photons which are emitted by the liquid argon volume stem from excited states which have been produced in an interaction with one single beam-ion only.

11.1.4 "Fogging" of the Windows

In the course of monitoring the light intensity in the VUV range with the salicylate-coated sapphire filter and the UV-Vis grating spectrometer, and during the measurement of the attenuation length of liquid argon [Neu12, Neu12a] a technical problem was found: the MgF_2-window of the target cell got cold enough to have residual gas from the insulating vacuum continuously deposited on it[5]. This growing layer causes the window's transmission to reduce significantly, especially in the important VUV-range. It is no problem for visible light and for the time-resolved measurements at a certain wavelength, however, it has a non-negligible impact on the short-wavelength parts of the scintillation spectrum.

To be able to correct for the diminishing transmission a set of transmission curves for different times after start of the cool-down was recorded using the setup for the attenuation experiments [Neu12, Neu12a], as the transmission, and with it the "fogging" of the window, cannot be determined directly with the beam-line setup. In the setup for the attenuation experiments the target cell had a MgF_2-window both on the front and the back end (instead of the beam entrance flange with titanium foil and the endcap). Light from a deuterium arc lamp was collimated, sent through the empty cell, and detected on the other end with a monochromator and a detector consisting of a microchannel plate and a photodiode array [Neu12]. Except for the replacement of the beam entrance flange and endcap by the windows the whole setup with the target cell was the same, especially the cooling equipment. This ensures comparable conditions, e.g. cooling speed and cooling time. The usage of the photodi-

[4]For the sulfur beam equilibrium densities of $1.1{\cdot}10^{9}$ (singlet state) and $5.7{\cdot}10^{10}$ (triplet state) per mm^3 are obtained.

[5]This effect will be called "fogging" in the following.

ode array as detector allowed to record a wavelength interval of 75 nm in one exposure, which made the measurements rather fast. Typically, recording one full spectrum, covering wavelengths from 118 nm (cut-off wavelength of the light source used [Neu12]) through 250 nm, took only a few minutes. In this way, any systematic effects of the transmission changing during the measurement were excluded.

In order to obtain the transmission curves the recorded spectra were corrected for dark-noise and stray-light, and divided by a reference spectrum which was recorded with the empty warm cell and also dark-noise and stray-light corrected. The measurement was repeated each hour after the start of the cooling for in total 26 hours (interrupted by a 16 hours gap during the night), which is longer than the longest time difference needed between filling of LN_2 and recording the final wavelength-resolved spectra with the ion beam. Hence, the transmission curves obtained can be used to correct the spectra for the "fogging" effect, provided that the time of the measurement is known. As all measurements are computer-controlled time and date of each spectrum can precisely be determined in the offline analysis by using the time-stamp of the creation of the file. Fig. 11.3 shows the transmission curves as a function of wavelength, covering wavelengths from 118 nm through 250 nm. For wavelengths longer than 220 nm the "fogging" effect is small and does not show any additional features. In case a "fogging" correction had to be applied to data at wavelengths beyond 250 nm the transmission curves were linearly extrapolated. The transmission curves were recorded again in a second independent measuring campaign using the same setup; both measurements show good agreement, verifying the obtained results.

In fig. 11.4 the transmission is plotted as a function of time for a set of dedicated wavelengths, including a set of exponential fits to the data. These fits match the recorded data quite well, which can be understood for a linear growth of the residual-gas layer, assuming an attenuation of the light following Lambert-Beer's law [Mor10]:

$$\frac{I(l)}{I(l=0)} \propto e^{-\frac{l}{l_0(\lambda)}} \quad . \tag{11.1}$$

I(l) denotes the transmitted intensity, l the thickness of the absorbing layer; l_0 is the absorption length. As the latter is wavelength-dependent, different attenuation values are obtained for different wavelengths. The functions fitted to the data, averaged over an interval of 1 nm in wavelength to reduce the effect of statistical fluctuations, are used to correct the beam-time data for the "fogging" of the MgF_2-window.

However, the correction for the diminishing transmission has to be taken with some care. The vacuum during the transmission measurements started at about $4{\cdot}10^{-6}$ mbar in the surrounding CF-100 cross piece and reached $3{\cdot}10^{-7}$ mbar for the cold cell [Neu12] when the cryo-getter materials in the dewar vacuum became active, while the vacuum at the beam line was worse (about $1{\cdot}10^{-5}$ mbar for the warm cell and $8{\cdot}10^{-7}$ mbar for the cold cell) during the beam time with the sulfur beam. During the beam time with the gold beam the insulating vacuum had to be broken twice to replace a damaged titanium entrance foil. This caused the vacuum to become considerably worse (about three times) during these measurements. The beam time with the proton beam was only five days after the gold beam time, therefore, the vacuum still was not at its best, and the residual pressure was about $2{\cdot}10^{-5}$ mbar for the warm cell and $\sim 1.4{\cdot}10^{-6}$ mbar for the cold cell. These pressure differences are properly taken into account for the "fogging" corrections: assuming a linear growth of the absorbing coating with time which is proportional to the residual pressure, the time constants of the exponential diminution of the transmission scale with pressure, too. For example, for the data recorded

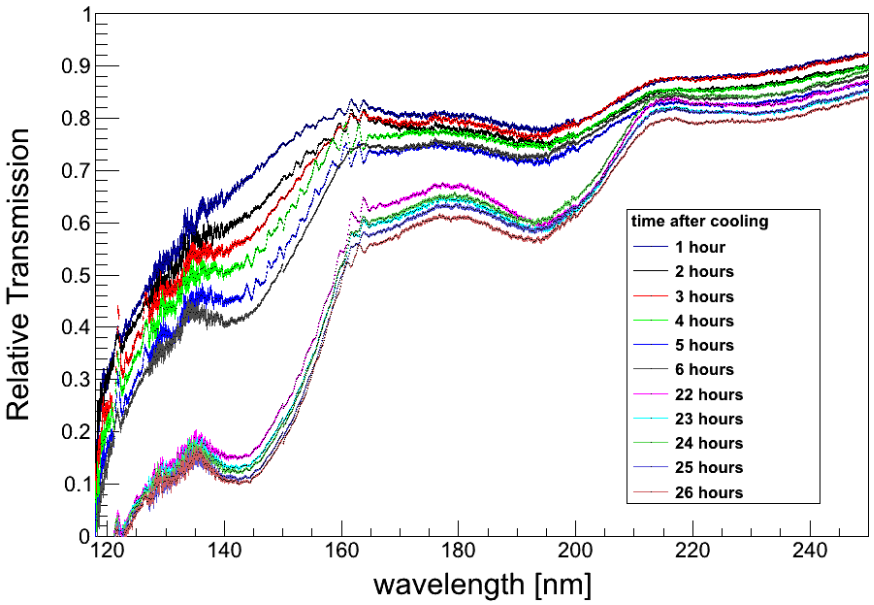

Figure 11.3: *Transmission curves of the MgF_2-windows of the target cell as a function of wavelength for different times after cool-down recorded in the setup for the attenuation length measurements [Neu12]. The single curves are corrected for stray-light and dark-noise; a wavelength region from 118 nm to 250 nm is covered. The transmission is greatly reduced for long times, especially for very short wavelengths. This effect is due to a "fogging" of the entrance windows with particles from the residual gas in the insulating vacuum, most likely water vapour.*

with the proton beam, where the insulating vacuum was about five times worse than during the determination of the "fogging", all time constants of the exponential decreases are divided by five.

However, the beam line setup has only one MgF_2-window, while the transmission is measured with two windows, doubling the attenuating effect. This is taken into account by simply cutting the measured attenuation by half, assuming a homogeneous growth of the absorbing layer on both windows.

During the beam time with the sulfur beam the scintillation-light spectrum of liquid argon was recorded twice, once directly after finishing the cool-down (the actual measurement; top panel of fig. 11.5), and once again 56 hours later at the end of the beam time (for cross-checking; displayed again in top panel of fig. 11.5). The target cell was hereby permanently cold. The two spectra are corrected for the "fogging" effect, each time applying the correct time delay between start of the cool-down and measurement. The result of this procedure is shown in the bottom panel of fig. 11.5. While for the raw-data spectra the intensity ratio between second and third excimer continuum clearly differs, it is equal for the corrected spectra. This proves the validity of the method described above, even for time differences between cool-down and measurement, which are considerably larger than the 26 hours when the last calibration measurement (fig. 11.3) was performed.

The validity of the "fogging" correction method could also be confirmed with a measure-

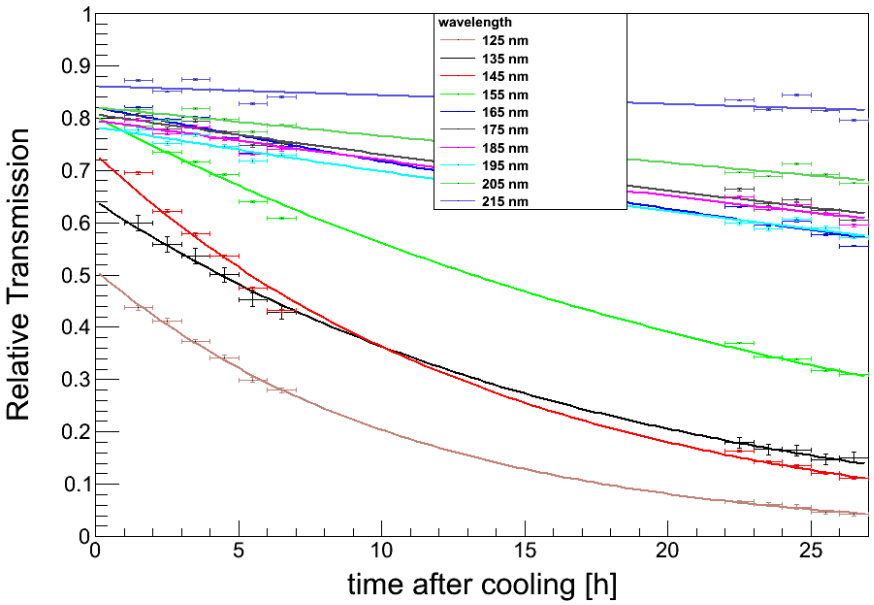

Figure 11.4: *Transmission curves of the MgF_2-windows of the target cell as a function of time after cool-down for a set of dedicated wavelengths. Again, the data are corrected for stray-light and dark-noise. The data are fitted with exponential decay curves, which match rather well, indicating a linear growth of the absorbing layer due to "fogging".*

ment performed with the proton beam: in fig. 11.6 a zoomed-in view of two wavelength-resolved spectra are shown, one spectrum (blue) covering wavelengths from 110 nm through 250 nm and recorded nearly 19 hours after start of the cool-down, and one spectrum (red) covering wavelengths from 140 nm through 250 nm and recorded about 14 hours after start of the cool-down. While the raw data spectra (top panel; only corrected for dark-noise as determined with the aluminium plate in the optical path) clearly show a difference, the spectra corrected for the "fogging" (bottom panel) match each other quite well. Especially the xenon impurity emission line (at 148.8 nm) has the same intensity in both plots, which is expected, as the gas - and with it the concentration of xenon - is the same in both cases.

Although the "fogging" effect can be corrected rather well, an experimental setup which avoids such a "fogging", or, at least, minimises its extent, would be desirable. This could be achieved by considerably improving the quality of the insulating vacuum, or by installing cryo baffles in front of the target cell. If these baffles were colder than the cell itself (e.g. cooled with liquid helium), and already cooled down before the actual cool-down of the target cell starts, deposition of any residual gas would mainly happen on the surfaces of these baffles and not on the MgF_2-window, thereby greatly diminishing the "fogging" effect.

11.1.5 The Detector Response Function

In order to correct the spectra recorded for any detector-related effects like the wavelength-dependent quantum efficiency of the photomultiplier or the reflectivity of the imaging optics the detector response function has been determined. A spectrum of gaseous argon at 300 mbar

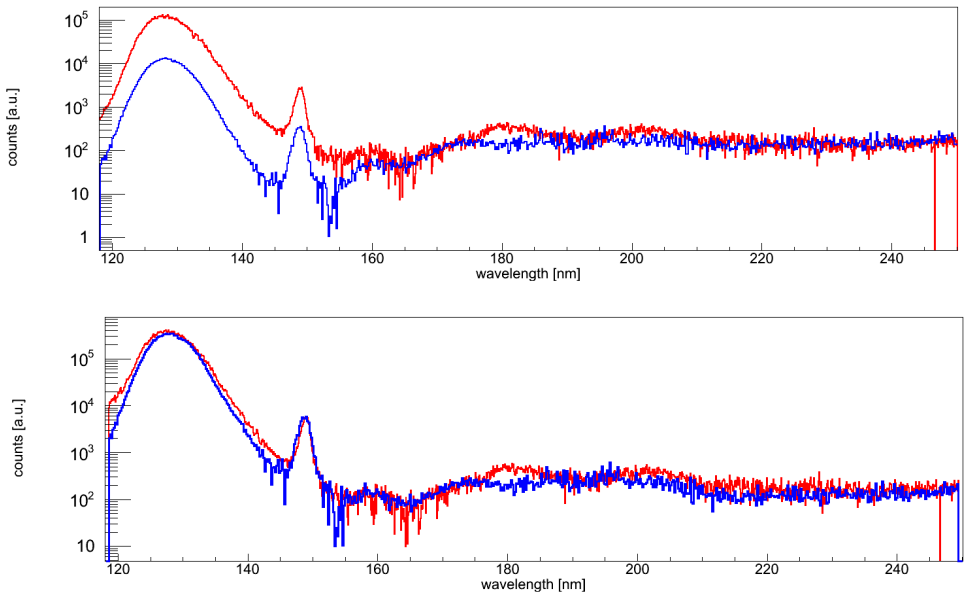

Figure 11.5: *Top panel: two raw-data spectra of liquid argon excited by the sulfur beam shown on a logarithmic scale for a wavelength interval from 118 nm to 245 nm. The spectrum in red is recorded directly after finishing the cool-down, the spectrum in blue 56 hours later. The spectra are scaled to match each other at 250 nm. Due to the "fogging" of the MgF_2-window the intensity of the third excimer continuum seems to be enhanced compared to the second excimer continuum. Bottom panel: same spectra but corrected for the "fogging" effect. Here, the intensity ratio between second and third excimer continuum is equal for both spectra, validating the correction method. Between 180 nm and 200 nm the blue spectrum suffers from an instability of the beam current. For this reason it was not used in the further analysis.*

and room temperature recorded with the detector system at the beam line [Ulr12] has therefore been compared to an absolutely calibrated spectrum of gaseous argon again at 300 mbar and room temperature [Mor08]. Both spectra are shown in fig. 11.7.

The ratio of these two spectra gives the wavelength-dependent detector response function, fig. 11.8. At short wavelengths it is steeply rising towards longer wavelengths, and becomes constant for wavelengths above ~ 180 nm, i.e. in the region of the third excimer continuum of argon. All data recorded with the beam line setup are corrected with this response function in the following. The detector response function was assumed to be flat beyond 220 nm up to 310 nm. For longer wavelengths the spectra obtained with the UV-Vis grating spectrometer were used for an analysis (see below).

Both the absolutely calibrated spectrum and the spectrum obtained with the beam-line setup were recorded with a MgF_2-window between the scintillating argon gas and the detector. Therefore, the transmission of MgF_2 cancels out in the calculation of the detector response function. As all the data obtained within the scope of the present thesis is recorded through a MgF_2-window light-losses due to attenuation and reflection at this window have in principle to be accounted for. Fig. 11.9 shows the wavelength-dependent correction factor f which has to be applied to the data to correct for reflections at the surfaces of the window. It is calculated using the Fresnel formula for unpolarised light perpendicular to the optical surfaces:

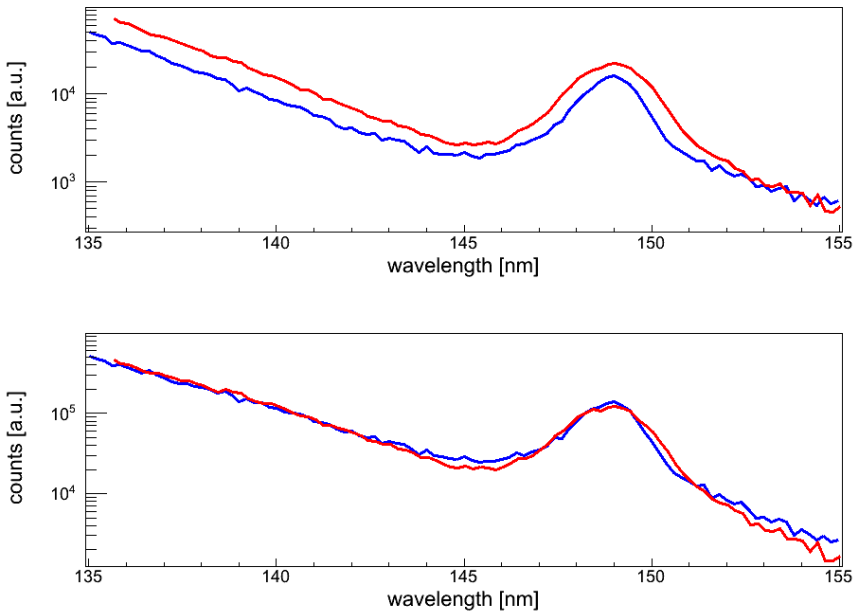

Figure 11.6: *Zoomed-in view (135 nm to 155 nm) of two scintillation spectra of liquid argon recorded with the proton beam at different times after start of the cool-down (blue: ∼ 19 h, red: ∼ 14 h). The top panel shows the raw data only corrected for the detector's dark-noise; the bottom panel the same spectra but corrected for the "fogging" effect. The raw-data spectra clearly deviate from each other, the corrected spectra match each other well. Especially the intensity of the xenon impurity emission line at 148.8 nm is the same, which is expected as the gas composition is not changed between recording the two spectra.*

$$f = \frac{1}{\left[1 - \left(\frac{n_{Ar} - n_w}{n_{Ar} + n_w}\right)^2\right] \cdot \left[1 - \left(\frac{n_w - 1}{n_w + 1}\right)^2\right]} \quad ; \tag{11.2}$$

the indices of refraction of cold argon gas and liquid argon, respectively, have been taken from [Ant04, Bid80], the index of refraction n_w of MgF_2 from [Lap83].

The correction is wavelength-dependent and reaches its highest values at short wavelengths. However, the index of refraction of MgF_2 has only been measured in a wavelength interval of 111 nm to 200 nm [Lap83], the index of refraction of gaseous argon at standard conditions (273.15 K, 1013 mbar) between 140 nm and 254 nm [Bid80]. The indices of refraction of argon gas at lower temperatures and higher pressures and of liquid argon, respectively, are calculated from the latter data by scaling with density [Ant04]. Therefore, the correction factor would have to be extrapolated for wavelengths below 140 nm (this is done in fig. 11.9) and above 200 nm, respectively. As this introduced big uncertainties, and as the index of refraction of liquid argon is unknown, a correction for the reflection at the MgF_2-window is not performed in the following. This, of course, additionally contributes to the total error margin with maximally ∼ 7% for liquid argon and ∼ 13% for cold argon gas (estimated from fig. 11.9 at 118 nm, the lower wavelength-end of the "fogging" correction, and assuming a flat distribution of the Fresnel correction factor for wavelengths longer than 200 nm).

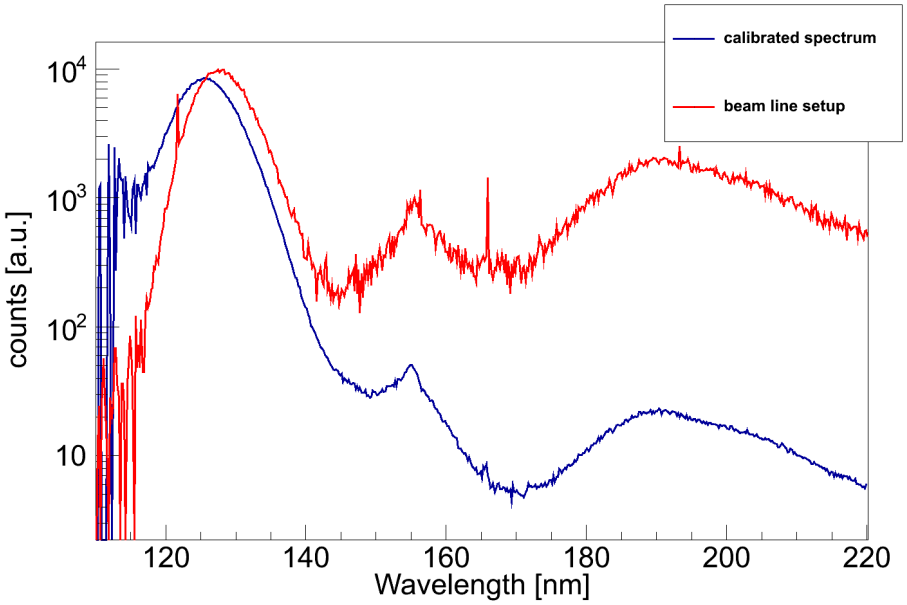

Figure 11.7: *Two spectra of gaseous argon at 300 mbar and room temperature. The spectrum in red [Ulr12] was recorded with the detector system at the beam line setup (imaging optics, McPherson 218 monochromator, and the VUV-sensitive PMT); the spectrum in blue is absolutely calibrated using a deuterium arc lamp [Mor08]. The spectra are scaled in such a way that they match at the peak intensity of the calibrated spectrum at 125.7 nm. Above 220 nm the second diffraction order of the second excimer continuum appears, therefore, spectra extending to longer wavelengths were not recorded. Both spectra show tiny residual impurities, in particular hydrogen (Lyman-α-line at 121.57 nm [NIS12]) and carbon (line at 165.7 nm [NIS12]). The impurity emission lines are erased from the detector response function by fitting the continuous scintillation spectra in a small wavelength interval around the lines.*

However, a comparison of scintillation-light spectra of liquid and gaseous argon can still be performed, as the overall shape of the correction function is the same[6], and the spectra are scaled to match each other at a certain wavelength. In addition, in any realistic experiment using liquid argon as scintillating medium some VUV-transparent window has to be used between the liquid and the detector, which could be, for example, the entrance window for some VUV-sensitive PMT. Hence, similar light-losses due to reflection happen as in the experiments presented here.

A determination of the index of refraction of liquid argon and the window material (MgF_2) in a broad wavelength interval would allow a correction of the data obtained for light losses due to reflection at the liquid-argon window surface (Fresnel correction). Hence, the comparison between the scintillation light spectra obtained for argon in gaseous and liquid phase, respectively, would become even more precise. A determination of the indices of refraction would, in addition, be very useful for measurements of the attenuation length of argon, which is best performed by a transmission measurement [Neu12, Neu12a].

The attenuation of the scintillation light in the MgF_2 is not taken into account, as it is very small and nearly independent of the wavelength for a broad wavelength interval (110 nm

[6]This is only the case if the assumption that the liquid behaves just like a dense gas holds true.

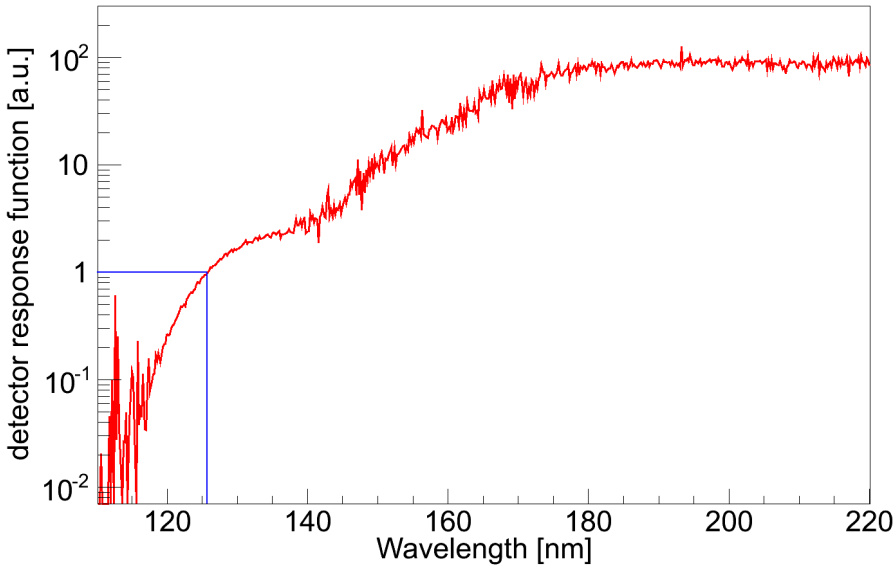

Figure 11.8: *Detector response function of the detector system (imaging optics, McPherson 218 monochromator, and PMT) used at the beam line setup on a logarithmic scale. It was calculated from the two argon spectra shown in fig. 11.7. The normalisation of the curve was arbitrarily chosen to one for the peak emission wavelength of the calibrated spectrum at 125.7 nm (blue lines); the response function covers a wavelength range from 110 nm through 220 nm. Towards shorter wavelengths it drops steeply; for wavelengths longer than 180 nm it becomes constant.*

through $\sim 4\,\mu m$) [Kor12].

The detector response function of the UV-Vis grating spectrometer (OceanOptics model QE65000 [Oce12]) is known [Dan12] in a wavelength interval from 185 nm through 970 nm, see fig. 11.10. This function was used to correct the spectra recorded with the grating spectrometer at longer wavelengths. Again, no correction for the different indices of refraction of gaseous and liquid argon were taken into account, for the same reasons as mentioned above.

11.2 Wavelength-Resolved Emission Spectra from the VUV to the Infrared with Different Incident Particles

The scintillation-light emission of liquid argon has been recorded for different ion beams in a broad wavelength interval covering the VUV-range from ~ 110 nm, the cut-off wavelength of the MgF_2-windows used, throughout the visible range up to 950 nm. The liquid was hereby stabilised at a temperature[7] of (86.2 ± 1.2) K (measured with the PT-100 thermometer directly at the target cell) and a gas pressure of 970 mbar. In addition, the full scintillation spectrum of gaseous argon at low temperatures ((98.8 ± 1.2) K) and 1200 mbar has been recorded, as well

[7] As was explained above the energy deposition by the ion beam causes the local temperature of the light emitting volume to be slightly above this value. However, this local temperature could not be measured, and only the cell's temperature is quoted.

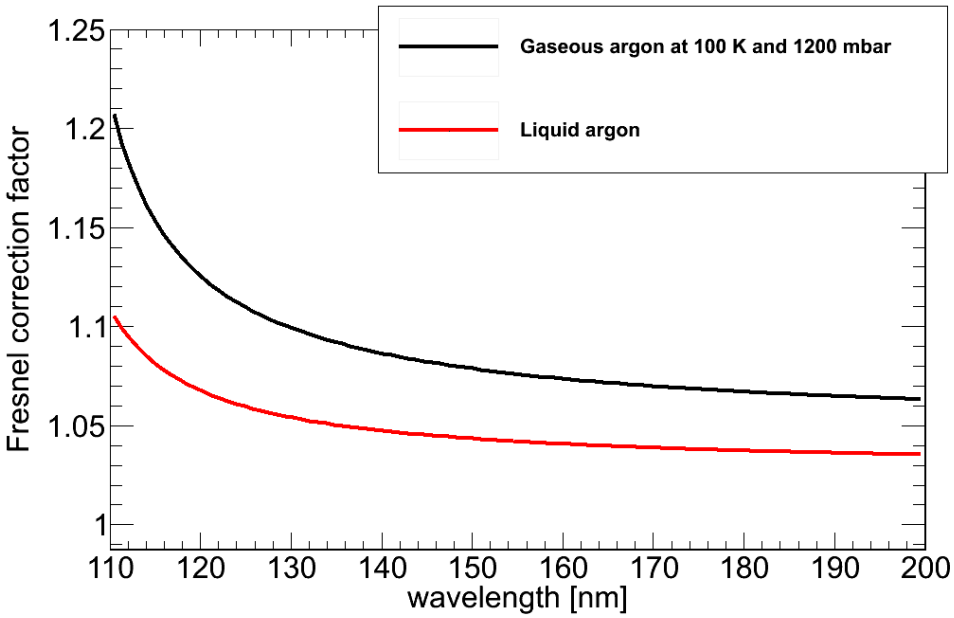

Figure 11.9: *Optical surface correction factors calculated with the Fresnel formula (eq. (11.2)) for unpolarised light and perpendicular light incidence, both for liquid argon and cold argon gas. Towards shorter wavelengths the transmission decreases, hence the correction factor which has to be multiplied to the data rises. Data adapted from [Ant04, Bid80, Lap83].*

as the second excimer continuum emission of warm argon gas (room temperature; 1200 mbar pressure). The wavelength-resolved scintillation spectrum of gaseous argon at room temperature is already rather well known (e.g. [Mor08, Wie00]), hence the latter measurement served to cross-check the obtained results and to obtain information on a wavelength shift of the peak emission with temperature.

The scintillation spectrum of cold argon gas, on the other hand, is of particular interest for two-phase experiments which use both the scintillation light of liquid and gaseous argon for particle discrimination (for example ArDM [Mar11], WARP [Ben08], or DarkSide [Wri11]). Therefore, the light emission of the cold gas was also investigated in each case. Differences between the scintillation spectra of argon in the liquid and the gas phase, respectively, yield information about density related effects.

11.2.1 Light Emission in the Vacuum Ultraviolet

The full raw-data spectra obtained with the Czerny-Turner monochromator were put together from two single spectra recorded with different filter settings: without any filter for the wavelength region from ~ 105 nm to 245 nm, and with the sapphire filter for the region from 225 nm to 345 nm. The spectra recorded with the glass filter for wavelengths longer than 325 nm (up to ~ 800 nm) were not used in the final analysis, as the efficiency of the detection system used fades for wavelengths above ~ 300 nm, mainly due to the blaze of the grating used. For these wavelengths the spectra recorded with the UV-Vis grating spectrometer (see sec. 11.2.2) are taken.

At first, the spectrum recorded without filter was corrected for dark-noise: a constant

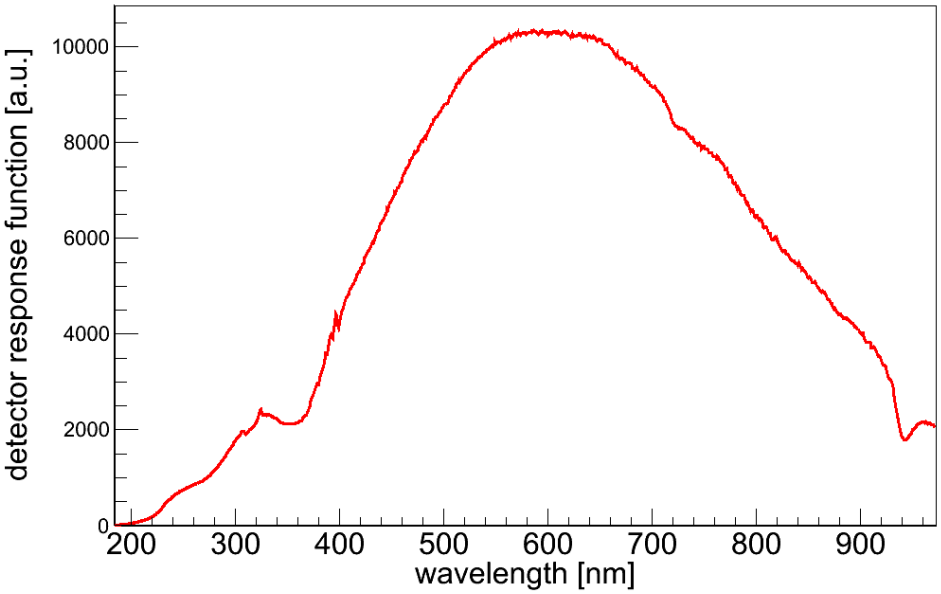

Figure 11.10: *Detector response function of the UV-Vis grating spectrometer (OceanOptics QE65000) in the wavelength interval from 185 nm through 970 nm [Dan12].*

was fitted to the spectrum in the wavelength region below 110 nm, where the MgF_2-window is opaque, and subsequently subtracted from the spectrum. The spectrum recorded with the sapphire filter at longer wavelengths was then scaled to match the spectrum at shorter wavelengths in the overlap region. By this, both the dark-count rate and the attenuation by the sapphire filter were accounted for. The transmission of sapphire is known not to be strongly wavelength-dependent in the wavelength interval of interest ($\gtrsim 240$ nm) [Kor12a].

Scintillation Spectra of Liquid Argon with Ion-Beam Excitation

In section 9.2 it has been shown that for gaseous argon the spectral shape of the scintillation light changes when using different incident particles. One of the main aims to be addressed in the present thesis is the question if these differences are also visible for the liquid phase, and if they could be used for particle discrimination. Therefore, first of all, scintillation light spectra covering a broad wavelength region have been recorded with different ion beams.

The resulting full raw-data spectrum of liquid argon excited by a sulfur beam is shown in fig. 11.11 (red spectrum). The by far dominant spectral feature is the second excimer continuum below 145 nm. Towards longer wavelengths the various emission features of the third excimer continuum follow. A tiny residual xenon impurity causes the emission line at 148.8 nm. However, this is the only line which can be seen in the spectrum, all emission lines stemming from transitions of excited or ionised argon atoms, respectively, are suppressed in the liquid phase due to the high density and thus collision rate (see chapter 9). The small variations of the spectrum are caused by short-term variations of the current of the ion beam and counting statistics. The former are of the order of 5% (see above), the latter are simply determined by the square-root of the number of counts at the respective wavelength in the raw-data spectrum. Errors coming from the uncertainty of the corrections for "fogging" of

the MgF_2-window, the detector response function, and the Fresnel correction are not taken into account. An estimate of the total error budget of the scintillation light spectrum which is introduced by the three effects last mentioned yields less than 10% for liquid argon and about 15% for argon in gas phase.

The raw-data spectrum is corrected for the "fogging" of the target cell's windows and convoluted with the detector response function (fig. 11.8); the outcome is also shown in fig. 11.11 (blue spectrum). Compared to the raw-data spectrum (red) the light intensity in the wavelength regime of the third excimer continuum compared to the second excimer continuum is much less, as both the "fogging" effect and the detector response function tend to suppress the light emission at short wavelengths. Consequently, the total light output (number of photons) in the regime of the third excimer continuum (calculated by integrating the spectrum from 170 nm to 310 nm) is only 0.016% of the number of scintillation photons emitted in the second excimer continuum (118 nm to 145 nm). The energy output (number of photons times the photon energy at the respective wavelength) is 0.0094%. For comparison: in the gas phase at ~ 99 K, 0.77% of the photons (0.43% of the light energy) are emitted in the wavelength region of the third excimer continuum with respect to the light emission in the second excimer continuum, which translates into an intensity suppression of about a factor of 46 in connection with the phase transition between gaseous and liquid state.

In the luminescence-light spectrum of liquefied argon in the VUV and UV range five more or less prominent spectral features stemming from argon itself, and the xenon impurity emission at 148.8 nm (fig. 11.11), can be seen. All of these features are found to be structureless continua[8] with different widths. The by far dominant spectral feature is the second excimer continuum peaking at 126.4 nm (see also tab. 11.1 on page 176). Towards longer wavelengths, in the wavelength range of the third excimer continuum, four additional structures are found. The continuum at (160.1 ± 0.2) nm with a width of (5.1 ± 0.2) nm (1σ-width obtained from a Gaussian fit) is possibly attributed to the classical LTP; the other structures are found at (182.1 ± 0.1) nm (width: (7.9 ± 0.1) nm), at (201.8 ± 0.1) nm (width: (8.7 ± 0.2) nm), and a broader continuum at (272.9 ± 0.1) nm (width: (16.5 ± 0.2) nm). An attribution of these continua to underlying scintillation mechanisms is tried in sec. 11.3 together with the investigation of the respective time structure.

The strong suppression of the third excimer continua is observed for all three exciting ions used in the present work: protons (10 MeV), sulfur (S^{10+}; 120 MeV), and gold (Au^{14+}; 195 MeV); fig. 11.12. As a result, independently of the exciting ion beam only about every 6500^{th} photon is emitted in the wavelength region of the third excimer continuum at all. The light yield of liquefied argon is about 40,000 photons per MeV (in the absence of an electric field) [Dok88], hence an incident particle depositing 1 MeV energy in the liquid will create only ~ 6 photons in the third excimer continuum[9]. As was deduced in chapter 9 the main differences between different incident particles should, however, show up in this wavelength region. As a result, particle discrimination in the liquid by means of the (wavelength-resolved) scintillation spectrum alone is rather difficult, as the number of photons of the third continuum is very small, at least for low-energetic incident particles, which produce only little light.

[8] In dedicated measurements with very high resolution (100 µm slit width, i.e. $\Delta\lambda = 0.3$ nm, and 0.05 nm step size) parts of these continua were investigated for any substructures, however, none were found.

[9] Applying an electric field, as is done in the argon TPC detectors, decreases the light yield [Dok02]. In case the third excimer continuum is not (or only little) affected by an external electric field, the intensity ratio of second to third excimer continuum rises. However, the absolute number of photons in the long-wavelength part of the emission spectrum stays tiny.

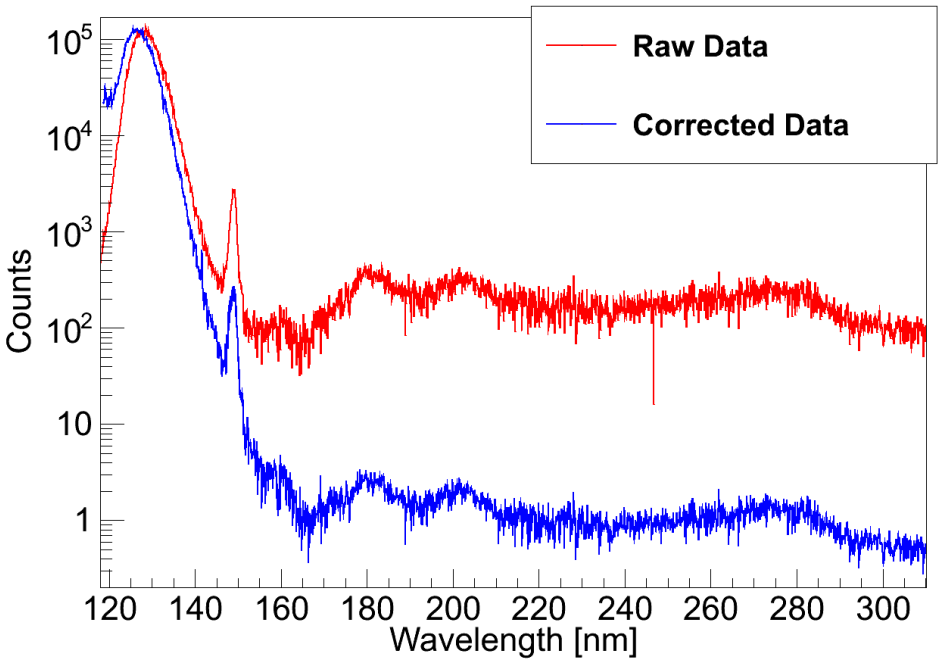

Figure 11.11: *Scintillation spectrum in a wavelength interval from 118 nm to 310 nm of liquid argon (86 K; raw data in red, data corrected for the "fogging" effect and the detector response function in blue) when excited by a sulfur beam. The "fogging" correction is only known down to 118 nm, therefore, no shorter wavelengths are shown. The width of the monochromator's entrance slit was set to 100 µm, which translates into an optical resolution of 0.3 nm. The by far dominant emission feature is the second excimer continuum below 145 nm. At 148.8 nm the emission line of a residual xenon impurity can be seen; towards longer wavelengths the structures of the third excimer continuum follow, centered around 180 nm, 202 nm, and 271 nm, respectively. The structure at 160 nm is possibly attributed to the classical left turning point (LTP). For wavelengths above 310 nm the efficiency of the detection system becomes worse; these wavelengths are explored with the grating spectrometer (see sec. 11.2.2), which has a higher sensitivity there. The short variations of the spectrum are due to short-term variations of the beam intensity (about 5%) and counting statistics. For the corrected data the intensity ratio between second and third excimer continuum is drastically changed. The total energy output in the third excimer continuum (170 nm through 310 nm) is only $9.4 \cdot 10^{-3}$ % of the total light intensity. The small shift of the peak emission wavelength of the second excimer continuum is caused by applying the two correction functions.*

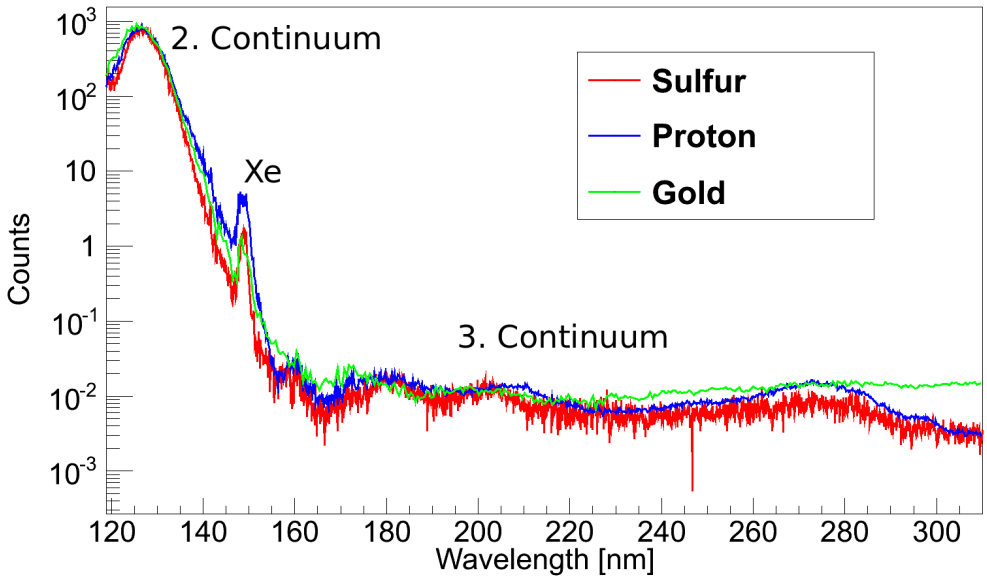

Figure 11.12: *Scintillation spectrum of liquid argon excited by protons, a sulfur and a gold beam and corrected for the "fogging" effect and the detector response function. The single spectra are scaled to match each other at the peak emission of the second excimer continuum. Except for the broad underlying continuum in the spectrum recorded with the gold beam (see text) the single spectra look very similar. In particular, the same emission features can be distinguished, and the intensity ratios of second to third excimer continua are equal.*

In addition, the scintillation spectra obtained with the different ion beams are nearly equal, see figs. 11.12 and 11.13. Except for the broad continuum[10] at wavelengths longer than $\sim 220\,\text{nm}$ underlying the spectrum recorded with the gold beam, no clear enhancement or suppression of the scintillation light spectrum can be seen for any of the projectiles used. In contrast - the spectrum obtained with protons as exciting particles, which are expected to produce fewer highly ionised species than heavier projectiles, nearly looks the same as the spectrum recorded with a sulfur beam. This could either mean that the population of the progenitor states of the third excimer continuum (highly ionised atoms) is the same for different incident ions, or the emission spectra obtained with ion beam excitation are dominated so much by the secondary electrons that the differences which would appear in the scintillation light spectra produced by the primary ions are no longer visible.

No dependence of the spectral shape of the luminescence light on the specific energy loss per track length of the incident particles was found: for the proton beam, which has a non-negligible range in the liquid argon volume ($\sim 1.2\,\text{mm}$), the spectrum was scanned along the beam track by turning a mirror in the optics box. In this way, different parts of the proton track, and thus different specific energy losses, were investigated. However, no changes in the scintillation spectrum were observed.

A comparison of the spectrum obtained with the sulfur beam to the spectrum with

[10]This continuum is most likely attributed to bremsstrahlung from secondary electrons. Its shape is very similar to the continuum found in studies of the scintillation light of liquid argon with an applied electric HF field [Dan12].

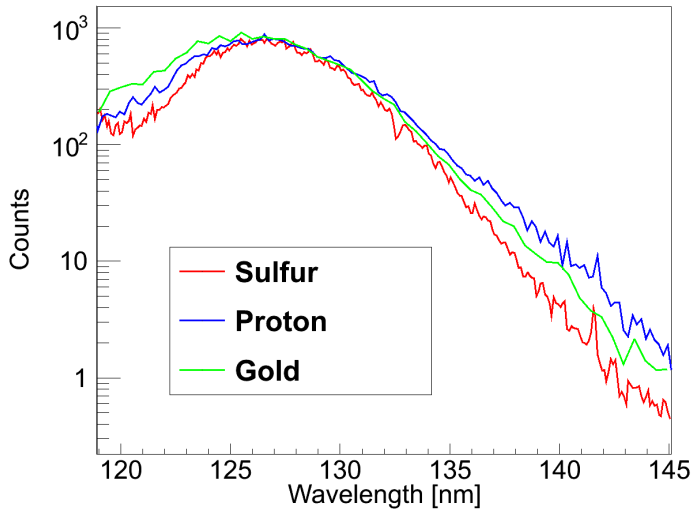

Figure 11.13: *Zoomed-in view on the scintillation spectrum of liquid argon in the region of the second excimer continuum (119 nm to 145 nm). Again, the spectra excited by protons, a sulfur and a gold beam are shown, corrected for the "fogging" effect and the detector response function. The single spectra are scaled to match each other at the peak emission. Gaussian fits (not shown) to the data yield center wavelengths of the second continua of (126.4 ± 0.1) nm (sulfur beam), (125.8 ± 0.2) nm (gold beam), and (126.8 ± 0.1) nm (proton beam), see also tab. 11.1.*

electron-beam excitation is given below.

The peak emission wavelengths of the second excimer continuum are nearly equal for the different ion beams; cf. tab. 11.1 on page 176. However, the shapes (widths of the right wing[11]) of these continua are not equal, but clearly deviate from each other. This could possibly be attributed to different temperatures of the liquid in the volume of light production[12], with protons causing the biggest heating. However, due to the anharmonicity of the molecular potential (fig. 9.1) different temperatures should also cause the peak emission wavelength to be shifted (towards shorter wavelengths for higher temperatures; see also fig. 9.6), which is however not observed here. To fully understand the behaviour of the shape of the second excimer continuum further measurements have to be performed, in which the influence of the various parameters (temperature, state of aggregation, pressure of the gas phase, type and energy of the incident particles, etc.) is investigated systematically. At present, no conclusive results can be given.

Comparison of the Emission from the Liquid with that of the Gas Phase

For argon gas excited by an electron beam a small shift of the peak emission of the second excimer continuum has been reported when comparing dilute warm gas (300 mbar, room

[11] The width of the left wing is strongly influenced by the "fogging" correction and shall therefore not be regarded here.

[12] As was explained above only the average temperature of the target cell can be measured directly, the local temperature of the liquid argon emitting the scintillation light is unknown. Due to different beam powers this temperature might be different for the various ion beams.

temperature) with the liquid phase [Hei10, Hei11]; see also fig. 9.6 in section 9.3. This was also studied here with ion-beam excitation. In fig. 11.14 the second excimer continuum of gaseous argon at 1200 mbar and room temperature is compared to that of the liquid. No correction for the different indices of refraction (Fresnel formula) has been applied. However, as was deduced above (sec. 11.1.5) the wavelength dependence of these indices is expected to be similar, hence no spectral distortions are expected.

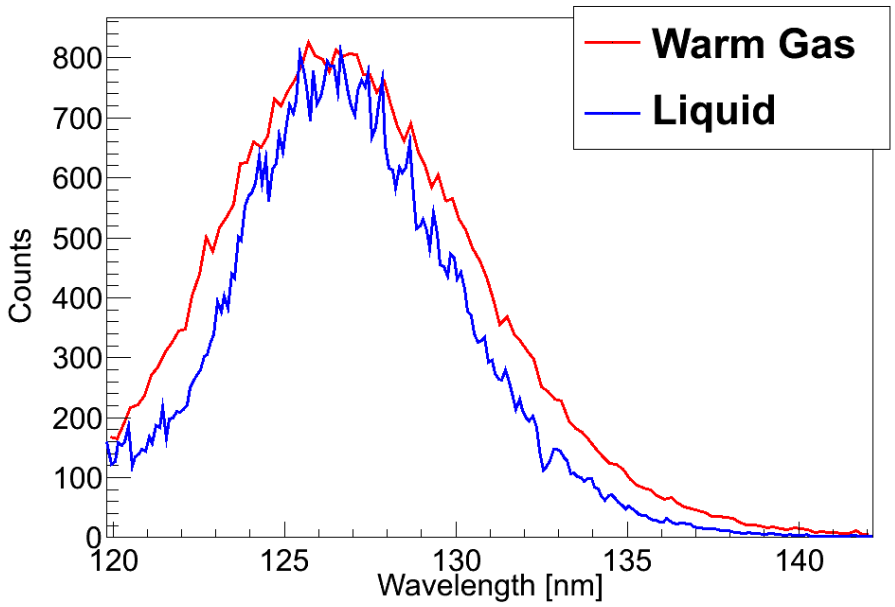

Figure 11.14: *Second excimer continuum of gaseous argon at 1200 mbar and room temperature (red) compared to the second excimer continuum of liquid argon (86 K; blue). The spectra are scaled to match each other at the peak emission. The overall shape is similar, hinting to the same underlying scintillation mechanism, but the width of the continuum of the liquid phase is narrower. This is a temperature related effect [Mor89]. No wavelength shift of the peak emission is observed.*

Again, no systematic wavelength shift of the peak emission is obtained in fig. 11.14, although such a shift would be expected from the results of the experiments with electron-beam excitation [Hei10, Hei11] and synchrotron radiation [Mor89]. At present, this is not understood. As was already mentioned above, further experiments quantifying the impact of the free parameters in the present experiments on the shape and the centre wavelength of the second excimer continuum are needed to fully understand this issue. The width of the continuum is temperature dependent [Mor89], and therefore much broader for the warm gas than for the liquid (and also the cold gas). The data are also summarised in tab. 11.1.

A comparison of the scintillation spectra of cold argon gas (1200 mbar, $\sim$99 K) and liquid argon ($\sim$86 K), both excited by the S^{10+}-beam is shown in fig. 11.15. Again, no correction for the index of refraction has been applied.

The most obvious difference between gas and liquid phase is the intensity and spectral shape of the third excimer continuum. Following the idea of applying the same gas kinetic processes to both the gas and the liquid phase, i.e. the liquid behaves just like a dense gas, the

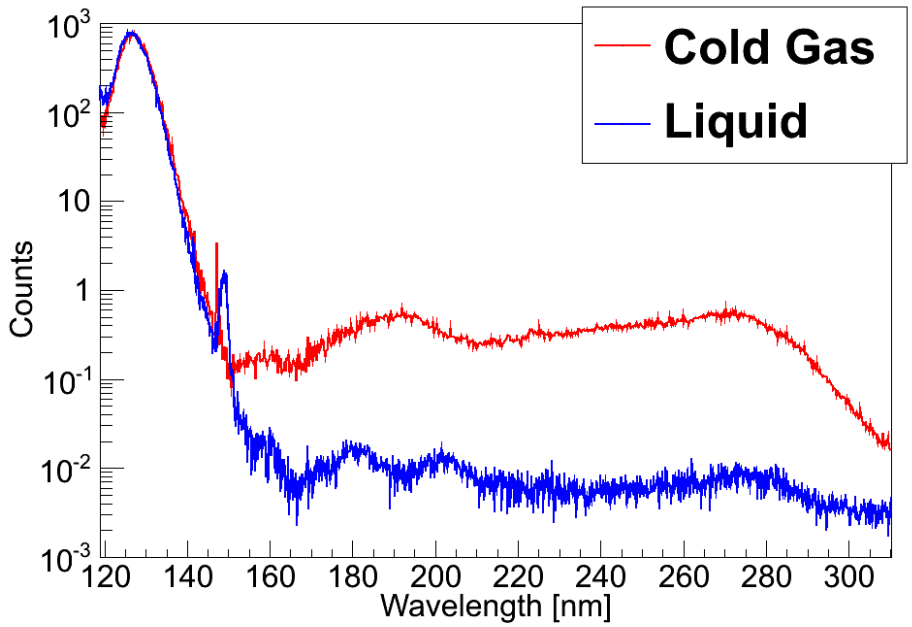

Figure 11.15: *Scintillation-light spectrum in a wavelength interval from 118 nm to 310 nm of cold argon gas (1200 mbar, ∼ 99 K; red) and liquid argon (∼ 86 K; blue) excited by a sulfur beam. The spectra are scaled to match each other at the peak emission. The second excimer continuum at wavelengths shorter than ∼ 145 nm is very similar for both states of aggregation, the third excimer continuum is strongly suppressed in the liquid. In the spectrum of the liquid the impurity emission line of neutral xenon (XeI) can be seen at (148.8 ± 0.2) nm with a width of (1.8 ± 0.4) nm (FWHM). In the gas phase, however, this line is found at 146.96 nm [NIS12] and has a width which is smaller than the instrumental resolution. This shift is also reported in literature [Che72].*

great suppression of intensity observed for liquid argon might be related to the much higher density: in the interpretation of the origin of the third excimer continuum given in sec. 9.1 there is a competition between radiative decays and non-radiative formation of new molecules for each of the intermediate steps of the gas kinetic processes after ionisation of an argon atom (cf. fig. 9.3 on page 138). The high density of the liquid could shift the equilibrium in favour of the non-radiative processes. Therefore, light emission in the third excimer continuum would be strongly suppressed, but nearly all excitation energy is in various steps (molecule formation and recombination with thermalised electrons) transferred to neutral argon excimers, the lowest excited state possible, whose decay gives rise to luminescence photons in the second excimer continuum.

However, at present, other explanations cannot be excluded. The study of energy transfer mechanisms in liquid argon will be a topic for forthcoming measurements. Doping liquid argon deliberately with xenon could, for example, allow such studies, as single steps of the kinetic processes might possibly be identified by their energy transfer to xenon atoms, or by the formation of ArXe-mixed molecules radiating at a different wavelength. Such experiments, however, require a deep understanding of the energy transfer mechanism between the argon bulk material and impurity atoms.

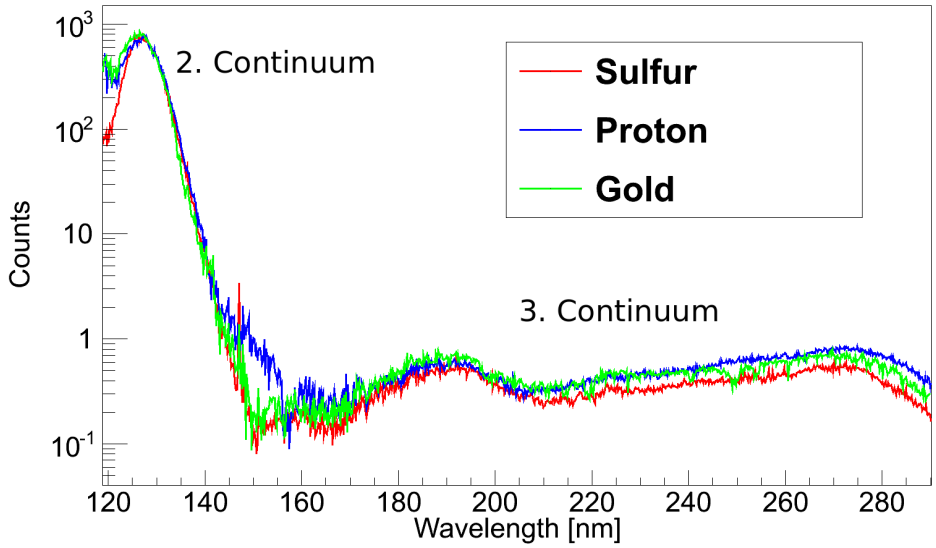

Figure 11.16: *Scintillation spectrum (covering 118 nm through 290 nm in wavelength) of gaseous argon at ∼ 99 K and 1200 mbar pressure excited by three different particle beams: protons, S^{10+}, and Au^{14+}. The width of the monochromator's entrance slit was set to 100 µm (500 µm for protons), which translates into an optical resolution of 0.3 nm (1.5 nm). The spectra are corrected for the detector response function and the "fogging" effect. The deviation in the spectrum recorded with protons between 145 nm and 160 nm is most likely caused by an instability of the beam current. Besides this the three spectra are similar. For the excitation by the sulfur beam a tiny emission from a xenon impurity can be seen at 146.96 nm [NIS12].*

The pressure of the argon gas (1200 mbar) is already high enough to strongly suppress the emission of the classical LTP at 155 nm. In principle, one would also expect such a suppression for the first continuum (at wavelengths below ∼ 115 nm), however, the cut-off wavelength of the MgF_2-window of 110 nm [Kor12] and the shorter wavelength of the "fogging" correction (118 nm) prevent the first continuum to be seen in the spectra presented here. Therefore, its intensity cannot be judged. The third excimer continuum of the cold argon gas looks very similar to that reported for the warm gas [Wie00], however, redshifted by ∼ 10 nm.

Finally, the scintillation spectra of cold argon gas recorded with different ion beams are shown in fig. 11.16. As in the case of liquid argon for gaseous argon the single scintillation-light spectra obtained with the different exciting ions look alike. Both the spectral shape and the relative intensity of second to third excimer continuum are very similar. Again, particle discrimination using the wavelength-resolved scintillation light alone is not feasible.

To all of these spectra a Gaussian fit is applied to a wavelength region ± 3 nm around the peak emission of the second excimer continuum[13] to check for any systematic shifts (tab. 11.1). As already mentioned above, neither the temperature nor the state of aggregation seem to cause such a shift, at least when comparing gaseous argon under pressure (1200 mbar) and the liquid phase.

[13]Due to the anharmonicity of the molecular potential (fig. 9.1) the second excimer continuum is not Gaussian shaped. However, its central wavelength region can be fitted rather well with a single Gaussian.

Projectile	Warm Gas		Cold Gas		Liquid	
	μ [nm]	σ [nm]	μ [nm]	σ [nm]	μ [nm]	σ [nm]
p^+	126.8 ± 0.1	3.93 ± 0.14	126.8 ± 0.1	3.57 ± 0.11	126.8 ± 0.1	3.64 ± 0.12
S^{10+}	126.5 ± 0.1	3.80 ± 0.13	126.9 ± 0.1	3.15 ± 0.08	126.4 ± 0.1	3.20 ± 0.06
Au^{14+}	126.8 ± 0.1	3.86 ± 0.14	126.3 ± 0.1	3.52 ± 0.10	125.8 ± 0.2	3.79 ± 0.19

Table 11.1: *Center wavelengths (μ) and widths (σ) of the Gaussian fits applied to a wavelength interval ± 3 nm around the peak position of the second excimer continuum in the different spectra recorded for the different projectiles and states of aggregation. No systematic shifts of the peak emission wavelength are found, neither with temperature nor with the aggregation state. The values obtained for the different ion beams are similar, too. For the excitation by electrons a peak emission wavelength of 126.8 nm is found for liquid argon [Hei10, Hei11]. However, the second excimer continua recorded for the cold gas and the liquid, respectively, are narrower than those of the warm gas. This effect is temperature related [Mor89].*

Comparison to Data Obtained with Electron-Beam Excitation

The data recorded with ion-beam excitation can also be compared to the scintillation-light spectrum obtained for electron-beam excitation [Hei10, Hei11], see fig. 11.17.

The spectrum obtained with the ion beam is corrected both for the "fogging" effect and the detector response, see fig. 11.11; the spectrum recorded with the electron beam, on the other hand, is only corrected for the associated detector response function, no corrections for a "fogging" of the windows have been applied [Hei11]. The electron-beam data was recorded using a different setup than for the ion-beam experiments, comprising a different target cell and cooling system (with different cryo-getter materials), and a different optics to collect the scintillation light. Most of these aspects should cancel out by applying the detector response function, however, the "fogging" of the system might behave differently as for the ion-beam setup. In particular, the residual pressure in the insulating vacuum, the cooling speed, and possibly also the composition of the residual gas, differed between the two experimental setups. As the electron-beam setup was not used to record transmission data - in contrast to the ion-beam setup - no reliable data for a "fogging" correction is available. Therefore, no such corrections have been carried out.

The peak emission wavelengths of the second excimer continuum are comparable ((126.4 ± 0.1) nm for the sulfur-beam excitation and 126.8 nm for the electron beam [Hei10, Hei11]), only the width of the continuum recorded with electron-beam excitation is slightly higher (9.7 nm compared to 7.3 nm). This might hint on a slightly higher temperature of the light emitting volume, however, minor differences in the shape of the red wing of the second excimer continuum are also observed for the different ion beams; see fig. 11.13. This has to be clarified

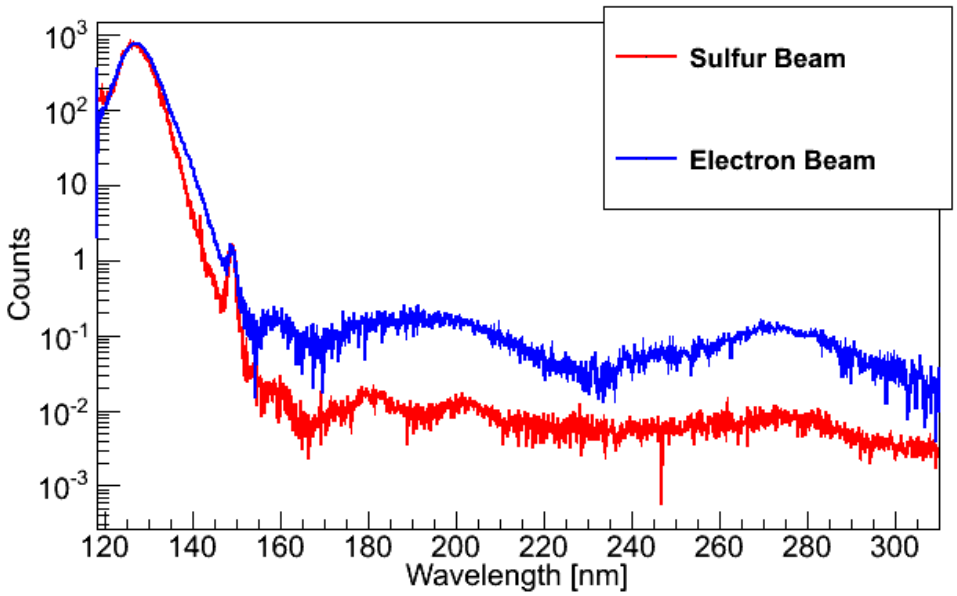

Figure 11.17: *Wavelength-resolved scintillation-light spectrum obtained with sulfur-beam excitation (red) and electron-beam excitation (blue), scaled to match each other at the peak emission of the second excimer continuum. The spectrum recorded with the ion beam is corrected both for the "fogging" effect and the detector response function of the beam-line setup, the data recorded with the electron beam, however, only for the response function of the table-top setup used [Hei11]. Details see text.*

in separate experiments, best performed using the same setup for all exciting particles.

The light emission in the wavelength range of the third excimer continuum is clearly enhanced in the spectrum recorded with the electron beam compared to the ion-beam spectrum. This could be attributed to the missing "fogging" correction, as the "fogging" effect considerably shifts the intensity ratio between the short-wavelength and the long-wavelength parts of the scintillation light; cf. fig. 11.11. However, at present, it cannot be excluded that the different intensities are due to a true effect.

In addition, the spectral shape of the scintillation-light spectrum between $\sim 180\,\text{nm}$ and $\sim 220\,\text{nm}$ is different with the different exciting particles: the ion-beam spectrum shows two distinct continua centered at 182 nm and 202 nm, while for the electron-beam spectrum only one broad continuum centered at about 195 nm can be seen. This continuum looks similar to that visible for the cold gas, see fig. 11.16, and could therefore hint to a slightly too high temperature at the volume of light production causing the liquid argon to boil. The third excimer continuum is more intense in the gas phase, which could also cause the scintillation-light spectrum to be enhanced in this wavelength region[14]. However, also for the excitation by electrons the beam current was adjusted well below the evaporation threshold of liquid argon [Hei11, Hei11a], and the 4p-4s transition lines indicating argon in gaseous state were not observed at all. Therefore, a real difference in the spectral shape between electrons and

[14]The "fogging" correction obtained for the beam-line setup influences the spectral shape only minimally, see fig. 11.11. Hence, assuming that this is also true for the setup used to record the scintillation-light spectrum with electron-beam excitation the different spectral shapes cannot be explained with this effect.

heavy ions as incident particles is also possible and cannot be excluded. Again, an additional experiment is desired where both electrons and heavy ions can be used as exciting particles in the same setup. At even longer wavelengths the two spectra obtained with ions and electrons look similar, except for the higher intensity obtained for the electron beam.

Because of the technical issues listed above, at present no conclusive results on the feasibility of particle discrimination between electrons and heavy ions based on the wavelength-resolved scintillation light only can be given. However, also for the electron beam the spectrum is by far dominated by the second excimer continuum and the intensity in the wavelength region of the third excimer continuum is small, making particle discrimination rather difficult, even in case the differences visible in fig. 11.17 would turn out to be (at least partly) real.

11.2.2 Emission Spectra in the Visible and Near IR Range

The emission spectra of liquid and gaseous argon, respectively, were recorded with the UV-Vis grating spectrometer in a wavelength region from $\sim 250\,\text{nm}$ to $\sim 970\,\text{nm}$. The data obtained with this system are automatically corrected for dark-noise and absolutely calibrated in wavelength. The relative calibration in intensity was carried out by applying the detector response function (fig. 11.10) to the data.

No corrections for the adaption of the index of refraction[15] and the "fogging" effect, respectively, were taken into account. The latter was disregarded as for wavelengths longer than $\sim 220\,\text{nm}$ the reduction of the transmission is small and, in particular, nearly equal for all wavelengths, i.e. the spectral shape of the emitted light is not affected.

A lead shielding around the grating spectrometer reduced the background due to X-ray emission, the biggest source of experimental background, to a possible minimum. The remaining X-ray background was eliminated from the spectra by subtracting the spectra recorded with the mylar foil turned in at the filter wheel. These spectra directly show the amount of background induced by X-rays, as any optical photons were blocked, but X-ray emission could pass the thin foil undisturbedly.

For each of the results presented below it was thoroughly checked that neither the current of the ion beam used nor the parameter settings of the spectrometer (such as integration time or number of averaging cycles) have an influence on the spectral shape. In addition, as recording a spectrum is rather fast with the UV-Vis grating spectrometer each spectrum was recorded three times to cross-check the results and to allow an identification of detector pixels which are in saturation due to X-ray photons. The beam current of the ion beam was monitored with a retractable Faraday cup directly in front of the target cell before and after each measurement, and spectra identified to be recorded under unstable beam conditions were rejected from the final analysis. However, as the full spectrum was recorded simultaneously at all wavelengths time-dependent beam current variations do not affect the measurements as much as for the experiments with the Czerny-Turner monochromator, where the wavelength-resolved spectra were recorded sequentially.

Figure 11.18 shows the scintillation-light spectrum of liquid and gaseous argon ($\sim 90\,\text{K}$, 1200 mbar) excited by protons (10 MeV). In the case of gaseous argon a tiny[16] broad con-

[15] I.e. the Fresnel corrections for light losses due to reflection at optical surfaces were not included. However, as was discussed above these corrections were again not taken into account because of the lack of information on the indices of refraction of liquid argon and MgF_2, respectively.

[16] The total intensity of the line radiation (integrated in a wavelength interval ranging from 650 nm to 950 nm) is a factor of 2 higher than the intensity of the continuum around 270 nm (integrated from 250 nm to 320 nm).

tinuum centered at 270 nm can be seen; except for this continuum only the line radiation (from 680 nm to 950 nm) of excited argon atoms (ArI) is emitted. The continuum - which is observed for all incident particles at the same wavelength - is most likely the long-wavelength part of the third excimer continuum; see fig. 11.16.

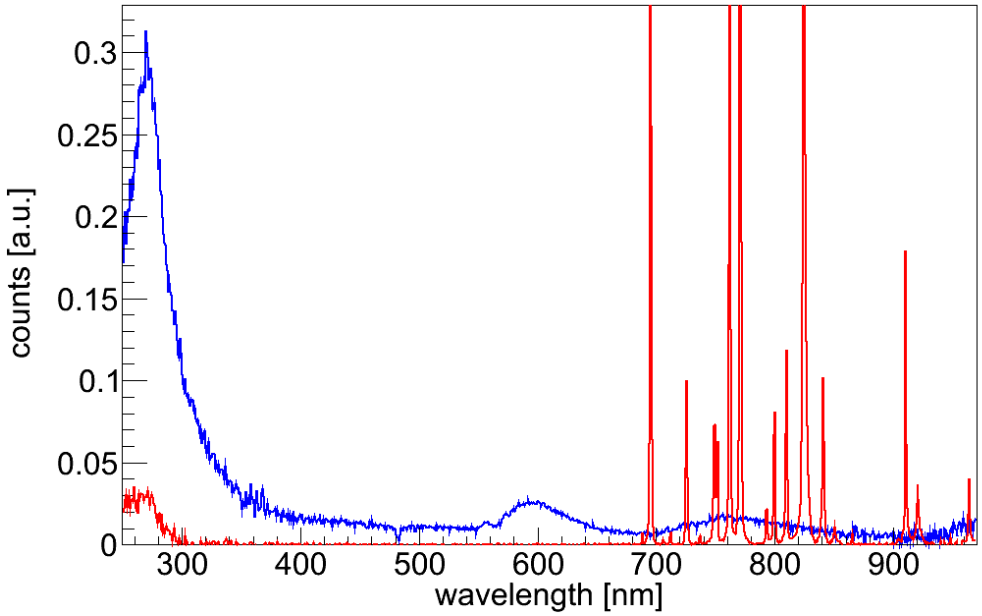

Figure 11.18: *Long-wavelength part (covering 250 nm to 950 nm) of the scintillation spectrum of liquid (blue) and gaseous argon (red; ∼ 90 K, 1200 mbar) excited by a proton beam (7 nA beam current in case of argon gas and 5 nA in case of the liquid), corrected for the detector response. The spectrum of the liquid is recorded with a six times longer integration time. For liquid argon three distinct continua on top of a very broad underlying continuum can be seen (see text); the spectrum of gaseous argon shows except for a tiny continuum at 270 nm only the emission lines of neutral excited argon atoms (ArI). The dip in the spectrum of the liquid at about 480 nm is an artifact from the stray-light correction; the tiny narrow structure at 559 nm can be attributed to a residual contamination with oxygen.*

The scintillation spectrum of the liquid, on the other hand, shows three distinct emission continua centered at about 274 nm, 595 nm, and 755 nm, respectively, on top of an underlying broad emission continuum[17]. The latter causes the scintillation light of liquid argon to appear whitish to the eye. A tiny structure at 558 nm is visible, which can be attributed to a small remaining contamination with oxygen. The emission lines of ArI are strongly suppressed, indicating that in the very dense liquid the formation of excimer molecules and the subsequent de-excitation by means of radiationless collisions dominate by far. However, the broad continuum between 700 nm and 880 nm might be attributed to 4p-4s transitions of excited argon atoms, but considerably broadened in the liquid phase.

[17] And possibly another continuum starting from ∼ 940 nm. This structure might be attributed to the $^3\Sigma_u \rightarrow {}^3\Pi_g$ transition of argon excimer molecules [Sue79], and was also observed with electron-beam excitation [Hei10, Hei11]. However, the detector's wavelength range is limited at 970 nm making clarifying measurements at longer wavelengths impossible with this setup.

The continuum centered at 274 nm is also indicated in the spectra recorded with the Czerny-Turner monochromator (see fig. 11.12) can possibly be attributed to transitions of Ar^{3+} ions (ArIV) [Hei11]. A further discussion of this continuum, including its time structure, follows in sec. 11.3. The continuum centered around 597 nm is probably due to a X-ray-induced fluorescence of the MgF_2-window [Ulr12a].

The underlying broad continuum could stem from bremsstrahlung emitted by secondary electrons [Dan12]. It could also be attributed to considerably broadened line emission by neutral argon atoms (ArI) or argon ions (ArII + ArIII) [Hei11], or a combination of both. The high density of the liquid phase possibly disturbes the energy levels of initial and final state of the respective transition so much that the narrow emission lines which are observed for the gas phase are considerably broadened, and the transition energy is emitted in broad continua.

Figure 11.19 compares the scintillation-light emission obtained with three different ion beams (sulfur, protons, and oxygen) and electrons. For all three ions two continua on top of an underlying broad continuum can be seen in the wavelength region displayed. The peak emission of the left continuum is at $\sim$270 nm for the case of the electron-, the sulfur- and the oxygen-beam excitation, while it is slightly shifted to longer wavelengths (274 nm) for the proton beam. With the ion beams its red wings are broadened. The continuum of MgF_2-fluorescence, however, centers around 597 nm for all three ion beams; it is not visible for excitation by electrons. In each case it was checked that the beam current does not affect the spectral shape at all; only the intensity of the spectral features scales with the beam current. Any influence of a "fogging" of the window can be excluded, too, as between the measurements with the different ion beams the cell was heated up each time, and the spectra shown in fig. 11.19 were recorded at nearly exactly the same time difference after start of the cool-down. In addition, as already mentioned above, the influence of the "fogging" is negligibly small for wavelengths longer than $\sim$220 nm. Again, the background induced by X-rays was subtracted from the spectra; its impact on the shape is small anyway as it has a flat shape over the full wavelength range.

The underlying broad continuum is enhanced for the two heavier projectiles. This can be understood if this continuum is indeed (partly) attributed to bremsstrahlung by secondary electrons: after the titanium entrance foil the ions in the oxygen (sulfur) beam have a remaining energy[18] of about 65 MeV (104 MeV), the beam current is 12 nA (9 nA). Consequently, the resulting power depositions are 130 mW (O^{6+}) and 94 mW (S^{10+}), while the power deposition with the 10 MeV-proton beam is 50 mW. Hence, the number of secondary electrons produced is expected to be largest for the oxygen beam and smallest for the proton beam, and bremsstrahlung-related effects should be larger, too. Furthermore, the same continuum is observed in experiments where the scintillation light of liquid argon is studied with electron-beam excitation but with an additionally applied high-frequency electric field [Dan12], additionally supporting the bremsstrahlung hypothesis.

The several tiny continua[19] reported for excitation by electrons at wavelengths above 300 nm [Hei10, Hei11] and attributed to broadened emission lines of neutral argon atoms (ArI) and argon ions (ArII - ArIV) are covered in the spectra obtained with the various ion beams by the broad bremsstrahlung emission and the fluorescence spectrum of MgF_2.

[18] See tab. 10.1 in section 10.2.

[19] In fig. 11.19 these continua are not visible, as their intensity is too small. They only appear in a logarithmically scaled spectrum. A presentation of these continua can be found in [Hei11], figs. 4-3 and 4-4.

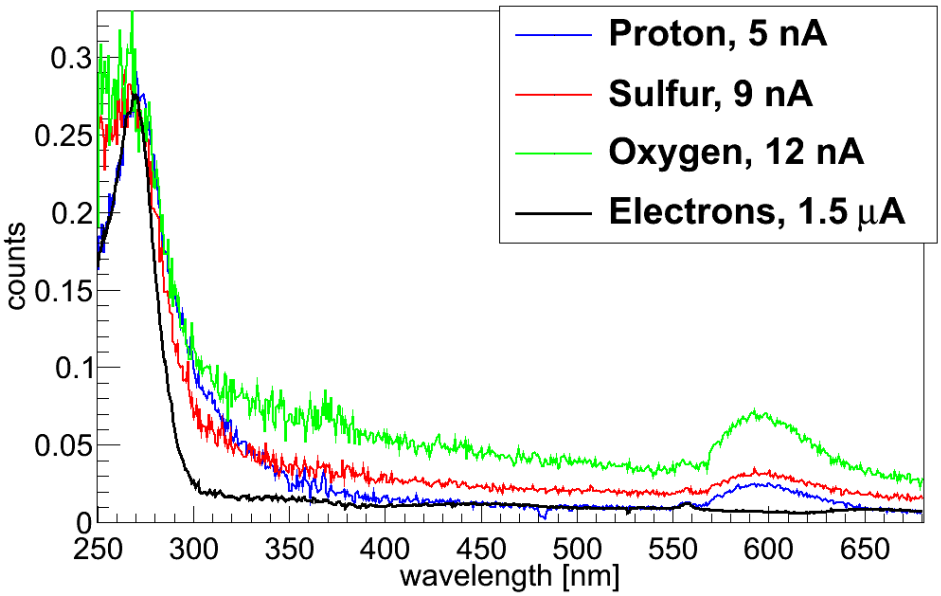

Figure 11.19: *Long-wavelength part (250 nm through 680 nm) of the scintillation spectrum of liquid argon excited by different ion beams: protons (10 MeV, blue; same spectrum as shown in fig. 11.18), sulfur (115 MeV, red), and oxygen (70 MeV, green), as well as with electron excitation (black). Because of the different beam currents the spectra are scaled to match each other at 270 nm. The respective beam currents are indicated in the inset, too. For all three incident ions two continua on top of a broad underlying continuum can be seen (see text. The continuum at 755 nm stemming from the ArI-lines looks alike for all ion beams and is not shown here). Again, the tiny dip at at 480 nm in the proton spectrum is caused by the stray-light correction; at 558 nm the emission of a tiny residual oxygen impurity is indicated.*

11.2.3 Particle Discrimination Potential

The wavelength-resolved scintillation-light spectra of liquefied argon when excited by different ion beams have been presented, covering a wavelength range from the VUV (118 nm) to the near infrared (950 nm). Comparing these spectra allows to conclude that particle discrimination between different nucleons which is based on the (wavelength-resolved) scintillation spectrum alone seems not feasible in any realistic low-energy experiment: the spectral differences due to different incident nuclei are very small, and the overall intensity of luminescence light in the wavelength region of the third excimer continuum ($\sim$170 nm to $\sim$300 nm), where most of the differences were expected, are extremely small compared to the intensity of the second excimer continuum ($\sim$115 nm to $\sim$145 nm), the by far dominant light emitting feature in liquid argon. This conclusion also applies to the scintillation light emitted by argon in the gas phase, however, the intensity of the third excimer continuum is greatly enhanced compared to the liquid.

At even longer wavelengths the scintillation spectrum of liquid argon has very little intensity, too, and is also found to be independent of the incident particle. The data presented here allows, at present, no clear statement on the discrimination potential between (heavy) ions and electrons. This issue needs to be addressed in future experiments, best performed

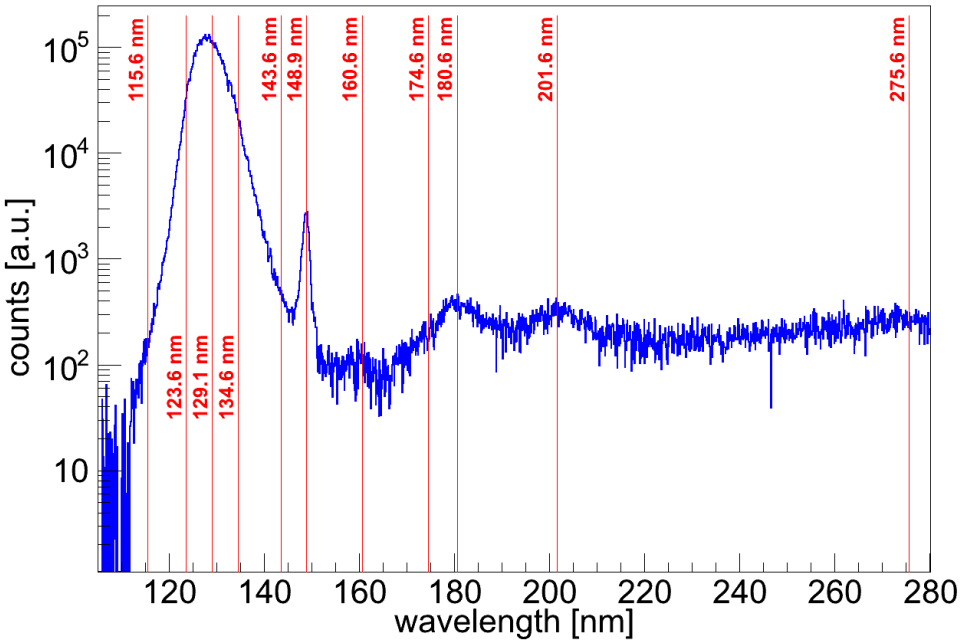

Figure 11.20: *Logarithmically scaled scintillation spectrum of liquid argon (raw data) when excited by a sulfur beam. The wavelengths investigated in the time-resolved measurements (red lines) are indicated. The numbers give the exact wavelengths. The set of time-resolved measurements was chosen to cover all interesting emission features like the third and the second excimer continuum (including its wings), as well as the xenon impurity line at 148.8 nm.*

with a system which allows to excite liquid argon with electron and ion beams in the same setup.

11.3 Time-Resolved Spectra and Emission Time Constants Obtained with Different Heavy-Ion Beams

Besides the wavelength-resolved scintillation spectra of argon presented in sec. 11.2 time-resolved measurements have been performed for a dedicated set of wavelengths with three different ion beams: protons (10 MeV), sulfur (S^{10+}; 120 MeV), and gold (Au^{14+}; 195 MeV).

11.3.1 Investigated Wavelengths and Beam-Pulse Profile

The time structure of the emission light of liquefied argon was investigated at several wavelengths with the method described above. Fig. 11.20 shows again the scintillation-emission spectrum of liquid argon (raw data; sulfur beam excitation), with the investigated wavelengths indicated.

The set of wavelengths was chosen in such a way that all interesting spectral features of the scintillation light are covered: for the most prominent emission feature, the second excimer continuum between 115 nm and 145 nm, the time structure of the peak emission was

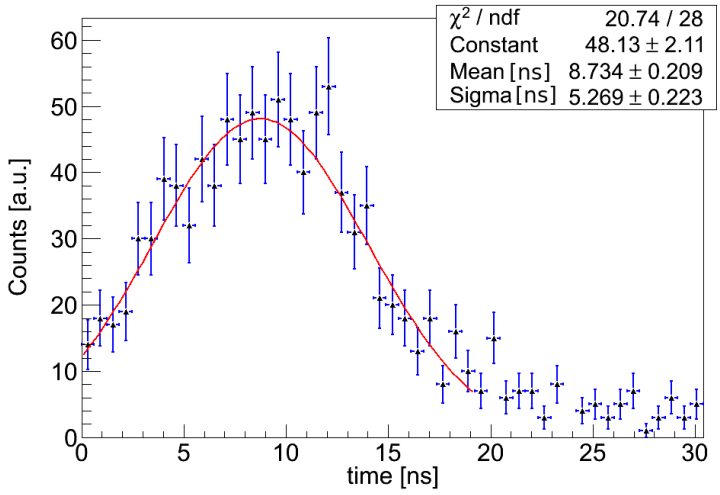

Figure 11.21: *Beam-pulse profile of the S^{10+}-beam as recorded with the X-ray fluorescence light. A Gaussian is fitted to the data; the inset quotes its parameters: the center position ("Mean"; in units of ns), its width ("Sigma"; in units of ns), and a multiplicative normalisation constant. The beam pulse can be described well with this Gaussian, and a pulse-width of 5.36 ns is obtained after correcting for the TAC range, see fig. G.3. The start of the time axis is defined by the chopper trigger signal.*

investigated as well as the time structure at its wings. Furthermore, the peak emissions of the third excimer continuum were examined as well as the xenon impurity emission line at 148.8 nm and the structure at ~ 160 nm which could be attributed to the classical left turning point. For each of these wavelengths a time-resolved spectrum was recorded, either with a TAC range of 500 ns or 5 µs, depending on the emission time constant.

However, for determining the short scintillation time constants (e.g. those of the third excimer continuum; cf. sec. 11.3.3) at first the pulse profile of the exciting beam pulse had to be examined. This was carried out by measuring the X-ray fluorescence light emitted by the materials hit by the ion beam. These photons are emitted within a very short time interval after the excitation pulse ($<$ ps) [Dan89], thus their time structure directly represents the profile of the beam pulse which typically has a width of few nanoseconds. To avoid any scintillation light to disturb this measurement the direct optical path was blocked by an aluminium plate in the filter wheel; the X-ray light traveled to the PMT on a direct way through the surrounding CF-100 cross piece and was detected there. The beam profile obtained with this method for the sulfur beam is shown in fig. 11.21. Its shape can well be fitted with a Gaussian; applying the correction factor given in appendix G for the 5 µs TAC range its FWHM was found to be (5.36 ± 0.23) ns.

For the other two projectiles, Au^{14+} and p^+, similar but slightly shorter pulse widths of (3.03 ± 0.05) ns and (2.32 ± 0.02) ns, respectively, were found using the same method. In each case the settings of the Tandem Accelerator were chosen not to have any secondary peaks[20] in the pulse profile.

[20] In case the settings of the Tandem Accelerator (sec. 10.2) in pulsed mode are not properly chosen, e.g. the phases of the two beam choppers do not match perfectly, the beam pulse does not only consist of one main pulse, but has (smaller) secondary pulses, which arrive shortly before or after the main pulse.

11.3.2 Emission Time Constants of the Second Excimer Continuum

Knowing the profile of the exciting pulse and the range calibration of the TAC (which is given in appendix G), the recorded scintillation-time spectra can be analysed. Fig. 11.22 shows the time-resolved spectrum of liquefied argon at 128.6 nm (peak emission wavelength of the second excimer continuum) with a TAC range of 5 µs. The function

$$f(t) = \underbrace{A_s \cdot exp\left\{-\frac{t}{\tau_s} + c_s\right\}}_{singlet} + \underbrace{A_t \cdot exp\left\{-\frac{t}{\tau_t} + c_t\right\}}_{triplet} + \underbrace{\frac{A_{rec}}{\left(1 + \frac{(t-t_{rec})}{\tau_{rec}}\right)^2}}_{recombination} + C_0 \qquad (11.3)$$

is fitted to the spectrum. The two exponential functions take into account the light emission by the singlet and triplet decays of neutral argon excimer molecules with decay time constants τ_s and τ_t, respectively. The parameters A_i (i = s,t) scale the exponential functions to the right intensity; the parameters c_i (i = s,t) shift them in time. The latter is needed as the peak emission is not at t = 0 ns. These two exponential functions, however, do not fully describe the time behaviour of the scintillation-light emission, but another function describing the delayed recombination of electrons and ionic excimer molecules is needed.

For xenon in the gas phase this recombination was found to be approximated very well by a function equal to the third term in eq. (11.3) [Rib94]. This functional dependence is gained from the solution of the differential equation describing the recombination processes under the assumptions that the densities of electrons and ions are equal, the electrons are distributed homogeneously over the excitation volume, and the recombination rate does not depend on time, i.e. the electrons have already cooled down to surrounding temperature. The former two assumptions are quite reasonable, especially as liquid argon is electrically neutral, the latter assumption is expected to be valid for the liquid phase already few nanoseconds after the end of the exciting beam pulse due to the much higher density[21]. Again, the parameter A_{rec} scales the function to the right intensity, t_{rec} accounts for the time delay between the start of the time scale and the time of the peak emission. τ_{rec} is the recombination time constant, which is also assumed to be independent of time. Excimer molecules produced in the singlet state in recombination processes decay rather quickly (few ns; see below) and lead to additional scintillation light in the transition region between fast and slow component, whose time scale is governed by the time scale of the recombination processes; excimer molecules produced in the triplet state, however, contribute only to the delayed component of the scintillation light because of their long life time.

For the excitation by the sulfur beam, decay time constants of (7.35 ± 0.18) ns for the singlet and (1208.5 ± 17.7) ns for the triplet decays are obtained; the best fit value for the recombination time scale is $\tau_{rec} = (37.4 \pm 0.2)$ ns.

This time-resolved measurement was repeated twice to check for the dependence of the obtained time constants on the slit width which is set at the monochromator, and the intensity of the ion beam current. At first, the width of the monochromator slits was changed from 100 µm to 350 µm, which translates into a change of the wavelength resolution of $\Delta\lambda = 0.3$ nm to 1.05 nm. In addition, the measured light intensity increases by a factor of ~ 3.5. In

[21] For xenon in the gas phase at 1500 mbar the electrons are cooled down to room temperature ~ 800 ns after the exciting beam pulse [Rib94]. For liquid argon thermalisation times of hot electrons are reported to be below 1 ns [Sow82].

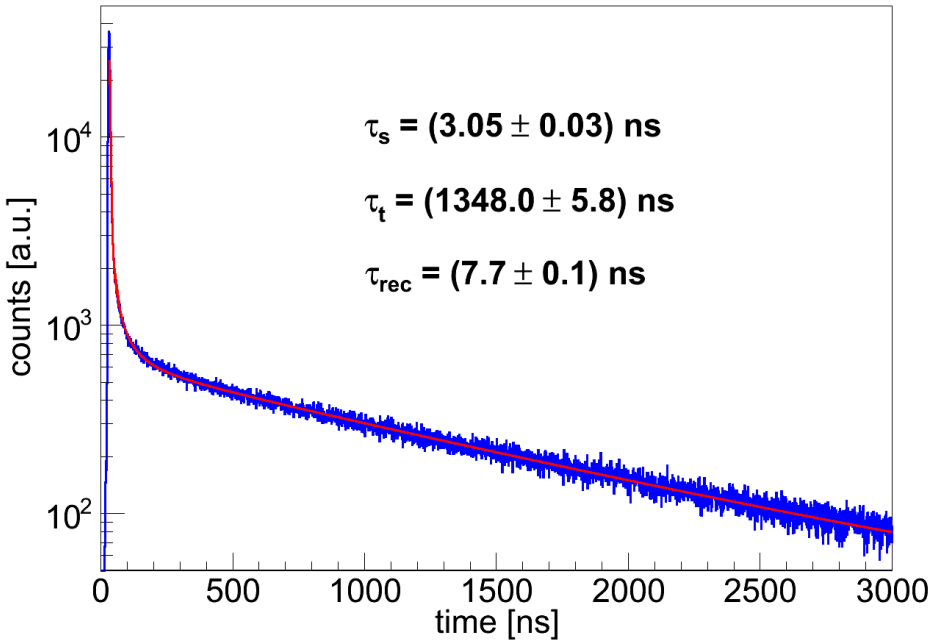

Figure 11.22: *Scintillation time spectrum (on a logarithmic scale) of liquid argon at 128.6 nm ($\Delta\lambda = 1.5$ nm) excited by a pulsed proton beam. The data (blue) is fitted by the function defined in eq. (11.3) (red line); the emission time constants of the singlet and the triplet decay as well as the time scale of the recombination obtained from this fit are quoted.*

this measurement time constants of (7.30 ± 0.07) ns (singlet), (1142.8 ± 12.2) ns (triplet), and (34.5 ± 0.1) ns (recombination) are obtained (cf. also tab. 11.2). These constants are slightly lower than those obtained with 100 µm slit width, but still in good agreement. Therefore, for the following measurements (unless otherwise noted) the bigger slit width is used, as this notably increases counting statistics.

After checking for the dependence on the slit width also the intensity of the beam current was considerably changed (reduced by a factor of ten), and the three decay time constants were measured again. The outcome is (7.35 ± 0.21) ns, (1199.3 ± 18.3) ns, and (34.2 ± 0.2) ns, respectively. Hence, no dependence on the beam current was found.

The time-resolved scintillation-light emission obtained at the peak emission wavelength of the second excimer continuum with proton excitation can again be fitted well with function (11.3); see also fig. 11.22. Here, scintillation time constants of (3.05 ± 0.03) ns for the singlet transition and (1348.0 ± 5.8) ns for the triplet transition are found. The best fit value for the recombination time is (7.7 ± 0.1) ns.

As already discussed above, during the beam time with the gold projectiles twice the problem of a ruptured titanium foil at the cell's beam entrance flange was encountered. The repair was rather time-consuming, hence, the remaining time for recording spectra - and thus their statistics - was limited. Therefore, the decay-time constant of the excimer triplet state and the recombination could not be obtained for this case. However, the singlet decay-time constant is fitted quite well to the light-emission spectrum at 129 nm; the obtained value is $\tau_s = (6.98 \pm 0.10)$ ns. All time constants are summarised in tab. 11.2. In each case the

values of the fastest time constant obtained from the fit are cross-checked by fitting the time spectrum with a convolution of a Gaussian (representing the beam pulse with a fixed width as obtained above) and an exponential function. However, no changes of the results are observed, i.e. the shape of the beam pulse has no influence.

An important parameter in the context of particle discrimination is the intensity ratio of scintillation light of singlet and triplet decays, which is calculated as

$$\frac{I_s}{I_t} = \frac{\int_{t_0}^{\infty} A_s \cdot exp\{-\frac{t}{\tau_s} + c_s\} \cdot dt}{\int_{t_0}^{\infty} A_t \cdot exp\{-\frac{t}{\tau_t} + c_t\} \cdot dt} \quad . \tag{11.4}$$

A_s and A_t denote the normalisation constants and c_s and c_t the time-shift constants obtained from the fits to the data, τ_s and τ_t are the respective decay-time constants. The integration starts at time t_0, the time of peak emission. For the sulfur-beam excitation an intensity ratio of 1.6 ± 0.6 is obtained; the singlet-to-triplet intensity ratio in case of excitation by protons is 0.25 ± 0.05. As the triplet decay cannot be fitted for the gold-beam data $\frac{I_s}{I_t}$ cannot be calculated in that case. The values obtained for the intensity ratio are quoted in tab. 11.2, too.

The light intensity due to recombination is hereby not taken into account, only the integrals of singlet and triplet decays. In this way, the values obtained for the singlet-to-triplet ratio can be compared best to the values quoted in literature, where the time-resolved scintillation-light spectrum is most often only approximated by a sum of two exponential functions, completely ignoring deviations in the transition region between fast component (singlet decay) and slow component (triplet decay) due to delayed recombination.

The singlet time constants τ_s obtained for the heavier projectiles, sulfur and gold, are in rather good agreement, however, the τ_s for the proton beam is considerably shorter[22]. This might be explained with the mixing between excimer molecules in the singlet state and in the triplet state in collisions with hot (i.e. not thermalised) electrons:

$$Ar_2^*(^3\Sigma_u^+) + e^- \longleftrightarrow Ar_2^*(^1\Sigma_u^+) + (e^-)' \quad . \tag{11.5}$$

Such collisions with hot electrons become more likely for excitation by heavier particles as these produce more secondary electrons from ionisation processes and a higher ionisation density. The singlet decay time obtained from the fits to the time-resolved scintillation light spectra could therefore be only "effective" time constants, i.e. a convolution of the "true" life time of excimer molecules in the singlet state and the time scale of the mixing process. In case the latter is slower than the singlet life time, and more dominant for heavier projectiles, the observed differences in the singlet life times could be explained. The time resolution of the presented measurements, however, does not allow to disentangle the two possible time scales of singlet decay and mixing, but the fast component of the data is described best with a single exponential function. Experiments with a much higher time resolution could help to clarify this point. In experiments with pulsed synchrotron radiation with pulse widths of only 130 ps [Wil83] and excitation energies which were chosen to selectively excite argon molecules to the precursor of the singlet state [Mor89] an emission time constant of $\tau_s = (1.65 \pm 0.1)$ ns is found (see tab. 11.3). As effects of hot electrons can be neglected in these measurements

[22] This is also observed for other wavelengths in the second excimer continuum, see tab. 11.4.

Beam projectile	τ_s [ns]	τ_t [ns]	τ_{rec} [ns]	$\frac{I_s}{I_t}$
S^{10+}	7.35 ± 0.18	1208.5 ± 17.7	37.4 ± 0.2	1.6 ± 0.6
S^{10+}	7.30 ± 0.07	1142.8 ± 12.2	34.5 ± 0.1	1.9 ± 0.5
S^{10+}	7.35 ± 0.21	1199.3 ± 18.3	34.2 ± 0.2	1.5 ± 0.7
p^+	3.05 ± 0.03	1348.0 ± 5.8	7.7 ± 0.1	0.25 ± 0.05
Au^{14+}	6.96 ± 0.10	-	-	-

Table 11.2: *Fitted decay-time constants of the time-resolved measurements close to the peak emission wavelength of the second excimer continuum (129.1 nm for the sulfur and the gold beam, 128.6 nm for the proton beam) with the different ion beams (see text). The intensity ratio $\frac{I_s}{I_t}$ of light from singlet decays to light from triplet decays is given, too. The slit width is set to 500 µm for the proton and the gold beam (100 µm for the sulfur beam; data quoted in the first row), which translates into an optical resolution of $\Delta\lambda = 1.5$ nm ($\Delta\lambda = 0.3$ nm). The data obtained with the sulfur beam is cross-checked and verified with two additional measurements, however, with a slit width of 350 µm ($\Delta\lambda = 1.05$ nm; second row in the table) and, in the second case, with a ten times reduced beam current (third row). In case of the gold beam the triplet component could not be determined due to lack of statistics.*

(the excitation energy was too low for ionisation), this decay time might represent the "true" life time of the singlet state.

The triplet life time τ_t, on the other hand, found for proton-beam excitation is longer than that obtained for sulfur beam excitation. This cannot be explained with the mixing process (11.5), as hot electrons are only available during and in the first few nanoseconds after the exciting beam pulse. The data presented in tab. 11.2 show that the obtained triplet life times do not depend on the ion-beam current, i.e. the density of excited states. This also excludes the hypothesis that a quenching of the excimer molecules [Mei08] (and references therein), e.g.

$$Ar_2^* + Ar_2^* \longrightarrow Ar_2^+ + 2Ar + e^- \quad , \tag{11.6}$$

causes the observed differences in the life times of the triplet state with protons and sulfur ions, which produce different excitation densities. Process (11.6) is in contradiction to the data.

However, impurities are known to diminish the life time of the excimer triplet state [Hei11] by quenching processes. Therefore, the shorter triplet life time observed for sulfur-beam

excitation might also be attributed to a higher level of remnant impurities in argon during the beam time with the S^{10+}-beam. However, besides the impurity emission lines of xenon at 148.8 nm and the only indicated emission caused by oxygen at 558 nm no further impurity emissions are found in the spectra, neither for sulfur nor for proton excitation. In addition, the intensity of both emission lines is of comparable size for both ion beams, indicating a similar impurity concentration. The decrease of the triplet life time at the peak emission wavelength of liquid argon as a function of the concentration of any impurity could be studied in future experiments using the setup presented here by deliberately doping the argon bulk material with varying concentrations of certain impurities (like xenon, nitrogen, or oxygen).

The time scales for recombinations, τ_{rec}, are different for proton- and sulfur-beam excitation, but characteristic for one exciting species (see tab. 11.4). For electron-beam excitation a time constant of $\tau_{\mathrm{rec}} = 175\,\mathrm{ns}$ has been reported [Hei11]. At present, the behaviour of this time scale is not understood and should be addressed in future experiments.

A key result of the present studies is the dependence of the singlet-to-triplet ratio on the mass of the incident particle: the heavy ion beam (sulfur) gives rise to a ratio $\frac{I_s}{I_t}$ which is about a factor of six[23] higher than the ratio obtained for the light ion beam (protons). The proposed mechanism [Hei11] to account for this difference is again the mixing, eq. (11.5), between excimer molecules in the singlet and molecules in the triplet state in collisions with hot (i.e. not thermalised) electrons. This mixing significantly increases the singlet-to-triplet ratio, as excimer molecules in the singlet state have a much higher probability to decay than molecules in the triplet state because of the huge difference in life time of the singlet and the triplet state (more than two orders of magnitude). Collisions with hot electrons become more likely for excitation by heavier particles as these produce more secondary electrons from ionisation processes and a higher density of excited molecules.

Consequently, the singlet-to-triplet ratio is a parameter which allows to perform particle discrimination between light incident particles (like electrons or protons) and heavy exciting particles (heavy ions or argon nuclei recoiling after a collision) by means of the scintillation light only. In a typical pulse shape discrimination algorithm making use of a tail-to-total value of the pulse the ratio $\frac{I_s}{I_t}$ depends on the time cut which is used to separate the "fast" component of the pulse from the "slow" one, as this cut determines if the recombination light is considered to be part of the "fast" or part of the "slow" component, as its time scale is of the order of few tens of nanoseconds; see tab. 11.2. However, the intensity of the scintillation light due to delayed recombination is small, therefore, the singlet-to-triplet ratio depends only weakly on the time cut chosen.

The results of the present analysis, see tab. 11.2 are also compared to values reported in literature. Table 11.3 gives an overview of the emission time constants (singlet and triplet decays of excimer molecules in liquid argon) as well as the light-intensity ratio quoted by different authors for different exciting particles. Most of these values have been obtained by exciting liquid argon by radioactive sources [Car79, Hit83, Lip08, Pei08], either from outside or by directly immersing the source into the argon bulk material. Only the emission time constants quoted in [Car79] are measured without wavelength shifter, the other references use a wavelength-shifting material to record the scintillation light. The fluorescence decay time constants of these materials are of the order of a few nanoseconds [Hit83], which introduces additional errors to the determination of the argon emission time constants, especially for the

[23] This result is found to be independent of the beam current, i.e. the density of excited states, within the parameter ranges of the present experiment.

fast singlet decay. The values quoted in [Mor89] are obtained by excitation of liquid argon by synchrotron radiation; the light produced is detected with CsI-coated microchannel plates. In [Hei11] a technique similar to that presented in this thesis is used: liquid argon is excited by an electron beam, which is coupled into the liquid through a thin ceramic membrane; the scintillation light is measured with a Czerny-Turner monochromator (McPherson 218) and a VUV-sensitive PMT.

Exciting Particle	τ_s [ns]	τ_t [ns]	$\frac{I_s}{I_t}$	Ref.
γ	1.65 ± 0.1	-	-	[Mor89]
γ	-	1463 ± 55	-	[Lip08]
γ	10 ± 5	1200 ± 20	0.30 ± 0.01	[Pei08]
e^-	< 6.2	1300 ± 60	0.51 ± 0.05	[Hei11]
e^-	4.6	1540	0.26	[Car79]
e^-	6 ± 2	1590	0.3	[Hit83]
α	4.4	1100	3.3	[Car79]
α	7.1 ± 1.0	1660 ± 100	1.3	[Hit83]
α	10 ± 5	1200 ± 20	2.6 ± 0.1	[Pei08]
n	10 ± 5	1200 ± 20	3.5 ± 0.2	[Pei08]
fission fragments	6.8 ± 1.0	1550 ± 100	3	[Hit83]

Table 11.3: *Literature values [Car79, Hei11, Hit83, Lip08, Mor89, Pei08] for the light-emission time constants of singlet and triplet liquid argon excimer decays as well as the light-intensity ratio $\frac{I_s}{I_t}$ quoted for different exciting particles.*

The values quoted in tab. 11.3 are in reasonable agreement with the emission time constants obtained within the scope of the present thesis. In particular, the singlet-to-triplet ratio obtained for strongly ionising particles (α-particles and fission fragments) is found to be much bigger than those for electrons. Again, this illustrates the particle discrimination potential of this parameter.

Assuming that the singlet-to-triplet intensity ratio stays constant with the energy of the incident particle, an estimation for the energy threshold of the discrimination potential can be determined: in a dedicated Monte-Carlo simulation each photon of a number of scintillation photons N was randomly chosen to be either a singlet or a triplet photon using the probabilities

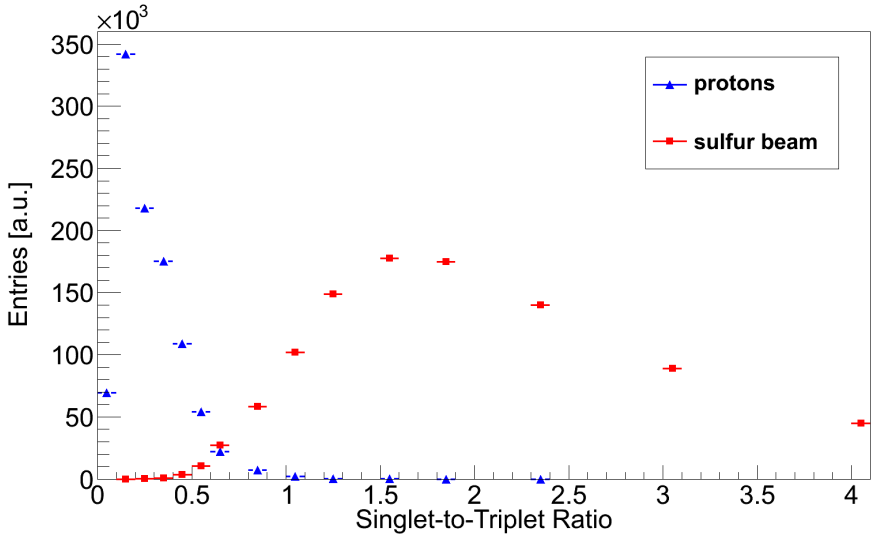

Figure 11.23: *Simulated singlet-to-triplet ratios for the proton (blue triangles) and the sulfur beam (red squares) for in total 20 detected photons. For this photon number the distributions overlap at* $\frac{I_s}{I_t} = 0.6$*. Both distributions peak at the singlet-to-triplet ratio which was obtained from the ion-beam experiments;* ~ 1.6 *for* S^{10+} *and* ~ 0.25 *for* p^+*.*

$$P_s = \frac{\frac{I_s}{I_t}}{(1 + \frac{I_s}{I_t})} \quad , \quad P_t = 1 - P_s \quad . \tag{11.7}$$

The singlet-to-triplet ratio was consequently calculated as the number of photons found be singlet photons divided by the number of triplet photons. This simulation was carried out both for the sulfur beam with $\frac{I_s}{I_t} = 1.6$ and the proton beam with $\frac{I_s}{I_t} = 0.25$, in each case 1,000,000 times. The resulting distributions of the simulated singlet-to-triplet ratio are displayed in fig. 11.23 for $N = 20$.

The higher the photon number N the narrower are the obtained distributions. For $N \approx 90$ the two distributions cease to overlap, hence the discrimination potential becomes 100%. In an ideal experiment, i.e. an experiment where all created scintillation photons are detected, 90 photons correspond to a deposited energy of 2.25 keV (with a light yield of liquid argon of 40,000 photons per MeV [Dok88]). This energy threshold increases with decreasing detection efficiency. Of course, particle discrimination is principally also possible at lower energies, however, for overlapping distributions rejecting 100% of one species results in an acceptance smaller than 100% for the other one. The energy-independence of the singlet-to-triplet intensity ratio, however, has to be proven or rejected in forthcoming measurements, where the energy of the ion beam is varied. This is an important aspect for predictions for the low-energetic regime.

Besides the peak emission of the second excimer continuum also the time structures of its long- and short-wavelength wings were investigated, at about ± 5 nm and, in the case of sulfur beam excitation, also at ± 14 nm off the peak emission.

For these time-resolved spectra again function (11.3) was fitted to the data, i.e. the light intensity is, except for one case, still sufficient to determine the triplet life time, too. The

time constants obtained from these fits as well as the intensity ratio of singlet-to-triplet light are listed in tab. 11.4 for the different investigated wavelengths and beam projectiles.

The decay time constants are to first order independent of the precise wavelength within the second excimer continuum. This is important for not-wavelength-resolved detection methods, as no selection for a specific wavelength has to be done in order to achieve particle discrimination by time-resolved studies. In contrary, wavelength-integrating measurements can be performed, which also greatly increases the usable intensity of scintillation light: the whole second excimer continuum can be used, and not only one single wavelength, or a narrow wavelength interval. This also applies to the singlet-to-triplet intensity ratio, the parameter which can be used for a discrimination between light incident particles (like electrons or protons) and heavy ions. The discrimination potential of such wavelength-integrating methods was also confirmed in dedicated experiments [Lip08, Pol07, Pei08].

However, although the singlet-to-triplet ratio is considerably different for the two ion beams and allows a wavelength-integrated particle discrimination, there is a trend for a decreasing ratio $\frac{I_s}{I_t}$ with rising wavelength. This possibly reflects the spectral displacement of the scintillation light from singlet decays (peak emission wavelength 126.6 nm [Mor89]), which is dominant in the blue wing of the second excimer continuum, and light from triplet decays (peak emission wavelength 127.6 nm [Mor89]) dominating the red wing. Therefore, in wavelength-integrating measurements the singlet-to-triplet ratio might deviate from the values quoted in the present thesis which were recorded for a small wavelength interval.

11.3.3 Emission Time Constants at Longer Wavelengths

Besides the second excimer continuum also the emission time constants of the diverse structures in the wavelength region of the third excimer continuum (see fig. 11.20) have been studied. As some of these structures have a rather fast emission time constant (see below), the shape of the exciting beam pulse was fully taken into account. This was performed by fitting the time-resolved emission spectrum with a convolution of a Gaussian and an exponential function plus a constant. The widths of the Gaussian were hereby set to the value obtained from the Gaussian fit to the time-resolved spectrum recorded with X-ray fluorescence light (see fig. 11.21). The emission time constants were obtained from the fitted decay-time constant of the exponential function; the constant accounts for the dark-count rate. The fit was carried out analytically using the toolkit program RooFit [ROO08], where the convolution of a Gaussian with an exponential function is implemented.

Using this method, for the structure at 160 nm one single decay time constant of (39.1 ± 2.7) nm is obtained, see fig. 11.24, when excited by the sulfur beam.

This structure is thus much faster than the triplet light emission in the second excimer continuum, but considerably slower than the singlet. In the gas phase at 155 nm the light emission of the classical left turning point (LTP) is found [Wie00], which stems from the decays of vibrationally excited excimer molecules (see sec. 9.1). The emission feature at 160 nm found in liquid argon could be the analogue to the LTP, but redshifted[24].

However, for gaseous argon the decay time constant of the LTP is observed to be fast: at a pressure of 1000 mbar its intensity has completely decayed after ~ 16 ns [Wie00]. The time constant of ~ 39 ns obtained for the liquid phase could therefore hint to a slower relaxation of vibrationally excited molecules in liquid argon than in the gas phase. Additional information

[24] A Gaussian fit to the emission spectrum yields a center wavelength of (160.1 ± 0.2) nm and a width of the structure of (5.1 ± 0.2) nm.

wavelength	τ_s [ns]	τ_t [ns]	τ_{rec} [ns]	$\frac{I_s}{I_t}$
Sulfur beam				
115.6 nm	5.79 ± 0.53	1051.0 ± 96.9	36.4 ± 0.4	4.7 ± 5.5
123.6 nm	7.41 ± 0.05	1330.1 ± 28.8	38.1 ± 0.1	3.5 ± 1.1
129.1 nm	7.35 ± 0.18	1208.5 ± 17.7	37.4 ± 0.2	1.6 ± 0.6
134.6 nm	6.26 ± 0.07	1173.7 ± 13.0	38.1 ± 0.1	1.0 ± 0.4
143.6 nm	6.96 ± 0.33	-	32.6 ± 0.7	-
Proton beam				
121.6 nm	3.25 ± 0.15	1273.9 ± 95.6	8.2 ± 0.1	0.59 ± 0.95
123.6 nm	3.06 ± 0.04	1286.0 ± 10.1	8.0 ± 0.1	0.40 ± 0.14
128.6 nm	3.05 ± 0.03	1348.0 ± 5.8	7.7 ± 0.1	0.25 ± 0.05
133.6 nm	3.20 ± 0.07	1311.1 ± 18.7	8.6 ± 0.1	0.21 ± 0.15

Table 11.4: *Fitted decay-time constants of the time-resolved measurements close to the peak emission wavelength of the second excimer continuum (129.1 nm and 128.6 nm, respectively) and at its wings with the different ion beams. The intensity ratio $\frac{I_s}{I_t}$ of light from singlet decays to light from triplet decays is given, too. In one case the spectrum contained too little statistics to fit the long-lived component; in this case no value is quoted.*

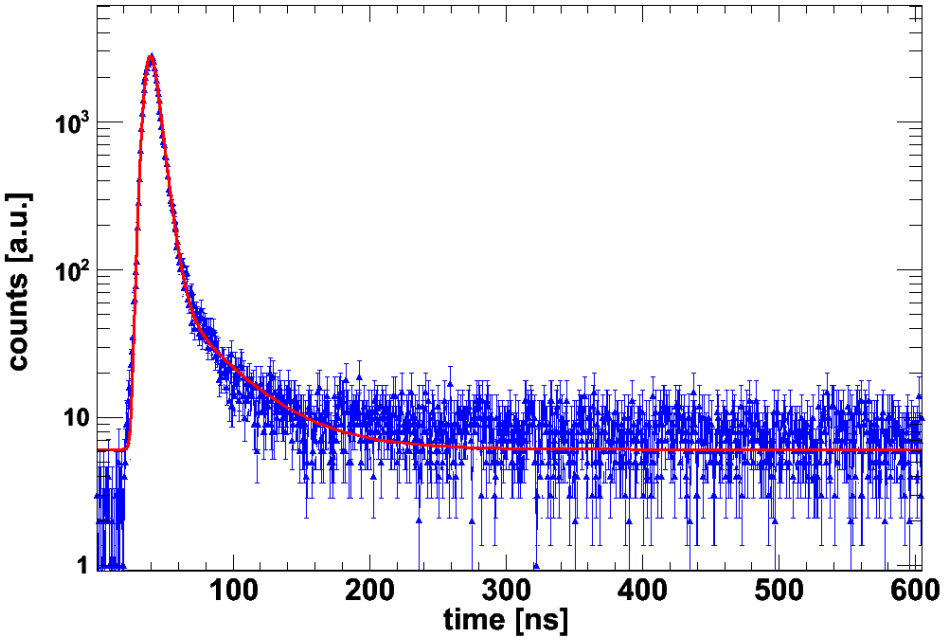

Figure 11.24: *Time resolved spectrum of the emission structure at 160 nm ($\Delta\lambda = 1.5$ nm) with sulfur-beam excitation and fitted with a convolution of a Gaussian and an exponential function plus a constant. A single emission time constant of (39.1 ± 2.7) ns is obtained.*

on relaxation processes in the liquid phase could be obtained from recording the scintillation light spectrum of liquid argon down to wavelengths shorter than 110 nm, looking for the first excimer continuum, a further emission feature related to the decay of vibrationally excited excimer molecules. Such an experiment could, for example, be performed with the setup presented in this thesis, but using a LiF-window with a cut-off wavelength of 105 nm [Kor12b] instead of the MgF_2-window with a cut-off at 110 nm [Kor12]. In addition, the correction functions for the "fogging" effect would be needed down to these wavelengths, or, even better, a deposition of residual gas onto the cell's window has to be avoided (see sec. 11.1.4).

Towards longer wavelengths the next emission structure is found at (182.1 ± 0.1) nm with a width of (7.9 ± 0.1) nm, see fig. 11.20. The time structure of this continuum is investigated both with the sulfur and the proton beam (at 180.6 nm), in the latter case, however, with three times less statistics; in addition, its wings are investigated at 174.6 nm (sulfur beam) and 190.6 nm (proton beam).

Both time-resolved spectra recorded with the two different exciting particles are best fitted with the fit function defined in eq. (11.3), tab. 11.5, as well as the time-resolved spectrum at 174.6 nm. At 190.6 nm, however, only an upper limit for the decay time can be given with the time resolution achieved here. This time constant was obtained from fitting a convolution of a Gaussian and an exponential function to the data.

The time behaviour and the emission time constants of the continuum at 182 nm are very similar to those obtained for the second excimer continuum; cf. tabs. 11.2 and 11.4. A direct contribution from the red wing of the latter can, however, be excluded, as the intermediate structure at 160 nm has a very different time structure. The time structure of the 182 nm-continuum could be explained if (part of) the emission light stems from a rather quick process

Beam projectile	Wavelength	τ_s [ns]	τ_{rec} [ns]	τ_t [ns]
S^{10+}	180.6 nm	5.15 ± 0.02	38.7 ± 0.2	1155.4 ± 24.3
p^+	180.6 nm	4.24 ± 0.01	10.2 ± 0.3	-
S^{10+}	174.6 nm	5.08 ± 0.01	40.6 ± 0.1	1022.4 ± 22.1
p^+	190.6 nm	< 2.91	-	-

Table 11.5: *Fitted decay-time constants of the continuum around 182 nm. Both with the proton and the sulfur beam a time-resolved spectrum at 180.6 nm (close to the centre wavelength) was recorded with a resolution of $\Delta\lambda$ =1.5 nm; in addition, the red and blue wings of the continuum were investigated. For the proton beam, statistics was too low to fit the long time constant. Except for the spectrum at 190.6 nm, which shows a very fast time behaviour like all emission features at even longer wavelengths (see below), the time structure of the continuum is very similar to that of the second excimer continuum.*

($\tau \lesssim$ few ns), which is excited by luminescence light from the second argon excimer continuum.

As from the emission spectra (fig. 11.12) a residual xenon impurity was identified, possibly part of the observed light stems from the second excimer continuum of xenon, which peaks at ~ 172 nm in the gas phase [Mor08]; see also fig. 9.4. This continuum stems from the decay of vibrationally relaxed xenon excimer molecules, which form in the collision of an excited and a ground-state xenon atom[25]. The excitation energy could hereby stem from the decay of an argon excimer molecule, which lies energetically higher than the lowest excited states of xenon atoms [Pol07] (and references therein). The decay-time constants of xenon excimer molecules have been reported to be much faster than those of argon [Mor89], too.

In a dedicated study where the wavelength-resolved scintillation-light spectrum was recorded between 165 nm and 200 nm, but only in a time interval from 40 ns to 3180 ns after the peak intensity of the exciting beam pulse, it could be shown that the slow components of the light emission in this wavelength region peak at ~ 174 nm. Hence, this spectral feature could indeed be the second excimer continuum of xenon, redshifted by about 2 nm, which is probably an effect related to temperature and/or the surrounding matrix of argon atoms.

The time-resolved spectra at still longer wavelengths, however, show a very fast time behaviour of the luminescence-light emission: within the time resolution possible here, which is limited by the width of the exciting ion-beam pulse, only upper limits for the decay time constants can be quoted. With the sulfur-beam excitation time constants of < 3.85 ns at (201.6 ± 1.5) nm and < 4.15 ns at (275.6 ± 1.5) nm are obtained, with the proton beam

[25]The processes are analogous to the formation and decay of argon excimer molecules, which were more thoroughly explained in ch. 9.

$< 2.08\,\text{ns}$ at $(210.6 \pm 3.0)\,\text{nm}$ and $< 2.04\,\text{ns}$ at $(275.6 \pm 3.0)\,\text{nm}$.

The fast light-emission times support the theory that the emission features in the long-wavelength part of the scintillation light spectra ($\gtrsim 190\,\text{nm}$) can indeed be attributed to processes analogous to the third excimer continuum in the gas phase, i.e. decays of ionic excimer molecules (cf. sec. 9.1), which are already in the gas phase found to be very fast (most of the intensity has already decayed some tens of nanoseconds after excitation) [Wie00]. It is important to note that the fast time scales of these luminescence-light emissions are possibly worsening the particle discrimination by means of the pulse shape in wavelength-integrating measurements, as they might be misidentified as singlet decays of neutral excimer molecules (second excimer continuum) modifying the singlet-to-triplet ratio. However, the total intensity of scintillation light in the wavelength regime of the third excimer continuum is so low (see sec. 11.2.1) that its impact on such measurements is probably negligible. Pulse-shape based particle discrimination in argon is also possible in wavelength-integrating measurements, as was already successfully shown [Lip08, Pei08, Pol07].

The small influence of the third excimer continuum can be derived from the data presented here: adding the time-resolved spectrum recorded with the sulfur beam at 129.1 nm with a properly scaled[26] time-resolved spectrum of the third excimer continuum (the spectrum at 275.6 nm was chosen as a typical spectrum) and fitting the resulting spectrum with function (11.3) yields exactly the same time constants and the same singlet-to-triplet ratio as the fit to the time-resolved spectrum at 129.1 nm alone. However, this conclusion is only valid if the sensitivity of the photon detector system is equal at both wavelengths. In case the detector sensitivity steeply rises for wavelengths longer than $\sim 170\,\text{nm}$, thereby pronouncing the third excimer continuum, the values obtained for the decay time constants and for $\frac{\text{I}_\text{s}}{\text{I}_\text{t}}$ might change.

11.3.4 Time Structure of the Xenon Impurity Line

Unlike the scintillation-light emission from argon itself the time structure of the xenon impurity emission line (148.8 nm) shows a slow "build-up" with a time constant of $\tau_\text{Ar} = (319.2 \pm 6.5)\,\text{ns}$ (with sulfur beam excitation) before the scintillation light is emitted with $\tau_\text{Xe} = (5120.7 \pm 35.8)\,\text{ns}$ (fig. 11.25). The time-resolved spectrum can therefore be fitted well with a sum of two exponential functions:

$$f_{xe}(t) = \frac{A}{\frac{\tau_{Ar}}{\tau_{Xe}} - 1} \cdot \left(\exp\left\{ -\frac{t - t_0}{\tau_{Ar}} \right\} - \exp\left\{ -\frac{t - t_0}{\tau_{Xe}} \right\} \right) \quad . \tag{11.8}$$

τ_Ar and τ_Xe are the single time constants, t_0 is an offset parameter, and A a multiplicative normalisation constant. The time behaviour of the xenon impurity emission hints to an energy transfer from excited argon atoms or argon excimer molecules, respectively, to the xenon atoms dissolved in the liquid. For the proton beam, an even longer time constant for the "build-up" is obtained, $\tau_\text{Ar} = (1433.8 \pm 61.7)\,\text{ns}$, while the decay shows a time constant with a similar value, $\tau_\text{Xe} = (5056.4 \pm 116.5)\,\text{ns}$, compared to that obtained with sulfur-beam excitation[27].

The energy transfer from the argon bulk material to the xenon atoms likely happens via long-range dipole-dipole coupling [Che72] of argon excimer molecules to the impurity

[26] The scale was chosen to be 0.00016, as this corresponds to the fraction of photons emitted in the wavelength region of the third excimer continuum, see above.

[27] For comparison: with electron excitation a decay time constant of $\tau_\text{Xe} = (3.7 \pm 0.1)\,\mu\text{s}$ has been reported [Hei11].

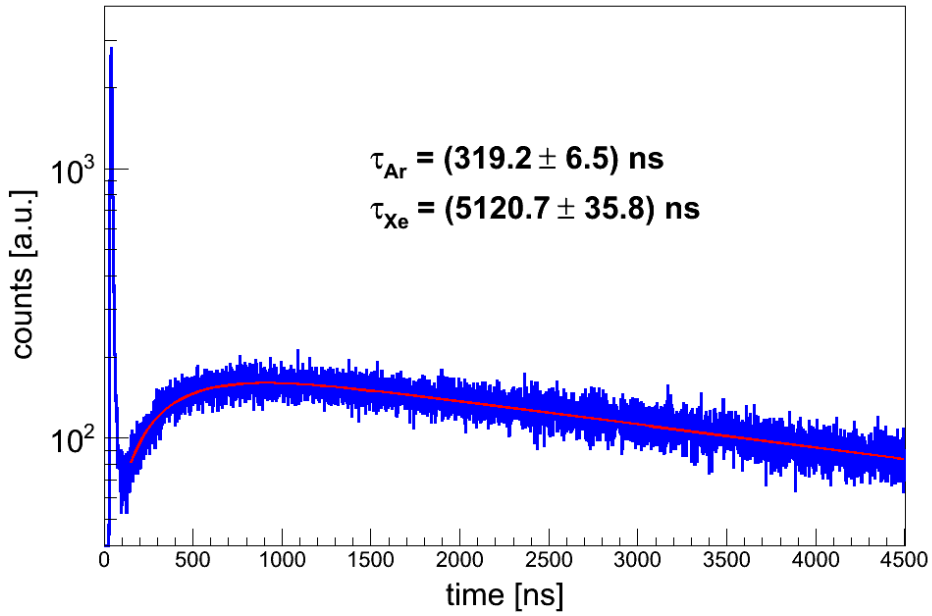

Figure 11.25: *Time structure of the xenon impurity emission at 148.8 nm ($\Delta\lambda = 1.5$ nm) when excited by the sulfur beam. The data (blue) was fitted with a sum of two exponential functions (red line), see eq. (11.8); the time constants of these fit functions are also quoted. At first, the light emission builds up with a slow time constant and decays afterwards. This hints to an energy transfer from the excited argon atoms in the surrounding matrix to the dissolved xenon atoms.*

atoms. The time constant τ_{Ar} obtained for the proton beam is quite similar to the decay time constant of the triplet excimer state, see tab. 11.4, which reinforces the hypothesis of an energy transfer from argon excimer molecules to the xenon impurity atoms. The decay of argon excimer molecules after excitation by a sulfur beam yields more than five times more fast singlet decays than triplet decays compared to the proton beam. Hence, the weighted average decay time of argon excimer molecules is much faster than for the proton beam. Consequently, the energy transfer to xenon should happen faster, too, and might explain the shorter "build-up" time τ_{Ar} observed for the sulfur beam.

The very long emission time constant of the xenon light could be explained with an initial population of the $^3\mathrm{P}_1$ excited state of xenon. In the gas phase the decay of this state gives rise to the xenon emission line at 146.96 nm [NIS12], which can, for example, be seen in fig. 11.15. In collisions with surrounding argon atoms the $^3\mathrm{P}_1$-state can be de-excited into the $^3\mathrm{P}_2$-state [Che72], which has no allowed dipole transition into the ground state. In the surrounding argon bulk material the transition might, however, happen [Hei11], explaining the long time constant observed. The emission wavelength of this transition is at 149.2 nm [NIS12] and thereby close to the observed wavelength (148.8 nm).

To summarise, the emission time constants of the various scintillation-light emission features of liquefied argon have been studied in time-resolved measurements. For the second excimer continuum two clearly distinct decay time constants have been found, which can be attributed to the decays of vibrationally relaxed argon excimer molecules in the singlet and

the triplet state into the (repulsive) ground state. For sulfur-beam excitation the singlet life time is found to be (7.35 ± 0.18) ns, the triplet life time is (1208.5 ± 17.7) ns. These time constants have been proven to be independent of the beam current and the monochromator's slit width. The singlet life time is in good agreement with that obtained with a gold beam, (6.98 ± 0.10) ns, however, for proton-beam excitation a considerably shorter decay time of (3.05 ± 0.03) ns has been found, which might be explained by the mixing between singlet and triplet states in collisions with hot electrons. This process is expected to be dominating for heavy incident particles, which create a higher density of excited states and more secondary electrons in ionisation processes. For proton-beam excitation a triplet life time of (1348.0 ± 5.8) ns is obtained. The life times of the decays of argon excimer molecules turned out to be independent of the exact wavelength within the second excimer continuum.

The same time structure as for the second excimer continuum of argon was found for an emission feature at ~ 174 nm, which is likely the second excimer continuum of xenon [Che72]. The other spectral feature related to a residual xenon impurity, the emission line at 148.8 nm, has an even slower decay time constant of (5120.7 ± 35.8) ns (sulfur-beam excitation) and (5056.4 ± 116.5) ns (proton-beam excitation). The other emission features of liquid argon, especially the third excimer continuum, were found to be rather fast.

The intensity ratio of decays of excimer molecules in the singlet and triplet state was found to be considerably different for the excitation by a heavy-ion beam (sulfur, (1.6 ± 0.6)) and protons, (0.25 ± 0.05). This finding is again independent of the exact wavelength, however, the ratio shifts over the wavelength region of the second excimer continuum. The singlet-to-triplet ratio consequently allows a particle discrimination by means of the scintillation light only, even in wavelength-integrating measurements. In the latter case, however, some care has to be taken that the fast light emission in the wavelength region of the third excimer continuum does not mimic the singlet decays. This is rather unlikely for any detection system which has a comparable detection efficiency both for wavelengths in the second and the third excimer continuum as the intensity of the latter is so small, but the singlet-to-triplet ratio could be spoiled by light from the third excimer continuum in case the detector's sensitivity greatly increases for wavelengths longer than ~ 170 nm.

Chapter 12

Conclusion and Outlook

The standard model of particle physics has proven to be very successful in describing many processes of elementary particles. However, despite this success, there are still open questions concerning this model, and different experimental observations clearly indicate physics beyond it. One of these observations is the periodic change of the neutrinos' flavour during propagation, commonly referred to as neutrino oscillations, which requires - in contradiction to the standard model - the neutrinos to be massive, and at least four additional parameters are introduced, three mixing angles and one CP-violating phase.

Only recently the third mixing angle ϑ_{13} has been measured in reactor electron antineutrino disappearance experiments (Double Chooz [Abe12, Abe12a], Daya Bay [An12], and RENO [Ahn12]) and accelerator based searches (T2K [Abe11] and MINOS [Ada08]). ϑ_{13} was found to be non-zero, and the best fit value is $\sin^2(2\vartheta_{13}) = 0.098 \pm 0.013$ [PDG12]. The first of the reactor experiments to publish an indication for antineutrino disappearance was Double Chooz, which measures reactor electron antineutrinos by means of the Inverse Beta Decay (IBD):

$$\bar{\nu}_e + p^+ \rightarrow e^+ + n \quad . \tag{12.1}$$

The signature of this reaction, a prompt event with at least 1 MeV and a delayed event with an energy of ~ 8 MeV, can be distinguished rather well from background. However, some kind of background can nevertheless mimic this event signature. Besides muon-induced correlated background these are mainly random coincidences between a signal in the energy window of the prompt event (0.7 - 12.2 MeV) and a neutron-like event. The former are hereby mainly caused by radioactivity in the detector. Therefore, the amount of radioimpurities in Double Chooz has to be kept under control by thoroughly selecting only very pure materials. This is best achieved by direct gamma spectroscopy and neutron activation analysis. Both have been performed for selected materials and parts of the Double Chooz far detector within the scope of the present thesis, using a dedicated germanium detector setup in the Garching underground laboratory.

In direct gamma spectroscopy samples from the Double Chooz shielding steel, parts of the InnerVeto PMTs and of the filling system, as well as various samples from the InnerVeto itself like the mounting structures of the reflecting VM2000 foil, and the electrodes used for welding the steel vessels were investigated; by means of the Double Chooz Monte-Carlo simulation the resulting singles trigger rates above the antineutrino detection threshold of 0.7 MeV in the Target volume were determined. The shielding steel material finally accepted to be used

in Double Chooz was found to be rather clean with a total activity of less than 80 $\frac{\text{mBq}}{\text{kg}}$, which leads to a negligibly small trigger rate[1] in the Target of less than 0.013 Hz. The trigger rate induced by the parts of the filling system (pressure sensors and the level measurement tubes) is dominated by the quite radioactive pressure sensor placed in the bottom middle of the GammaCatcher vessel. This sensor has an activity of $(13.2 \pm 9.1)\,\frac{\text{Bq}}{\text{kg}}$, however, the induced trigger rate is only $\sim 14.5{\cdot}10^{-3}$ Hz.

The contribution of all InnerVeto parts investigated in the present thesis to the total singles rate in Double Chooz can be safely neglected: in sum, all InnerVeto PMTs and the VM2000 holders give rise to only $(17.7 \pm 4.8){\cdot}10^{-4}$ Hz in the relevant energy region in the Target. The welding electrodes showed a relatively high amount of radioactivity, in total $(10.9 \pm 2.2)\,\frac{\text{Bq}}{\text{kg}}$, however, their mass in the final detector setup is so low compared to other detector parts that their contribution to the singles trigger rate is very low ($(2.72 \pm 0.64){\cdot}10^{-2}$ Hz), too.

The content of ^{40}K in the PPO used as wavelength shifter in the Target and GammaCatcher liquid as well as in the acrylic material of the vessels was measured with neutron activation analysis (NAA). The total content of ^{40}K in the PPO finally used in Double Chooz was found to be $(3.03 \pm 0.05){\cdot}10^{-11}\,\frac{\text{g}}{\text{g}}$, averaged over the results for three different samples. This value is in rather good agreement with the result from an atomic absorption spectroscopy measurement, $(2.5 \pm 0.4){\cdot}10^{-11}\,\frac{\text{g}}{\text{g}}$ [Abe12b, Buc09], which was done at the MPIK Heidelberg. For the acrylic material a ^{40}K-content of $(5.26 \pm 0.21){\cdot}10^{-11}\,\frac{\text{g}}{\text{g}}$ was obtained. These ^{40}K-contaminations give rise to a non-negligible total singles trigger rate in the Target of (0.295 ± 0.007) Hz, which is, however, tolerable and still far below the design goal.

A major part of the singles trigger rate is, however, not caused by external gamma rays entering the Target region but comes from uranium and thorium impurities in the detector liquids themselves. The mass concentrations of these impurities are tiny, but can be determined rather precisely by analysing the detector data for bismuth-polonium (BiPo) coincidences. Using a set of dedicated selection cuts these coincidences between the β^--decay of the Bi-isotope and the subsequent fast α-decay of the respective Po-isotope can be extracted from the raw data, and the mass concentrations of uranium and thorium can be calculated from the number of BiPo coincidences found: in 101.5 live days of detector data, 42182 BiPo-214-like coincidences and 10659 BiPo-212-like coincidences have been found, which translates into mass concentrations of $(1.71 \pm 0.08){\cdot}10^{-14}\,\frac{\text{g}}{\text{g}}$ for uranium and $(8.16 \pm 0.49){\cdot}10^{-14}\,\frac{\text{g}}{\text{g}}$ for thorium in the Double Chooz far detector (assuming radioactive equilibrium). The number of random BiPo-like coincidences has thereby been obtained from an analysis where the time-coincidence window was shifted backwards by 2 ms, and subtracted statistically. Both mass concentrations are well below the design goal of Double Chooz, $2 \cdot 10^{-13}\,\frac{\text{g}}{\text{g}}$ [Ard06], showing the high level of radiopurity reached. The concentration of thorium is considerably higher in the Target liquid than in the GammaCatcher, which might be attributed to the Gd-complex added, while more uranium is found in the GammaCatcher. The latter shows a slightly inhomogeneous vertex distribution with event clusters close to the detector's chimney and the Target vessel feet. This might hint at either a radon emanation by some component of the acrylic material, for example the glue, or an adsorption of radioimpurities on the acrylic's surface.

The half-lives of the respective polonium isotopes obtained from the data sample are (163.4 ± 1.4) µs for ^{214}Po and (295.0 ± 3.9) ns for ^{212}Po, which match the literature values, (164.3 ± 2.0) µs and (299 ± 2) ns [Fir96], respectively, rather well, indicating a very pure sam-

[1] The total trigger rate in the Target above 0.7 MeV was intended to be kept well below 20 Hz [Ard06].

ple. This allows to study detector properties: from the peak position of the α-peaks the α-quenching factors of the respective detector liquids can be calculated. For the Target liquid, quenching factors of (9.94 ± 0.04) at 7.7 MeV and (9.05 ± 0.01) at 8.8 MeV, for the GammaCatcher liquid (13.69 ± 0.02) at 7.7 MeV and (14.3 ± 0.1) at 8.8 MeV are obtained. The α-quenching factors at 7.7 MeV have been measured independently in a dedicated laboratory experiment [Abe11a], showing good agreement. The peak position of the ^{214}Po α-peak monitored over time additionally showed the very stable performance of the Double Chooz far detector at very low visible energies.

The mass concentrations of uranium and thorium obtained from the presented analysis of the BiPo coincidences serve as input parameters for forthcoming studies: the full attribution of all features seen in the energy spectrum of all single events to the underlying physics processes, in particular radioactive decays, benefits from the precise determination of the mass concentration of U and Th. This attribution is also an important input parameter for studies concerning the hypothetic $0\nu\beta\beta$-decay of ^{160}Gd. In addition, the analysis of BiPo coincidences provides a very clean sample of β^-- and α-events in the detector, allowing to study pulse shape properties of the detector, which might eventually lead to an algorithm for particle discrimination. This would help to further suppress (radioactivity-induced) background.

Besides accidental coincidences also correlated background due to (α,n)-reactions in the detector liquid has to be taken into account. The analysis of the detector data at low energies, however, shows that the correlated background induced by (α,n)-events is less than 0.06 per day in Target and GammaCatcher together, which can safely be neglected compared to the antineutrino rate of nearly 40 events per day [Abe12a].

Not only neutrino oscillations demonstrate physics beyond the standard model, but also experimental hints requiring the presence of Dark Matter in the universe cannot be explained using particles from the standard model only. In order to clarify the nature of Dark Matter, direct search experiments are performed on the Earth's surface. Different experimental techniques are utilised hereby, amongst them detectors with liquefied rare gases as target and detection medium, particularly argon and xenon. This technique, however, can also be used for the search for the $0\nu\beta\beta$-decay, a rare event which might occur for specific nuclei in case neutrinos are massive Majorana particles. As both the detection of Dark Matter particles and the $0\nu\beta\beta$-decay are rare event searches, a particle discrimination on an event-by-event basis is favoured, which requires a superior knowledge of the scintillation properties of the detection medium used.

Therefore, a dedicated experiment has been set up at the Munich Tandem Accelerator Laboratory (MLL) to study the scintillation properties of liquefied argon wavelength- and time-resolved in a broad wavelength region (110 nm through 950 nm) with high resolution and best statistics using different incident ion beams (protons, oxygen, sulfur, and gold). The centrepiece of this experiment was an all metal-sealed target cell made of copper with a thin titanium entrance foil for the ion beam and a MgF_2-exit window for the emitted scintillation light.

In four different beam times the scintillation light of argon was measured with an UV-Vis grating spectrometer (from ~ 250 nm to ~ 950 nm) and a Czerny-Turner monochromator with an attached VUV-sensitive PMT for wavelengths down to 110 nm, the cut-off wavelength of MgF_2 [Kor12]. The latter system also allowed to record time-resolved spectra at selected wavelengths using a pulsed beam with a pulse width of a few nanoseconds, and a time-to-amplitude converter in the read-out electronics.

The wavelength-resolved scintillation-light spectra of argon in the liquid (at $\sim 86\,\mathrm{K}$) and in the gas phase ($\sim 99\,\mathrm{K}$; 1200 mbar) recorded with the different ion beams are very similar, in particular in the wavelength region of the third excimer continuum ($\sim 170\,\mathrm{nm}$ to $\sim 300\,\mathrm{nm}$), where most of the differences were expected. In addition, in the liquid phase the energy output in this wavelength region is only 0.0094%, a great suppression compared to the gas phase, where 0.43% of the light intensity is emitted in the third excimer continuum. Therefore, the number of detectable photons from liquid argon with wavelengths longer than 170 nm is very small. For both states of aggregation the wavelength-resolved spectra are by far dominated by the second excimer continuum at wavelengths shorter than 145 nm; the light intensity at wavelengths longer than 300 nm is also tiny.

The time structure of the scintillation light of the second excimer continuum and its wings can be fitted well with a sum of two exponential functions accounting for the decays of excimer molecules in singlet and triplet states, and a function which takes into account the delayed recombination of thermalised electrons and ionic excimer molecules. The obtained decay time constants of the singlet state are $(7.35 \pm 0.18)\,\mathrm{ns}$ for sulfur-beam excitation, $(6.98 \pm 0.10)\,\mathrm{ns}$ for gold-beam excitation, and $(3.05 \pm 0.03)\,\mathrm{ns}$ for excitation by protons. The latter time constant is possibly shorter due to a reduced mixing between singlet and triplet states at lower excitation densities.

For the triplet state, similar life times of $(1208.5 \pm 17.7)\,\mathrm{ns}$ for sulfur-beam excitation and $(1348.0 \pm 5.8)\,\mathrm{ns}$ (protons) have been found. The time constants have been proven to be independent of beam current and the exact wavelength within the second excimer continuum. The intensity ratio of singlet and triplet decays, however, is considerably different for the different exciting particles: (1.6 ± 0.6) for the sulfur beam and (0.25 ± 0.05) for the proton beam. These differences are obtained throughout the whole second excimer continuum, although a dependence of the singlet-to-triplet ratio on the wavelength is found, which likely reflects the small spectral displacement of the singlet and the triplet emission spectrum. The different intensity ratios allow a particle discrimination by means of the scintillation light only, even in wavelength-integrating measurements. In an experiment with 100% photon detection efficiency the singlet-to-triplet-ratio distributions obtained for sulfur ions and protons cease to overlap at a deposited energy of 2.25 keV. Such a separation threshold would be sufficient for $0\nu\beta\beta$-experiments and likely also for direct Dark Matter search.

However, some care has to be taken in wavelength-integrating experiments, as the time structure of all argon-related emission features at longer wavelengths is very fast (below few nanoseconds). Hence, these light emissions might falsely be tagged as singlet decays of neutral argon excimer molecules, spoiling the singlet-to-triplet ratio. This effect is small in case the detector efficiency is of the same order of magnitude for both wavelength regimes, as the intensity of the third excimer continuum is tiny. However, this effect might become important for detector systems which are much more sensitive at wavelengths above $\sim 170\,\mathrm{nm}$.

Possible upgrades of the experimental setup would be the possibility to excite liquid argon by electrons and ions in the same setup to provide comparable conditions, and to vary the incident particle's energy to study the energy-dependence of the scintillation properties. As some of the present detectors for Dark Matter search utilise two-phase TPCs [Ben08, Mar11, Wri11], also a study of the scintillation of liquid argon in presence of an applied electric drift field would be desirable.

The spectra obtained for liquid argon containing tiny traces of a residual xenon impurity already indicate the possible potential of rare gas admixtures as detection media for large volume experiments: the tiny amount of xenon doped to the argon bulk material acts like

a wavelength shifter. Energy is transferred from the argon excimer luminescence peaking at $\sim 127\,\mathrm{nm}$ to the xenon emission line at $\sim 149\,\mathrm{nm}$ (and possibly to even longer wavelengths for higher concentrations of xenon and the appearance of emission structures of xenon excimer molecules). Such a wavelength shift could be used to read out the scintillation light with commonly available photosensors and makes the utilisation of additional wavelength-shifting materials or VUV-sensitive photon detection techniques dispensable.

In addition, for these admixtures time-resolved measurements should be performed. The light emission of the xenon impurity line is rather slow (compared to the time structures of the argon light emission), which could deteriorate the time resolution, and thus the spatial reconstruction of a possible xenon-doped liquid-argon detector. For wavelength-integrated measurements a considerable effect on the time behaviour of the scintillation light emission has been reported, too, which has, however, been found to improve the particle discrimination potential [Pei08]. This has to be studied more thoroughly in time- and wavelength-resolved measurements, best with varying xenon concentration. Further key questions to be addressed in these measurements are if the impurity atoms dissolve homogeneously in the host liquid, or if gradients in the concentrations occur[2], and how long are the attenuation lengths of such admixtures for their own scintillation light. The latter is especially important for the design of large-scale detectors, where the luminescence light has to traverse several metres of detector material before it is detected. For pure liquid argon the attenuation length has been measured recently [Neu12, Neu12a], however, it was shown that the attenuation is strongly wavelength-dependent and therefore no universal attenuation length can be given. As a further result it could be shown that already small concentrations of a xenon impurity have a major impact on the light attenuation in liquid argon.

Nevertheless, in case rare gas admixtures turn out to be not suitable for large detector systems as used in astroparticle physics, wavelength- and time-resolved measurements are still useful in clarifying the underlying scintillation mechanisms: the energy transfer from excited or ionised argon atoms (or excimer molecules) to xenon impurity atoms might be used to tag specific processes and, by varying the concentration of xenon, study the gas kinetic processes leading to luminescence light emission.

Also other rare gases, xenon in particular, are of great interest for rare event search experiments. Therefore, it is also desirable to study the scintillation properties, wavelength- and time-resolved, of pure xenon in forthcoming experiments using the same detection techniques as presented in this thesis.

[2]For xenon-doped liquid argon such gradients have been reported recently [Pei08, Pol07].

Part IV

Appendix

Appendix A

Decay Chains of Uranium and Thorium

This appendix shows the decay chains of ^{238}U and ^{232}Th including all branchings with a branching ratio greater than 1%. The colour code of the radioisotopes is the same as is used in the Karlsruhe nuclide chart: yellow stands for α-decay, light blue for β^--decay, and black for stable isotopes. The red numbers close to the transition arrows depict the energies (in keV) and branching ratios of the subsequent gamma emissions, but only for those with an emission probability greater than 5%. The tag "no γ" means either that there is no gamma emission at all, as the decay goes directly to the ground state of the daughter isotope, or that all single gamma emissions have an emission probability below the 5% threshold. For each isotope half-life and Q-value of the decay are given. All data taken from [Fir96].

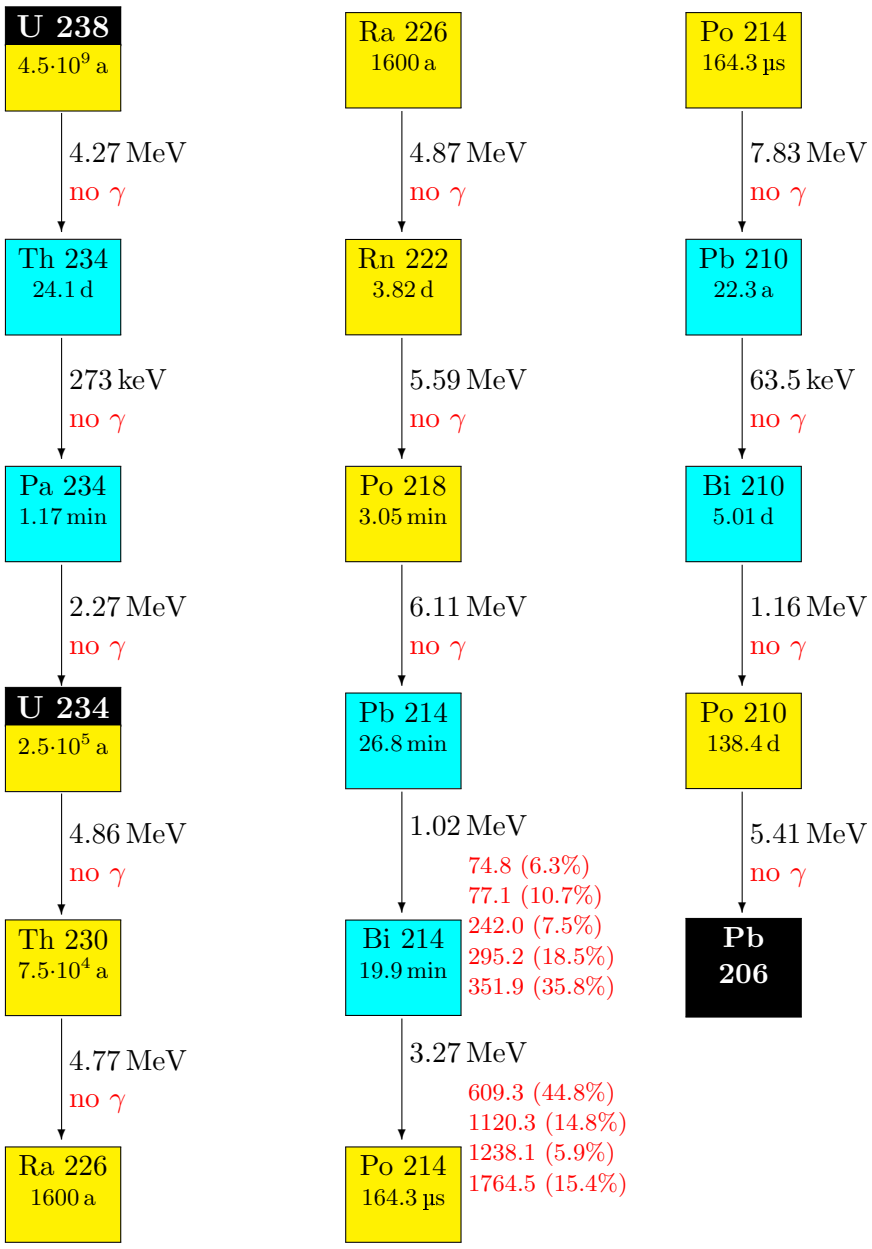

Figure A.1: *Full decay chain of ^{238}U. All branchings with a branching ratio less than 1% are neglected. The half-lives of the radioisotopes are given, as well as the Q-values of the decays. Note that in the decay of ^{234}Th the isotope ^{234}Pa is populated in an isomeric state, which does not de-excite to the ground state, but undergoes a β^--decay into ^{234}U in 99.84% of all cases.*

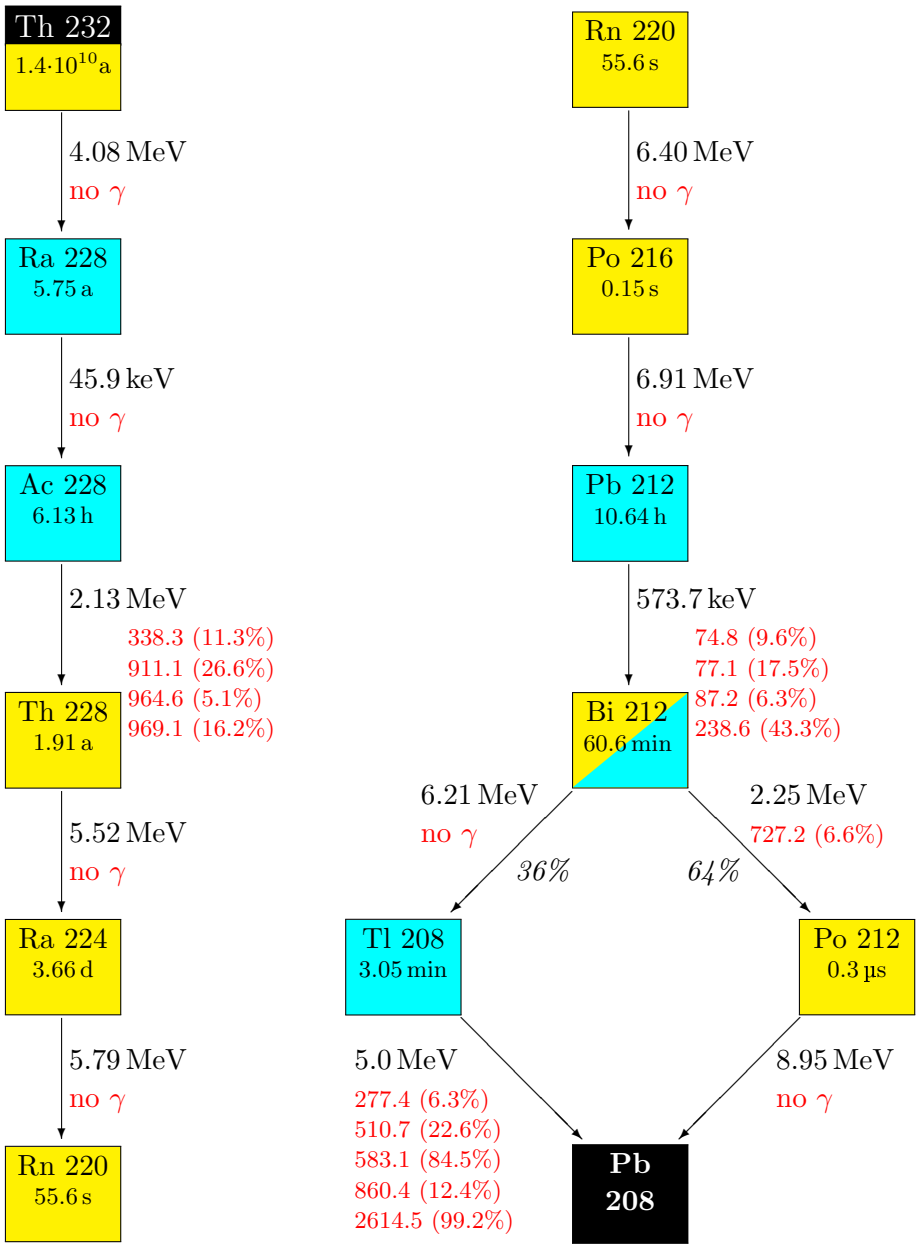

Figure A.2: *Full decay chain of ^{232}Th. All branchings with a branching ratio less than 1% are neglected. The half-lives of the radioisotopes are given, as well as the Q-values of the decays.*

Appendix B

Gamma Lines

This appendix lists the most important gamma lines of the background in the measurements with the germanium detector, sorted by their energy.The background in the spectra recorded with the germanium detector contains lots of gamma lines which are of various origin: most of the gamma lines seen stem from one of the natural decay chains[1] (appendix A), but also gamma emitting decays of anthropogenic isotopes as well as de-excitations of different germanium isotopes after interaction with a cosmic muon (or its secondaries) can be seen. Muon interactions as well as interactions of any kind of radiation (γ's, X-ray) in the surrounding shielding material, especially the lead shielding, also give rise to the emission of X-ray fluorescence. All muon-induced gamma lines are indicated by a "µ" in the column *production*, radiation-induced lines by "radiation". However, excited states of germanium nuclei with half-lives much shorter than $\sim 20\,\mu s$ cannot be seen in the spectra with running veto systems (in particular the muon veto), as their energy deposition in the germanium crystal happens within the veto time window. Therefore, for the excited states of germanium the half-lives are quoted, too. The half-lives of the gamma emitting isotopes from the decay chains can be found in appendix A. All data taken from [Fir96].

[1] In principle, there exist three natural decay chains: of ^{238}U, ^{235}U, and ^{232}Th. However, the natural abundance of ^{235}U is only 0.72% [Fir96], hence, its gamma lines appear very rarely, too, and are therefore neglected in the following.

***energy* [*keV*]**	***emitting nucleus***	***production***	***half-life***
46.5	$^{210}\mathrm{Pb} \xrightarrow{\beta^-} {}^{210}\mathrm{Bi}$	primordial, ^{238}U-chain	
66.7	$^{73}\mathrm{Ge}^*$	$^{72}\mathrm{Ge}(\mathrm{n},\gamma)^{73}\mathrm{Ge}^*$, $^{73}\mathrm{Ge}(\mathrm{n},\mathrm{n}')^{73}\mathrm{Ge}^*$, $^{74}\mathrm{Ge}(\mathrm{n},2\mathrm{n})^{73}\mathrm{Ge}^*$, μ	0.49 s
68.8	$^{73}\mathrm{Ge}^*$	$^{73}\mathrm{Ge}(\mathrm{n},\mathrm{n}')^{73}\mathrm{Ge}^*$, $^{74}\mathrm{Ge}(\mathrm{n},2\mathrm{n})^{73}\mathrm{Ge}^*$, μ	1.74 ns
72.8	Pb $\mathrm{K}_{\alpha 2}$	radiation, μ	
75.0	Pb $\mathrm{K}_{\alpha 1}$	radiation, μ	
84.5	Pb $\mathrm{K}_{\beta 3}$	radiation, μ	
84.9	Pb $\mathrm{K}_{\beta 1}$	radiation, μ	
87.3	Pb $\mathrm{K}_{\beta 2}$	radiation, μ	
92.4	$^{234}\mathrm{Th} \xrightarrow{\beta^-} {}^{234}\mathrm{Pa}$	primordial, ^{238}U-chain	
92.8	$^{234}\mathrm{Th} \xrightarrow{\beta^-} {}^{234}\mathrm{Pa}$	primordial, ^{238}U-chain	
93.3	$^{228}\mathrm{Ac} \xrightarrow{\beta^-} {}^{228}\mathrm{Th}$	primordial, Th-chain	
139.7	$^{75}\mathrm{Ge}^*$	$^{74}\mathrm{Ge}(\mathrm{n},\gamma)^{75}\mathrm{Ge}^*$, $^{76}\mathrm{Ge}(\mathrm{n},2\mathrm{n})^{75}\mathrm{Ge}^*$	47.7 s
159.7	$^{77}\mathrm{Ge}^*$	$^{76}\mathrm{Ge}(\mathrm{n},\gamma)^{77}\mathrm{Ge}^*$	52.9 s
186.2	$^{226}\mathrm{Ra} \xrightarrow{\alpha} {}^{222}\mathrm{Rn}$	primordial, ^{238}U-chain	
198.4	$^{71}\mathrm{Ge}^*$	$^{70}\mathrm{Ge}(\mathrm{n},\gamma)^{71}\mathrm{Ge}^*$, $^{72}\mathrm{Ge}(\mathrm{n},2\mathrm{n})^{71}\mathrm{Ge}^*$	20.4 ms
238.6	$^{212}\mathrm{Pb} \xrightarrow{\beta^-} {}^{212}\mathrm{Bi}$	primordial, Th-chain	
242.0	$^{214}\mathrm{Pb} \xrightarrow{\beta^-} {}^{214}\mathrm{Bi}$	primordial, ^{238}U-chain	
295.2	$^{214}\mathrm{Pb} \xrightarrow{\beta^-} {}^{214}\mathrm{Bi}$	primordial, ^{238}U-chain	
300.1	$^{212}\mathrm{Pb} \xrightarrow{\beta^-} {}^{212}\mathrm{Bi}$	primordial, Th-chain	

energy $[keV]$	***emitting nucleus***	***production***	***half-life***
338.3	$^{228}\mathrm{Ac} \xrightarrow{\beta^-} {}^{228}\mathrm{Th}$	primordial, Th-chain	
351.9	$^{214}\mathrm{Pb} \xrightarrow{\beta^-} {}^{214}\mathrm{Bi}$	primordial, ^{238}U-chain	
463.0	$^{228}\mathrm{Ac} \xrightarrow{\beta^-} {}^{228}\mathrm{Th}$	primordial, Th-chain	
510.7	$^{208}\mathrm{Tl} \xrightarrow{\beta^-} {}^{208}\mathrm{Pb}$	primordial, Th-chain	
511.0	e^+	pair production, β^+, µ	
562.9	$^{76}\mathrm{Ge}^*$	$^{76}\mathrm{Ge}(\mathrm{n},\mathrm{n}')^{76}\mathrm{Ge}^*$, µ	18.2 ps
583.1	$^{208}\mathrm{Tl} \xrightarrow{\beta^-} {}^{208}\mathrm{Pb}$	primordial, Th-chain	
595.9	$^{74}\mathrm{Ge}^*$	$^{73}\mathrm{Ge}(\mathrm{n},\gamma)^{74}\mathrm{Ge}^*$, $^{74}\mathrm{Ge}(\mathrm{n},\mathrm{n}')^{74}\mathrm{Ge}^*$, µ	12.35 ps
609.3	$^{214}\mathrm{Bi} \xrightarrow{\beta^-} {}^{214}\mathrm{Po}$	primordial, ^{238}U-chain	
661.7	$^{137}\mathrm{Cs} \xrightarrow{\beta^-} {}^{137\mathrm{m}}\mathrm{Ba}$	anthropogenic	
665.5	$^{214}\mathrm{Bi} \xrightarrow{\beta^-} {}^{214}\mathrm{Po}$	primordial, ^{238}U-chain	
691.6	$^{72}\mathrm{Ge}^*$	$^{72}\mathrm{Ge}(\mathrm{n},\mathrm{n}')^{72}\mathrm{Ge}^*$, $^{73}\mathrm{Ge}(\mathrm{n},2\mathrm{n})^{72}\mathrm{Ge}^*$, µ	444.2 ns
727.2	$^{212}\mathrm{Bi} \xrightarrow{\beta^-} {}^{212}\mathrm{Po}$	primordial, Th-chain	
768.4	$^{214}\mathrm{Bi} \xrightarrow{\beta^-} {}^{214}\mathrm{Po}$	primordial, ^{238}U-chain	
785.4	$^{212}\mathrm{Bi} \xrightarrow{\beta^-} {}^{212}\mathrm{Po}$	primordial, Th-chain	
785.9	$^{214}\mathrm{Pb} \xrightarrow{\beta^-} {}^{214}\mathrm{Bi}$	primordial, ^{238}U-chain	
794.9	$^{228}\mathrm{Ac} \xrightarrow{\beta^-} {}^{228}\mathrm{Th}$	primordial, Th-chain	
834.1	$^{72}\mathrm{Ge}^*$	$^{72}\mathrm{Ge}(\mathrm{n},\mathrm{n}')^{72}\mathrm{Ge}^*$, $^{73}\mathrm{Ge}(\mathrm{n},2\mathrm{n})^{72}\mathrm{Ge}^*$, µ	3.35 ps
860.4	$^{208}\mathrm{Tl} \xrightarrow{\beta^-} {}^{208}\mathrm{Pb}$	primordial, Th-chain	
911.1	$^{228}\mathrm{Ac} \xrightarrow{\beta^-} {}^{228}\mathrm{Th}$	primordial, Th-chain	

***energy* [*keV*]**	***emitting nucleus***	***production***	***half-life***
964.6	$^{228}\mathrm{Ac} \xrightarrow{\beta^-} {}^{228}\mathrm{Th}$	primordial, Th-chain	
969.1	$^{228}\mathrm{Ac} \xrightarrow{\beta^-} {}^{228}\mathrm{Th}$	primordial, Th-chain	
1001.0	$^{234\mathrm{m}}\mathrm{Pa} \xrightarrow{\beta^-} {}^{234}\mathrm{U}$	primordial, ^{238}U-chain	
1039.3	$^{70}\mathrm{Ge}^*$	$^{70}\mathrm{Ge}(\mathrm{n},\mathrm{n}')^{70}\mathrm{Ge}^*$, μ	1.3 ps
1120.3	$^{214}\mathrm{Bi} \xrightarrow{\beta^-} {}^{214}\mathrm{Po}$	primordial, ^{238}U-chain	
1173.2	$^{60}\mathrm{Co} \xrightarrow{\beta^-} {}^{60}\mathrm{Ni}$	anthropogenic	
1204.2	$^{74}\mathrm{Ge}^*$	$^{73}\mathrm{Ge}(\mathrm{n},\gamma)^{74}\mathrm{Ge}^*$, $^{74}\mathrm{Ge}(\mathrm{n},\mathrm{n}')^{74}\mathrm{Ge}^*$, μ	4.9 ps
1215.4	$^{70}\mathrm{Ge}^*$	$^{70}\mathrm{Ge}(\mathrm{n},\mathrm{n}')^{70}\mathrm{Ge}^*$, μ	3.7 ns
1238.1	$^{214}\mathrm{Bi} \xrightarrow{\beta^-} {}^{214}\mathrm{Po}$	primordial, ^{238}U-chain	
1332.5	$^{60}\mathrm{Co} \xrightarrow{\beta^-} {}^{60}\mathrm{Ni}$	anthropogenic	
1377.7	$^{214}\mathrm{Bi} \xrightarrow{\beta^-} {}^{214}\mathrm{Po}$	primordial, ^{238}U-chain	
1401.5	$^{214}\mathrm{Bi} \xrightarrow{\beta^-} {}^{214}\mathrm{Po}$	primordial, ^{238}U-chain	
1408.0	$^{214}\mathrm{Bi} \xrightarrow{\beta^-} {}^{214}\mathrm{Po}$	primordial, ^{238}U-chain	
1460.8	$^{40}\mathrm{K} \xrightarrow{\beta^+,\,\mathrm{EC}} {}^{40}\mathrm{Ar}$	primordial	
1463.8	$^{74}\mathrm{Ge}^*$	$^{73}\mathrm{Ge}(\mathrm{n},\gamma)^{74}\mathrm{Ge}^*$, $^{74}\mathrm{Ge}(\mathrm{n},\mathrm{n}')^{74}\mathrm{Ge}^*$, μ	1.7 ps
1464.1	$^{72}\mathrm{Ge}^*$	$^{72}\mathrm{Ge}(\mathrm{n},\mathrm{n}')^{72}\mathrm{Ge}^*$, $^{73}\mathrm{Ge}(\mathrm{n},2\mathrm{n})^{72}\mathrm{Ge}^*$, μ	4.5 ps
1495.9	$^{228}\mathrm{Bi} \xrightarrow{\beta^-} {}^{228}\mathrm{Th}$	primordial, Th-chain	
1509.2	$^{214}\mathrm{Bi} \xrightarrow{\beta^-} {}^{214}\mathrm{Po}$	primordial, ^{238}U-chain	
1587.9	$^{228}\mathrm{Ac} \xrightarrow{\beta^-} {}^{228}\mathrm{Th}$	primordial, Th-chain	
1620.6	$^{212}\mathrm{Bi} \xrightarrow{\beta^-} {}^{212}\mathrm{Po}$	primordial, Th-chain	

energy ***[keV]***	***emitting nucleus***	***production***	***half-life***
1630.6	$^{228}\mathrm{Ac} \xrightarrow{\beta^-} {}^{228}\mathrm{Th}$	primordial, Th-chain	
1661.3	$^{214}\mathrm{Bi} \xrightarrow{\beta^-} {}^{214}\mathrm{Po}$	primordial, ^{238}U-chain	
1728.4	$^{72}\mathrm{Ge}^*$	$^{72}\mathrm{Ge}(\mathrm{n},\mathrm{n}')^{72}\mathrm{Ge}^*$, $^{73}\mathrm{Ge}(\mathrm{n},2\mathrm{n})^{72}\mathrm{Ge}^*$, μ	1.5 ps
1729.6	$^{214}\mathrm{Bi} \xrightarrow{\beta^-} {}^{214}\mathrm{Po}$	primordial, ^{238}U-chain	
1764.5	$^{214}\mathrm{Bi} \xrightarrow{\beta^-} {}^{214}\mathrm{Po}$	primordial, ^{238}U-chain	
1847.4	$^{214}\mathrm{Bi} \xrightarrow{\beta^-} {}^{214}\mathrm{Po}$	primordial, ^{238}U-chain	
2118.5	$^{214}\mathrm{Bi} \xrightarrow{\beta^-} {}^{214}\mathrm{Po}$	primordial, ^{238}U-chain	
2204.2	$^{214}\mathrm{Bi} \xrightarrow{\beta^-} {}^{214}\mathrm{Po}$	primordial, ^{238}U-chain	
2447.8	$^{214}\mathrm{Bi} \xrightarrow{\beta^-} {}^{214}\mathrm{Po}$	primordial, ^{238}U-chain	
2614.5	$^{208}\mathrm{Tl} \xrightarrow{\beta^-} {}^{208}\mathrm{Pb}$	primordial, Th-chain	

Table B.1: *Selection of gamma lines which can be seen in gamma spectroscopy measurements with the germanium detector, sorted by their energy (given in units of keV). The columns "emitting nucleus" and "production" quote the mother isotope or process underlying the respective gamma emission, including the affiliation of radioactive isotopes to one of the primordial decay chains, if any; c.f. also appendix A. For the excited states of different germanium isotopes (marked with an asterisk) also the half-life is given.*

Appendix C

Decay Schemes of Selected Isotopes

On the following pages the decay schemes, or parts of the decay schemes of three selected isotopes, ^{212}Pb, ^{214}Bi, and ^{208}Tl, are shown. The horizontal black lines give the excited states (including their energy) of the daughter nucleus, which are populated in the decay of the mother isotope; the number above the horizontal arrows on the left give the population probabilities in the decays of the respective mother isotope. Vertical arrows indicate the subsequent gamma transitions; the energies and branching ratios are given, too. Note that the schemes of ^{214}Bi (fig. C.2) and ^{208}Tl (fig. C.3) are only extracts from the full decay schemes, therefore, the branching ratios need not to add up there to 100%. The gamma transitions marked in red can be used for the calculation of the activities of the respective radionuclides. The transitions marked in blue indicate gamma cascades, i.e. the population of low-energetic excited states by gamma transitions from high-energetic excited states. These emission lines cannot be used for an analysis as they might coincidentally create a signal in the germanium detector and the anti-Compton veto system, which means the corresponding count is vetoed by the gamma cascade itself. The transitions marked in black could, in principle, be used for an analysis, but are not, because their relative intensity is too low. All data taken from [Fir96].

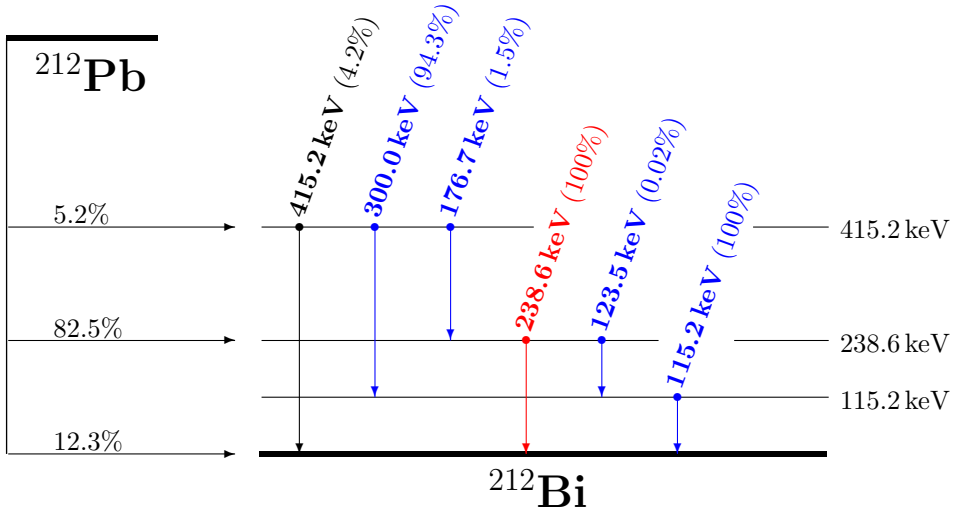

Figure C.1: *Full decay scheme of the β^--decay of ^{212}Pb into ^{212}Bi. For the 238.6 keV line of this isotope all effects from gamma cascades can be neglected, as the relative intensity of the 176.7 keV line is very low. The gamma transition with an energy of 238.6 keV comes from an excited state of ^{212}Bi which is highly populated in the decay of ^{212}Pb, and goes directly to the ground state of ^{212}Bi, not being followed by further gamma quanta. The 415.2 keV gamma line, in principle fulfilling all needs of the analysis, is not used, as its total intensity is far below 1% (5.2% from the branching ratio of the population times 4.2% from the relative intensity).*

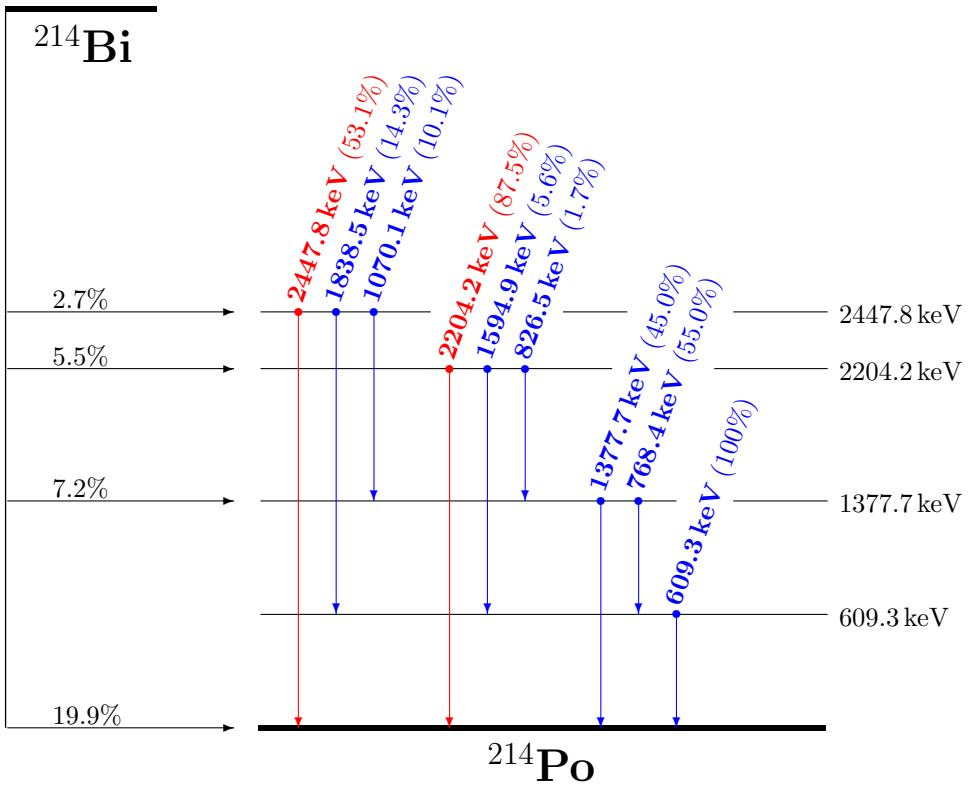

Figure C.2: *Simplified decay scheme of the β^--decay of ^{214}Bi into ^{214}Po. Not all excited states of this very complex scheme are shown; therefore, the sum of the single branching ratios deviates in some cases from 100%. The two high-energetic transitions with gamma energies of 2447.8 keV and 2204.2 keV, respectively, fulfill the requirements stated in chapter 7, i.e. they go directly to the ground state of ^{214}Po and are not populated from states with higher energy. The population of the state at 1377.7 keV from high-energetic excited states (also from many states not shown here) is not negligible. Therefore, this gamma line was excluded from the analysis. The state at 609.3 keV is not populated directly in the decay of ^{214}Bi and only part of gamma cascades, excluding this line, too.*

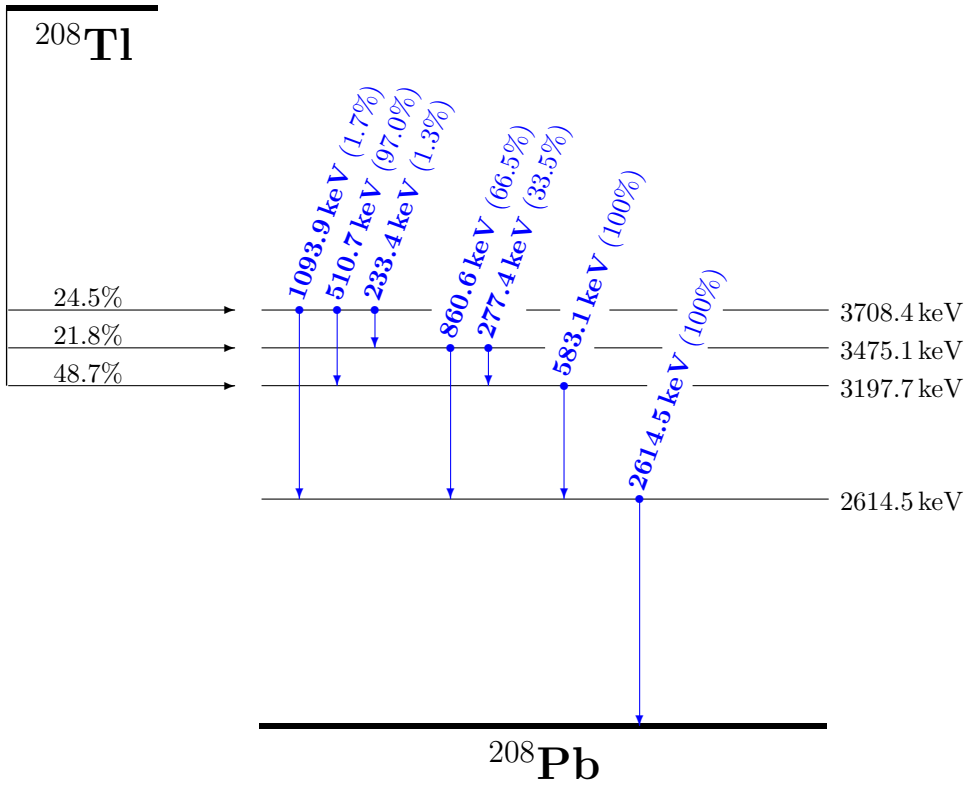

Figure C.3: *Simplified decay scheme of the β^--decay of ^{208}Tl into ^{208}Pb. Again, not all excited states of the daughter isotope are shown. All excited states, populated directly in the decay of ^{208}Tl, have no direct transition into the ground state of ^{208}Pb, but the excited state at 2614.5 keV is populated. Thus, all gamma lines are followed by 2614.5 keV gamma quanta, which results in the fact that the requirements given in chapter 7 (i.e. particularly direct transitions to the ground state of the daughter isotope) are not met. ^{208}Tl has no suitable gamma line for an analysis as described in the main text.*

Appendix D

Efficiency-Calibration of the Monte-Carlo Simulation

D.1 Radioactive Calibration Sources and Correction for Angular Correlations

The efficiency-calibration measurements (sec. 7.1.2) were carried out using radioactive sources with very small activities to prevent the spectra to be spoiled by any effects from detector pile-up, see tab. D.1.

However, some of the radionuclides used in these campaigns emit more than one gamma quantum per decay. This leads to sum peaks in the recorded spectra, or, in case both gamma quanta hit the germanium detector, but one or both did not deposit their full energy there, to events with some energy off the photopeaks. This needs to be corrected for, as these events do not contribute to the single photopeaks and, therefore, lead to apparently smaller detector efficiencies. As the gamma quanta emitted simultaneously in one decay have a certain angular correlation, a dedicated Monte-Carlo simulation has been set up to determine the probability of double hits in the germanium detector.

The angular correlation between two gamma quanta emitted in the same decay can be described by [But64]:

$$W(\theta) = 1 + a_1 \cdot \cos^2(\theta) + a_2 \cdot \cos^4(\theta) \quad . \tag{D.1}$$

This correlation function determines the distribution of the angle θ between the two gammas. In principle, also higher powers of $\cos(\theta)$ need to be taken into account, however, for the gamma cascade emitting isotopes used in the calibration campaigns (i.e. ^{60}Co, ^{133}Ba, and ^{88}Y) terms up to the fourth power are sufficient [But64]. The coefficients a_1 and a_2 are given by the angular momenta and parities of the initial and final levels of the gamma transitions; their values can be found in table D.2.

In the simulation at first an arbitrary directional vector for the first gamma quantum was chosen randomly (see e.g. appendix C in [Hof07]). Then, an angle θ was produced as a random number from the distribution (D.1), and an angle φ equally distributed from zero to 2π. These two angles specify the direction of the second gamma quantum with respect to the first one.

In case the first of the two gamma quanta hits the germanium detector (i.e. its directional

Isotope	Activity at the measurement [Bq]	Gamma energy [keV]	Emission probability [%]
Americium-241	386.5 ± 3.0 384.5 ± 3.0	59.5	35.9 ± 0.4
Barium-133	27.07 ± 0.27 22.39 ± 0.23	81.0 302.9 356.0 383.9	34.06 ± 0.27 18.33 ± 0.06 62.05 ± 0.19 8.94 ± 0.03
Cobalt-57	- 1329.2 ± 19.9	122.1 136.5	85.60 ± 0.17 10.68 ± 0.08
Cesium-137	73.82 ± 0.74 69.01 ± 0.70	661.7	85.1 ± 0.2
Manganese-54	0.200 ± 0.002 -	834.8	99.976 ± 0.001
Cobalt-60	206.8 ± 1.6 134.9 ± 1.0	1173.2 1332.5	99.90 ± 0.02 99.982 ± 0.001
Sodium-22	- 16776.9 ± 251.7	1274.5	99.944 ± 0.014
Yttrium-88	- 153.2 ± 2.3	898.0 1836.1	93.68 ± 0.36 99.24 ± 0.37

Table D.1: *Radioactive calibration sources used for the efficiency calibration of the Monte-Carlo simulation. The isotopes were chosen in such a manner that the full energy range from energies close to the lower detector threshold up to more than 1 MeV is covered. The low activities prevent the measurements to be spoiled by pile-up effects, even for a placement of the source directly in front of the entrance window of the germanium detector. The activities and their errors ($1\,\sigma$) are taken from the calibration source data sheets [DKD00, DKD06, DKD08, PTB01, PTB01a, PTB01b]. The black data depicts the activities at the first calibration run, the green data for the second one. The emission probabilities [Fir96] for the gamma lines and their uncertainties are given in the last column.*

isotope	*gamma energies*	a_1	a_2
^{60}Co	1173.2 keV & 1332.5 keV	$\frac{1}{8}$	$\frac{1}{24}$
^{88}Y	898.0 keV & 1836.1 keV	$-\frac{3}{29}$	0
^{133}Ba	356.0 keV & 81.0 keV	0.03	0.02
^{133}Ba	302.9 keV & 81.0 keV	-0.06	0.03

Table D.2: *Correlation coefficients a_1 and a_2 of the gamma cascades of the isotopes used for the efficiency calibration of the Monte-Carlo simulation.*

vector points towards the detector's front side) a counter A was increased. In case the second gamma quantum hits the detector, too, and deposits some energy there another counter B was increased. The ratio $\frac{\text{A}}{\text{A-B}}$ (for 1,000,000 simulated gammas in total) finally determined the correction which had to be applied to the number of counts in the photopeak of the first gamma (and analogously for the second one). The probability for an energy deposition in the detector was determined using the detector Monte-Carlo simulation, and cross-checked in all cases with the peak area of the sum peak as obtained from the recorded gamma spectra. This independently measured cross-check allowed to use the detector Monte-Carlo simulation for the correction of the measured detector efficiencies, although these are used to calibrate the simulation later-on.

D.2 Determination of the Geometrical Error

In the germanium spectra obtained with the calibration sources the photopeaks of the gamma lines to be analysed were fitted with a Gaussian (automatic fit routine implemented in the software package Genie2000 [GEN02]); the peak areas give the number N_{meas} of measured gamma events. Combining eqs. (7.3) and (7.4) from sec. 7.1.2 the measured detector efficiency is consequently calculated to

$$\varepsilon_{meas} = \frac{N_{meas}}{A \cdot t_{meas} \cdot P} \quad , \tag{D.2}$$

with the activity A of the calibration source, the measuring time t_{meas}, and the gamma emission probability P. The measuring time was typically one hour and is considered to be known exactly in the following[1]. The error of $\varepsilon_{\text{meas}}$ is a combined error of the statistical uncertainty, which is simply given by the error of the peak fit as calculated by Genie2000 [GEN02], and the systematical uncertainties. The latter include the error ΔA of the source activity (as quoted in tab. D.1), the error ΔP of the emission probability (tab. D.1; taken from [Fir96]), and the error of the detector efficiency induced by the uncertainty of the source position. The latter contribution to the total error of $\varepsilon_{\text{meas}}$ was evaluated by means of the

[1]Genie2000 records the measuring time with a precision of 0.01 s [GEN02], therefore, the relative error in a measurement of one hour length is of the order of 10^{-6}. All other errors like the uncertainty of the source activity are much bigger. The dead-time of the detector system is correctly accounted for.

Monte-Carlo simulation: for each source position of the efficiency measurements (directly at the entrance window of the germanium detector, 10 cm and 20 cm away from it) the detector efficiency curve was simulated[2] in steps of 4 keV, each time for the correct position (the position, where the source was placed in the actual measurement), one position slightly closer to the detector, and one position farther away. The deviations from the correct position were hereby chosen to be ±0.5 mm for the source position directly at the entrance window and ±2 mm for the other two source positions at 10 cm and 20 cm, respectively. The uncertainty of 2 mm reflects the precision the calibration source could be positioned in the detector system at an arbitrary point; the positioning of the source directly at the entrance window was rather accurate, because for that position it was glued directly to the magnesium housing of the germanium detector.

In fig. D.1 the simulated detector efficiencies $\varepsilon_{\mathrm{sim}}$ for a source position directly at the entrance window are shown for an energy range from zero to 2000 keV, once for the whole energy range and once in a zoomed-in view. Towards lower energies the efficiency curve drops steeply to zero because the transmission probability through the magnesium entrance window decreases significantly for low-energetic gamma quanta. $\varepsilon_{\mathrm{sim}}$ reaches a maximum at ~ 100 keV and then again reduces for higher energies, mostly because of energy losses in the germanium detector due to escaping gammas after Compton scattering or pair production processes. The error bars for the simulated efficiencies are statistical only, i.e.

$$\Delta\varepsilon_{sim} = \frac{\sqrt{N_{sim}}}{N_{sim}} \quad , \tag{D.3}$$

with the number $\mathrm{N_{sim}}$ of simulated hits in the photopeak. The simulation is considered to be free from any systematical uncertainties.

Fig. D.1 depicts not only the general behaviour of $\varepsilon_{\mathrm{sim}}$, but also its variations due to small displacements of the source position. The red and green data points indicate $\varepsilon_{\mathrm{sim}}$ respectively for a source position 0.5 mm closer to or farther away from the entrance window than the centre position (blue data points). To first approximation these deviations are not energy-dependent[3], hence, the systematic error of the detector efficiency due to variations of the source position can be averaged over energy. This is done in fig. D.2 where the ratio of $\varepsilon_{\mathrm{sim}}$ for the deviating positions to $\varepsilon_{\mathrm{sim}}$ for the correct position for each energy is plotted into a histogram, for all three different source positions. Each distribution is fitted with a Gaussian. The differences of the centre positions of these Gaussians to a ratio of 1.0 give an estimate for the source position-induced systematic error. Resulting from these simulations the following uncertainties are used below:

- 2.1% for the position at the entrance window
- 3.0% for the position at 10 cm
- 2.0% for the position at 20 cm.

[2] Simulated detector efficiencies are denoted by $\varepsilon_{\mathrm{sim}}$ in the following to distinguish them from measured efficiencies $\varepsilon_{\mathrm{meas}}$.

[3] This is, of course, not fully correct. For example, the transmission probability through the entrance window, which is an energy-dependent parameter, also depends on the distance to this window, as the averaged incident angle of the gamma quanta becomes larger, and thus the transmission path in the window longer, for smaller distances. Therefore, the window seems to be thicker for closer source positions, diminishing the detector efficiency especially at low energies. However, for minor displacements as regarded here this effect can be safely neglected without too big an error.

D.3 Measured and Simulated Efficiencies

Tables D.3 and D.4 give the measured detector efficiencies $\varepsilon_{\mathrm{meas}}$ (for both calibration campaigns) including their errors, which were calculated by means of a linear error propagation from the single errors quoted above. All measured efficiencies were corrected for sum peaks, too (appendix D.1). As already mentioned in sec. 7.1.2, the first calibration measurements were recorded with both the analogue and the digital signal processing chain to obtain efficiency calibration data for both; the second calibration measurements were only recorded with the DSP 9660A. In tab. D.5 the simulated detector efficiencies $\varepsilon_{\mathrm{sim}}$ for the same energies are listed; for each data point 1,000,000 gamma quanta were simulated. Here, the errors were calculated using eq. (D.3).

D.4 Energy-Dependent Correction Functions

The energy-dependent correction functions for the detector Monte-Carlo simulation were obtained from fits to the ratio of the measured detector efficiencies $\varepsilon_{\mathrm{meas}}$ to the simulated efficiencies $\varepsilon_{\mathrm{sim}}$, fig. 7.6. The fit function used is

$$\frac{\varepsilon_{meas}}{\varepsilon_{sim}} = a_0 - e^{a_1 \cdot E + a_2} \quad . \tag{D.4}$$

This was carried out for both the analogue and the digital read-out system, and for each of the three geometrical setups. The fit coefficients obtained are summarised in tab. D.6.

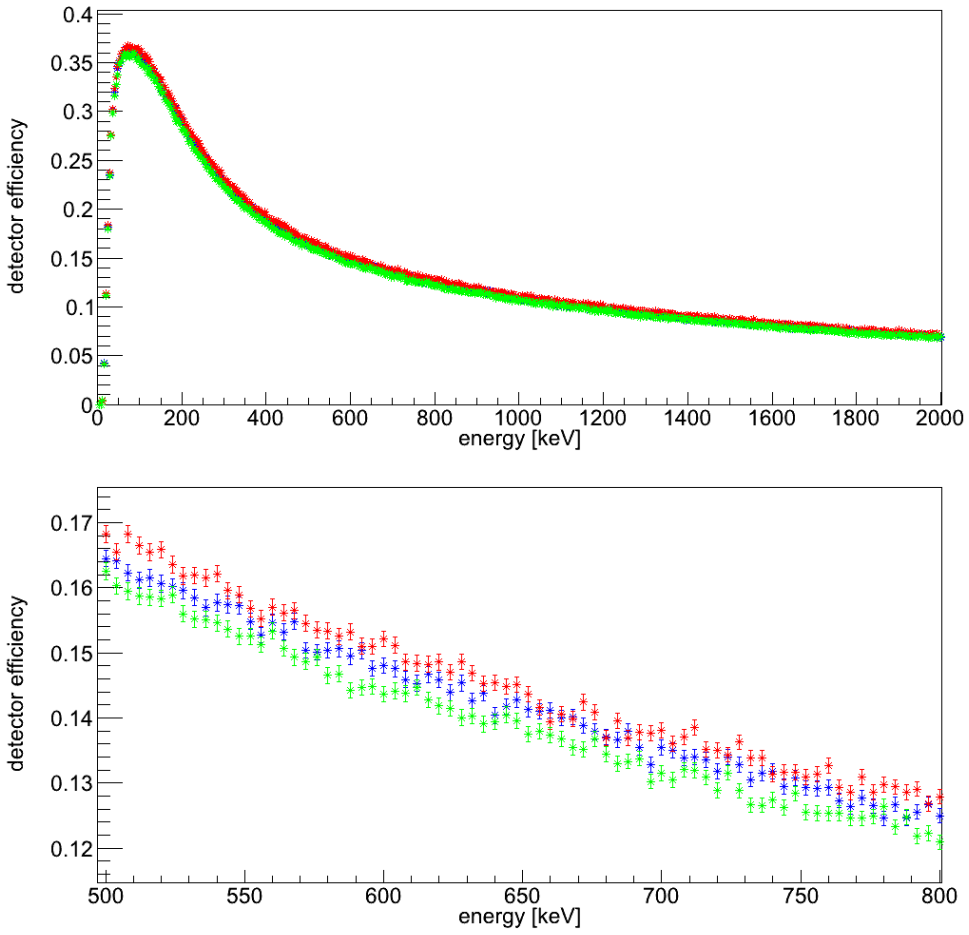

Figure D.1: *Simulated detector efficiency for a source position directly at the entrance window in steps of 4 keV. The upper plot shows the whole energy range, the lower plot a zoomed-in view. The blue data points represent the correct source position, the red (green) ones the simulated efficiencies for a closer (farther) position. The efficiencies obtained for a position closer to the detector are on average slightly higher, and slightly lower for a position farther away. Error bars are statistical only.*

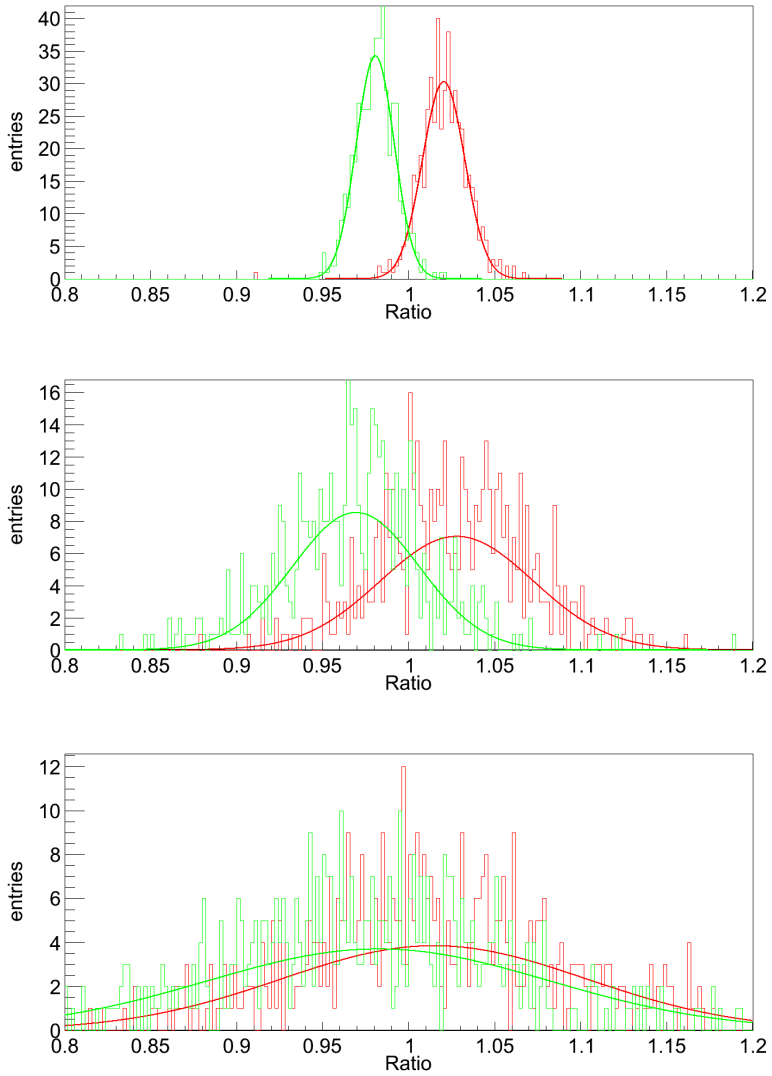

Figure D.2: *Ratio of the simulated detector efficiencies ε_{sim} for the shifted source positions to ε_{sim} for the correct position for each of the energies simulated (0 keV through 2000 keV in steps of 4 keV; cf. fig. D.1). One diagram is shown for each of the three different source positions: directly at the entrance window (top), 10 cm in front of it (middle), and 20 cm in front of it (bottom). Again, the red curve depicts the data for the closer point (slightly higher efficiency on average), and the green curve for the farther point (lower efficiency). Both distributions are each time fitted with a Gaussian; the centre positions of these Gaussians give an estimate for the systematical error of the detector efficiency due to the uncertainty of the positioning of the source in the detector system.*

Measured detector efficiencies $\varepsilon_{\mathrm{meas}}$			
analogue system			
energy [keV]	0 cm	10 cm	20 cm
59.5	0.0096±0.0006	0.0020±0.0002	
81.0	0.0577±0.0063	0.0135±0.0016	0.0030±0.0002
302.9	0.1957±0.0167	0.0147±0.0020	0.0045±0.0004
356.0	0.1714±0.0126	0.0137±0.0013	0.0032±0.0002
383.9	0.1517±0.0126	0.0132±0.0024	0.0036±0.0005
661.7	0.1060±0.0053	0.0103±0.0008	0.0028±0.0001
834.8	0.1000±0.0170		
1173.2	0.0805±0.0046	0.0073±0.0004	0.0022±0.0001
1332.5	0.0727±0.0042	0.0069±0.0004	0.0021±0.0001
DSP 9660A			
energy [keV]	0 cm	10 cm	20 cm
59.5	0.0095±0.0006	0.0020±0.0002	
81.0	0.0584±0.0058	0.0120±0.0015	0.0031±0.0002
302.9	0.1735±0.0148	0.0127±0.0017	0.0039±0.0004
356.0	0.1649±0.0122	0.0124±0.0011	0.0030±0.0002
383.9	0.1342±0.0109	0.0101±0.0020	0.0029±0.0004
661.7	0.1005±0.0050	0.0098±0.0007	0.0026±0.0001
834.8	0.0875±0.0161		
1173.2	0.0751±0.0043	0.0070±0.0004	0.0021±0.0001
1332.5	0.0674±0.0039	0.0065±0.0004	0.0020±0.0001

Table D.3: *Measured detector efficiencies ε_{meas} in the first calibration campaign given as absolute values both for the analogue and digital (DSP 9660A) read-out, each for the three source positions (see sec. 7.1.2). An empty space in the table means that the corresponding photopeak contained too little events to be distinguishable from the background. The efficiencies obtained with both systems are nearly equal, however, the DSP seems to cause a slightly lower detector efficiency. The reason for this behaviour is unknown, but as the efficiencies are properly taken into account in the analysis of the recorded spectra, this is no problem at all. All values are corrected for sum peaks and gamma correlations.*

Measured detector efficiencies $\varepsilon_{\mathrm{meas}}$			
DSP 9660A			
energy [keV]	0 cm	10 cm	20 cm
59.5	0.0092±0.0004	0.0011±0.0001	0.0007±0.0000
81.0	0.0588±0.0039	0.0102±0.0008	0.0031±0.0003
122.0	0.1522±0.0060	0.0171±0.0009	0.0051±0.0002
136.4	0.1681±0.0080	0.0178±0.0012	0.0056±0.0005
302.9	0.1565±0.0093	0.0124±0.0010	0.0040±0.0003
356.0	0.1479±0.0082	0.0118±0.0007	0.0039±0.0002
383.9	0.1391±0.0076	0.0117±0.0012	0.0028±0.0005
661.6	0.0998±0.0035	0.0091±0.0004	0.0032±0.0001
898.0	0.0841±0.0050	0.0078±0.0005	0.0024±0.0002
1173.2	0.0727±0.0043	0.0071±0.0005	0.0025±0.0002
1275.0	0.0706±0.0039	0.0067±0.0003	0.0023±0.0001
1332.5	0.0660±0.0039	0.0068±0.0004	0.0022±0.0002
1836.1	0.0512±0.0033	0.0051±0.0004	0.0017±0.0001

Table D.4: *Measured detector efficiencies ε_{meas} in the second calibration campaign given as absolute values for the DSP 9660A, each for the three source positions (0 cm, 10 cm, and 20 cm in front of the entrance window). All values are corrected for sum peaks and gamma correlations.*

Simulated detector efficiencies $\varepsilon_{\mathrm{sim}}$			
energy [keV]	0 cm	10 cm	20 cm
59.5	0.3650±0.0006	0.0361±0.0002	0.0103±0.0001
81.0	0.3712±0.0006	0.0351±0.0002	0.0104±0.0001
122.1	0.3576±0.0006	0.0327±0.0002	0.0097±0.0001
136.5	0.3497±0.0006	0.0312±0.0002	0.0096±0.0001
276.4	0.2542±0.0005	0.0224±0.0001	0.0071±0.0001
302.9	0.2415±0.0005	0.0209±0.0001	0.0068±0.0001
356.0	0.2182±0.0005	0.0192±0.0001	0.0060±0.0001
383.9	0.2075±0.0005	0.0183±0.0001	0.0059±0.0001
511.0	0.1743±0.0004	0.0154±0.0001	0.0050±0.0001
661.7	0.1495±0.0004	0.0136±0.0001	0.0045±0.0001
834.8	0.1303±0.0004	0.0117±0.0001	0.0039±0.0001
898.0	0.1247±0.0004	0.0113±0.0001	0.0038±0.0001
1173.2	0.1068±0.0003	0.0099±0.0001	0.0035±0.0001
1274.5	0.1011±0.0003	0.0093±0.0001	0.0032±0.0001
1332.5	0.0984±0.0003	0.0092±0.0001	0.0031±0.0001
1836.1	0.0792±0.0003	0.0075±0.0001	0.0026±0.0001

Table D.5: *Simulated detector efficiencies ε_{sim} given as absolute values, for the three different source positions (0 cm, 10 cm, and 20 cm in front of the entrance window). The errors are statistical only.*

Analogue system			
fit coefficients	0 cm	10 cm	20 cm
a_0	0.742 ± 0.003	0.7452 ± 0.0003	0.7524 ± 0.0001
a_1 [keV^{-1}]	-0.0111 ± 0.0004	-0.0293 ± 0.0002	-0.0067 ± 0.0001
a_2	0.32 ± 0.02	1.36 ± 0.01	-0.12 ± 0.01
DSP 9660A			
fit coefficients	0 cm	10 cm	20 cm
a_0	0.672 ± 0.002	0.6969 ± 0.0002	0.688 ± 0.005
a_1 [keV^{-1}]	-0.0135 ± 0.0002	-0.0210 ± 0.0001	-0.0207 ± 0.0001
a_2	0.36 ± 0.01	0.835 ± 0.003	0.746 ± 0.001

Table D.6: *Fit coefficients for the exponential fit to the efficiency ratio ε_{meas} to ε_{sim} as given in eq. (D.4).*

Appendix E

Neutron Activation Analysis

The neutron activation analysis of the PPO and acrylic samples allows not only to determine the content of ^{40}K, but also other trace elements are activated by thermal neutrons and can consequently be analysed regarding their mass concentrations. These elements are not critical for Double Chooz, as they have no long-lived radioactive isotopes, however, the analysis of their mass concentrations yields some additional information on the samples, e.g. the total content of impurity atoms. The results of these analyses are therefore depicted in this appendix. In addition, the time lines of the gamma spectroscopy measurements are displayed, to give an impression of the time differences between neutron irradiation and start of the first measurement, as well as the live and real times of the different measurements performed in the different time segments.

E.1 Time Lines

Figs. E.1 through E.4 depict the time lines for the four neutron activation analyses (acrylic and three PPO samples). The acrylic sample was irradiated for 1200 s, the three PPO samples 600 s each. In each case the live times (red numbers) and the real times (numbers quoted in black) for each time segment used are given. The start of the usage of the anti-Compton veto system is indicated for each case, too.

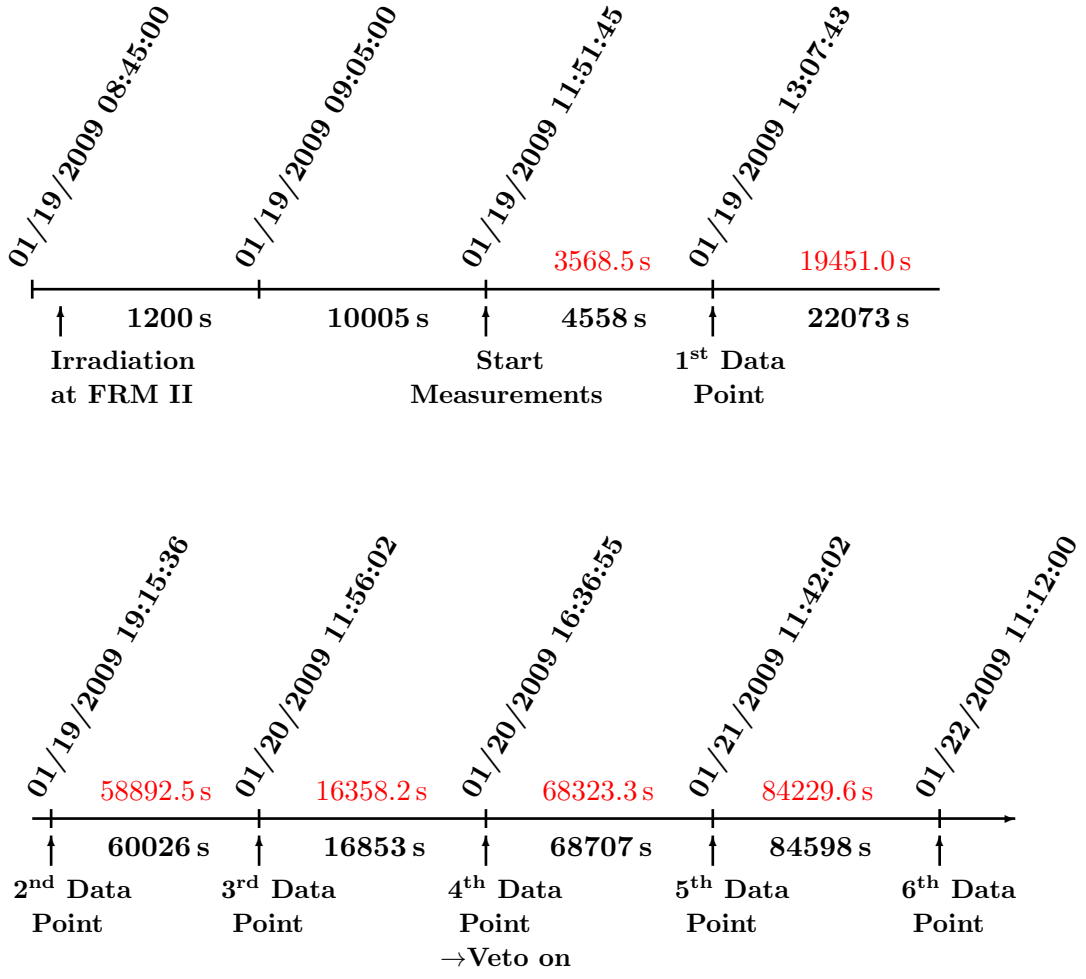

Figure E.1: *Time line for the NAA measurement of the acrylic sample. Numbers in red depict the live time of each measurement, numbers in black real times. In total, six separate time bins have been used for the measurement; for the last two time bins the anti-Compton veto system was switched on. Irradiation time was 1200 s.*

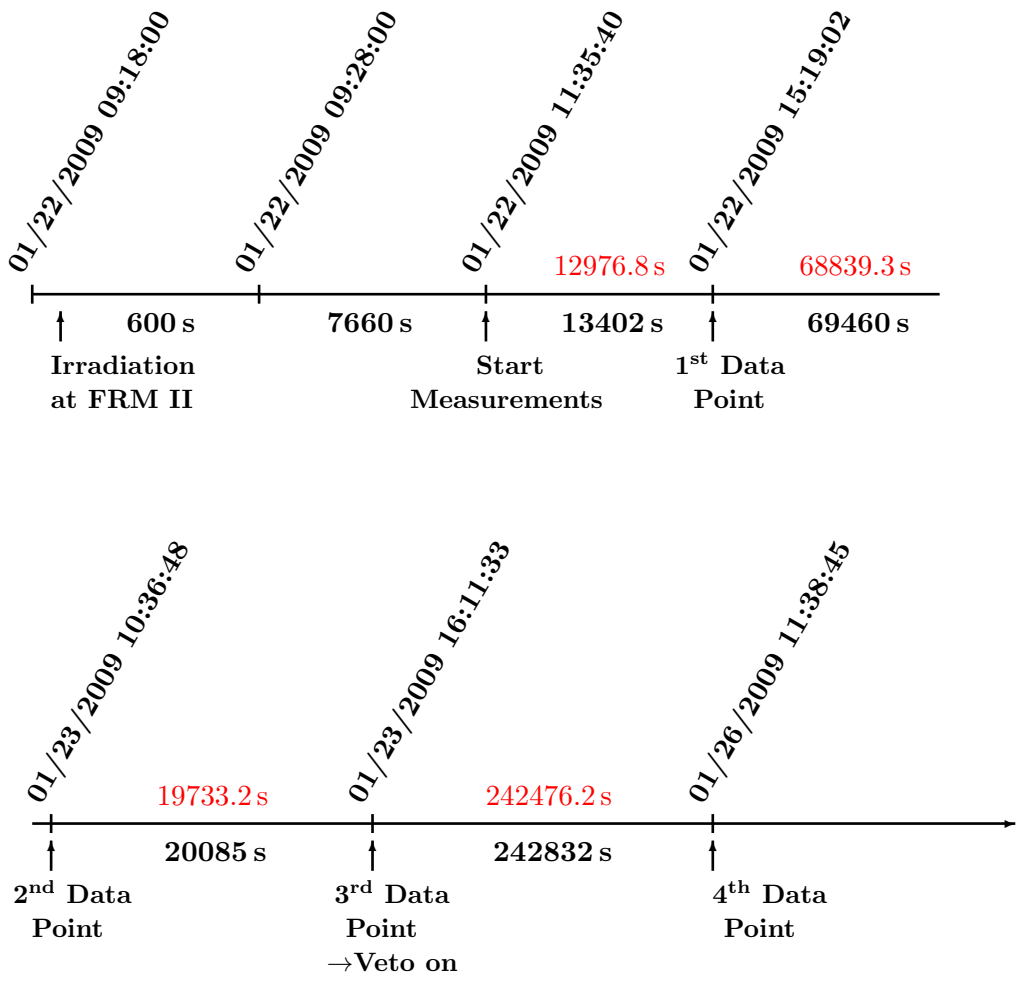

Figure E.2: *Time line for the NAA measurement of the PPO sample LOT 26-1003. Numbers in red depict the live time of each measurement, numbers in black real times. In total, four separate time bins have been used for the measurement; for the last time bin the anti-Compton veto system was switched on. Irradiation time was 600 s.*

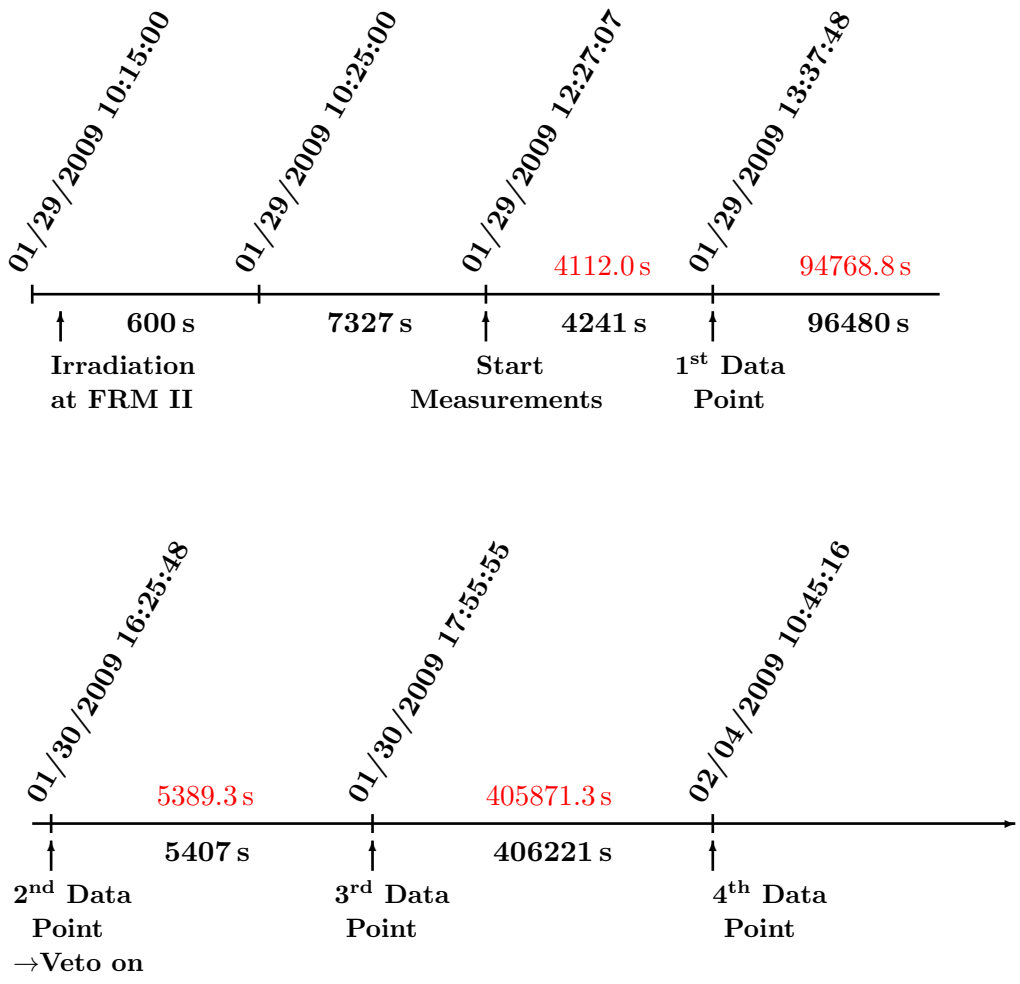

Figure E.3: *Time line for the NAA measurement of the PPO sample LOT 26-1005. Numbers in red depict the live time of each measurement, numbers in black real times. In total, four separate time bins have been used for the measurement; for the last two time bins the anti-Compton veto system was switched on. Irradiation time was 600 s.*

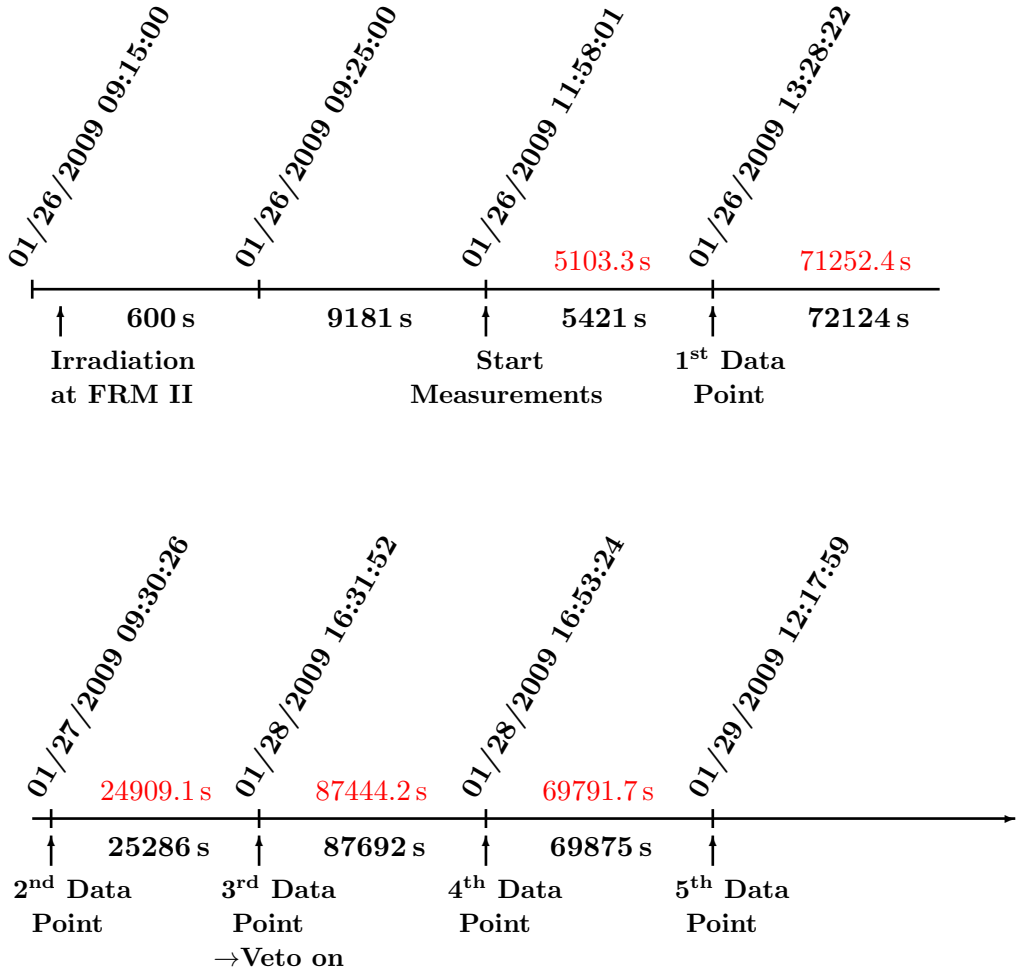

Figure E.4: *Time line for the NAA measurement of the PPO sample LOT 26-1007. Numbers in red depict the live time of each measurement, numbers in black real times. In total, five separate time bins have been used for the measurement; for the last two time bins the anti-Compton veto system was switched on. Irradiation time was 600 s.*

E.2 Analysis of Other Trace Elements

The following trace elements are identified and analysed[1] (all data taken from [Fir96]):

- ^{40}**Ar:** half-life of the activated isotope ^{41}Ar: 109.3 min; gamma emission at 1293.6 keV
- ^{81}**Br:** 35.3 h; 221.5 keV, 554.3 keV, 619.1 keV, 698.4 keV, 776.5 keV, 827.8 keV, 1044.0 keV, 1317.5 keV, 1474.9 keV
- ^{37}**Cl:** 37.2 min; 1642.7 keV, 2167.4 keV
- ^{50}**Cr:** 27.7 d; 320.1 keV
- ^{115}**In:** 54.3 min; 138.3 keV, 416.9 keV, 818.7 keV, 1097.3 keV, 1507.4 keV
- ^{55}**Mn:** 2.58 h; 846.8 keV, 1810.7 keV, 2113.1 keV
- ^{23}**Na:** 14.96 h; 1368.6 keV, 2754.0 keV
- ^{186}**W:** 23.7 h; 72.0 keV, 134.2 keV, 479.6 keV, 551.5 keV, 625.5 keV, 685.7 keV, 772.9 keV

The trace elements identified and analysed for the first measuring campaign of the different PPO samples are listed in tab. E.1. The second sample of the PPO "Neutrino Grade" turned out to be best fitting for Double Chooz, not only because of its small content of ^{40}K (see tab. 7.9 in sec. 7.3) but also due to the smallest concentration of other trace elements, especially sodium.

In the second measuring campaign all the above listed trace elements were analysed, again separately for each time segment. Figures E.5 through E.8 depict the results of these analyses for the acrylic sample as well as the three PPO samples LOT 26-1003, LOT 26-1005, and LOT 26-1007, for each gamma line separately. Not in all time bins all gamma lines were visible in the spectra recorded; especially in the last time bins the short-lived elements have already decayed. In addition, some of the trace elements analysed have a very tiny cross-section for thermal neutron capture, resulting in only tiny gamma lines which might be indistinguishable from the continuous background. However, in case more than one gamma line could be analysed (for example for the isotopes ^{81}Br and ^{55}Mn) the figures show both the good agreement of the mass concentrations as calculated from the different gamma lines as well as the agreement for different time bins. Note that no corrections for gamma cascades have been made, i.e. the last time segments with running anti-Compton veto system seemingly have a smaller activity of the respective isotope in case its decay emits more than one gamma quantum at the same time. For the time bins without anti-Compton veto the lacking corrections are, however, no problem, as the highly active samples were placed in a big distance to the germanium detector (typically 20 cm) to prevent the spectra to suffer from a too big dead-time. Therefore, the solid angle covered by the detector was very small and coincident hits by two gamma quanta became very unlikely. Time bins with a concentration of the investigated isotope that is spoiled due to the missing cascade correction were excluded from the final analysis. Tables E.2 and E.3 finally depict the resulting mass concentrations of the trace elements, once separately for all analysed gamma lines (weighted averages of

[1] ^{40}Ar is not really a contamination of the samples themselves, but gets activated in the air surrounding the sample during neutron irradiation and is subsequently adsorbed at the sample's surface. However, especially at the beginning its activity dominates the total activity of the sample, and it is analysed nevertheless.

PPO samples (first measuring campaign)		
Isotope	***Sigma-Aldrich***	***PE standard***
^{81}Br	$(1.58 \pm 0.38) \cdot 10^{-8}$ $\frac{g}{g}$	$(3.01 \pm 0.50) \cdot 10^{-7}$ $\frac{g}{g}$
^{55}Mn	$(7.8 \pm 1.3) \cdot 10^{-8}$ $\frac{g}{g}$	-
^{40}Ar	$(1.43 \pm 0.37) \cdot 10^{-5}$ $\frac{g}{g}$	$(1.56 \pm 0.85) \cdot 10^{-5}$ $\frac{g}{g}$
^{23}Na	$(2.05 \pm 0.40) \cdot 10^{-5}$ $\frac{g}{g}$	$(1.26 \pm 0.23) \cdot 10^{-4}$ $\frac{g}{g}$
^{37}Cl	$(1.00 \pm 0.47) \cdot 10^{-5}$ $\frac{g}{g}$	-
Isotope	***PE ν-grade***	***PE ν-grade (2)***
^{81}Br	$(9.6 \pm 1.6) \cdot 10^{-8}$ $\frac{g}{g}$	$(1.69 \pm 0.27) \cdot 10^{-7}$ $\frac{g}{g}$
^{55}Mn	$(2.14 \pm 0.35) \cdot 10^{-8}$ $\frac{g}{g}$	$(7.9 \pm 1.3) \cdot 10^{-9}$ $\frac{g}{g}$
^{40}Ar	$(1.65 \pm 0.42) \cdot 10^{-5}$ $\frac{g}{g}$	$(1.58 \pm 0.41) \cdot 10^{-5}$ $\frac{g}{g}$
^{23}Na	$(7.2 \pm 1.4) \cdot 10^{-7}$ $\frac{g}{g}$	$(6.0 \pm 1.1) \cdot 10^{-7}$ $\frac{g}{g}$
^{37}Cl	$(1.83 \pm 0.67) \cdot 10^{-6}$ $\frac{g}{g}$	$(5.8 \pm 3.4) \cdot 10^{-7}$ $\frac{g}{g}$

Table E.1: *Mass concentrations of the identified trace elements in the PPO samples investigated in the first measuring campaign: one PPO sample from the manufacturer Sigma-Aldrich, and three samples from PerkinElmer ("PE"; standard, Neutrino Grade first sample, Neutrino Grade second sample). In case that one activated isotope emits more than one gamma line, the quoted concentration is the weighted average of the single values obtained from the respective gamma emissions.*

the single values obtained for the different time segments, excluding zero values and, in case cascade corrections would have been necessary, with running anti-Compton veto), and once as weighted averages of all single results obtained for the gamma lines. Once again it shall be emphasized that none of these isotopes is of particular relevance for Double Chooz as they do not have long-lived radioisotopes. This analysis is a by-product of the determination of the mass concentration of ^{40}K, however, it contains some useful information on the general purity of the investigated samples.

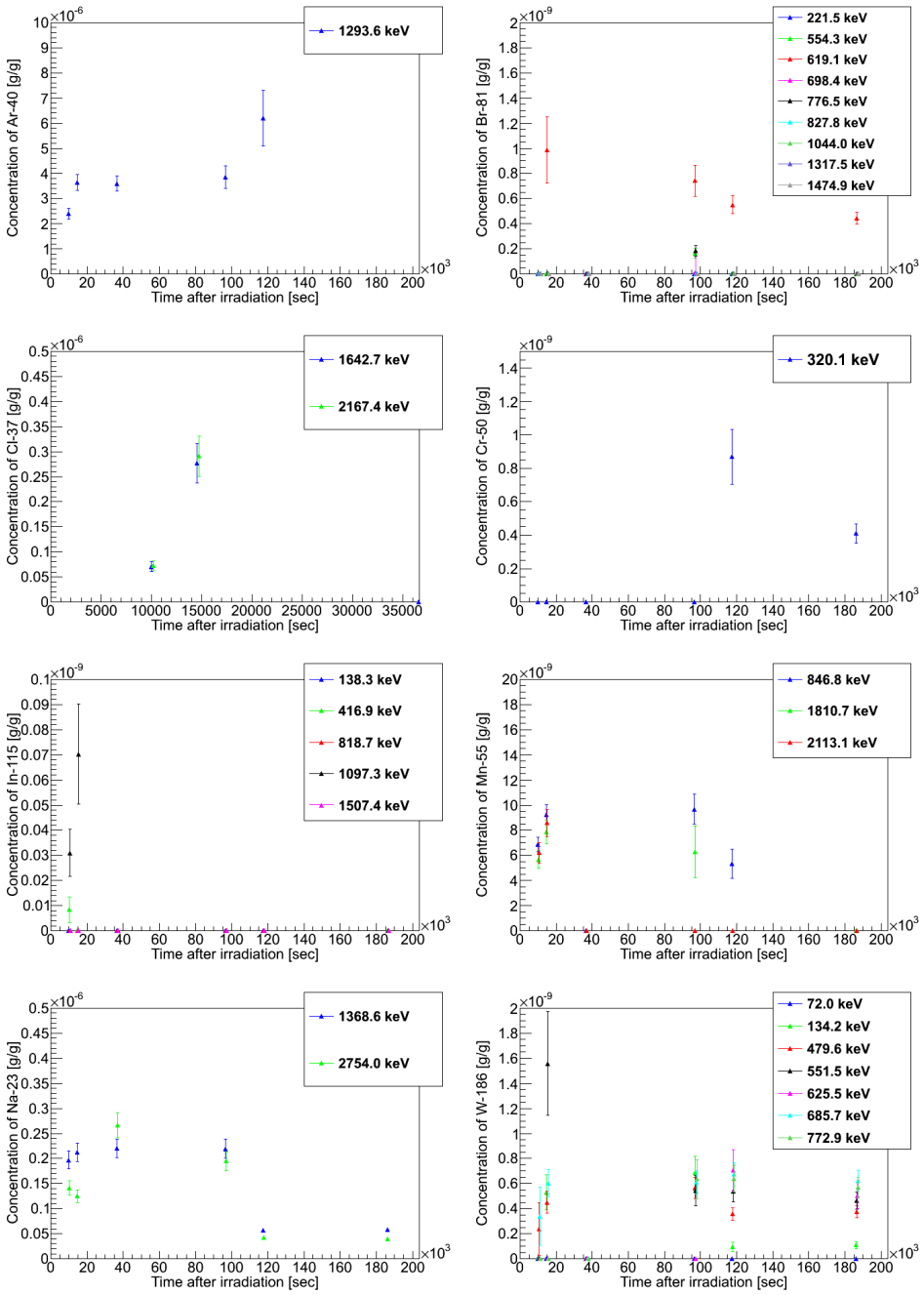

Figure E.5: *Mass concentrations of the trace elements (see list beginning of appendix E.2) found in the neutron activation analysis of the acrylic sample. From top left to bottom right:* ^{40}Ar, ^{81}Br, ^{37}Cl, ^{50}Cr, ^{115}In, ^{55}Mn, ^{23}Na, *and* ^{186}W. *For this sample six time segments have been recorded, the last two with running anti-Compton veto system. Note that for* ^{37}Cl *a zoomed-in view is shown.*

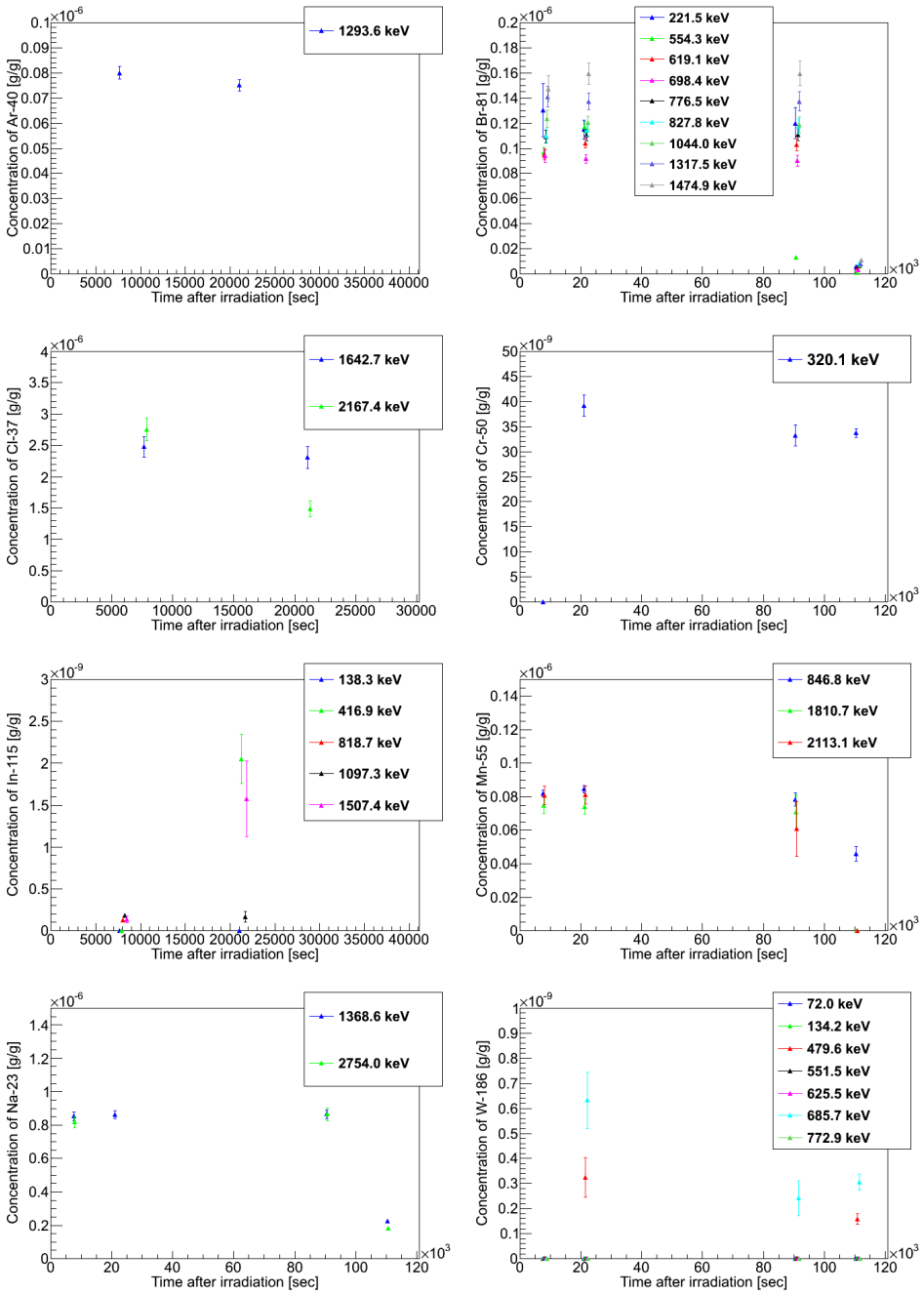

Figure E.6: *Mass concentrations of the trace elements (see list beginning of appendix E.2) found in the neutron activation analysis of the PPO sample LOT 26-1003. From top left to bottom right:* ^{40}Ar, ^{81}Br, ^{37}Cl, ^{50}Cr, ^{115}In, ^{55}Mn, ^{23}Na, *and* ^{186}W. *For this sample four time segments have been recorded, the last one with running anti-Compton veto system. Note that for* ^{40}Ar, ^{37}Cl, *and* ^{115}In *a zoomed-in view is shown.*

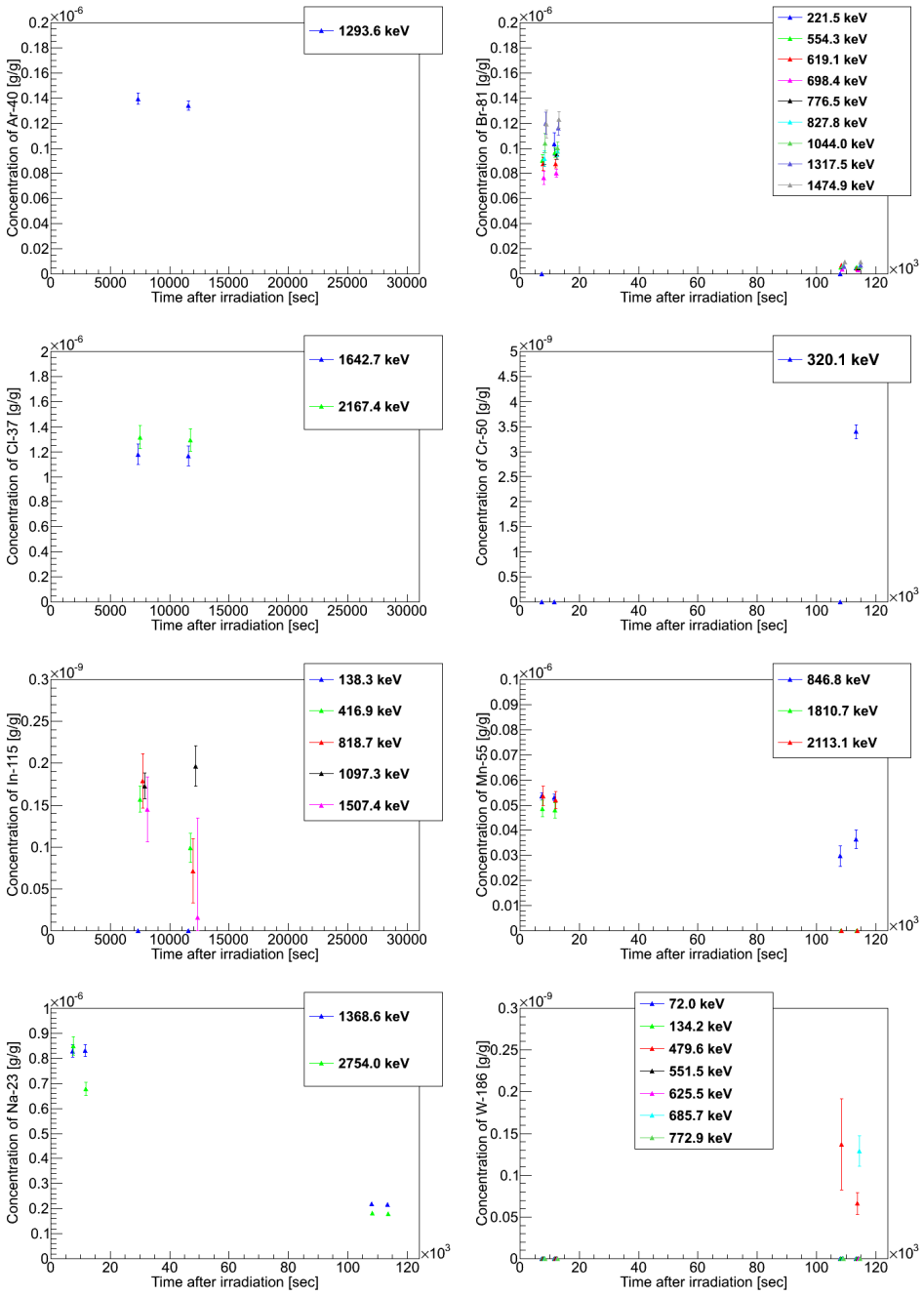

Figure E.7: *Mass concentrations of the trace elements (see list beginning of appendix E.2) found in the neutron activation analysis of the PPO sample LOT 26-1005. From top left to bottom right: ^{40}Ar, ^{81}Br, ^{37}Cl, ^{50}Cr, ^{115}In, ^{55}Mn, ^{23}Na, and ^{186}W. For this sample four time segments have been recorded, the last two with running anti-Compton veto system. Note that for ^{40}Ar, ^{37}Cl, and ^{115}In a zoomed-in view is shown.*

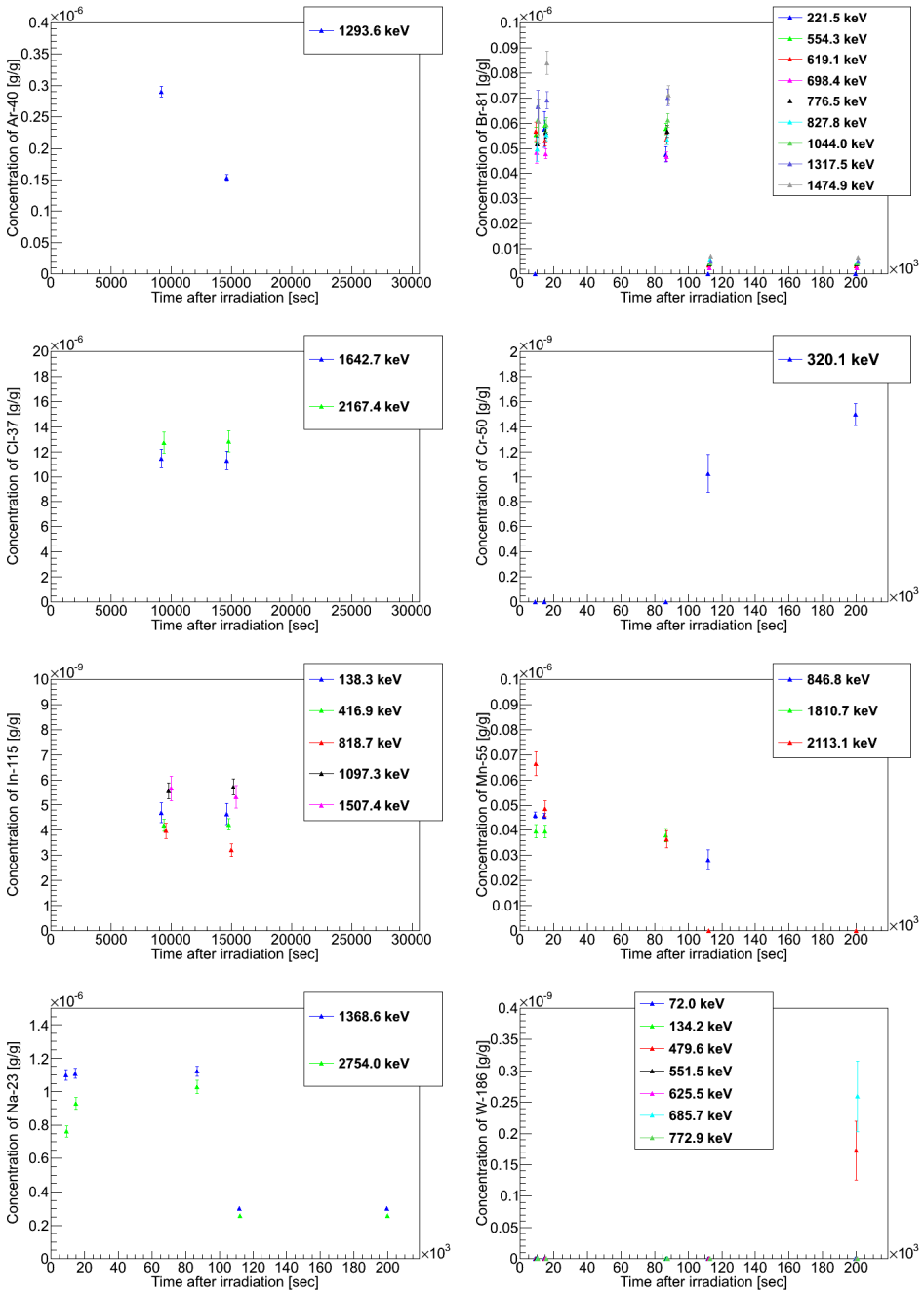

Figure E.8: *Mass concentrations of the trace elements (see list beginning of appendix E.2) found in the neutron activation analysis of the PPO sample LOT 26-1007. From top left to bottom right:* ^{40}Ar, ^{81}Br, ^{37}Cl, ^{50}Cr, ^{115}In, ^{55}Mn, ^{23}Na, *and* ^{186}W. *For this sample five time segments have been recorded, the last two with running anti-Compton veto system. Note that for* ^{40}Ar, ^{37}Cl, *and* ^{115}In *a zoomed-in view is shown.*

Isotope	***gamma energy*** $[keV]$	***Acrylic*** $[\frac{g}{g}]$	***PPO LOT 26-1003*** $[\frac{g}{g}]$
Ar-40	1293.6	$(3.16 \pm 0.24) \cdot 10^{-6}$	$(7.73 \pm 0.53) \cdot 10^{-8}$
Br-81	221.5	-	$(1.19 \pm 0.11) \cdot 10^{-7}$
	554.3	-	$(1.06 \pm 0.08) \cdot 10^{-7}$
	619.1	$(7.8 \pm 1.1) \cdot 10^{-10}$	$(1.01 \pm 0.06) \cdot 10^{-7}$
	698.4	-	$(9.17 \pm 0.59) \cdot 10^{-8}$
	776.5	-	$(1.10 \pm 0.07) \cdot 10^{-7}$
	827.8	-	$(1.14 \pm 0.08) \cdot 10^{-7}$
	1044.0	-	$(1.21 \pm 0.08) \cdot 10^{-7}$
	1317.5	-	$(1.38 \pm 0.10) \cdot 10^{-7}$
	1474.9	-	$(1.55 \pm 0.11) \cdot 10^{-7}$
	total	$(7.8 \pm 1.1) \cdot 10^{-10}$	$(1.11 \pm 0.03) \cdot 10^{-7}$
Cl-37	1642.7	$(8.30 \pm 0.99) \cdot 10^{-8}$	$(2.39 \pm 0.23) \cdot 10^{-6}$
	2167.4	$(8.52 \pm 0.97) \cdot 10^{-8}$	$(1.83 \pm 0.19) \cdot 10^{-6}$
	total	$(8.41 \pm 0.69) \cdot 10^{-8}$	$(2.06 \pm 0.15) \cdot 10^{-6}$
Cr-50	320.1	-	$(3.48 \pm 0.22) \cdot 10^{-8}$
In-115	138.3	-	-
	416.9	-	-
	818.7	-	$(1.28 \pm 0.37) \cdot 10^{-10}$
	1097.3	-	$(1.78 \pm 0.26) \cdot 10^{-10}$
	1507.4	-	$(1.34 \pm 0.47) \cdot 10^{-10}$
	total	-	$(1.57 \pm 0.19) \cdot 10^{-10}$
Mn-55	846.8	$(7.71 \pm 0.83) \cdot 10^{-9}$	$(8.32 \pm 0.54) \cdot 10^{-8}$
	1810.7	$(6.43 \pm 0.87) \cdot 10^{-9}$	$(7.44 \pm 0.68) \cdot 10^{-8}$
	2113.1	$(7.06 \pm 0.98) \cdot 10^{-9}$	$(8.09 \pm 0.76) \cdot 10^{-8}$
	total	$(7.09 \pm 0.51) \cdot 10^{-9}$	$(8.01 \pm 0.37) \cdot 10^{-8}$
Na-23	1368.6	$(2.11 \pm 0.16) \cdot 10^{-7}$	$(8.60 \pm 0.47) \cdot 10^{-7}$
	2754.0	$(1.55 \pm 0.13) \cdot 10^{-7}$	$(8.40 \pm 0.64) \cdot 10^{-7}$
	total	$(1.77 \pm 0.10) \cdot 10^{-7}$	$(8.53 \pm 0.38) \cdot 10^{-7}$
W-186	479.6	$(3.95 \pm 0.47) \cdot 10^{-10}$	$(1.74 \pm 0.30) \cdot 10^{-10}$
	551.5	$(5.05 \pm 0.69) \cdot 10^{-10}$	-
	685.7	$(6.35 \pm 0.75) \cdot 10^{-10}$	$(3.15 \pm 0.43) \cdot 10^{-10}$
	772.9	$(6.03 \pm 0.84) \cdot 10^{-10}$	-
	total	$(4.92 \pm 0.32) \cdot 10^{-10}$	$(2.20 \pm 0.25) \cdot 10^{-10}$

Table E.2: *Mass concentrations of the identified trace elements in the acrylic sample and the PPO LOT 26-1003 sample. The quoted concentrations are the weighted averages over the different time bins, excluding zero values and, in case cascade corrections would be needed, time bins with running anti-Compton veto. For isotopes with more than one gamma line the weighted averages over the single lines are given, too. Details see text.*

Isotope	***gamma energy*** $[keV]$	***PPO LOT 26-1005*** $[\frac{g}{g}]$	***PPO LOT 26-1007*** $[\frac{g}{g}]$
Ar-40	1293.60	$(1.37 \pm 0.09) \cdot 10^{-7}$	$(1.81 \pm 0.04) \cdot 10^{-7}$
Br-81	221.50	$(1.03 \pm 0.15) \cdot 10^{-7}$	$(5.00 \pm 0.52) \cdot 10^{-8}$
	554.30	$(9.37 \pm 0.72) \cdot 10^{-8}$	$(5.74 \pm 0.36) \cdot 10^{-8}$
	619.10	$(8.78 \pm 0.71) \cdot 10^{-8}$	$(5.40 \pm 0.35) \cdot 10^{-8}$
	698.40	$(7.87 \pm 0.66) \cdot 10^{-8}$	$(4.74 \pm 0.32) \cdot 10^{-8}$
	776.50	$(9.36 \pm 0.74) \cdot 10^{-8}$	$(5.50 \pm 0.36) \cdot 10^{-8}$
	827.80	$(9.52 \pm 0.81) \cdot 10^{-8}$	$(5.34 \pm 0.37) \cdot 10^{-8}$
	1044.00	$(1.02 \pm 0.09) \cdot 10^{-7}$	$(6.04 \pm 0.43) \cdot 10^{-8}$
	1317.50	$(1.18 \pm 0.10) \cdot 10^{-7}$	$(6.90 \pm 0.50) \cdot 10^{-8}$
	1474.90	$(1.21 \pm 0.12) \cdot 10^{-7}$	$(7.33 \pm 0.58) \cdot 10^{-8}$
	total	$(9.48 \pm 0.28) \cdot 10^{-8}$	$(5.58 \pm 0.13) \cdot 10^{-8}$
Cl-37	1642.70	$(1.17 \pm 0.11) \cdot 10^{-6}$	$(1.14 \pm 0.15) \cdot 10^{-5}$
	2167.40	$(1.30 \pm 0.12) \cdot 10^{-6}$	$(1.27 \pm 0.17) \cdot 10^{-5}$
	total	$(1.23 \pm 0.08) \cdot 10^{-6}$	$(1.20 \pm 0.11) \cdot 10^{-5}$
Cr-50	320.10	$(3.40 \pm 0.35) \cdot 10^{-9}$	$(1.30 \pm 0.14) \cdot 10^{-9}$
In-115	138.30	-	$(4.68 \pm 0.47) \cdot 10^{-9}$
	416.90	$(1.25 \pm 0.17) \cdot 10^{-10}$	$(4.22 \pm 0.36) \cdot 10^{-9}$
	818.70	$(1.24 \pm 0.31) \cdot 10^{-10}$	$(3.52 \pm 0.36) \cdot 10^{-9}$
	1097.30	$(1.81 \pm 0.22) \cdot 10^{-10}$	$(5.64 \pm 0.48) \cdot 10^{-9}$
	1507.40	$(1.45 \pm 0.49) \cdot 10^{-10}$	$(5.49 \pm 0.58) \cdot 10^{-9}$
	total	$(1.43 \pm 0.12) \cdot 10^{-10}$	$(4.46 \pm 0.19) \cdot 10^{-9}$
Mn-55	846.80	$(5.33 \pm 0.35) \cdot 10^{-8}$	$(4.58 \pm 0.30) \cdot 10^{-8}$
	1810.70	$(4.83 \pm 0.45) \cdot 10^{-8}$	$(3.96 \pm 0.37) \cdot 10^{-8}$
	2113.10	$(5.28 \pm 0.51) \cdot 10^{-8}$	$(5.46 \pm 0.53) \cdot 10^{-8}$
	total	$(5.17 \pm 0.24) \cdot 10^{-8}$	$(4.52 \pm 0.21) \cdot 10^{-8}$
Na-23	1368.60	$(8.30 \pm 0.56) \cdot 10^{-7}$	$(1.11 \pm 0.06) \cdot 10^{-6}$
	2754.00	$(7.42 \pm 0.57) \cdot 10^{-7}$	$(8.83 \pm 0.55) \cdot 10^{-7}$
	total	$(7.87 \pm 0.40) \cdot 10^{-7}$	$(9.87 \pm 0.41) \cdot 10^{-7}$
W-186	479.60	$(7.1 \pm 1.7) \cdot 10^{-11}$	$(1.73 \pm 0.58) \cdot 10^{-10}$
	551.50	-	-
	685.70	$(1.29 \pm 0.27) \cdot 10^{-10}$	$(2.59 \pm 0.73) \cdot 10^{-10}$
	772.90	-	-
	total	$(8.7 \pm 1.4) \cdot 10^{-11}$	$(2.06 \pm 0.45) \cdot 10^{-10}$

Table E.3: *Mass concentrations of the identified trace elements in the PPO samples LOT 26-1005 and LOT 26-1007. The quoted concentrations are the weighted averages over the different time bins, excluding zero values and, in case cascade corrections would be needed, time bins with running anti-Compton veto. For isotopes with more than one gamma line the weighted averages over the single lines are given, too. Details see text.*

Appendix F

Double Chooz Physics Run List

For the first stage of data analysis in Double Chooz, 2594 physics runs were used; this appendix lists the run numbers. Typically, one run has a length of one hour; the total time of all these runs is 101 days.

11001 11007 11008 11009 11010 11011 11012 11013 11014 11015 11016 11017 11018 11019 11152 11153
11154 11155 11164 11165 11166 11167 11168 11169 11171 11181 11182 11183 11192 11193 11210 11219
11220 11221 11222 11231 11232 11233 11234 11243 11244 11245 11246 11255 11256 11477 11478 11479
11480 11489 11490 11491 11492 11504 11505 11506 11507 11516 11518 11519 11520 11521 11545 11546
11547 11548 11549 11558 11559 11560 11561 11570 11571 11572 11574 11583 11584 11585 11586 11587
11596 11597 11598 11599 11608 11609 11610 11611 11634 11635 11636 11637 11639 11648 11650 11651
11652 11661 11662 11663 11664 11673 11674 11675 11676 11700 11701 11702 11703 11704 11713 11714
11715 11716 11725 11726 11727 11728 11729 11739 11740 11741 11742 11751 11752 11753 11754 11775
11776 11777 11778 11787 11788 11789 11790 11799 11800 11801 11802 11814 11815 11816 11817 11826
11827 11828 11829 11830 12046 12047 12048 12057 12058 12059 12060 12069 12070 12071 12072 12073
12074 12083 12084 12085 12086 12107 12108 12109 12110 12119 12121 12122 12131 12132 12133 12134
12143 12144 12145 12146 12155 12156 12157 12158 12179 12180 12181 12182 12191 12192 12193 12194
12203 12204 12205 12206 12215 12216 12217 12218 12227 12228 12229 12230 12239 12240 12241 12242
12263 12264 12265 12266 12275 12276 12277 12278 12287 12288 12289 12290 12299 12300 12302 12303
12313 12314 12315 12316 12325 12326 12327 12328 12349 12350 12351 12352 12361 12362 12363 12364
12373 12375 12376 12377 12387 12388 12389 12398 12399 12400 12402 12423 12424 12425 12426 12435
12436 12437 12438 12447 12448 12449 12450 12459 12460 12461 12462 12471 12472 12473 12690 12691
12692 12693 12703 12704 12705 12714 12715 12716 12717 12726 12727 12728 12729 13119 13120 13121
13122 13143 13144 13145 13146 13155 13156 13157 13158 13167 13168 13169 13170 13179 13180 13181
13182 13191 13192 13193 13194 13203 13204 13205 13206 13207 13228 13229 13230 13240 13241 13242
13243 13244 13253 13255 13256 13265 13266 13267 13268 13289 13290 13291 13292 13301 13302 13303
13304 13313 13314 13315 13316 13326 13327 13328 13329 13338 13339 13340 13341 13362 13363 13364
13365 13374 13375 13376 13378 13379 13388 13389 13390 13391 13392 13401 13402 13403 13404 13413
13414 13415 13416 13425 13426 13427 13428 13449 13450 13451 13452 13461 13462 13463 13464 13473
13474 13475 13476 13485 13486 13487 13488 13497 13498 13499 13501 13527 13528 13529 13531 13534
13535 13537 13538 13547 13548 13549 13550 13559 13561 13562 13571 13572 13573 13574 13599 13611
13612 13613 13622 13623 13624 13625 13635 13636 13637 13638 13647 13648 13649 13650 13659 13660
13661 13662 13686 13689 13690 13691 13700 13701 13702 13703 13712 13713 13714 13715 13724 13725
13726 13727 13926 13927 13928 13929 13930 13939 13941 13954 13955 13956 13966 13967 13968 13969
13979 13980 13982 13983 14004 14005 14006 14007 14015 14016 14017 14018 14027 14028 14029 14039
14040 14043 14044 14053 14054 14055 14056 14057 14066 14067 14069 14082 14083 14084 14085 14094
14095 14096 14097 14106 14107 14108 14118 14119 14120 14121 14142 14143 14144 14145 14154 14155
14156 14157 14158 14159 14161 14170 14171 14172 14173 14174 14175 14184 14185 14186 14187 14188

14197 14198 14199 14200 14201 14202 14223 14224 14225 14226 14235 14236 14237 14238 14252 14253
14254 14255 14264 14266 14267 14268 14277 14278 14279 14280 14281 14282 14303 14304 14305 14306
14307 14316 14317 14318 14319 14320 14321 14331 14332 14333 14342 14343 14344 14354 14355 14356
14357 14366 14367 14368 14369 14370 14392 14393 14394 14395 14404 14405 14406 14407 14415 14417
14418 14427 14428 14429 14430 14439 14440 14453 14454 14455 14466 14467 14468 14477 14478 14479
14480 14489 14490 14491 14492 14502 14503 14504 14505 14693 14694 14695 14696 14697 14706 14707
14708 14709 14718 14719 14720 14721 14730 14731 14732 14733 14742 14743 14744 14745 14746 14767
14768 14769 14770 14779 14780 14781 14792 14793 14794 14803 14804 14805 14806 14815 14816 14817
14818 14819 14820 14821 14842 14843 14844 14845 14855 14856 14857 14859 14869 14870 14871 14872
14873 14882 14883 14884 14885 14895 14896 14898 14899 14900 14901 14922 14923 14924 14925 14935
14936 14937 14938 14939 14948 14949 14950 14951 14960 14961 14962 14963 14972 14973 14974 14975
14984 14985 14999 15000 15001 15002 15011 15012 15013 15014 15023 15024 15025 15026 15035 15036
15037 15048 15049 15051 15052 15066 15067 15068 15069 15070 15079 15080 15081 15082 15091 15092
15093 15094 15103 15104 15105 15106 15115 15116 15117 15317 15318 15319 15320 15329 15330 15331
15332 15341 15342 15343 15344 15353 15354 15355 15356 15357 15379 15380 15381 15382 15392 15393
15394 15395 15404 15405 15406 15407 15408 15409 15418 15419 15420 15421 15430 15431 15432 15433
15434 15443 15444 15445 15446 15455 15457 15471 15472 15473 15482 15483 15484 15485 15494 15495
15496 15497 15506 15507 15508 15509 15519 15520 15522 15523 15533 15546 15547 15548 15557 15558
15559 15560 15569 15570 15571 15572 15581 15582 15583 15584 15605 15606 15607 15608 15617 15618
15619 15620 15629 15630 15631 15632 15641 15642 15643 15644 15653 15654 15655 15656 15665 15666
15667 15668 15669 15670 15691 15692 15693 15694 15703 15704 15705 15706 15715 15716 15717 15718
15719 15720 15729 15730 15731 15733 15742 15745 15746 15767 15768 15770 15779 15780 15781 15782
15791 15792 15793 15794 15803 15804 15805 15806 15815 15816 15818 15820 15924 15925 15926 15927
15936 15937 15938 15939 15948 15949 15950 15951 15960 15961 15962 15963 16072 16073 16074 16075
16084 16085 16086 16087 16096 16097 16098 16099 16108 16109 16111 16112 16121 16122 16123 16124
16133 16136 16137 16138 16159 16161 16162 16163 16164 16173 16174 16175 16176 16185 16194 16195
16196 16197 16206 16207 16208 16209 16224 16225 16226 16235 16236 16237 16238 16239 16248 16249
16250 16260 16262 16263 16264 16276 16277 16279 16300 16301 16303 16304 16313 16314 16316 16325
16326 16327 16328 16337 16338 16339 16340 16349 16350 16351 16352 16374 16375 16376 16377 16387
16388 16389 16390 16391 16400 16402 16403 16412 16413 16414 16415 16416 16425 16426 16427 16428
16450 16451 16452 16453 16454 16463 16464 16465 16466 16467 16468 16477 16478 16479 16480 16489
16490 16491 16492 16595 16596 16597 16598 16607 16608 16609 16610 16611 16620 16621 16622 16623
16632 16633 16634 16635 16752 16753 16754 16755 16764 16765 16766 16767 16776 16777 16778 16779
16788 16789 16790 16791 16800 16801 16802 16803 16804 16815 16816 16817 16818 16840 16841 16842
16843 16852 16853 16854 16855 16864 16865 16866 16867 16876 16878 16879 16880 16882 16884 16893
16894 16895 16896 16905 16918 16919 16920 16921 16931 16933 16934 16935 16944 16945 16946 16947
16956 16957 16958 16959 16968 16969 16970 16971 16992 16993 16994 16995 17004 17005 17006 17008
17017 17018 17019 17020 17029 17030 17031 17032 17033 17054 17055 17056 17057 17066 17067 17068
17069 17078 17079 17080 17081 17090 17091 17092 17093 17102 17103 17105 17114 17115 17116 17117
17138 17139 17140 17141 17159 17161 17162 17171 17172 17173 17174 17183 17184 17185 17186 17195
17196 17197 17198 17207 17208 17209 17210 17219 17221 17222 17231 17232 17234 17243 17244 17245
17246 17255 17256 17257 17258 17267 17268 17269 17270 17280 17281 17284 17293 17294 17295 17296
17305 17306 17307 17308 17317 17319 17328 17329 17330 17331 17332 17353 17354 17355 17356 17365
17366 17367 17368 17377 17378 17379 17380 17389 17391 17392 17393 17394 17403 17404 17405 17406
17427 17428 17429 17430 17439 17440 17441 17442 17451 17452 17453 17454 17463 17464 17467 17476
17477 17478 17479 17500 17501 17502 17503 17512 17513 17514 17515 17524 17525 17526 17527 17536
17538 17539 17540 17549 17550 17551 17552 17573 17576 17577 17578 17587 17588 17589 17590 17599
17600 17601 17602 17611 17612 17613 17614 17615 17625 17626 17627 17637 17650 17651 17652 17653
17662 17663 17665 17674 17675 17676 17677 17686 17687 17688 17689 17690 17718 17719 17720 17721
17812 17813 17814 17829 17838 17839 17840 17841 17850 17851 17852 17853 17971 17985 17994 17995
17997 18006 18007 18008 18009 18018 18019 18020 18021 18051 18053 18054 18056 18065 18066 18067
18068 18077 18078 18195 18196 18197 18198 18207 18208 18209 18210 18219 18220 18221 18222 18231
18232 18233 18235 18338 18339 18340 18341 18342 18351 18352 18353 18354 18355 18364 18365 18366

18367 18376 18377 18378 18379 18388 18389 18390 18391 18412 18413 18414 18415 18424 18425 18426
18427 18428 18437 18438 18439 18440 18441 18450 18451 18452 18453 18462 18463 18464 18465 18486
18487 18488 18490 18499 18500 18501 18502 18511 18512 18513 18514 18523 18524 18525 18526 18536
18537 18538 18559 18560 18561 18562 18571 18572 18573 18574 18575 18584 18585 18586 18588 18597
18598 18599 18600 18609 18610 18611 18612 18728 18729 18730 18739 18740 18741 18742 18751 18752
18753 18754 18763 18764 18765 18766 18787 18788 18789 18790 18799 18801 18802 18812 18813 18814
18815 18824 18825 18826 18827 18836 18837 18838 18839 18840 18841 18863 18864 18865 18866 18875
18876 18877 18878 18879 18888 18889 18890 18891 18900 18901 18902 18904 18913 18914 18915 18916
18925 18928 18949 18950 18951 18952 18961 18962 18963 18964 18973 18974 18975 18976 18985 18986
18987 18988 18997 18998 18999 19000 19244 19245 19246 19247 19256 19257 19258 19259 19268 19269
19270 19271 19280 19281 19282 19293 19295 19296 19413 19414 19415 19416 19425 19426 19427 19428
19437 19439 19440 19441 19450 19451 19452 19453 19474 19475 19476 19477 19486 19487 19488 19489
19498 19499 19500 19501 19510 19512 19513 19522 19523 19524 19525 19534 19535 19536 19537 19558
19559 19560 19561 19570 19571 19572 19573 19582 19583 19584 19585 19594 19595 19596 19597 19606
19607 19608 19609 19704 19705 19706 19707 19716 19717 19718 19719 19728 19729 19730 19731 19740
19741 19742 19743 19752 19753 19755 19756 19777 19778 19779 19780 19789 19790 19791 19792 19801
19802 19803 19804 19813 19814 19815 19817 19826 19828 19829 19851 19852 19855 19864 19865 19867
19869 19878 19879 19880 19881 19890 19891 19892 19893 19894 19903 19904 19905 19906 20010 20011
20012 20013 20023 20024 20025 20026 20027 20028 20037 20038 20039 20041 20050 20051 20052 20053
20170 20171 20172 20173 20182 20183 20184 20185 20194 20195 20196 20197 20206 20207 20208 20209
20218 20219 20220 20221 20242 20244 20254 20255 20256 20257 20267 20268 20269 20278 20279 20281
20282 20283 20292 20293 20294 20295 20316 20317 20318 20327 20328 20329 20330 20339 20340 20341
20343 20352 20353 20354 20355 20365 20366 20367 20390 20391 20392 20402 20405 20414 20415 20416
20417 20427 20428 20438 20439 20440 20442 20463 20464 20466 20475 20476 20477 20478 20488 20489
20490 20499 20500 20501 20502 20511 20512 20513 20514 20523 20524 20525 20526 20527 20548 20549
20550 20560 20561 20562 20563 20572 20573 20575 20584 20587 20588 20597 20599 20621 20622 20623
20624 20633 20634 20635 20636 20645 20646 20647 20648 20649 20658 20659 20660 20661 20670 20671
20672 20673 20694 20695 20696 20697 20706 20708 20709 20719 20720 20721 20722 20723 20733 20734
20735 20744 20745 20746 20747 20768 20769 20770 20771 20780 20781 20782 20783 20792 20793 20794
20795 20804 20805 20806 20807 20816 20817 20818 20819 20828 20832 20891 20892 20893 20894 20903
20904 20906 20909 20910 20911 20912 20933 20934 20935 20936 20945 20946 20947 20948 20957 20958
20959 20960 20969 20970 20972 20973 20982 20983 20984 20985 20994 20995 20996 20997 20998 20999
21000 21001 21055 21056 21058 21079 21080 21134 21135 21136 21137 21138 21147 21149 21150 21151
21160 21161 21162 21163 21164 21255 21256 21257 21258 21267 21268 21269 21270 21279 21280 21281
21282 21291 21292 21293 21294 21303 21304 21305 21306 21307 21316 21317 21318 21319 21328 21329
21330 21331 21335 21336 21337 21338 21348 21349 21350 21359 21360 21361 21362 21363 21364 21483
21484 21486 21487 21496 21497 21498 21499 21508 21509 21510 21511 21520 21521 21522 21523 21532
21533 21534 21535 21569 21570 21571 21572 21581 21582 21583 21584 21593 21594 21595 21596 21605
21606 21607 21608 21629 21630 21631 21632 22015 22016 22017 22018 22027 22028 22029 22030 22039
22040 22041 22042 22043 22052 22068 22069 22079 22082 22083 22084 22085 22094 22095 22096 22097
22106 22107 22108 22109 22118 22119 22120 22121 22131 22132 22134 22142 22143 22144 22145 22146
22155 22156 22157 22159 22168 22169 22170 22171 22180 22181 22182 22183 22287 22288 22289 22298
22299 22301 22302 22303 22312 22313 22314 22315 22324 22325 22326 22327 22449 22451 22452 22453
22462 22463 22464 22466 22467 22476 22477 22478 22479 22488 22489 22490 22491 22515 22516 22517
22518 22527 22528 22537 22538 22539 22540 22549 22550 22551 22552 22561 22562 22563 22564 22585
22586 22587 22588 22597 22598 22609 22610 22611 22620 22621 22622 22623 22632 22633 22634 22635
22644 22645 22646 22648 22703 22704 22705 22706 22715 22716 22717 22718 22727 22728 22729 22730
22739 22740 22741 22783 22784 22785 22795 22796 22797 22798 22807 22808 22809 22810 22849 22850
22852 22861 22862 22863 22864 22873 22874 22875 22876 22885 22886 22888 22990 22991 22992 23002
23003 23004 23014 23016 23017 23026 23027 23029 23030 23039 23041 23042 23160 23161 23162 23163
23164 23173 23174 23209 23210 23211 23212 23223 23224 23233 23234 23236 23245 23246 23247 23248
23257 23259 23260 23269 23272 23281 23282 23284 23293 23294 23295 23296 23306 23307 23308 23317
23318 23319 23321 23330 23331 23332 23333 23336 23599 23600 23601 23602 23603 23604 23605 23606

23615 23616 23617 23619 23620 23621 23622 23802 23803 23821 23822 23823 23824 23825 23826 23827
23828 23829 23830 23839 23840 23842 23843 23844 23845 23846 23847 23865 23866 23867 23876 23877
23878 23879 23880 23881 23882 23883 23884 23948 23949 23950 23954 23957 23966 23967 23968 23973
23999 24000 24001 24002 24003 24004 24005 24006 24007 24008 24009 24018 24043 24044 24046 24047
24048 24049 24050 24051 24052 24053 24054 24063 24064 24065 24066 24067 24068 24069 24070 24071
24073 24074 24169 24170 24171 24172 24173 24174 24175 24176 24177 24178 24179 24180 24189 24190
24191 24192 24193 24194 24296 24297 24298 24303 24304 24305 24314 24315 24316 24318 24319 24320
24321 24322 24323 24324 24325 24345 24346 24347 24348 24556 24567 24568 24569 24574 24575 24578
24579 24581 24586 24587 24597 24598 24599 24600 24601 24602 24603 24604 24605 24606 24607 24702
24703 24704 24705 24706 24708 24709 24710 24711 24712 24713 24722 24723 24724 24725 24727 24728
24729 24730 24731 24732 24833 24834 24871 24890 24891 24892 24893 24894 24895 24900 24901 24902
24903 24904 24905 24906 24916 24917 24918 24919 24920 24921 24922 25015 25016 25017 25018 25023
25025 25028 25029 25030 25031 25032 25033 25042 25043 25044 25045 25046 25047 25048 25090 25091
25092 25094 25095 25096 25097 25098 25099 25100 25101 25102 25111 25112 25199 25200 25201 25202
25203 25208 25209 25210 25211 25212 25213 25223 25224 25225 25226 25227 25228 25229 25230 25231
25332 25333 25605 25606 25607 25608 25609 25610 25611 25612 25613 25614 25615 25616 25625 25626
25627 25628 25715 25716 25717 25718 25723 25724 25725 25726 25735 25736 25737 25738 25740 25741
25742 25744 25745 25746 25791 25792 25801 25802 25877 25878 25879 25880 25881 25882 25883 25884
25885 25886 25895 25896 25897 25898 25900 25919 25920 25921 25922 25923 25924 25925 25926 25939
25948 25950 25951 25952 25953 25954 25955 25956 25957 25958 25959 26095 26096 26101 26102 26103
26104 26105 26110 26111 26112 26113 26114 26115 26124 26125 26126 26127 26128 26129 26130 26131
26155 26156 26170 26171 26172 26173 26174 26175 26176 26179 26180 26181 26190 26191 26192 26193
26280 26283 26285 26286 26291 26292 26301 26302 26303 26304 26305 26306 26307 26308 26309 26310
26311 26312

Appendix G

Time Calibration of the Read-Out Electronics

For the time-resolved measurements of the scintillation light of liquid argon the read-out electronics had to be calibrated in time, in particular the time-to-amplitude converter (TAC). For that reason a set of time spectra of liquid argon with the pulsed sulfur beam was recorded for a wavelength[1] of 174.6 nm; each of these spectra had a different and precisely determined delay[2] of the chopper trigger signal, which was used as stop signal for the TAC. The respective start signal was given by the PMT pulse each time, therefore, the different settings of the delay shifted the peak emission within the time window of the TAC. In the offline analysis the region around the peak emission was fitted with a Gaussian. This is displayed in fig. G.1, once for the full time-resolved spectrum recorded (red), and once in a zoomed-in view to the peak of the emission. The Gaussian fit to the spectrum is shown in blue; its fitted centre position determines the measured delay of the corresponding calibration spectrum.

Afterwards, the mean position of the Gaussian fit with the obtained uncertainty was plotted as a function of the set delay for both TAC-ranges used (500 ns and 5 µs, respectively). A straight line was fitted to these data, checking for any non-linearities of the TAC. Figures G.2 and G.3 display these data and the applied fit functions. Besides the linearity check, the fit allows a precise determination of the width of the TAC range.

In both cases the linearity of the TAC proves to be perfect, however, the width of the time window does not match the preset value precisely enough: the 500 ns time window turned out to have a width of about 520.7 ns, therefore, the time constants obtained from any time-resolved measurement with this setting of the TAC have to be corrected by a factor of 1.041. For the 5 µs time window a correction factor of 1.0182 was found. In addition, this time window has a minor time offset of ~ 35 ns, which causes a constant shift of the recorded data with respect to the start point of the TAC scale, but does not affect the obtained time constants of the light-emission features.

[1] The choice of the wavelength is not so important here. 174.6 nm has been chosen as it has a prominent fast component; see sec. 11.3.3.

[2] Created with a Stanford Gate Generator DG535; delay precise to ~ 1.5 ns [Sta12]. The precision of this delay determines the precision of the calibration.

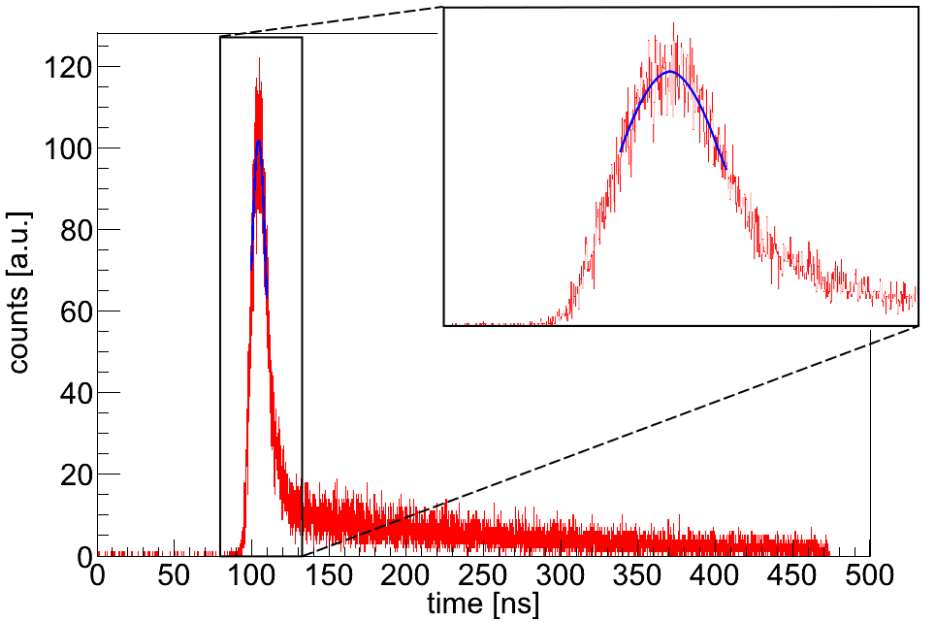

Figure G.1: *Time spectrum recorded with the pulsed sulfur beam at 174.6 nm. A Gaussian is fitted to the peak emission (blue). The inset shows a zoomed-in view of the peak emission and the fit function.*

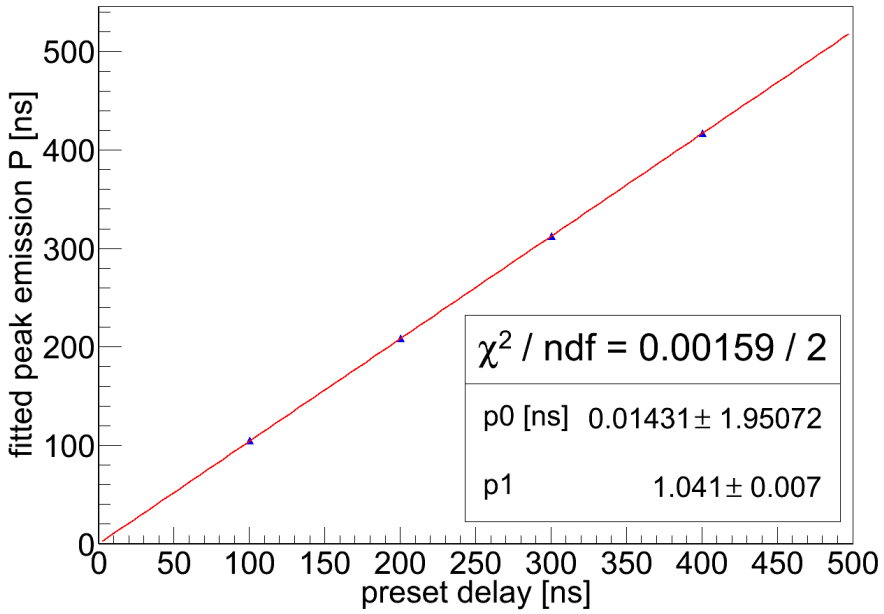

Figure G.2: *Fitted peak-emission positions as a function of the preset delay values (blue data points) for the 500 ns-TAC range. The error bars are much smaller than the symbols used. A straight line, $P = p0 + p1 \cdot t$, is fitted to the data, showing the linearity of the TAC. However, the full range is 520.7 ns instead of 500 ns, i.e. all time data obtained with this TAC-setting has to be corrected by a factor of 1.041 ± 0.007 afterwards.*

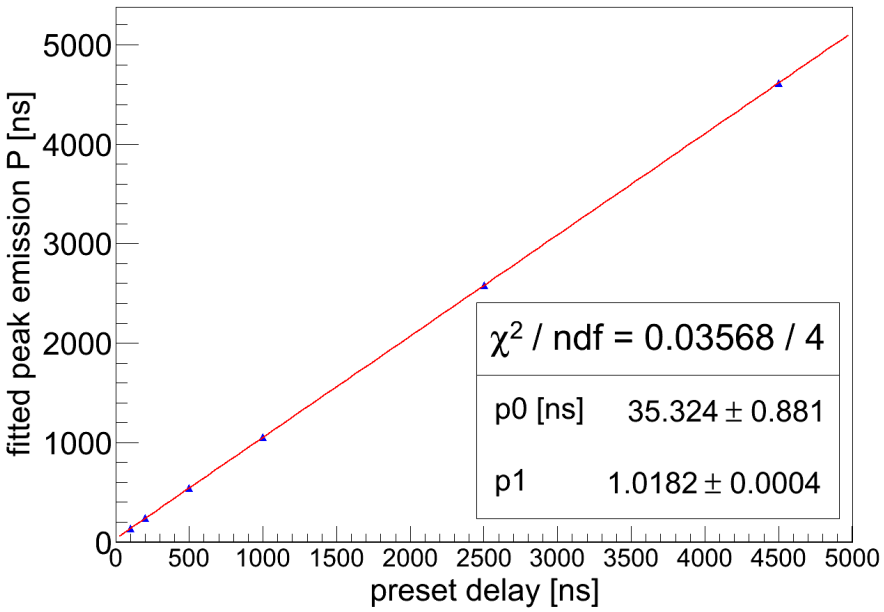

Figure G.3: *Fitted peak-emission positions as a function of the preset delay values (blue data points) for the 5000 ns-TAC range. Again, the error bars are much smaller than the symbols used. A straight line, $P = p0 + p1 \cdot t$, is fitted to the data, showing the linearity of the TAC. For this TAC range an offset of ~ 35 ns is observed. However, this only causes a time shift of the data with respect to the start point of the TAC range and does not spoil the time constants obtained. The correction factor is 1.0182 ± 0.0004 in this case.*

List of Figures

List of Tables

Bibliography

[Aal02] C.E. Aalseth et al.: *"IGEX ^{76}Ge neutrinoless double-beta decay experiment: Prospects for next generation experiments"*, Phys. Rev. D**65**, 092007 (2002) [arXiv:hep-ex/0202026]

[Aal02a] C.E. Aalseth et al.: *"Comment on 'Evidence for Neutrinoless Double Beta Decay' "*, Mod. Phys. Lett. A**17**, 1475 (2002) [arXiv:hep-ex/0202018v3]

[Aal10] C.E. Aalseth et al., MAJORANA collaboration: *"The MAJORANA Experiment"*, Nucl. Phys. B**217**, 44 (2011) [arXiv:1101.0119 [nucl-ex]]

[Aal11] C.E. Aalseth et al., CoGeNT collaboration: *"Results from a Search for Light-Mass Dark Matter with a P-type Point Contact Germanium Detector"*, Phys. Rev. Lett. **106**, 131301 (2011) [arXiv:1002.4703v2 [astro-ph.CO]]

[Aal11a] C.E. Aalseth et al., CoGeNT collaboration: *"Search for an Annual Modulation in a P-type Point Contact Germanium Dark Matter Detector"*, Phys. Rev. Lett. **107**, 141301 (2011) [arXiv:1106.0650v3 [astro-ph.CO]]

[Abb11] R. Abbasi et al., IceCube collaboration: *"Search for Dark Matter from the Galactic Halo with the IceCube Neutrino Observatory"*, Phys. Rev. D**84**, 022004 (2011) [arXiv:1101.3349 [astro-ph.HE]]

[Abe08] S. Abe et al., KamLAND collaboration: *"Precision Measurement of Neutrino Oscillation Parameters with KamLAND"*, Phys. Rev. Lett. **100**, 221803 (2008) [arXiv:0801.4589v3 [hep-ex]]

[Abe11] K. Abe et al., T2K collaboration: *"Indication of Electron Neutrino Appearance from an Accelerator-Produced Off-Axis Muon Neutrino Beam"*, Phys. Rev. Lett. **107**, 041801 (2011) [arXiv:1106.2822v2 [hep-ex]]

[Abe11a] C. Aberle: *"Optimization, simulation and analysis of the scintillation signals in the Double Chooz experiment"*, Ph.D. thesis, Ruprecht-Karls-Universität Heidelberg (2011)

[Abe12] Y. Abe et al., Double Chooz collaboration: *"Indication for the disappearance of reactor electron antineutrinos in the Double Chooz experiment"*, Phys. Rev. Lett. **108**, 131801 (2012) [arXiv:1112.6353v3 [hep-ex]]

[Abe12a] Y. Abe et al., Double Chooz collaboration: *"Reactor $\bar{\nu}_e$ disappearance in the Double Chooz experiment"*, Phys. Rev. D**86**, 052008 (2012) [arXiv:1207.6632v4 [hep-ex]]

[Abe12b] C. Aberle et al.: *"Large scale Gd-beta-diketonate based organic liquid scintillator production for antineutrino detection"*, JINST **7**, P06008 (2012)

[Acc10] R. Acciarri et al.: *"Oxygen contamination in liquid Argon: combined effects on ionization electron charge and scintillation light"*, JINST **5**, P05003 (2010) [arXiv:0804.1222 [nucl-ex]]

[Ack11] N. Ackerman et al., EXO Collaboration: *"Observation of Two-Neutrino Double-Beta Decay in ^{136}Xe with the EXO-200 Detector"*, Phys. Rev. Lett. **107**, 212501 (2011) [arXiv:1108.4193v2 [nucl-ex]]

[Ada08] P. Adamson et al., MINOS collaboration: *"Measurement of Neutrino Oscillations with the MINOS Detectors in the NuMI Beam"*, Phys. Rev. Lett. **101**, 131802 (2008)

[Ada11] P. Adamson et al.: *"Improved search for muon-neutrino to electron-neutrino oscillations in MINOS"*, Phys. Rev. Lett. **107**, 181802 (2011) [arXiv:1108.0015 [hep-ex]]

[Ago03] S. Agostinelli et al.: *"Geant4 - a simulation toolkit"*, Nucl. Instr. Meth. A**506**, 250 (2003)

[Ahl80] S.P. Ahlen: *"Theoretical and experimental aspects of the energy loss of relativistic heavily ionizing particles "*, Rev. Mod. Phys. **52**, 121 (1980)

[Ahn12] J.K. Ahn et al., RENO Collaboration: *"Observation of Reactor Electron Antineutrino Disappearance in the RENO Experiment"*, Phys. Rev. Lett. **108**, 191802 (2012) [arXiv:1204.0626v2 [hep-ex]]

[Ait89] I.J.R. Aitchison and A.J.G. Hey: *"Gauge theories in Particle Physics"*, 2$^{\text{nd}}$ edition, Adam Hilger, Bristol and Philadelphia (1989)

[Akh97] E.K. Akhmedov: *"The Neutrino Magnetic Moment and Time Variations of the Solar Neutrino Flux"*, arXiv:hep-ph/9705451v2 (1997)

[Akh00] E.K. Akhmedov: *"Neutrino physics"*, arXiv:hep-ph/0001264v2 (2000)

[Akh06] E.K. Akhmedov: *"Neutrino oscillations: theory and phenomenology"*, arXiv:hep-ph/0610064v2 (2006)

[Akh11] E.K. Akhmedov: *"Neutrino oscillations: Entanglement, energy-momentum conservation and QFT"*, Found. Phys. **41**, 1279 (2011) [arXiv:1008.2077v3 [hep-ph]]

[Aki07] D.Yu. Akimov et al.: *"The ZEPLIN-III dark matter detector: Instrument design, manufacture and commissioning"*, Astropart. Phys. **27**, 46 (2007) [arXiv:astro-ph/0605500]

[Alb86] T.S. Van Albada et al.: *"Dark Matter in Spiral Galaxies"*, Phil. Trans. R. Sac. Land. A**320**, 447 (1986)

[All02] S.W. Allen, R.W. Schmidt, and A.C. Fabian: *"Cosmological constraints from the X-ray gas mass fraction in relaxed lensing clusters observed with Chandra"*, Mon. Not. R. Astron. Soc. **334**, L11 (2002)

[All06] J. Allison et al.: *"Geant4 developments and applications"*, IEEE Trans. Nucl. Sci. **53**, 270 (2006)

[Alt05] G. Altarelli: *"The Standard Model of Particle Physics"*, arXiv:hep-ph/0510281 (2005)

[Alv11] V. Álvares et al., NEXT collaboration: *"The NEXT-100 experiment for neutrinoless double beta decay searches"*, arXiv:1106.3630 [physics.ins-det] (2011)

[An12] F.P. An et al., Daya Bay Collaboration: *"Observation of electron-antineutrino disappearance at Dyay Bay"*, Phys. Rev. Lett. **108**, 171803 (2012) [arXiv:1203.1669v2 [hep-ex]]

[And04] K. Anderson et al.: *"White paper report on using nuclear reactors to search for a value of ϑ_{13}"*, arXiv:hep-ex/0402041 (2004)

[Ang12] G. Angloher et al.: *"Results from 730 kg days of the CRESST-II Dark Matter Search"*, Eur. Phys. J. C**72**, 1971 (2012) [arXiv:1109.0702 [astro-ph.CO]]

[Ant04] M. Antonello et al.: *"Detection of Cherenkov light emission in liquid argon"*, Nucl. Inst. Meth. A**516**, 348 (2004)

[Apo03] M. Apollonio et al., CHOOZ collaboration: *"Search for neutrino oscillations on a long base-line at the CHOOZ nuclear power station"*, Eur. Phys. J. C**27**, 331 (2003) [arXiv:hep-ex/0301017]

[Apr05] E. Aprile et al.: *"The XENON dark matter search experiment"*, New Astron. Rev. **49**, 289 (2005)

[Apr06] E. Aprile et al.: *"Noble gas detectors"*, Wiley-VCH Verlag, Welnheim (2006)

[Ard04] F. Ardellier et al.: *"Letter of Intent for Double-CHOOZ: a Search for the Mixing Angle Theta13"*, arXiv:hep-ex/0405032 (2004)

[Ard06] F. Ardellier et al.: *"Double Chooz, A Search for the Neutrino Mixing Angle theta-13"*, arXiv:hep-ex/0606025v4 (2006)

[Aur97] P. Aurenche: *"The Standard Model of Particle Physics"*, arXiv:hep-ph/9712342 (1997)

[Bak05] A.M. Bakalyarov et al.: *"Results of the experiment on investigation of Germanium-76 double beta decay. Experimental data of Heidelberg-Moscow collaboration November 1995 - August 2001"*, Phys. Part. Nucl. Lett. **2**, 77 (2005) [arXiv:hep-ex/0309016]

[Bal65] G. Baldini: *"Trapped Excitons in Dilute Rare-Gas Alloys"*, Phys. Rev. **137**, A508 (1965)

[Bar11] A.S. Barabash: *"75 years of double beta decay: yesterday, today and tomorrow"*, arXiv:1101.4502 [nucl-ex] (2011)

[Bas70] N.G. Basov et al.: *"Luminescence of condensed Xe, Kr, Ar and their mixtures in vacuum region of spectrum under excitation by fast electrons"*, J. Lumin. **12**, 834 (1970)

[Beg91] K.G. Begeman, A.H. Broeils, and R.H. Sanders: *"Extended rotation curves of spiral galaxies - Dark haloes and modified dynamics"*, Mon. Not. R. Astron. Soc. **249**, 523 (1991)

[Bel00] A.G. Belov et al.: *"Luminescence of oxygen-rare gas exciplex compounds in rare gas matrices"*, J. Lumin. **91**, 107 (2000)

[Ben03] C.L. Bennett et al.: *"First Year Wilkinson Microwave Anisotropy Probe (WMAP) Observations: Preliminary Maps and Basic Results"*, Astroph. J. Suppl. **148**,1 (2003) [arXiv:astro-ph/0302207v3]

[Ben08] P. Benetti et al., WARP collaboration *"First results from a Dark Matter search with liquid Argon at 87 K in the Gran Sasso Underground Laboratory"*, Astropart. Phys. **28**,495 (2008) [arXiv:astro-ph/0701286v2]

[Ber02] R. Bernabei et al.: *"Investigation of $\beta\beta$ decay modes in ^{134}Xe and ^{136}Xe"*, Phys. Lett. B**546**, 23 (2002)

[Ber04] L. Bergström and A. Goobar: *"Cosmology and Particle Astrophysics"*, 2nd edition, Springer, Berlin, Heidelberg (2004)

[Ber04a] S. Berridge et al.: *"Proposal for U.S. participation in Double-CHOOZ: A New theta-13 Experiment at the Chooz Reactor"*, arXiv:hep-ex/0410081 (2004)

[Ber05] G. Bertone, D. Hooper, and J. Silk: *"Particle Dark Matter: Evidence, Candidates and Constraints"*, Phys. Rept. **405**,279 (2005) [arXiv:hep-ph/0404175v2]

[Ber09] R. Bernabei et al.: *"Particle Dark Matter and DAMA/LIBRA"*, arXiv: 0912.0660 [astro-ph.GA] (2009)

[Ber10] R. Bernabei et al.: *"New results from DAMA/LIBRA"*, Eur. Phys. J. C**67**, 39 (2010) [arXiv:1002.1028 [astro-ph.GA]]

[Bet30] H. Bethe: *"Zur Theorie des Durchgangs schneller Korpuskularstrahlen durch Materie"*, Ann. Phys. **397**, 325 (1930)

[Bev69] P.R. Bevington: *"Data reduction and error anaylsis for the physical sciences"*, McGraw-Hill Companies, New York (1969)

[Bid80] A. Bideau-Mehu et al.: *"Measurement of Refractive Indices of Neon, Argon, Krypton and Xenon in the 253.7-140.4 nm Wavelength Range. Dispersion Relations and Estimated Oscillator Strengths of the Resonance Lines"*, J. Quant. Spectrosc. Radiat. Transfer **25**, 395 (1981)

[Bil78] S.M. Bilenky and B. Pontecorvo: *"Lepton mixing and neutrino oscillations"*, Phys. Rept. **41**, 225 (1978)

[Bil80] S.M. Bilenky, J. Hošek, and S.T. Petcov: *"On the Oscillations of Neutrinos with Dirac and Majorana Masses"*, Phys. Lett. **94**, 495 (1980)

[Bil99] S.M. Bilenky, C. Giunti, and W. Grimus: *"Phenomenology of Neutrino Oscillations"*, Prog. Part. Nucl. Phys. **43**, 1 (1999) [arXiv:hep-ph/9812360v4]

[Bir51] J.B. Birks: *"Scintillations from Organic Crystals : Specific Fluorescence and Relative Response to Different Radiations"*, Proc. Phys. Soc. A**64**, 874 (1951)

[Bir53] J.B. Birks: *"Scintillation Counters"*, Pergamon Press, London (1953)

[Bir64] J.B. Birks: *"The Theory and Practice of Scintillation Counting"*, Pergamon Press, London (1964)

[Boe12] Böhler Welding Group, `http://www.bohlerweldinggroup.ch/german/files/D_Info_Schweissmaterialkalkulation_2012-06-22.pdf`, retrieved August 23th, 2012

[Bor03] M. Born: *"Die Relativitätstheorie Einsteins"*, 7th edition, Springer, Berlin, Heidelberg (2003)

[Bor05] L. Bornschein, KATRIN collaboration: *"The KATRIN experiment - a direct measurement of the electron antineutrino mass in the sub-eV region"*, Nucl. Phys. A**752**, 14 (2005)

[Boy09] A. Boyarsky, O. Ruchayskiy, and M. Shaposhnikov: *"The Role of Sterile Neutrinos in Cosmology and Astrophysics"*, Ann. Rev. Nucl. Part. Sci. **59**, 191 (2009)

[Boy11] A. Boyarsky, D. Malyshev, and O. Ruchayskiy: *"A comment on the emission from the Galactic Center as seen by the Fermi telescope"*, Phys. Lett. B**705**, 165 (2011) [arXiv:1012.5839 [hep-ph]]

[Buc09] C. Buck et al.: *"Status scintillator production at MPIK Heidelberg"*, DCDocDB 715-v1, only available at `http://www.dchooz.org/DocDB/` (2009)

[But64] H.v. Buttlar: *"Einführung in die Grundlagen der Kernphysik"*, Akademische Verlagsgesellschaft, Frankfurt am Main (1964)

[Cal91] D.O. Caldwell: *"Double beta decay - present and future"*, J. Phys. G**17**, S137 (1991)

[Cao07] J. Cao: *"Reactor Neutrino Experiments"*, arXiv:0712.0897 [hep-ex] (2007)

[Car79] M.J. Carvalho and G. Klein: *"Luminescence decay in condensed argon under high energy excitation"*, J. Lumin. **18**, 487 (1979)

[Cen11] B. Censier: *"Review on non-directional direct dark matter searches"*, arXiv: 1110.0191 [astro-ph.CO] (2011)

[CER12] CERN press release: *"CERN experiments observe particle consistent with long-sought Higgs boson"*, `http://press.web.cern.ch/press/PressReleases/Releases2012/PR17.12E.html`, retrieved July 14th, 2012

[CER12a] CERN Geant4 homepage: `http://geant4.cern.ch/`, retrieved February 6th, 2012

[Che72] O. Cheshnovsky, B. Raz, and J. Jortner: *"Emission Spectra of Deep Impurity States in Solid and Liquid Rare Gas Alloys"*, J. Chem. Phys. **57**, 4628 (1972)

[Cie11] C. Ciemniak: *"Setup of a Neutron Scattering Facility for the Measurement of Scintillation Light Quenching Factors of Low-Temperature Detectors Used in the Direct Dark Matter Search Experiments CRESST and EURECA"*, Ph.D. thesis, Technische Universität München (2011)

[Clo06] D. Clowe et al.: *"A Direct Empirical Proof of the Existence of Dark Matter"*, Astroph. J. **648**, L109 (2006) [arXiv:astro-ph/0608407]

[Col76] E.A. Colbourn and A.E. Douglas: *"The spectrum and ground state potential curve of Ar_2"*, J. Chem. Phys. **65**, 1741 (1976)

[Con28] E. Condon: *"A Theory of Intensity Distribution in Band Systems"*, Phys. Rev. **28**, 1182 (1928)

[Cur09] A. Curioni: *"Noble liquid detectors for fundamental physics and applications"*, Nucl. Phys. B (Proc. Suppl.) **197**, 48 (2009)

[Dan89] H. Daniel: *"Atome, Festkörper, Kerne, Teilchen"*, de Gruyter, Berlin, New York (1998)

[Dan11] T. Dandl et al.: *"Electron-beam-ignited, high-frequency-driven vacuum ultraviolet excimer light source"*, EPL **94**, 53001 (2011)

[Dan12] T. Dandl, Technische Universität München, *private communication* (2012)

[DC11] Double Chooz collaboration: *"Blessed plots"*, only available at `http://doublechooz.in2p3.fr/Private/Working_Groups/Analysis/AnalysisBlessPlots/` (2011)

[Del60] G.F. Dell'Antonio and E. Fiorini: *"Experimental and Theoretical Remarks on the Double β-decay"*, Nouv. Ciem. Suppl. **17**, 132 (1960)

[DeR99] A. De Rújula, M.B. Gavela, and P. Hernández: *"Neutrino oscillation physics with a neutrino factory"*, Nucl. Phys. B**547**, 21 (1999) [arXiv:hep-ph/9811390v2]

[Dic65] R.H. Dicke et al.: *"Cosmic Black-Body Radiation"*, Astroph. J. **142**, 414 (1965)

[Die11] D. Dietrich: *"Cosmic muon studies"*, DCDocDB 3223-v2, only available at `http://www.dchooz.org/DocDB/` (2011)

[DKD00] Deutscher Kalibrierdienst: *Calibration certificate 07683 DKD-K-06501 00-05*, Braunschweig (2000)

[DKD06] Deutscher Kalibrierdienst: *Calibration certificate 016278 DKD-K-06501 06-02*, Braunschweig (2006)

[DKD08] Deutscher Kalibrierdienst: *Calibration certificate 020668 DKD-K-06501 2008-11*, Braunschweig (2008)

[Dok88] T. Doke et al.: *"LET Dependence of Scintillation Yields in Liquid Argon"*, Nucl. Instr. Meth. A**269**, 291 (1988)

[Dok02] T. Doke et al.: *"Absolute Scintillation Yields in Liquid Argon and Xenon for Various Particles"*, Jpn. J. Appl. Phys. **41**, 1538 (2002)

[DRA12] DRAGON Simulation Code, `http://www.polymtl.ca/nucleaire/DRAGON/en/`, retrieved August 25$^{\text{th}}$, 2012

[DSP00] Canberra Eurisys GmbH, Walter-Flex-Str. 66, D-65428 Rüsselsheim: *"Model 9660/9660A ICB Digital Signal Processor - Users Manual"* (2000)

[Eft97] T. Efthimiopoulos, D. Zouridis, and A. Ulrich: *"Excimer emission spectra of rare gas mixtures using either a supersonic expansion or a heavy-ion-beam excitation"*, J. Phys. D: Appl. Phys. **30**, 1746 (1997)

[Ell87] S.R. Elliott, A.A. Hahn, and M.K. Moe: *"Direct Evidence for Two-Neutrino Double-Beta Decay in ^{82}Se"*, Phys. Rev. Lett. **59**, 2020 (1987)

[Fed04] A. Fedenev et al.: *"Applications of a broadband electron-beam pumped XUV radiation source"*, J. Phys. D: Appl. Phys. **37**, 1586 (2004)

[Fei82] F. von Feilitzsch, A.A. Hahn, and K. Schreckenbach: *"Experimental Beta-Spectra from ^{239}Pu and ^{235}U Thermal Neutron Fission Products and their Correlated Antineutrino Spectra"*, Phys. Lett. B**118**, 162 (1982)

[Fir96] R.B. Firestone and V.S. Shirley (ed.): *"Table of isotopes"*, 8$^{\text{th}}$ edition, John Wiley & sons, New York (1996)

[Fix96] D.J. Fixsen et al.: *"The Cosmic Microwave Background Spectrum from the full COBE FIRAS Data Set"*, Astroph. J. **473**, 576 (1996)

[For51] T. Förster: *"Fluoreszenz organischer Verbindungen"*, Vandenhoeck & Ruprecht, Göttingen (1951)

[For12] N. Fornengo et al.: *"Galactic synchrotron emission from WIMPs at radio frequencies"*, JCAP **01**, 005 (2012) [arXiv:1110.4337v2 [astro-ph.GA]]

[Fra26] J. Franck and E. G. Dymond: *"Elementary processes of photochemical reactions"*, Trans. Faraday Soc. **21**, 536 (1926)

[Fre01] M. Freund: *"Analytic Approximations for Three Neutrino Oscillation Parameters and Probabilities in Matter"*, Phys. Rev. D**64**, 053003 (2001) [arXiv:hep-ph/0103300]

[Fuk03] S. Fukuda et al., Super-Kamiokande collaboration: *"The Super-Kamiokande Detector"*, Nucl. Inst. Meth. A**501**, 418 (2003)

[Gai98] M.K. Gaillard, P.D. Grannis, and F.J. Sciulli: *"The Standard Model of Particle Physics"*, Rev. Mod. Phys. **71**, 96 (1999) [arXiv:hep-ph/9812285]

[Gar57] R.L. Garwin, L.M. Lederman, and M. Weinrich: *"Observations of the Failure of Conservation of Parity and Charge Conjugation in Meson Decays: the Magnetic Moment of the Free Muon"*, Phys. Rev. **105**, 1415 (1957)

[Gas10] D. Gastler et al.: *"Measurement of scintillation efficiency for nuclear recoils in liquid argon"*, arXiv:1004.0373v3 [physics.ins-det]

[GEN02] Canberra Eurisys GmbH, Walter-Flex-Str. 66, D-65428 Rüsselsheim: *"Genie-2000 Benutzerhandbuch für die Gammaspektrometrie"*, Version 2.1 (2002)

[Ger74] J.B. Gerardo and A.W. Johnson: *"Photoattenuation in the extreme red wings of Xe and Kr resonance lines"*, Phys. Rev. A**10**, 1204 (1974)

[Giu98] C. Giunti and C.W. Kim: *"Coherence of neutrino oscillations in the wave packet approach"*, Phys. Rev. D**58**, 017301 (1998) [arXiv:hep-ph/9711363v2]

[Gol58] M. Goldhaber, L. Grodzins, and A.W. Sunyar: *"Helicity of Neutrinos"*, Phys. Rev. **109**, 1015 (1958)

[Gra09] D. Grant, D.J. Koskinen, and C. Rott, IceCube collaboration: *"Fundamental Neutrino Measurements with IceCube DeepCore"*, Proceedings of the 31st ICRC, Łódź (2009)

[Haa12] N. Haag: *"The antineutrino spectrum of the fission products of ^{238}U"*, Ph.D. thesis, *in preparation*, Technische Universität München (2012)

[Hah89] A.A. Hahn et al.: *"Antineutrino Spectra from ^{241}Pu and ^{239}Pu Thermal Neutron Fission Products"*, Phys. Lett. B**218**, 365 (1989)

[Hal84] F. Halzen and A.D. Martin: *"Quarks & Leptons"*, 1st edition, John Wiley & sons, New York (1984)

[Hal10] F. Halzen and S.R. Klein: *"IceCube: An instrument for neutrino astronomy"*, Rev. Sci. Instrum. **81**, 081101 (2010) [arXiv:1007.1247v2 [astro-ph.HE]]

[Hei10] T. Heindl et al.: *"The scintillation of liquid argon "*, EPL **91**, 62002 (2010)

[Hei11] T. Heindl: *"Die Szintillation von flüssigem Argon"*, Ph.D. thesis, Technische Universität München (2011)

[Hei11a] T. Heindl et al.: *"Table-top setup for investigating the scintillation properties of liquid argon"*, JINST **6**, P02011 (2011)

[Hen99] R. von Hentig: *"Spurenanalyse primordialer Radionuklide für das solare Neutrinoexperiment BOREXINO"*, Ph.D. thesis, Technische Universität München (1999)

[Heu06] G.Heusser, M.Laubenstein, and H.Neder: *"Radionuclides in the environment"*, Int.Conf.Iso.Env.Studies, Elsevier, Amsterdam, 495 (2006)

[Him11] A. Hime, MiniCLEAN collaboration: *"The MiniCLEAN Dark Matter Experiment"*, arXiv:1110.1005 [physics.ins-det] (2011)

[Hit83] A. Hitachi et al.: *"Effect of ionization density on the time-dependence of luminescence from liquid argon and xenon"*, Phys. Rev. B**27**, 5279 (1983)

[Hit84] A. Hitachi: *"Exciton kinetics in condensed rare gases"*, J. Chem. Phys. **80**, 745 (1984)

[Hof07] M. Hofmann: *"Low-background gamma spectroscopy for the neutrino oscillation experiment Double Chooz"*, Diploma thesis, Technische Universität München (2007)

[Hoo11] D. Hooper and T. Linden: *"On The Origin Of The Gamma Rays From The Galactic Center"*, arXiv:1110.0006 [astro-ph.HE] (2011)

[Hoo11a] D. Hooper and T. Linden: *"Gamma Rays From The Galactic Center and the WMAP Haze"*, Phys. Rev. D**83**, 083517 (2011) [arXiv:1011.4520v2 [astro-ph.HE]]

[Hoo12] D. Hooper: *"The Empirical Case For 10 GeV Dark Matter"*, arXiv:1201.1303 [astro-ph.CO] (2012)

[Hor05] G. Horton-Smith: *"An introduction to GLG4sim features"*, available at `http://neutrino.phys.ksu.edu/MAND-sim/MAND-sim talks/` (2005)

[Hub03] P. Huber et al.: *"Reactor Neutrino Experiments compared to Superbeams"*, Nucl. Phys. B**665**, 487 (2003) [arXiv:hep-ph/0303232v3]

[Iso12] ISO Elektrodenfabrik AG, `www.isoarc.ch/Info_Datenbank/schweisskalkulation.pdf`, retrieved August 23rd, 2012

[Jab35] A. Jabloński: *"Über den Mechanismus der Photolumineszenz von Farbstoffphosphoren"*, Z. Phys. **94**, 38 (1935)

[Jag06] T. Jagemann, F. v.Feilitzsch, and J. Jochum: *"Measurement of the scintillation light quenching at room temperature of sodium recoils in NaI(Tl) and hydrogen recoils in NE 213 by the scattering of neutrons"*, Nucl. Inst. Meth. A**564**, 549 (2006)

[Jar11] N. Jarosik et al.: *"Seven-Year Wilkinson Microwave Anisotropy Probe (WMAP) Observations: Sky Maps, Systematic Errors, and Basic Results"*, Astroph. J. Suppl. **192**, 14 (2011) [arXiv:1001.4744v1 [astro-ph.CO]]

[Jas09] M. Jaskolski1 and M. Wojcik: *"Electronion recombination in radiation tracks in liquid argon: a computer simulation study"*, Res. Chem. Interm. **35**, 453 (2009)

[Jol12] C. Jollet-Meregaglia, IPHC, Université de Strasbourg, CNRS/IN2P3, *private communication* (2012)

[Jor65] J. Jortner et al.: *"Localized Excitations in Condensed Ne, Ar, Kr, and Xe "*, J. Chem. Phys. **42**, 4250 (1965)

[Kat12] U. Katz: *"PINGU - An IceCube extension for low-energy neutrinos"*, European Strategy for Neutrino Oscillation Physics - II, available at `ecap.nat.uni-erlangen.de/members/katz/talks/UliKatz_cern12.pdf`

[Kel11] C. Kelso, D. Hooper, and M.R. Buckley: *"Toward A Consistent Picture For CRESST, CoGeNT and DAMA"*, arXiv:1110.5338 [astro-ph.CO] (2011)

[Kla88] H.V. Klapdor (ed.): *"Neutrinos"*, Springer, Berlin, Heidelberg (1988)

[Kla01] H.V. Klapdor-Kleingrothaus et al.: *"Latest results from the HEIDELBERG-MOSCOW double beta decay experiment"*, Eur. Phys. J. A**12**, 147 (2001) [arXiv:hep-ph/0103062]

[Kla01a] H.V. Klapdor-Kleingrothaus et al.: *"Evidence for Neutrinoless Double Beta Decay"*, Mod. Phys. Lett. A**16**, 2409 (2001) [arXiv:hep-ph/0201231]

[Kla04] H.V. Klapdor-Kleingrothaus et al.: *"Search for neutrinoless double beta decay with enriched ^{76}Ge in Gran Sasso 19902003"*, Phys. Lett. B**586**, 198 (2004) [arXiv:hep-ph/0404088]

[Kla06] H.V. Klapdor-Kleingrothaus and I.V. Krivosheina: *"The Evidence for the Observation of $0\nu\beta\beta$ Decay: The Identification of $0\nu\beta\beta$ Events from the full Spectra"*, Mod. Phys. Lett. A**21**, 1547 (2006)

[Kno10] G.F. Knoll: *"Radiation Detection and Measurement"*, 4$^{\text{th}}$ edition, Wiley, New York (2010)

[Kob05] K. Kobayashi et al., Super-Kamiokande collaboration: *"Search for nucleon decay via modes favored by supersymmetric grand unification models in Super-Kamiokande-I"*, Phys. Rev. D**72**, 052007 (2005) [arXiv:hep-ex/0502026]

[Kol90] E.W. Kolb and M.S. Turner: *"The Early Universe"*, Frontiers in Physics 69, Westview Press, Boulder (CO), Oxford (1990)

[Kor12] Korth Kristalle GmbH, `http://www.korth.de/index.php/162/items/21.html`, retrieved July 10$^{\text{th}}$, 2012

[Kor12a] Korth Kristalle GmbH, `http://www.korth.de/index.php/162/items/5.html`, retrieved August 21$^{\text{st}}$, 2012

[Kor12b] Korth Kristalle GmbH, `http://www.korth.de/index.php/162/items/18.html`, retrieved September 10$^{\text{th}}$, 2012

[Kos10] S. Koschartz, Maier-Leibnitz-Laboratorium Garching, *private communication* (2010)

[Kra86] L.M. Krauss, M. Srednicki, and F. Wilczek: *"Solar System constraints and signatures for dark-matter candidates"*, Phys. Rev. D**33**, 2079 (1986)

[Kro91] W. Krötz et al.: *"3rd excimer continua in neon and argon"*, Laser Part. Beams **11**, 521 (1991)

[Lan88] H. Langhoff: *"The origin of the third continua emitted by excited rare gases"*, Opt. Comm. **68**, 31 (1988)

[Lan07] J.-C. Lanfranchi, Technische Universität München, *private communication* (2007)

[Lap83] P. Laporte et al.: *"Vacuum-ultraviolet refractive index of LiF and MgF_2 in the temperature range 80-300 K"*, J. Opt. Soc. Am. **73**, 1062 (1983)

[Lar11] D. Larson et al.: *"Seven-Year Wilkinson Microwave Anisotropy Probe (WMAP) Observations: Power Spectra and WMAP-Derived Parameters"*, Astroph. J. Suppl. **192**, 16 (2011) [arXiv:1001.4635v2 [astro-ph.CO]]

[Las05] T. Lasserre and H.W. Sobel: *"Reactor neutrinos"*, Comp. Rend. Phys. **6**, 749 (2005) [arXiv:nucl-ex/0601013]

[Las12] T. Lasserre et al.: *"Comment on Phys. Rev. Lett. 108, 191802 (2012): Observation of Reactor Electron Antineutrino Disappearance in the RENO Experiment"*, arXiv:1205.5626 [hep-ex] (2012)

[LBL12] The Isotopes Project Home Page, `http://ie.lbl.gov/ interact/anfl.pdf`, retrieved March 22nd, 2012

[Len71] B.A. Lengyel: *"Lasers"*, 2nd edition, Wiley, New York (1971)

[Leo87] W.R. Leo: *"Techniques for Nuclear and Particle Physics Experiments"*, Springer, Berlin, Heidelberg (1987)

[Li08] X. Li, Forschungs-Neutronenquelle Heinz Maier-Leibnitz Garching, *private communication* (2008)

[Li11] Y.F. Li and Zhi-zhong Xing: *"Neutrinos as Hot or Warm Dark Matter"*, Acta Phys. Polon. B**42**, 2193 (2011) [arXiv:1110.2293v2 [hep-ph]]

[Lin88] P. Lindblom and O. Solin: *"Atomic near-infrared noble gas scintillations I: Optical spectra"*, Nucl. Instr. Meth. A**268**, 204 (1988)

[Lin11] T. Linden, D. Hooper, and F. Yusef-Zadeh: *"Dark Matter and Synchrotron Emission from Galactic Center Radio Filaments"*, arXiv:1106.5493v2 [astro-ph.HE] (2011)

[Lip08] W. Lippincott et al.: *"Scintillation time dependence and pulse shape discrimination in liquid argon"*, Phys. Rev. C**78**, 035801 (2008) [arXiv:0801.1531v4 [nucl-ex]]

[Lop02] M.I. Lopes, V. Chepel: *"Liquid rare gas detectors: recent developments and applications"*, Proc. 14th ICDL, 405 (2002)

[Lor76] D.C. Lorents: *"The physics of electron beam excited rare gases at high densities"*, Physica B+C**82**, 19 (1976)

[Mac09] K.J. Mack and P.J. Steinhardt: *"Cosmological Problems with Multiple Axion-like Fields"*, arXiv:0911.0418 [astro-ph.CO] (2009)

[Mac09a] K.J. Mack: *"Axions, Inflation and the Anthropic Principle"*, arXiv:0911.0421 [astro-ph.CO] (2009)

[Mac12] P.A.N. Machado et al.: *"Combining Accelerator and Reactor Measurements of θ_{13}; The First Result"*, arXiv:1111.3330v4 [hep-ph]

[Mak62] Z. Maki, M. Nakagawa, and S. Sakata: *"Remarks on the Unified Model of Elementary Particles"*, Progr. Theor. Phys. **28**, 870 (1962)

[Mar08] T. Marrodán: *"Measurement of light emission in organic liquid scintillators and studies towards the search for the proton decay in the future large-scale detector LENA"*, Ph.D. thesis, Technische Universität München (2008)

[Mar11] A. Marchionni et al.: *"ArDM: a ton-scale LAr detector for direct Dark Matter searches"*, J. Phys. Conf. Ser. **308**, 012006 (2011) [arXiv:1012.5967 [physics.ins-det]]

[McC84] M. McCusker: *"The Rare Gas Excimers"* in C.K. Rhodes (ed.): *"Excimer Lasers"*, 2nd edition, Springer Topics in applied Physics 30, Berlin, Heidelberg (1984)

[McK10] D.N. McKinsey et al.: *"The LUX Dark Matter Search"*, J. Phys. Conf. Ser. **203**, 012026 (2010)

[McP12] McPHERSON Inc., `http://www.mcphersoninc.com/spectrometers/vuvuvvis/model218.htm`, retrieved March 26th, 2012

[Med09] E. Mediavilla et al.: *"Microlensing-Based Estimate of the Mass Fraction in Compact Objects in Lens"*, arXiv:0910.3645 [astro-ph.CO] (2009)

[Mei08] D.M. Mei et al.: *"A model of nuclear recoil scintillation efficiency in noble liquids"*, Astropart. Phys. **30**, 12 (2008) [arXiv:0712.2470v2 [nucl-ex]]

[Men08] O. Mena: *"Optimisation of future long baseline neutrino experiments"*, arXiv: 0809.4829 [hep-ph] (2008)

[Men11] G. Mention et al.: *"The Reactor Antineutrino Anomaly"*, Phys. Rev. D**83**, 073006 (2011) [arXiv:1101.2755v4 [hep-ex]]

[Mik85] S.P. Mikheyev and A.Y. Smirnov: *"Resonance Amplification of Oscillations in Matter and Spectroscopy of Solar Neutrinos"*, Sov. J. Nucl. Phys. **42**, 913 (1985)

[Min10] A. Minamino et al., XMASS collaboration: *"XMASS experiment, dark matter search with liquid xenon detector"*, Nucl. Inst. Meth. A**623**, 448 (2010)

[Moe12] R. Möllenberg, Technische Universität München, *private communication* (2012)

[Mor89] E. Morikawa et al.: *"Argon, krypton, and xenon excimer luminescence: From the dilute gas to the condensed phase"*, J. Chem. Phys. **91**, 1469 (1989)

[Mor08] A. Morozov et al.: *"Conversion efficiencies of electron beam energy to vacuum ultraviolet light for Ne, Ar, Kr, and Xe excited with continuous electron beams"*, J. Appl. Phys. **103**, 103301 (2008)

[Mor10] C.E. Mortimer and U. Müller: *"Das Basiswissen der Chemie"*, 10th edition, Thieme, Stuttgart (2010)

[Mot05] D. Motta: *"Simulations for Double Chooz"*, available at `http://neutrino.phys.ksu.edu/MAND-sim/MAND-sim talks/` (2005)

[Mue11] T. Mueller et al.: *"Improved Predictions of Reactor Antineutrino Spectra"*, Phys. Rev. C**83**, 054615 (2011) [arXiv:1101.2663v3 [hep-ex]]

[MUR12] MCNP Utility for Reactor Evolution, `http://lpsc.in2p3.fr/MURE/html/MURE/MURE.html`, retrieved August 25$^{\text{th}}$, 2012

[Nan84] D.V. Nanopoulos, K. Olive, and M. Srednicki: *"Supersymmetric Relics from the Big Bang"*, Nucl. Phys. B**238**, 453 (1984)

[NAS12] NASA/IPAC Extragalactic Database, `http://ned.ipac.cal- tech.edu/`, retrieved January 19$^{\text{th}}$, 2012

[Neu12] A. Neumeier: *"Optical Transmission of Liquid Argon in the Vacuum Ultraviolet"*, Diploma thesis, Technische Universität München (2012)

[Neu12a] A. Neumeier et al.: *"Attenuation of vacuum ultraviolet light in liquid argon"*, submitted to Eur. Phys. Jour. C (2012)

[Nis09] H. Nishino et al., Super-Kamiokande collaboration: *"Search for Proton Decay via $p \to e^+\pi^0$ and $p \to \mu^+\pi^0$ in a Large Water Cherenkov Detector"*, Phys. Rev. Lett. **102**, 141801 (2009) [arXiv:0903.0676v2 [hep-ex]]

[NIS12] NIST atomic spectra database, `http://www.nist.gov/ pml/data/asd.cfm`, retrieved March 19$^{\text{th}}$, 2012

[Obe92] L. Oberauer and F. von Feilitzsch: *"Neutrino Oscillations"*, Rep. Prog. Phys. **55**, 1093 (1992)

[Obe06] L. Oberauer: *"Search for ϑ_{13} with reactor experiments"*, Prog. Part. Nucl. Phys. **57**, 127 (2006)

[Oce12] OceanOptics, `http://www.oceanoptics.com/products/qe65000.asp`, retrieved March 26$^{\text{th}}$, 2012

[Ols09] K.S. Olsen, DEAP/CLEAN collaboration: *"Analysis of alpha backgrounds in the DEAP-1 detector"*, arXiv:0906.0348 [hep-ex] (2009)

[Pal09] C. Palomares, Double Chooz collaboration: *"Double-Chooz Neutrino Experiment"*, PoS EPS-HEP2009 2009:275 (2009) [arXiv:0911.3227 [hep-ex]]

[Pal12] C. Palomares: *"Light-Noise"*, DCDocDB 3824-v1, only available at `http://www.dchooz.org/DocDB/` (2012)

[PDG12] J. Beringer et al., Particle Data Group: *"Review of Particle Physics"*, J. Phys. D**86**, 010001 (2012)

[Pei07] P. Peiffer: *"Liquid argon as active shielding and coolant for bare germanium detectors"*, Ph.D. thesis, Ruprecht-Karls-Universität Heidelberg (2007)

[Pei08] P. Peiffer et al.: *"Pulse shape analysis of scintillation signals from pure and xenon-doped liquid argon for radioactive background identification "*, JINST **3**, P08007 (2008)

[Pen65] A.A. Penzias and R.W. Wilson: *"A Measurement of Excess Antenna Temperature at 4080 Mc/s"*, Astroph. J. **142**, 419 (1965)

[Per00] D.H. Perkins: *"Introduction to High Energy Physics"*, 4th edition, Cambridge University Press, Cambridge (2000)

[Pfa12] P. Pfahler: *"Towards a measurement of the last unknown neutrino mixing angle ϑ_{13} with the Double Chooz Experiment"*, Ph.D. thesis, *in preparation*, Technische Universität München (2012)

[Pol07] T. Pollmann: *"Pulse shape discrimination studies in a liquid Argon scintillation detector"*, Diploma thesis, Max-Planck-Institut für Kernphysik Heidelberg (2007)

[Pon67] B. Pontecorvo: *"Mesonium and anti-mesonium"*, Sov. Phys. JETP **6**, 429 (1957)

[Pov04] B. Povh et al.: *"Teilchen und Kerne"*, 6th edition, Springer, Berlin, Heidelberg (2004)

[Pre94] R. Prem: *"Untersuchung der Excimerlichtemission von Argon in Abhängigkeit von Temperatur und Gasreinheit"*, Diploma thesis, Technische Universität München (1994)

[Pre95] W.H. Press and D.N. Spergel: *"Capture by the sun of a galactic population of weakly interacting, massive particles"*, Astroph. J. **296**, 679 (1985)

[PTB01] Physikalisch-Technische Bundesanstalt: *Calibration certificate PTB-6.11-2001-1557*, Braunschweig (2001)

[PTB01a] Physikalisch-Technische Bundesanstalt: *Calibration certificate PTB-6.11-2001-1668*, Braunschweig (2001)

[PTB01b] Physikalisch-Technische Bundesanstalt: *Calibration certificate PTB-6.11-212/11.2001-1*, Braunschweig (2001)

[Raf85] G. Raffelt: *"Neutrino radiative-lifetime limits from the absence of solar γ rays"*, Phys. Rev. D**31**, 3002 (1985)

[Raf06] G. Raffelt: *"Axions - Motivation, limits and searches"*, J. Phys. A**40**, 6607 (2007) [arXiv:hep-ph/0611118]

[Raf12] G. Raffelt and L.J. Rosenberg: *"Axions and other Similar Particles"*, available online: `http://pdglive.lbl.gov/Rsummary.brl?nodein=S029` (2012)

[Rau11] W. Rau: *"Dark Matter Search Experiments"*, arXiv:1103.5267 [astro-ph.CO] (2011)

[Raz70] B. Raz and J. Jortner: *"Experimental Evidence for Trapped Exciton States in Liquid Rare Gases"*, Proc. Roy. Soc. A**317**, 113 (1970)

[Rib94] G. Ribitzki et al.: *"Electron-densities and temperatures in a xenon afterglow with heavy-ion excitation"*, Phys. Rev. E**50**, 3973 (1994)

[ROO08] W. Verkerke and D. Kirkby: *"RooFit Users Manual v2.91"* (2008)

[Ros00] L.J. Rosenberg and K.A. van Bibber: *"Searches for invisible axions"*, Phys. Rept. **325**, 1 (2000)

[Rub04] A. Rubbia: *"Experiments For CP-Violation: A Giant Liquid Argon Scintillation, Cerenkov And Charge Imaging Experiment?"*, arXiv:hep-ph/0402110 (2004)

[Rub11] C. Rubbia et al. ICARUS collaboration: *"Underground operation of the ICARUS T600 LAr-TPC: first results"*, JINST **6**, P07011 (2011) [arXiv:1106.0975v2 [hep-ex]]

[Sam67] J.A.R. Samson: *"Techniques of vacuum ultraviolet spectroscopy"*, Wiley, London, New York, Sydney (1967)

[Sar96] S. Sarkar: *"Big Bang nucleosynthesis and physics beyond the Standard Model"*, Rep. Prog. Phys. **59**, 1493 (1996) [arXiv:hep-ph/9602260v2]

[Sch66] H.F. Schopper: *"Weak interactions and Nuclear Beta Decay"*, North Holland, Amsterdam (1966)

[Sch85] K. Schreckenbach et al.: *"Determination of the Antineutrino Spectrum from ^{235}U Thermal Neutron Fission Products up to 9.5 MeV"*, Phys. Lett. B**160**, 325 (1985)

[Sch95] P. Schmüser: *"Feynman-Graphen und Eichtheorien für Experimentalphysiker"*, 2nd edition, Springer, Berlin, Heidelberg (1995)

[Sch97] N. Schmitz: *"Neutrinophysik"*, Teubner-Studienbücher, Stuttgart (1997)

[Sch12] K. Schreckenbach, Technische Universität München, *private communication* (2012)

[Sei02] G.M. Seidel, R.E. Lanou, and W. Yao: *"Rayleigh scattering in rare-gas liquids"*, Nucl. Instr. Meth. A**489**, 189 (2002) [arXiv:hep-ex/0111054v2]

[Sel82] S.M. Seltzer and M.J. Berger: *"Evaluation of the Collision Stopping Power of Elements and Compounds for Electrons and Positrons"*, Int. J. Appl. Radiat. Isot. **33**, 1189 (1982)

[Sex02] R.U. Sexl and H.K. Urbantke: *"Gravitation und Kosmologie"*, 5th edition, Spektrum Akademischer Verlag, Heidelberg, Berlin (2002)

[Shi99] X. Shi and G.M. Fuller: *"New Dark Matter Candidate: Nonthermal Sterile Neutrinos"*, Phys. Rev. Lett. **82**, 2832 (1999)

[Smi51] W.E. Forsythe: *"Smithsonian Physical Tables"*, 9th revised edition, The Lord Baltimore Press, Smithsonian Institution (1951)

[Smo97] G.F. Smoot: *"The Cosmic Microwave Background Spectrum"*, arXiv:astro-ph/9705101v2 (1997)

[Smo08] A.A. Smolnikov, GERDA collaboration: *"Status of the GERDA experiment aimed to search for neutrinoless double beta decay of ^{76}Ge"*, arXiv:0812.4194 [nucl-ex] (2008)

[Sow82] U. Sowada, J.M. Warman, and M.P. de Haas: *"Hot-electron thermalization in solid and liquid argon, krypton, and xenon"*, Phys. Rev. B**25**, 3434 (1982)

[Spe07] D.N. Spergel et al.: *"Three-Year Wilkinson Microwave Anisotropy Probe (WMAP) Observations: Implications for Cosmology"*, Astroph. J. Suppl. **170**, 377 (2007) [arXiv:astro-ph/0603449]

[Sta11] I. Stancu: *"RecoBAMA with and without Time Offsets: MC and Data"*, DCDocDB 2573-v1, only available at `http://www.dchooz.org/DocDB/` (2011)

[Sta12] Stanford Research Systems, `http://www.thinksrs.com/products/DG535.htm`, retrieved August 22nd, 2012

[Sto11] L. Stodolsky: *"Features of Fast Neutrons in Dark Matter Searches"*, Astropart. Phys. **35**, 114 (2011) [arXiv:1009.3791v2 [astro-ph.IM]]

[Str05] A. Strumia and F. Vissani: *"Implications of neutrino data circa 2005"*, Nucl. Phys. B**726**, 294 (2005) [arXiv:hep-ph/0503246]

[STS12] Process Measurement & Controls, Inc., STS Sensors, `http://www.pmc1.com/Capability.asp?CapabilityID=1057&Cat1ID=1179`, retrieved August 24th, 2012

[Stu12] A. Stüken: *"Trigger efficiency for 2nd pub (including new energy scale)"*, DCDocDB 3966-v2, only available at `http://www.dchooz.org/DocDB/` (2012)

[Sue79] T. Suemoto and H. Kanzaki: *"Time-resolved absorption spectroscopy of self-trapped excitons in condensed Ne, Ar, and Kr"*, J. Phys. Soc. Jpn. **46**, 1554 (1979)

[Tak75] T. Takahashi et al.: *"Average energy expended per ion pair in liquid xenon"*, Phys. Rev. A**12**, 1771 (1975)

[Tam12] Endress+Hauser, `http://www.endress.com/eh/home.nsf/#product/NMS5`, retrieved August 24th, 2012

[Tan11] T. Tanaka et al., Super-Kamiokande collaboration: *"An Indirect Search for WIMPs in the Sun using 3109.6 days of upward-going muons in Super-Kamiokande"*, Astroph. J. **742**, 78 (2011) [arXiv:1108.3384v2 [astro-ph.HE]]

[Tar08] O.B. Tarasov and D. Bazin: *"LISE++: Radioactive beam production with in-flight separators"*, Nucl. Instr. Meth. B**266**, 4657 (2008) [online: `http://lise.nscl.msu.edu`]

[Ter08] A. Terashima et al.: *"R&D for possible future improvements of KamLAND"*, J. Phys. Conf. Ser. **120**, 052029 (2008)

[Ter11] K. Terao: *"DCProd Manual"*, DCDocDB 2670-v1, only available at `http://www.dchooz.org/DocDB/` (2011)

[Tis07] P. Tisserand et al.: *"Limits on the Macho content of the Galactic Halo from the EROS-2 Survey of the Magellanic Clouds"*, A&A **469**, 387 (2007) [arXiv:astro-ph/0607207v2]

[Tro11] S. Troitsky: *"Unresolved problems in particle physics"*, arXiv:1112.4515 [hep-ph] (2011)

[TUN04] Triangle Universities Nuclear Laboratory (TUNL), Nuclear Data Evaluation: `http://www.tunl.duke.edu/nucldata/`, retrieved February 7$^{\text{th}}$, 2012

[Ulr87] A. Ulrich et al.: *"Heavyion excitation of raregas excimers"*, J. Appl. Phys. **62**, 357 (1987)

[Ulr11] A. Ulrich, Technische Universität München, *private communication* (2011)

[Ulr12] A. Ulrich: *"Light emission from particle beam induced plasma: An overview"*, Laser Part. Beams, *First View Articles* (2012)

[Ulr12a] A. Ulrich, Technische Universität München, *private communication* (2012)

[Var83] N.B. Vargaftik: *"Handbook of physical properties of liquids and gases - pure substances and mixtures"*, 2$^{\text{nd}}$ edition, Hemisphere Pub. Corp., Washington, USA (1983)

[Vas90] A.A. Vasenko et al.: *"New Results in the ITEP/YePI Double Beta-Decay Experiment with Enriched Germanium Detectors"*, Mod. Phys. Lett. A**5**, 1299 (1990)

[Veg10] H.J. de Vega and N.G. Sanchez: *"Model independent analysis of dark matter points to a particle mass at the keV scale"*, Mon. Not. R. Astron. Soc. **404**, 885 (2010) [arXiv:0901.0922v3 [astro-ph.CO]]

[Vik06] A. Vikhlinin et al.: *"Chandra Sample of Nearby Relaxed Galaxy Clusters: Mass, Gas Fraction, and Mass-Temperature Relation "*, Astroph. J. **640**, 691 (2006) [arXiv:astro-ph/0507092]

[Vit09] V. Vitale and A. Morselli, Fermi/LAT collaboration: *"Indirect Search for Dark Matter from the center of the Milky Way with the Fermi-Large Area Telescope"*, arXiv:0912.3828 [astro-ph.HE] (2009)

[Wag12] S. Wagner: *"Production and Properties of the Liquid Scintillators in the Double Chooz Experiment and their Influence on Data Analysis"*, Ph.D. thesis, *in preparation*, Ruprecht-Karls-Universität Heidelberg

[Wei74] S. Weinberg: *"Recent progress in the gauge theories of the weak, electromagnetic and strong interactions"*, Rev. Mod. Phys. **46**, 255 (1974)

[Wie00] J. Wieser et al.: *"Novel pathways to the assignment of the third rare gas excimer continua"*, Opt. Comm. **173**, 233 (2000)

[Wil77] W.D. Wilson, L.G. Haggmark, and J.P. Biersack: *"Calculations of nuclear stopping, ranges, and straggling in the low-energy region "*, Phys. Rev. B**15**, 2458 (1977)

[Wil83] H. Wilcke et al.: *"High Flux and High Resolution VUV Beam Line for Luminescence Spectroscopy"*, Nucl. Instr. Meth. **208**, 59 (1983)

[Win10] W. Winter: *"Performance Comparison: Superbeams, Beta Beams, Neutrino Factory"*, arXiv:1011.4468 [hep-ph] (2010)

[Wol78] L. Wolfenstein: *"Neutrino oscillations in matter"*, Phys. Rev. D**17**, 2369 (1978)

[Wri11] A. Wright, DarkSide collaboration: *"The DarkSide Program at LNGS"*, arXiv: 1109.2979 [physics.ins-det] (2011)

[Wu57] C.S. Wu et al.: *"Experimental Test of Parity Conservation in Beta Decay"*, Phys. Rev. **105**, 1413 (1957)

[Zde02] Y.G. Zdesenko, F.A. Danevich, and V.I. Tretyak: *"Has neutrinoless double β decay of ^{76}Ge been really observed?"*, Phys. Lett. B**546**, 206 (2002)

[Zwi37] F. Zwicky: *"On the Masses of Nebulae and of Clusters of Nebulae"*, Astroph. J. **86**, 217 (1937)

Danksagung

An dieser Stelle möchte ich mich ganz herzlich bei all denjenigen bedanken, die zum Gelingen der vorliegenden Arbeit einen mehr oder weniger großen Teil beigetragen haben. An erster Stelle danke ich Prof. Franz von Feilitzsch und seinem Nachfolger Prof. Stefan Schönert für die herzliche Aufnahme am Lehrstuhl E15 und die Möglichkeit, diese Arbeit anfertigen zu können.

Meinem Doktorvater Prof. Lothar Oberauer danke ich für die hervorragende Betreuung und dafür, dass er immer ein offenes Ohr für mich hatte. Ohne seine Ratschläge und Hilfestellungen wäre die vorliegende Arbeit nicht das geworden, was sie ist. Auch werden mir die zahlreichen lustigen Anekdoten aus der Welt der Physik und der Berge in guter Erinnerung bleiben.

Herzlichen Dank an die Mitarbeiter der flüssig-Edelgas-Gruppe, PD Andreas Ulrich, Dr. Thomas Heindl, Thomas Dandl, Alexander Neumeier und Dr. Jochen Wieser, für die tatkräftige Unterstützung bei der Vorbereitung, Durchführung und Auswertung der Experimente. Ohne dieses tolle Team wäre meine Arbeit in der vorliegenden Form niemals möglich gewesen. Danke auch, dass ihr die Geduld mit einem Astroteilchenphysiker hattet, der vor nicht allzu langer Zeit noch keine Ahnung von flüssigem Argon hatte. Thanks also to Dr. Alexander Fedenev for the help in preparing and during the beam times.

Dr. Walter Potzel möchte ich für die (wieder einmal) herausragende Korrektur der Arbeit und seine kritischen Kommentare danken. Durch seinen weitreichenden Wissenschatz hat er meine Arbeit entscheidend bereichert.

Den weiteren (aktuellen und ehemaligen) Mitgliedern der Double Chooz Gruppe am Lehrstuhl E15, Nils Haag, Patrick Pfahler, Vincenz Zimmer, Michael Franke, Dr. Marianne Göger-Neff, Dr. Hong-Hanh Trinh-Thi, Prof. Tobias Lachenmaier und Judith Meyer, danke ich ebenfalls für ihre vielfältigen großen und kleinen Beiträge zu dieser Arbeit, sowie allen, die mit mir auf Dienstreise waren, natürlich für all die schönen Tage und Aktivitäten rund um die diversen "Ausflüge" im Rahmen von Double Chooz.

Beim Umbau und Eichen des Germaniumdetektors, sowie bei der Durchführung einiger Spektroskopien waren mir Moritz von Sivers, Christoph Wiesinger, Thurid Mannel, Andrea Münster und Christian Fruck eine unersetzliche Hilfe - Dankeschön. Die Neutronenaktivierungsanalyse von PPO wäre ohne die Hilfe einiger Kollegen aus Heidelberg, insbesondere Dr. Christian Buck und Ute Schwan, nicht möglich gewesen. Je tiens à remercier Dr Thierry Lasserre et Dr Rachel Quéval pour aider à l'activation par neutrons des échantillons acryliques. Und natürlich auch danke nach Tübingen für die Hilfen und Proben für die Gammaspektrometrie der InnerVeto-Teile.

Many thanks to all of my colleagues of the Double Chooz collaboration. Without the great work of so many physicists from all over the world a project like Double Chooz would never be possible. Keep on measuring ϑ_{13}! I want to thank the members of the EU++ data analysis cluster for their contributions to my work, in particular Ines Gil Botella and Anatael Cabrera for the organisational work and Carmen Palomares Espiga for her advice in the BiPo

analyses and her help in the Monte-Carlo simulations. To all of you: Dankeschön, Thanks, Merci beaucoup, ¡Muchas gracias!

Ein herzliches Dankeschön geht auch an die Werkstätten der Lehrstühle E15 und E12, das technische Personal am Beschleuniger (insbesondere die Operateure) und am FRM II, sowie den Strahlenschutz, die einen ganz entscheidenden Beitrag zum erfolgreichen Gelingen dieser Arbeit beigetragen haben.

Danke an Dominikus Hellgartner für die Hilfe beim Fitten mit RooFit. Allen Mitgliedern des Lehrstuhls E15 (auch wenn sie hier nicht alle namentlich genannt sind) möchte ich auch ganz herzlich danken, nicht nur für ihre Beiträge zu meiner Arbeit, sondern auch für die gute Stimmung am Lehrstuhl und all die Aktivitäten abseits der Physik. Unserer lieben Sekretärin Maria Bremberger danke zusätzlich ich für die unzähligen Hilfen bei Verwaltungsformalitäten und auch den täglichen Weg zu genießbarem Essen.

Großer Dank geht an all meine Freunde und Bekannten, insbesondere die Schaffkopfrunde und die Handballer des TSV Gilching-Argelsried, die mehr zu dieser Arbeit beigetragen haben, als sie vielleicht meinen: Ohne die regelmäßige Abwechslung und Ablenkung von der Physik hätte ich diese Arbeit so sicherlich nicht erstellen können.

Der letzte, aber sicherlich größte Dank geht an meine Familie, ohne die meine Doktorarbeit wohl schon weit vor ihrem Beginn gescheitert wäre. Danke für eure immerwährende Unterstützung in jeglicher Hinsicht und eure Geduld.

Nothing shocks me.
I'm a scientist.

- Indiana Jones